Fault displacement profiles and off-fault deformation: interpreting the record of fault growth at the Chimney Rock fault array, Utah, USA

Zoe K. Shipton

Thesis submitted for the degree of
Doctor of Philosophy

University of Edinburgh
1999

ABSTRACT

As a fault grows and displacement is accumulated on a fault surface through time, deformation is generated in the volume surrounding the fault. Previous studies have tended to only look at parts of this entire fault system in isolation. This thesis is a systematic survey of fault zone architecture at millimetre to kilometre scales, which is linked to variations in fault displacement. Structural data and displacement variations have been measured from two isolated normal faults cutting the Jurassic Navajo Sandstone in the Chimney Rock fault array, Utah, USA. Both faults are approximately four kilometres long with maximum displacements of thirty metres. The faults are surrounded by deformation bands and slip-surfaces typical of deformation in high porosity sandstones. Deformation is seen ahead of the fault tip and to either side of the well-developed fault surface. On average, the width of this zone of deformation is twice the displacement on the main slip surface. This implies that while some deformation is generated ahead of the fault tip (a process zone) deformation is then continuously accumulated after a through-going fault surface has developed, intensifying and widening the zone of off-fault deformation. The latter is referred to as a kinematic damage zone. The relationship between off-fault deformation width and displacement is potentially useful for predicting fault zone architecture below seismic resolution. However the exact form of the scaling relationship is not well controlled and is expected to vary in different lithologies. The off-fault deformation consists of an orthorhombic pattern of deformation bands, with a low angle between strike sets. This can be attributed to a small component of along-strike extensional strain (due to variation in displacement along the fault) combined with larger extensions perpendicular to the fault. This confirms that the off-fault structures are growing in a locally controlled three-dimensional strain field and not in that of the regional fault array. Slip vectors at the fault tip are oblique whereas those on the well-developed fault surface are dip-slip. I interpret these in terms of propagation of a mixed-mode fault tip. Detailed surveys along the faults have revealed displacement profiles that are approximately symmetrical and triangular. The data in this study are of higher resolution than those in other published surveys and confirm that displacement profiles at isolated fault tips are

linear. Existing models of fault growth, based on the growth of a planar crack in an elastic medium, fail to predict linear fault tip gradients and do not incorporate off-fault deformation. The integrated approach taken in this thesis has led to the construction of a more realistic 'slip-patch' model for fault growth. This describes how faults grow by repeated slip on small patches, each of which relieves stress locally but loads the fault along strike at the slip-patch terminations. Post-rupture healing along the slip-patch allows it to support subsequent accumulation of stress. The effect of healing and reloading of slip-patches over many rupture events results in triangular fault displacement profiles with linear tip gradients. The model successfully reproduces the displacement profiles seen in the field. Although the model is essentially two-dimensional, predictions can be made about the distribution of off-fault deformation. Deformation beyond the fault tip, the process zone, will be of limited extent, reflecting the size of the last slip-patch to rupture the fault tip area. By superimposing the effect of stress enhancement at the termination of each slip-patch, the deformation adjacent to the well-developed fault, the kinematic damage zone, is predicted to be more intense at the centre of the fault where more slip events have taken place. To explain my field observations, the additional ingredient of strain hardening is required. In the Navajo Sandstone strain hardening has resulted in the formation of deformation bands at increasing distances from the fault. This highlights the fact that although this model can potentially be applied to the growth of any fault, the specific deformation mechanisms in different host rock lithologies will have an important control on the distribution of off-fault deformation. For instance, strain hardening in high porosity (>10%) sandstones results in the formation of macroscopic deformation bands without producing large population of microfractures such as those reported in other studies. This thesis has led to a better understanding of fault growth and the evolution of off-fault deformation by integrating observations and identifying the mechanisms operating through time. This will have important applications in the prediction of sub-seismic deformation, prediction of the permeability structure of fault zones and the general understanding of brittle fault growth in the Earth's crust.

DECLARATION

This thesis has been composed by myself and it has not been submitted in any previous application for a degree. The work presented is my own except where otherwise acknowledged.

Zoe K. Shipton

This thesis is dedicated to John,
for all the wit and wisdom, music and laughter,
and most of all, happiness,
that he has brought to me and my family.

ACKNOWLEDGEMENTS

Firstly, huge thanks go to Patience Cowie who set me off on the faulty road. She has been an enthusiastic and supportive supervisor, and has worked hard to persuade me and others of my capabilities.

The thesis and my understanding of structural geology have benefited greatly from discussions with: Nancye Dawers, Sanjeev Gupta, Jan Vermilye, Jim Evans, Iain Main, Quentin Fisher, Joe Cartwright, and Martin Casey. The computer modelling for the slip-patch model of fault growth in Chapter 7 was done by Patience Cowie. Kathryn Hardacre, Ruth Gilpin and Ellen Wolfenden have managed never to tell me to go away when I needed to bounce ideas off them. Brian Crawford, Tom Manzocchi and Richard Jackson introduced me to the delightful concept of arguing about faults in the pub. Dave Bailey, Mark Higgins and John Perry were patient computer gurus.

For a number of reasons I have ended up with a longer than usual list of field assistants who have provided help, sanity and cups of tea in the field. They are, in chronological order: Jan Vermilye, John Mayers, Steve Schulz, Amy Hochberg, Kevin Hughes, Kathryn Hardacre, Bertrand Maillot, Clare Bond, Kim Robeson, Jonathan Lim and Steve Thurber. I would like to thank them all for their enthusiasm and good humour, under occasionally difficult and unlikely conditions.

Financial support came from NERC with additional help from Bob Krantz (ARCO). The fourth season of fieldwork was undertaken during a three month suspension while working for the Big Hole Fault Drilling Project, run by Jim Evans at Utah State University.

Thanks to all the computer support and technical staff at Edinburgh University, with special thanks to Mike Hall for putting up with some tricky rocks. Quentin Fisher taught me to fly the SEM spaceship. Nancye Dawers, Ruth Gilpin, Kathryn Hardacre, Iain Main and Fiona Rogers kindly helped to proof-read all or part of the thesis. Sarah and Dave were fantastic thesis fairies.

Huge thanks to all the amazing friends that I have been so lucky to have. You have made my time in (and out) of Edinburgh so much fun. It is impossible to thank everyone who deserves it but, several people have been especially important through some tough times including, in no particular order: Clare, Anna, Ruth, Dave, Katy, Kathryn, Suzie, Sarah, Ben, Sue, Polly, Ellen, Hugh, Rachel, Lynne, Amy, Patricia and many, many others. Leigh was a loving and patient friend for much of my time in Edinburgh, and has left me with a lifetime's expensive CD habit to feed. Shukran to the dancing girls, Lorne, Emily, Roz, Angie, Ailsa, Sofia and Jane, who made Wednesday night a regular island of relaxation and giggles.

Finally my thanks to my family, Ali, Tiggy, John and Nick who have always believed I could make it. Thankyou for listening to me rave about "some ugly brown stone" on every beach we ever walked along. Your support has continued through thick and thin, and I couldn't have done it without you.

TABLE OF CONTENTS

1. INTRODUCTION 1

1.1. Rationale 1

1.1.1. Aims of the thesis 2
1.1.2. Structure of the thesis 4

1.2. Fault terminology 4

1.2.1. The ideal single fault 4
1.2.2. Off-fault deformation 7
1.2.3. Fault displacement and slip 9
1.2.4. Modes of fracture 9

1.3. Observations of faults 11

1.3.1. Displacement-length correlation 11
1.3.2. Fault displacement profiles 12
1.3.3. Off-fault deformation 15

1.4. Mathematical models of fault growth 19

1.4.1. Linear elastic fracture mechanics 19
1.4.2. Inelastic deformation at fault tips 21
1.4.3. Application of the model to real faults 24
1.4.4. Other models of fault growth 25

1.5. Summary 26

2. GEOLOGICAL SETTING 28

2.1. Introduction 28

2.2. Geological setting 28

2.2.1. The San Rafael Swell 28
2.2.2. The Chimney Rock fault array 30
2.2.3. Orthorhombic Faults 32
2.2.4. The Navajo Sandstone 34
2.2.5. The Carmel Formation 36

2.3. Deformation styles 36

2.3.1. Deformation in the Navajo Sandstone 36
2.3.2. Deformation in the Carmel Formation 39

2.4. Study areas 39

2.4.1. The Big Hole fault 39
2.4.2. The Blueberry fault 43

3. DISPLACEMENT PROFILES AND FAULT TIP GRADIENTS 46

3.1. Introduction 46

3.1.1. Rationale 46
3.1.2. Structure of this chapter 46

3.2. Methodology 47

3.2.1. Marker horizons 47
3.2.2. Surveying procedure 47

3.2.3. Constructing displacement profiles 51
3.2.4. Bedding strike 52
3.2.5. Limitations of the technique 52
3.3. Results **54**
3.3.1. Blueberry fault eastern tip 54
3.3.2. Big Hole fault: eastern tip to centre of fault 57
3.3.3. Big Hole fault: western tip 59
3.4. Interpretation **61**
3.4.1. Blueberry fault tip 61
3.4.2. Big Hole fault tips 64
3.4.3. Whole fault displacement profiles 66
3.5. Discussion **68**
3.5.1. Comparison to other tip gradients 68
3.5.2. Tip lines in three dimensions 70
3.6. Summary **71**

4. MACROSCOPIC OFF-FAULT DEFORMATION **73**

4.1. Introduction **73**
4.1.1. Rationale 73
4.1.2. Structure of this chapter 74
4.2. Methodology **74**
4.2.1. Fault-scale maps 74
4.2.2. Outcrop-scale maps 76
4.2.3. Transects 79
4.3. Blueberry fault **80**
4.3.1. The Blueberry fault Tip Canyon 80
4.3.2. Blueberry fault outcrop map 82
4.3.3. Blueberry fault transect 82
4.3.4. Orientations 84
4.4. Big Hole fault east end **86**
4.4.1. The Big Hole fault cluster map 86
4.4.2. Cement Bridge 88
4.4.3. Chipmunk Flat 92
4.4.4. Juniper Flat 99
4.4.5. Jan's cliffs 103
4.4.6. Melon fault 105
4.4.7. Amy's Hill 105
4.4.8. Orientation of structures around the Big Hole fault 108
4.4.9. Big Hole fault west end 110
4.5. Interpretation **112**
4.5.1. Defining the width of off-fault deformation 112
4.5.2. Off-fault deformation scaling 112
4.5.3. The fault core 116
4.5.4. Slip-surfaces 118
4.5.5. Orientations of off-fault deformation features 118
4.6. Summary **122**

5. MICROSCOPIC OFF-FAULT DEFORMATION **124**

5.1. Introduction **124**

5.1.1. Rationale 124
5.1.2. Structure of this chapter 125

5.2. Methodology **125**

5.2.1. Deformation band microstructure 125
5.2.2. Microfracture density 128

5.3. Results **132**

5.3.1. Host rock 132
5.3.2. Single-strand deformation bands 135
5.3.3. Zones of deformation bands 138
5.3.4. Slip surfaces 142
5.3.5. Fault planes 144
5.3.6. Microfracture density 147

5.4. Interpretation **149**

5.4.1. Porosity and grain size reduction 149
5.4.2. Microfracture density 151

5.5. Discussion **154**

5.5.1. Growth of deformation band clusters 154
5.5.2. Slip-surface initiation 154
5.5.3. Fluid flow through deformation bands 157
5.5.4. Microfracture density 159
5.5.5. Scaling of off-fault deformation 162

5.6. Summary **162**

6. OFF-FAULT STRAIN 165

6.1. Introduction **165**

6.1.1. Rationale 165
6.1.2. Structure of this chapter 165

6.2. Variation of strain along fault strike **166**

6.2.1. Methodology 166
6.2.2. Results 169

6.3. Variation of strain within the off-fault deformation zone **173**

6.3.1. Methodology 173
6.3.2. Results: Outcrop-scale maps 175
6.3.3. Results: Blueberry and Big Hole fault cluster maps 182

6.4. Orthorhombic symmetry and three-dimensional strain **185**

6.4.1. Introduction 185
6.4.2. Methodology 185
6.4.3. Results 189

6.5. Discussion **194**

6.5.1. Deformation density 194
6.5.2. Three-dimensional strain 196
6.5.3. Fault slip vectors 198
6.5.4. Variation between the fault tip and fault centre 199

6.6. Summary **200**

7. DISCUSSION 202

7.1. Introduction 202

7.2. Summary of displacement and off-fault deformation data 202

7.2.1. Displacement profiles 202
7.2.2. Off-fault deformation 203
7.2.3. Microstructures 204

7.3. Categories of off-fault deformation 205

7.3.1. The process zone 205
7.3.2. The kinematic damage zone 207
7.3.3. The linkage damage zone 208

7.4. The slip-patch model of fault growth 209

7.4.1. Conceptual framework 209
7.4.2. The slip-patch model 212
7.4.3. Implications of the slip-patch model for displacement profiles 216
7.4.4. Implications of the slip-patch model for off-fault deformation 220

7.5. The slip-patch model applied to the Big Hole and Blueberry faults 223

7.5.1. The Big Hole and Blueberry fault displacement profiles 223
7.5.2. The Blueberry fault process zone 225
7.5.3. The kinematic damage zone of the Big Hole and Blueberry faults 226

7.6. Integrated model for off-fault deformation and displacement accumulation through time 229

7.6.1. Evolution of a single isolated fault 229
7.6.2. Damage associated with fault linkage 231

8. CONCLUSIONS AND FUTURE WORK 234

8.1. Conclusions 234

8.2. Suggestions for future work 238

1. INTRODUCTION

1.1. Rationale

Faults are four-dimensional features: deforming a three-dimensional volume of rock and evolving through time. As a fault develops, strain is accommodated both on the main fault plane and within the rock around the fault. As displacement is accumulated on the fault it increases in length, propagating into undeformed rock at its margins. Deformation will occur away from the fault surface as a result of increased slip on the main fault, and due to propagation of the fault through previously unfaulted rock. A fault must therefore be considered as an inter-linked system consisting of slip along the main fault surface and deformation within a volume around that surface, accumulating strain (increasing in size and complexity) through time.

Previous studies of faults have tended to only look at parts of this entire fault system in isolation. Studies of the deformation around fault surfaces, often motivated by the search for systematics in the distribution of sub-seismic deformation, take the form of maps of fault geometry. These maps are only snapshots of the fault's evolution in time and are, in many cases, two-dimensional slices through the three-dimensional faulted volume. Rock deformation experiments allow the evolution of structures through time to be investigated, but are limited in time and length scales. Analytical fault growth models based on the accumulation of displacement through time have been limited, for computational simplicity, to two dimensions. In such models displacement accumulation is confined to the fault surface and deformation away from the main fault is not considered. This thesis presents a systematic study of fault zone architecture at several scales linked to displacement variation along fault strike and interpreted in terms of fault evolution. This process-oriented approach is critical to the understanding of fault growth and the geometry of off-fault deformation.

Existing data on along-strike displacement profiles are rarely of high enough resolution to distinguish the details of the displacement distribution at fault tips.

Fault tips are important because this is the region where fault propagation occurs. It has been suggested that the shape of the displacement profile depends on the properties of the rock through which the fault is propagating (Cowie and Scholz 1992a, Bürgmann *et al.* 1994). Thus the form of the fault tip displacement profile may contain information on the growth processes of faults. Additionally, fault displacement profiles for different numerical and analytical models of fault growth differ from one another markedly near the fault tip. A detailed survey of the displacement profile at an isolated (non-interacting) fault tip is therefore required to discriminate between different growth models. The survey in this thesis represents probably the highest resolution displacement data at a fault tip to date.

Characterising the architecture of structures in the zone of deformed rock around the main fault plane will help to constrain different fault growth models. In addition, the permeability of the fault zone depends critically on the geometry, intensity and connectivity of fracture and fault networks (Manzocchi *et al.* 1998) and on the repeated dilation and sealing of open fractures through time as the fault grows (Sibson 1977, Underhill and Woodcock 1987). Thus the architecture of this zone is important for studies of fluid flow through, or around, fault networks. Previous studies of fault zone architecture have focused on geometrical descriptions of off-fault damage (McGrath and Davison 1995, Martel and Boger 1998) and on quantifying the amount of strain represented by such deformation (Jamison and Stearns 1982, Little 1996). This study aims instead to quantify how the architecture of the zone of deformed rock around individual faults is controlled by the process of fault development and how this relates to the evolution of the fault displacement profile.

1.1.1. Aims of the thesis

The primary aim of this thesis is to evaluate and improve models of fault growth through time, using field data collected from an array of faults in the San Rafael Desert, central Utah, USA. This is an integrated study of fault displacement profiles and off-fault deformation with an emphasis on the evolution of the faults through

time. Small faults are often undetected in seismic reflection surveys, but may contribute significantly to the hydraulic properties of a hydrocarbon reservoir or aquifer. The Chimney Rock fault array is a network of medium sized faults (maximum displacement 30 m), which are close to the resolution limits of most modern-day 3D seismic datasets. They offset the aeolian Navajo Sandstone and are surrounded by zones of cataclasis with low permeability. Investigating the growth of these faults, and the off-fault deformation that surrounds them, will improve understanding of sub-seismic scale fault populations and therefore improve calculations of fluid flow in and around fault surfaces.

Fault tips are notoriously hard to map: a fault is recognised where it displaces some previously continuous geological marker, and the very small displacements that exist towards the tips can be hard to identify. One of the two faults studied here has a tip that is exceptionally well exposed. The form of the outcrop allows detailed displacement measurements as well as the quantification of the style and geometry of deformation around the tip. A high precision laser theodolite has been used to survey the faults in detail and to include these very small offsets in the fault displacement profiles. These data have then been compared with model predictions in order to re-evaluate the models and to help explain observed fault characteristics in a more realistic way.

This thesis presents the results of integrated mapping and petrographic analysis of two kilometre-scale faults in the high porosity Navajo Sandstone, and interprets the mechanisms of fault growth and development of faulting in this lithology. Detailed outcrop measurements of fault displacement and fracture geometry (from mm to km scale) reveal details of the fault zone structure. This has been achieved by characterising the style, intensity and relative timing of off-fault deformation at different scales and relating these to the displacement on the faults. Microstructural studies of this deformation have been used to investigate the mechanism of inelastic deformation that occurs during fault growth.

1.1.2. Structure of the thesis

This chapter is intended to provide a background to the thesis, introducing the terminology used throughout the thesis and some of the concepts and previous work that lie behind the study. Chapter 2 introduces the field area and lithologies that are going to be studied and provides some geological background to the project.

Chapter 3 presents the results of extremely high-resolution surveys of fault displacement profiles, concentrating on the fault tip region. The results of these surveys indicate that existing fault growth models are inadequate and that an alternative model is required. Chapters 4 and 5 present a systematic examination of the macroscopic and microscopic deformation around the fault, respectively. The geometry and scaling of the zone of deformed rock surrounding faults is linked to the displacement profile.

Chapter 6 presents interpretations of the data in terms of the strain represented by the structures. The results of all the chapters are synthesised in Chapter 7 and are discussed in the light of a new model for fault growth. This has resulted in the formulation of a new conceptual genetic model for the formation of off-fault deformation structures. A summary of the results in this thesis is presented in Chapter 8, followed by recommendations for future work that arise from this study.

1.2. Fault terminology

Fault terminology is not universally adhered to in the literature. This section defines the terms that are used in this thesis.

1.2.1. The ideal single fault

All faults are three-dimensional surfaces of finite extent. An 'ideal' single fault is a fault that does not intersect the surface as it grows and does not interact with any other faults (Walsh and Watterson 1987). Displacement, D, on an ideal fault ranges from a maximum at the centre, D_{max}, to zero at the tip line (Figure 1.1a). The tip line is approximately elliptical with contours of equal displacement forming concentric

ellipses about the maximum (Figure 1.1b) (Rippon 1985, Barnett *et al.* 1987, Walsh and Watterson 1987). The maximum horizontal dimension of a fault is the length, L, and its maximum vertical dimension is the height, H. From coal mine data (Rippon 1985) and faults reconstructed from offshore seismics (Barnett *et al.* 1987), it can be seen that fault ellipses have average L:H ratios between 1.25-3.0.

Displacement on a fault is defined by the offset of markers. The line of intersection between a planar marker and the fault surface is called the cut-off. Thus, for a normal fault, there is a hangingwall cut-off and footwall cut-off for the downthrown and uplifted blocks respectively (Figure 1.1a). An offset marker horizon gives the magnitude of displacement; the slip direction must also be measured in order to characterise the displacement vector fully. Slickenlines on the fault surface indicate the direction of the slip vector, and thus the true fault displacement can be quantified.

The fault trace is the line of intersection of the fault surface and the plane of observation (Figure 1.1b). This may not coincide with the centre line of the fault and therefore will define a chord on the fault ellipse. The maximum displacement measured on a fault trace must therefore be equal to or less than the D_{max} on the entire fault. Normalised displacement profiles along chords on the fault surface are not significantly different from those on the radius of the fault ellipse if the fault has a simple theoretical elliptical displacement profile (Walsh and Watterson 1987, Gupta and Scholz 1999 *in review*). However real faults have more complicated displacement distributions (Section 1.3.2) and so the displacement profile of a real fault may well vary depending on the location of the fault trace with respect to the centre of the fault (e.g. Gupta and Scholz 1999 *in review*). The length of a fault is usually defined as the tip to tip distance along its trace. This definition will tend to systematically underestimate the length of faults with complex fault trace geometries.

Although faults accommodate displacement on a relatively discrete plane, additional strain is geometrically necessary in the volume around the fault (Figure 1.1a). This can take the form of ductile flexure (reverse drag) of the beds around the fault surface, or brittle deformation on subsidiary faults. The magnitude of the flexure can

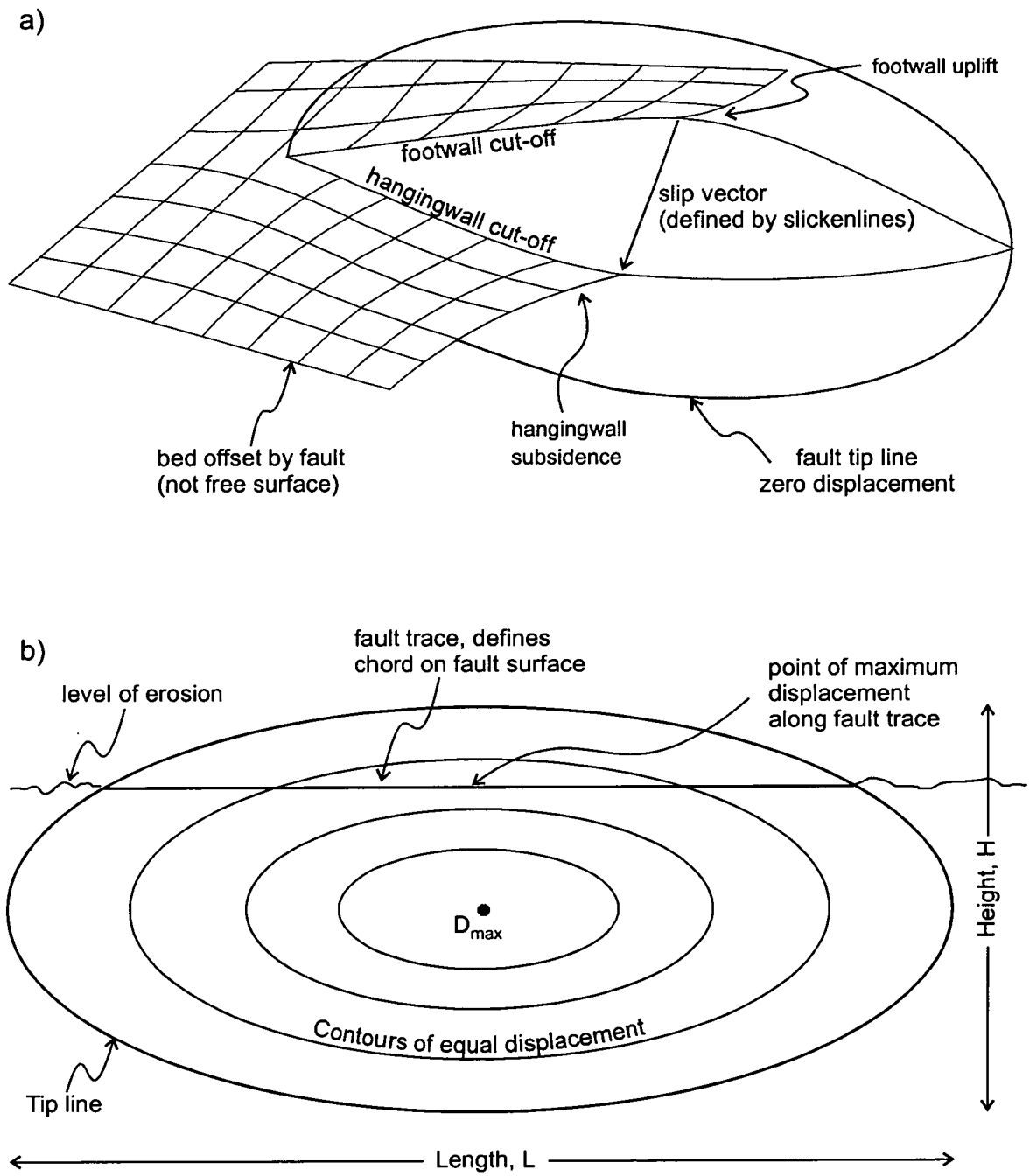

Figure 1.1. Features of an ideal single fault. a) Cartoon of a fault offsetting a gridded bedding plane with hangingwall subsidence and footwall uplift. The elliptical fault surface is shown in grey. b) Fault dimensions for an ideal single fault with an elliptical tip line. The length, L, is the maximum horizontal dimension of the fault surface, and the height, H, is the maximum vertical dimension. The maximum displacement, Dmax, occurs at the centre of the fault. The fault trace is the intersection of the fault surface with the topographic surface following erosion.

be accurately predicted by elastic models (Gupta and Scholz 1998, Gibson *et al.* 1989, Barnett *et al.* 1987) and is often referred to as reverse drag or rollover (Figure 1.1a). Observed large-scale normal faults often have asymmetrical uplift and subsidence with as much as ten times more hangingwall subsidence than footwall uplift (e.g. Stein and Barrientos 1985, Jackson and McKenzie 1983). This can be ascribed to the fault dip, free-surface effects, isostatic compensation and the effect of loading by sedimentation in the hangingwall. However small faults, which are not influenced by isostasy or sedimentation, can have symmetrical uplift and subsidence (Gupta and Scholz 1998). Brittle structures around faults are discussed in Section 1.4.2.

Single ideal faults grow by radial propagation, increasing in length by propagation of the tip line (Figure 1.2a). However isolated single faults are unusual in nature, and many faults are instead made up of a number of discrete segments (Figure 1.2b). Faults can grow by the interaction and linkage of such segments (Scholz *et al.* 1993, Cartwright *et al.* 1995 a and b, Dawers and Anders 1995). The region where displacement is transferred between segments is called a segment boundary, or relay ramp. When a fault has linked in such a way that it behaves as a single system it is said to be hard linked and to have geometric coherence (Walsh and Watterson 1991). Faults can link both along strike and down dip. Down-dip linkage of faults had been investigated by Willemse (1996) and Mansfield and Cartwright (1996).

1.2.2. Off-fault deformation

Faults are commonly surrounded by zones of fractures apparently associated with the growth and development of that fault (Figure 1.3). Chester and Logan (1986a) and Caine *et al.* (1996) describe the zone where slip is localised is referred to as the *fault core*, and the deformed area around the fault as the *damage zone*. Fault cores can range from single zones of cataclasis or gouge (Chester and Logan 1986a) to brecciated and geochemically altered zones (Sibson 1977), but are in all cases the zone where the majority of the displacement in the fault system is localised. Deformation around the fault can be a result of fault rupture events, propagation of

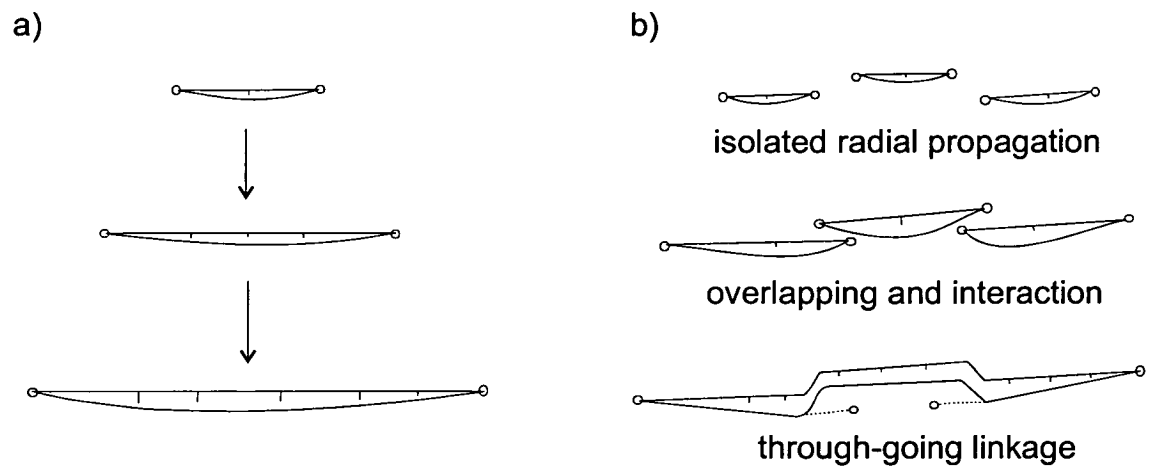

Figure 1.2. Conceptual model for the growth of a) an ideal single fault growing by radial propagation and b) a fault growing by linkage of three segments (after Cartwright *et al.* 1995a). See Figure 1.6 for the displacement profiles and D_{max} /L plots for these examples.

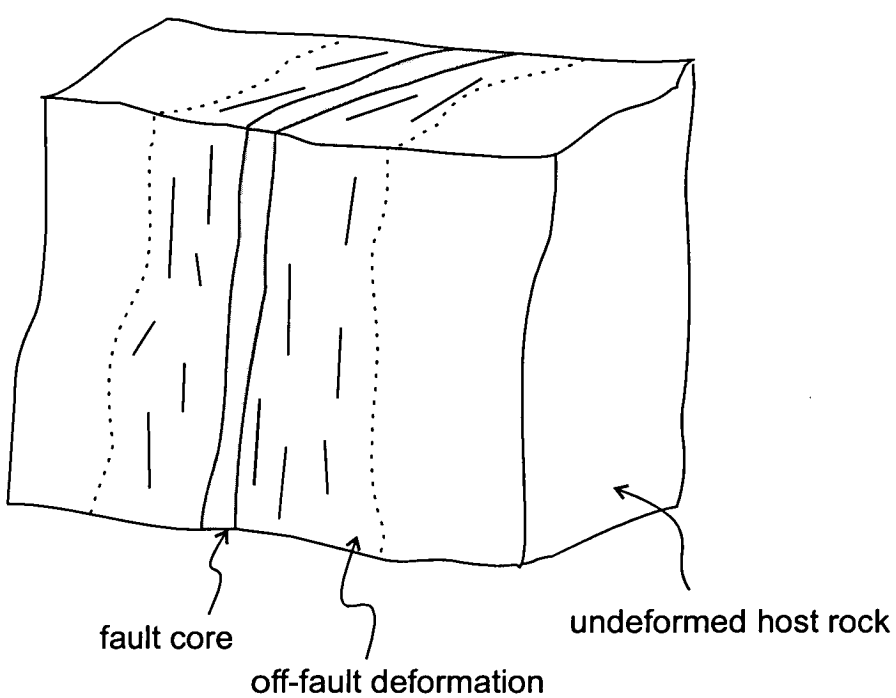

Figure 1.3. Cartoon of a fault surrounded by an off-fault deformation zone.

the fault tip, or flexure of the rock in the volume around a fault to accommodate displacement (Section 1.2.1). The processes of off-fault deformation can be extremely variable between rock types and at different scales. Deformation at fault tips is often referred to as the *process zone*. This reflects the concept that the fault must deform or 'process' the rock in some way before it can propagate through undamaged host rock (Section 1.4.1).

These terms are often used interchangeably in the literature, therefore in this thesis, the term *off-fault deformation* is used to describe all deformation around the fault. This term is intended to be purely descriptive and not to imply a particular genesis for the deformation. In Chapter 7, definitions for different categories of off-fault deformation are revised in the light of the faults studied in this thesis.

1.2.3. Fault displacement and slip

Walsh and Watterson (1987) distinguish between fault displacement and slip. The *displacement* on the fault refers to the total cumulative offset resulting from all deformation during the active lifetime of the fault, whereas *slip* refers to the offset accumulated during one deformation event, either through earthquakes or aseismic creep. Although other definitions of displacement and slip have been used (e.g. Bürgmann *et al.* 1994), this is the terminology used in this thesis.

1.2.4. Modes of fracture

Three fundamental modes of fracturing are recognised (Scholz 1990) (Figure 1.4). Mode I fracture occurs at the edge of extensional cracks and is characterised by slip occurring normal to both the crack plane and the edge of the crack. It is analogous to a wedge being driven into a solid. Mode II consists of the slip vector being in the plane of the crack and normal to the crack edge (in-plane shear). This is equivalent to an edge dislocation. Mode III fracturing comprises the slip vector being in the plane of the crack and parallel to the edge of the crack (anti-plane shear), and is equivalent to a screw dislocation.

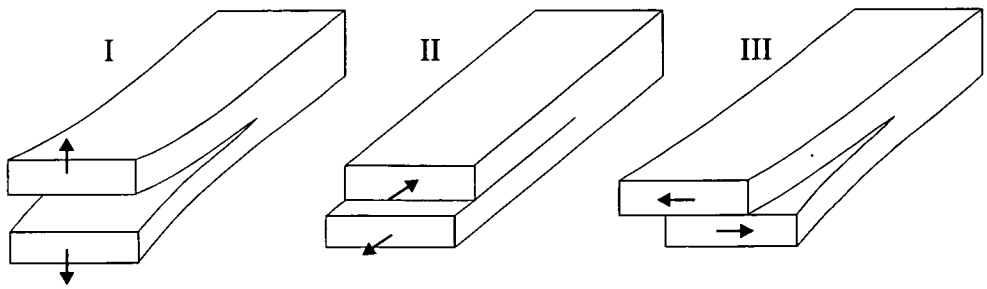

Figure 1.4. The three modes of fracture. I, opening mode or tensile; II, in-plane shear; III, anti-plane shear, from Scholtz (1982).

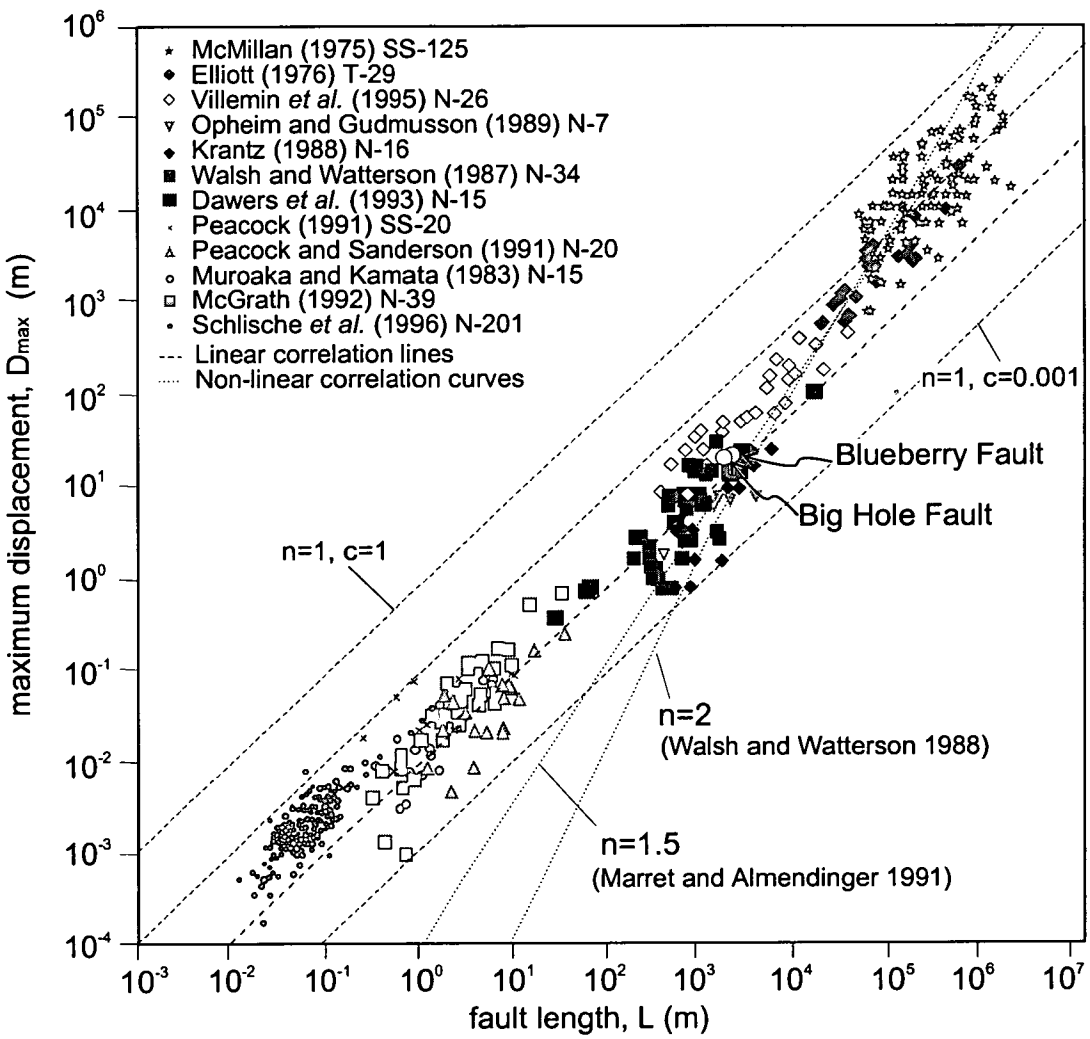

Figure 1.5. Log-log plot of maximum displacement vs. length for a number of fault populations, after Schlische *et al.* (1996). The two faults examined in this study are highlighted (the Big Hole and Blueberry faults). Each different symbol represents a set of results obtained by different workers. The type of fault (N=normal, SS=strike-slip, T=thrust) and the number of data points in each datset is indicated. See Cowie and Scholz (1992b), Schlische *et al.* (1996) and Clark and Cox (1996) for a detailed discussion of the data.

These modes can be superimposed to generalise for all crack tips. A dip-slip normal fault grows in Mode III at its laterally propagating tips and in Mode II at its upwards and downwards propagating tips. By definition, joints always propagate in Mode I.

1.3. Observations of faults

1.3.1. Displacement-length correlation

A positive correlation between the maximum displacement on a fault and its length exists over a scale range of several orders of magnitude (Figure 1.5). This has been interpreted in terms of fault growth: as the displacement on a fault increases, the fault grows in length. Data has been collected from a large range of areas, (McMillan 1975, Elliott 1976, Muraoka and Kamata 1983, Walsh and Watterson 1987, Krantz 1988, Opheim and Gudmundsson 1989, Peacock 1991, Peacock and Sanderson 1991, McGrath 1992, Dawers *et al.* 1993, Villemin *et al.* 1995, Schlische *et al.* 1996, Cartwright and Mansfield 1998) and although there is an order of magnitude scatter in both D_{max} and L, this relationship seems to be consistent regardless of rock type, fault style and tectonic environment. This relationship is also seen for Mode I fractures (Vermilye and Scholz 1995).

The relationship between the maximum displacement on a fault and length is described by a power law of the form,

$$D_{max} = nL^{c}, \qquad (1.1)$$

where D_{max} is maximum displacement, L is length of the fault, n is a constant and c is the slope of the line on a log-log plot. Differences of opinion exist about the precise form of this relationship: that is, whether the relationship is linear (Cowie and Scholz 1992c, Schlische *et al.* 1996) or has an exponent greater than 1.0 (Walsh and Watterson 1988, Marret and Allmendinger 1991, Gillespie *et al.* 1992), and whether it is possible to relate faults in different tectonic environments (Cowie and Scholz 1992c). However a linear relation is generally seen for individual fault populations, i.e. those within a particular rock type and tectonic setting (Dawers *et al.* 1993, Clark

and Cox 1996). The power law that can be fitted to the global dataset applies over eight orders of magnitude (Schlische *et al.* 1996)

This relationship implies that processes of fault growth result in a constant displacement/length ratio, of about 10^{-2}, as faults grow (Figure 1.6a). This is referred to as self-similar fault growth. The distribution of displacement on a fault reflects the physical properties of the host rock (Cowie and Scholz 1992a, Bürgmann *et al.* 1994), the history of slip events on the fault (Walsh and Watterson 1987, Peacock and Sanderson 1996) and the growth of the fault by linkage of fault segments (Figure 1.6b). A mathematical model that could accurately predict displacement as a function of distance along a fault would be a useful tool, for example, to estimate the length of faults that exist below the level of seismic resolution in oil reservoirs (Gauthier and Lake 1993, Pickering *et al.* 1997) or to estimate the total strain due to a population of faults in an area (Scholz and Cowie 1990, Marret and Allmendinger 1991).

1.3.2. Fault displacement profiles

Along-strike displacement profiles have been measured from a variety of different areas using many different techniques. Most published profiles appear to have a triangular or flat-topped shape with the maximum displacement in the centre of the mapped fault trace and the displacement decreasing to zero at the fault tip (Figure 1.7) (Muraoka and Kamata 1983, Walsh and Watterson 1987, Dawers *et al.* 1993, Schlische *et al.* 1996, Gross *et al.* 1997, Cartwright and Mansfield 1998). Real fault displacement profiles are rarely smooth and a variety of factors have been suggested which could influence the form of the profile.

Displacement profiles are influenced by change in lithology (Muraoka and Kamata 1983, Gross *et al.* 1997), and the length scale of lithology variation seems to control the form of the profile. Dawers *et al.* (1993) found that faults up to a critical length had triangular profiles (Figure 1.7a), and that longer faults had flat topped profiles (Figure 1.7b). They interpreted this as a consequence of the finite thickness of the welded tuff layer that the faults grew in. When the faults break through an entire

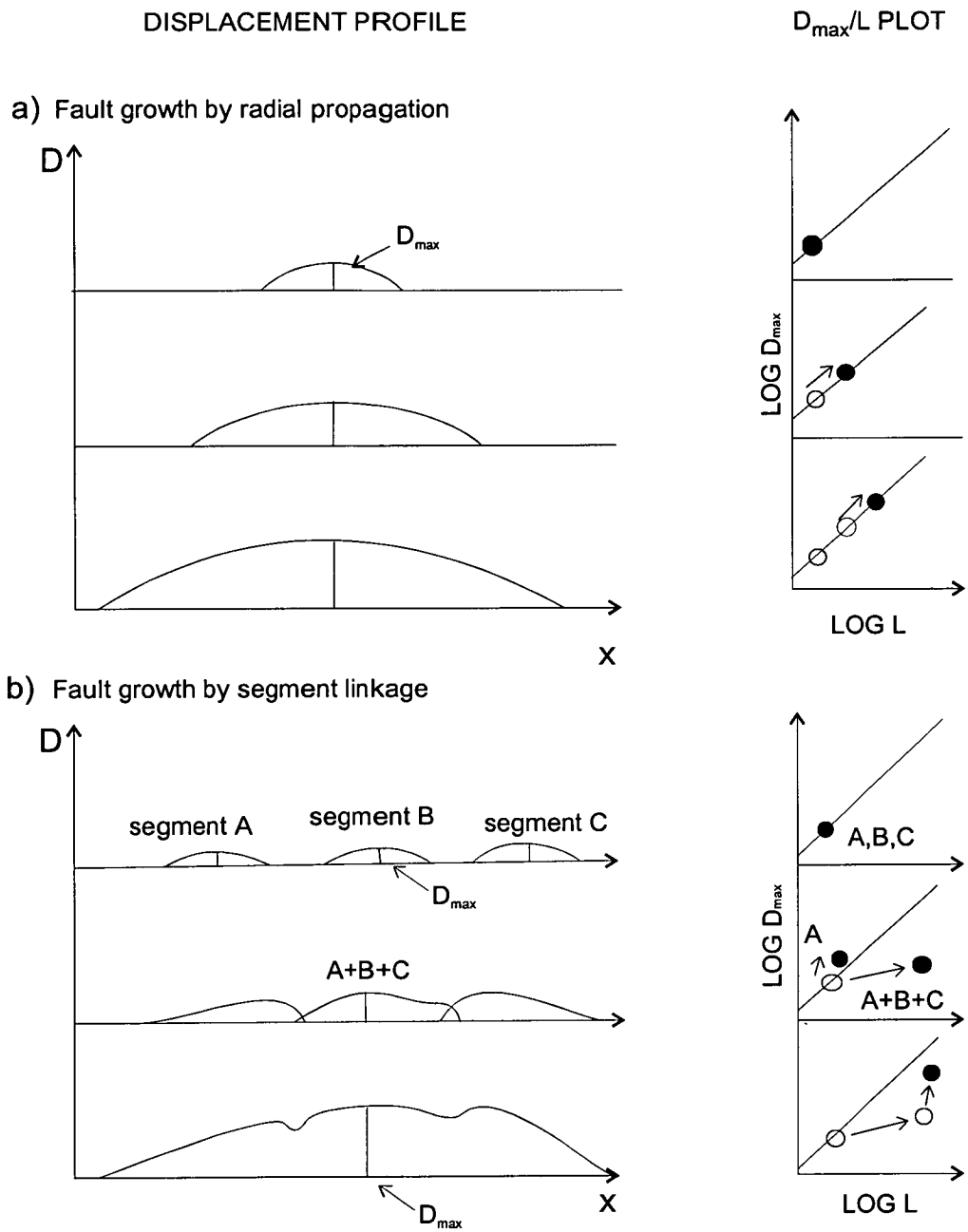

Figure 1.6. Displacement profile and D_{max}/L plot for the growth of a) an ideal single fault and b) three linked segments (after Cartwright *et al.* 1995a). The faults are shown in plan view in figure 1.2. In a) the fault grows by radial propagation with a constant D_{max}/L ratio (self-similar fault growth). In b) three initially isolated fault segments grow by radial propagation until they interact. The new linked system has a greater length than a single fault with the same displacement. The fault then accumulates displacement to re-adjust back to the D_{max}/L ratio expected for a fault of that length. Note the persistent displacement minima.

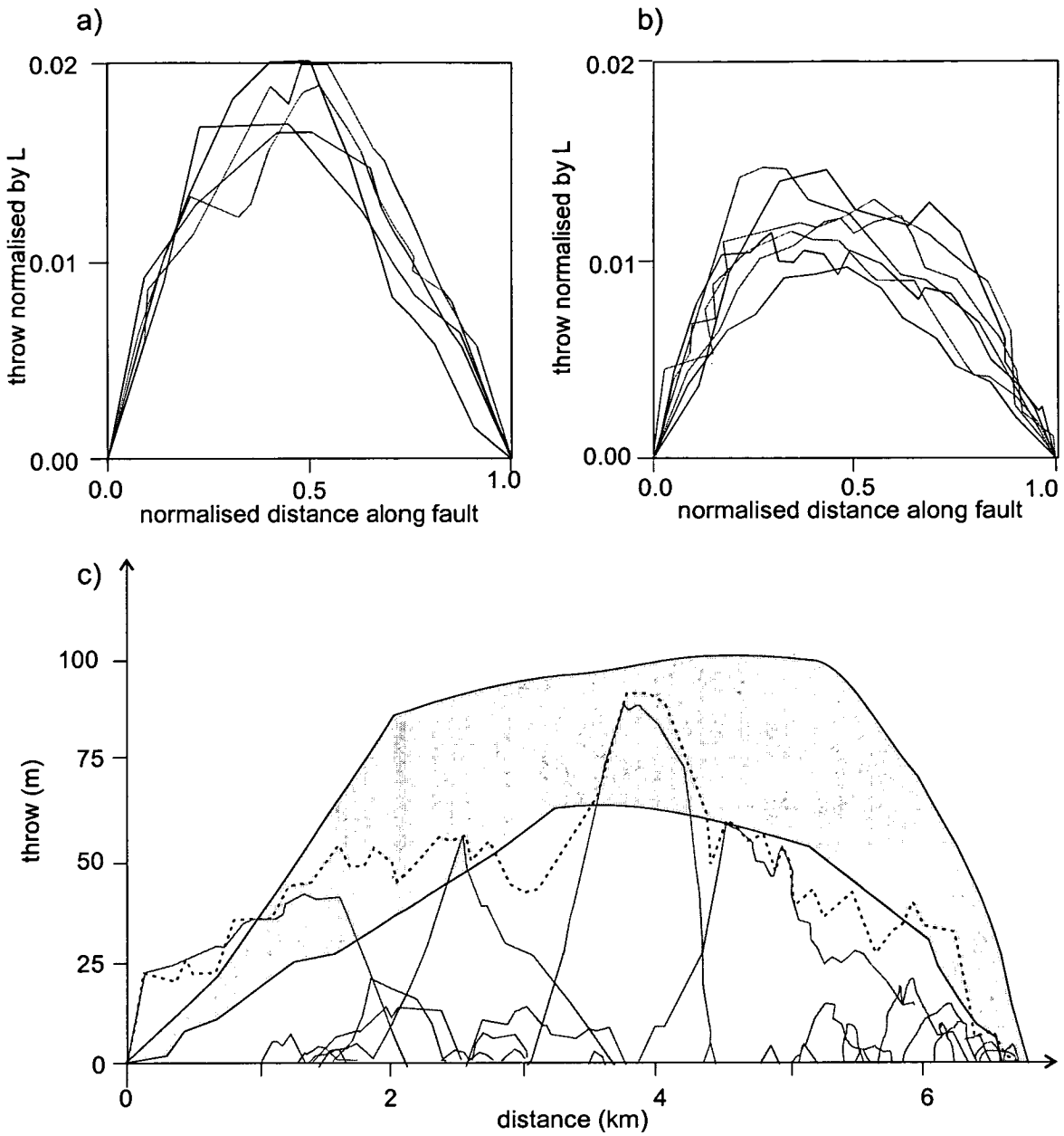

Figure 1.7. Examples of typical fault displacement profiles. a) Single-segment faults below a critical length with a peaked profile and b) single-segment faults over a critical length with a flat toppped profile from Dawers *et al.* (1993). The critical length is thought to be a function of the thickness of the competent layer through which these faults propagated. c) Displacement profile for a linked fault from Dawers and Anders (1995). Solid lines are D/L profiles for individual segments and the dotted line is the summed throw on all the faults. The shaded area is where a 7130 m long single-segment fault would be expected to plot. Note that although the faults are linked, displacement minima are still preserved at segment boundaries. The displacement gradients at the tips of all these fault appear to be linear.

layer, the change of material properties influences the displacement profile. Faults that have grown entirely within a relatively homogeneous layer have more even, triangular profiles (Muraoka and Kamata 1983, Dawers *et al.* 1993).

Faults that have grown by the linkage of several fault segments commonly have displacement minima preserved at the segment boundaries (Figure 1.7c) (Peacock and Sanderson 1991, 1994, Trudgill and Cartwright 1994, Cartwright *et al.* 1995a and b, Dawers and Anders 1995). Interaction between neighbouring segments locally increases the effective strength of the rock, allowing the rock to support steeper displacement gradients. Displacement minima associated with segment boundaries seem to be persistent with time, and in large fault systems may be associated with persistent barriers to fault rupture (e.g. King 1986). Faults can link in three-dimensions leading to a complex distribution of slip on a fault surface (Mansfield and Cartwright 1996, Nicol *et al.* 1996).

1.3.3. Off-fault deformation

Many workers have observed that fault planes are surrounded by concentrations of deformation, both on a microscopic and macroscopic scale (Figure 1.8). Chester and Logan (1986a) defined off-fault deformation as "the volume of rock containing a greater intensity of brittle deformation than typical of the surrounding rock". Brock and Engelder (1977) observed an increase in density of deformation (i.e. the number of structures intersected per metre along a transect perpendicular to fault strike) close to a large thrust fault. Such increases in deformation density have subsequently been reported from many other fault zones (e.g. Jamison and Stearns 1982, Chester and Logan 1986a and b, Little 1996). Knott *et al.* (1996) defined the point where the fracture density dropped to below one fault per metre as the edge of the off-fault deformation zone. Knipe *et al.* (1998) define the edge of the off-fault deformation as the point where the structural frequency drops to twice the background level. Analyses of the orientation of the structures within off-fault deformation have found that they are consistent with the deformation occurring on the main fault zone (Chester *et al.* 1993, Little 1996).

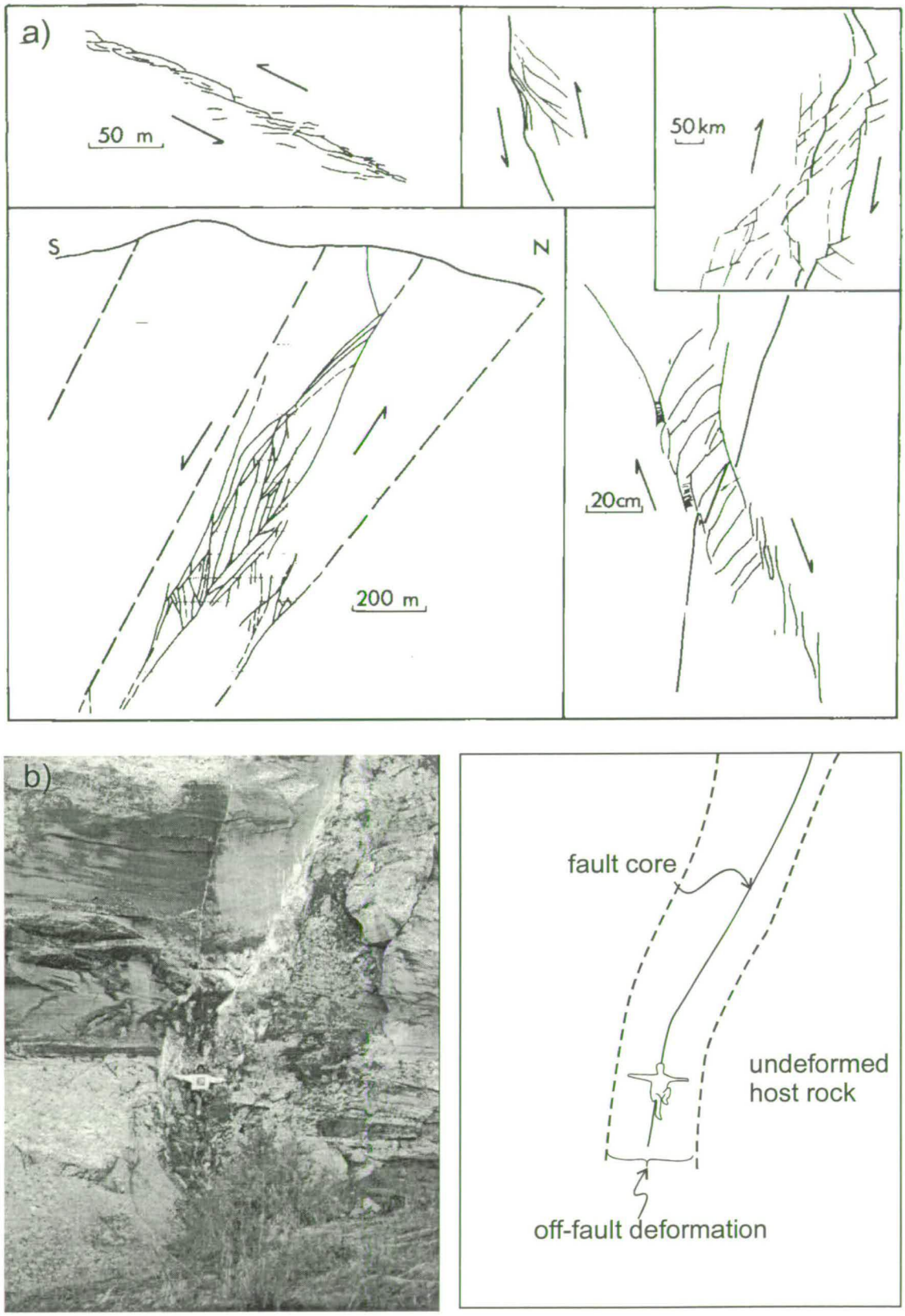

Figure 1.8. a) Examples of mapped fault traces with off-fault deformation at different scales (from Cox and Scholz 1988). b) Example of a fault surrounded by off-fault deformation, from the field area in this study.

Local variations in the density and clustering of deformation are common within off-fault deformation (Chester and Logan 1986a). Many studies have concentrated on characterising the geometry and scaling relationships (i.e. fractal, power law, exponential) of this deformation (e.g. Knipe 1998). However characterising the geometry in this fashion provides no information on the origin of, or controls on, the deformation distribution. Increased deformation density can be related to flexure of beds around faults (Jamison and Stearns 1982, Antonellini and Aydin 1994, Fossen and Gabrielsen 1996) and zones where different fault segments interact or link (Peacock and Sanderson 1991, Trudgill and Cartwright 1994). Clustering can also be caused by lithological variations in the host rock (Chester and Logan 1986b). The deformation style can be heterogeneous throughout the off-fault deformation. A progressive change in kinematic style has been observed by Little (1996) away from a large strike-slip fault. Knipe and Lloyd (1994) observed that different mechanisms can be active within the off-fault deformation zone at different times during the lifetime of the fault.

Deformation around fault surfaces can also occur as microfractures. Chester *et al.* (1993) and Brock and Engelder (1977) observed a zone of fault-associated microfracturing that extended at least an order of magnitude beyond the zone of macroscopic fractures. A decay of microfracture density with distance has been observed in the field (Brock and Engelder 1977, Anders and Wiltschko 1994, Knipe and Lloyd 1994, Vermilye and Scholz 1998). Anders and Wiltschko (1994) and Vermilye and Scholz (1998) observed a logarithmic decay of microfracture density with distance from the fault, and used the point where the microfracture density had decayed to a background level to define the width of the off-fault deformation (Figure 1.9). Both Anders and Wiltschko (1994) and Vermilye and Scholz (1998) found that displacement on the main fault surface had no effect on the maximum microfracture density adjacent to the fault surface.

Martel and Boger (1998) have quantified the change in orientation and style of fractures around a fault tip line in three-dimensions and related this to the mode of fracture at the tip line (Section 1.4.4). Segall and Pollard (1983) and Myers and

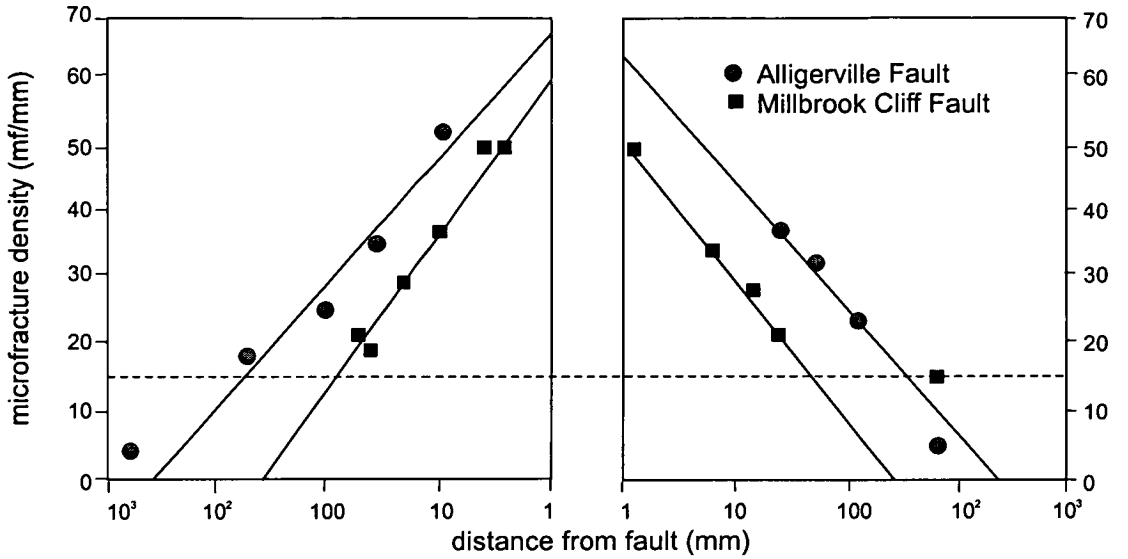

Figure 1.9. Example of microfracture densities around two faults, from Vermilye (1996). The density of microfractures decays logarithmically with distance (solid line) from the fault to a background level of about 15 microfractures per mm (dotted line).

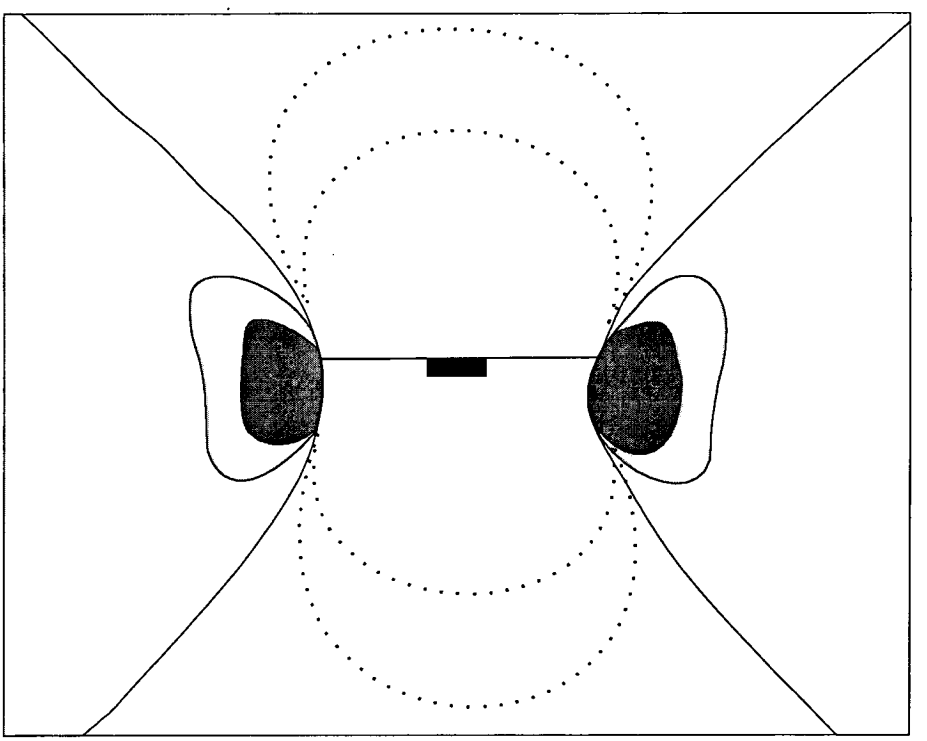

Figure 1.10. Cartoon of the stress change around a steeply dipping normal fault (after King *et al.* 1994, Hodgkinson *et al.* 1996). Regions of positive stress change (i.e. stress enhancement) are indicated by grey shading, areas of negative stress change (i.e. stress shadow) are indicated by dashed lines. The stress is concentrated at the fault tips and is relieved around the fault itself

Aydin (1999 *in review*) have shown that faults may nucleate from pre-existing extension fractures, and suggest that the fault tips do not propagate beyond the end of the original joint. In this case, the structures seen at the fault tip relate to the accumulation of shear displacement along the joint. However this is an unsatisfactory mechanism to explain fault growth in general, as all faults would have to be preceded by an earlier event of jointing that was oriented in the appropriate direction. If structures mapped at fault tips formed in response to stresses at the fault tip and the fault has propagated in several slip events, then inactive structures with similar geometries will be preserved behind the fault tip (an inactive "wake" of damage). However many structures that have been mapped at fault tips (Bürgmann and Pollard 1994, McGrath and Davison 1995, Martel and Boger 1998) are not observed as an inactive wake behind fault tips. This apparent paradox is a strong motivation for the investigation of off-fault structures.

Although the distribution and geometry of off-fault deformation is the key to deciphering fault growth mechanisms, a systematic investigation of these structures related to fault displacement has not been undertaken thus far. Such a study is important because the distribution of features in off-fault deformation zones will also have a critical effect on the movement of fluids through the fault system (Caine *et al.* 1996, Evans *et al.* 1997). For instance, as the amount of clustering increases, the size of fault-enclosed compartments becomes more variable (Manzocchi *et al.* 1998). Therefore the controls on fault clustering are critical investigations of fault zone permeability. This is especially important for the faults in high porosity sandstones that are investigated in this study (Section 2.3.1).

1.4. Mathematical models of fault growth

1.4.1. Linear elastic fracture mechanics

The simplest model of a fault is that of a planar crack in an elastic medium. Strain due to an individual earthquake can be approximated as elastic because the time scales are relatively short and the strain relatively low. The solutions for the stress field around an elastic crack (Pollard and Segall 1987) can be used to predict the

distribution of damage around a fault. This predicts a high stress at the tips of the crack and a stress shadow on either side of the crack (Figure 1.10). The distribution of aftershocks after earthquakes can be controlled by the location of stress highs and lows predicted by the elastic solution (Scholz 1990 p206, King *et al.* 1994, Hodgkinson *et al.* 1996). Fault growth is inhibited in the stress shadow region around a fault (Ackerman and Schlische 1997, Gupta and Scholz 1999 *in review*). Gupta and Scholz (1998) have shown that the elastic model can predict the deformation field accommodating displacement on small faults.

The decrease of microfracture density with distance from a fault surface has also been predicted from elastic crack models. Scholz *et al.* (1993) multiplied the near-field crack tip stress field in the elastic solution (Lawn and Wilshaw 1975) by an empirical relation between dilatancy and stress (Scholz 1968), to give crack density. This predicts the logarithmic decrease in microfracture density with distance from a fault, which has been observed both in studies of microfractures around natural faults (Section 1.3.3) and in experimental data. Vermilye and Scholz (1998) also found that the orientations of microfractures agreed with models for the orientation of the stress field around such crack tips (Pollard and Segall 1987).

Linear elastic fracture mechanics (LEFM) relates the energy needed for fault propagation to the stress at the fault tip. Faults are represented by a single, isolated crack in a perfectly elastic material, i.e. inelastic deformation is confined to an infinitesimally small zone at the fault tips; the host rock has homogeneous properties and remote loading. Assuming the crack is loaded by a remote stress σ_r, the distribution of displacement, D, with distance, x, is described by:

$$D(x) = \frac{(1-\nu)\sigma_r}{\mu}\sqrt{L^2 - 4x^2}\ , \qquad (1.2)$$

where L is the crack length, μ is the shear modulus and ν is Poisson's ratio. The resulting displacement versus length profile is elliptical (Figure 1.11).

The infinite displacement gradient at the fault tip for an elliptical profile results in an infinitely high stress concentration at the tip. This is unrealistic because real materials have a finite strength and thus can not support infinitely large stresses. In order to eliminate the infinitely high stress it is necessary to include inelastic deformation at the fault tip. In LEFM, faults are modelled as planar cracks in an elastic medium. The rationale for this is that rocks can support finite elastic strains, such as earthquakes or flexurally supported loads on the crust. However, the processes involved in creating new fault surface area during fault growth are inelastic. In order to understand fault off-fault deformation architecture, it is important to consider the area of inelastic deformation at the fault tip. At large strains and longer time scales, the deformation around a fault must be inelastic.

1.4.2. Inelastic deformation at fault tips

Inelastic deformation at fault tips often appears to be a process of microfracture initiation, propagation and linking (Cox and Scholz 1988, Lockner *et al.* 1991, 1992, Reches and Lockner 1994). These microfractures can occur either within grains or crystals, or along their boundaries (see Kranz 1983 for a review of fault-related microfractures). The complex breakdown process at the tip of propagating shear cracks has been investigated experimentally by Cox and Scholz (1988). Their experiments produced Mode III failure at the root of a slot. Initially an array of tensile cracks is generated near the slot tip oriented with the long-axis parallel to applied σ_1, and oblique to the plane of the slot. These orientations are consistent with the crack tip stress field as predicted from fracture mechanics (Section 1.4.1). With continued deformation, these fractures become linked together by shear cracks running parallel to the slot. When internal deformation has caused sufficient loss of cohesion, the extended rupture zone becomes the source for a subsequent generation of tensile crack formation. This deformation at the tip of a crack is what led to the concept of the *process zone* (Section 1.2.2).

These results were used as the basis for an elastic-plastic fracture mechanics model proposed by Cowie and Scholz (1992a). In this model displacement is related to

length by the yield strength, Poisson's ratio and elastic shear modulus of the host rock as well as to the remote stress. A crack is loaded by a remote stress σ_r, and has a resistance to propagation at the fault tip σ_y: the yield strength of the rock. The stress concentration at the tip can only rise to the value of σ_y before inelastic deformation occurs. The crack then extends a distance s, inelastically deforming the region ahead of the tip. The zone of inelastic deformation at the fault tip, s, is equivalent to the process zone described above. Outside this zone the material still behaves elastically. The model is two dimensional (plane strain), so no deformation is considered to have taken place perpendicular to the crack. This is justified if the rock containing the fault behaves in a linear elastic fashion. As σ_y becomes large, the material becomes perfectly elastic and the inelastic zone, s, becomes vanishingly small, and the displacement profile tends towards elliptical.

A fault loaded by a uniform remote stress grows in a self similar way such that

$$D(x) = L\frac{C(1-\nu)(\sigma_y - \sigma_f)}{2\pi\mu}, \tag{1.3}$$

where σ_f is the frictional shear stress on the fault, μ is the shear modulus, ν is Poisson's ratio, and C is a geometrical constant. This model predicts a linear scaling relationship between D and L, but the constant of proportionality will vary according to rock type (μ, ν and σ_y) and tectonic environment (σ_r, shown in equation 1.4).

In this model the displacement gradient decays to zero at the fault tip, that is, the displacement profile has a smooth bell-shape (Figure 1.11). The inelastic process zone is the part of the displacement profile between the tip and the inflection point on the curve at displacement d_o. The length of the process zone is given by

$$s = L\sin^2\frac{\pi(\sigma_r - \sigma_f)}{4(\sigma_y - \sigma_f)}. \tag{1.4}$$

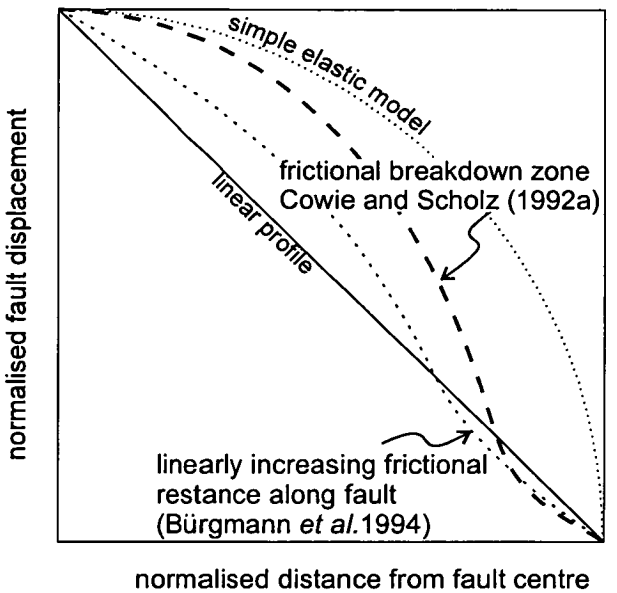

Figure 1.11. Comparison of theoretical displacement profiles from the fault centre to the tip plotted on normalised axes. The dotted line is an elliptical profile predicted by a simple elastic crack model. Wide dashed line is the model of Cowie & Scholz (1992a) and the narrow dashed line is the model of Burgmann *et al.* (1994).

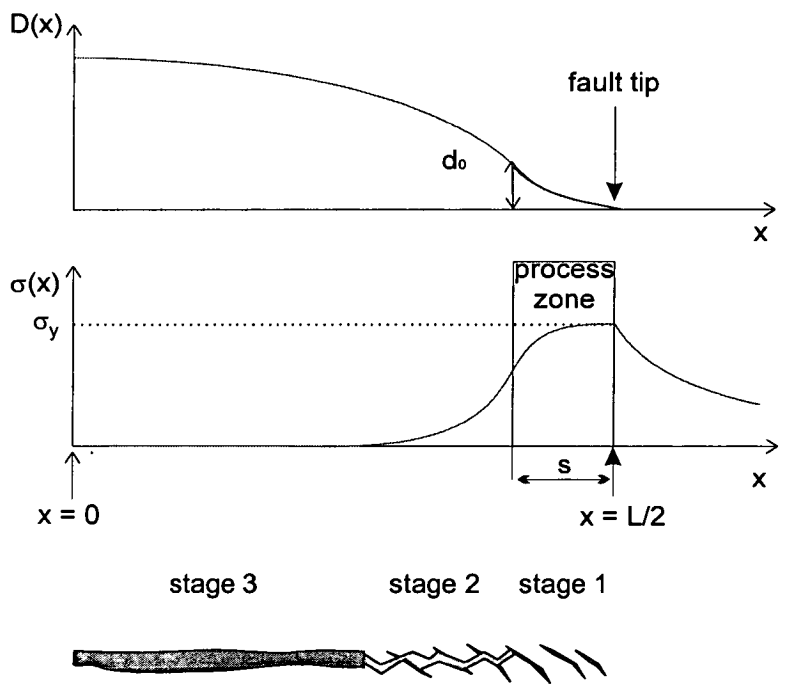

Figure 1.12. Adaptation of the Dugdale model to a fault from Scholz *et al.* (1993). Three stages in the development of a fault surface are defined: stage 1 - arrays of tension fractures break down rock at the fault tip; stage 2 - coalescence to form an immature irregular fault surface; stage 3 - continued wear of the fault surface produces a well developed fault with a layer of gouge.

The predicted ratio between the length of the process zone, s, and the length of the fault, L, is between 0.1 and 0.2 (Cowie and Scholz 1992a). Thus the shape of the displacement profile as well as the D_{max}/L ratio depends on rock properties and tectonic setting.

1.4.3. Application of the model to real faults

For real faults, the material yield strength, σ_y, is equated to the macroscopic shear strength of rock at ambient pressure and temperature conditions. At a microscopic scale, this shear strength is due to fracturing across grains and sliding along intergrain contacts. The process zone corresponds to a zone where fractures have formed but no through-going fault surface has yet developed (Figure 1.12). At the fault tip, the rock is broken down by the formation of fractures, which gradually coalesce to form an irregular slip surface. Continued shearing results in the development of a complex mesh of fractures that eventually breaks down to form a through-going fault zone. As the fault accumulates displacement, the process of frictional wear smoothes out the fault surface resulting in a smooth, planar slip surface (Figure 1.12).

Lockner *et al.* (1991, 1992) presented a new experimental technique using acoustic emissions (AE) as feedback to control the stability of fracture propagation. Each AE was inferred to be a microfracture event, and the location of the AEs was monitored. Prior to failure, distributed microfractures occurred throughout the sample, followed by localisation after peak stress. As the fracture propagated through the sample, a front of microfractures was observed ahead of a zone of relative quiescence. This fracture front was interpreted as a process zone of tensional microfractures developing at the fracture tip.

Dawers *et al.* (1993) have shown that the observed correlation between D_{max} and L in their field data does seem to be consistent with the model prediction, but the field evidence for a process zone and the significance and magnitude of the parameter, s, still remains untested. Although the incorporation of inelastic deformation at the fault

tip is more realistic than the simple elastic crack model, the predicted bell-shaped profiles are not the usual form of displacement profiles observed in the field (Section 1.3.2). Most observations of real faults have displacement profiles that are triangular in shape, i.e. they have finite displacement gradients at the fault tips. Bell-shaped profiles have been seen in very small faults (Schlische *et al.* 1996), which may be inferred to have a very short-lived growth history. The Cowie and Scholz (1992a) analytical model assumes plane strain, however, fractures at the fault tip are observed to develop out of the plane of the fault. The model also requires that the frictional resistance on the fault surface is less than the yield strength of the rock. While this is true for many faults, it is possible for a fault to be stronger than the surrounding rock. This strain hardening is a process characteristically found during cataclasis of porous sandstones, which typify the lithology found in the field area.

1.4.4. Other models of fault growth

Bürgmann *et al.* (1994) modelled a non-uniform stress drop due to changes in rock type, or the variation of friction along the fault, and the effect of fault interaction. Their model results have steeper tip displacement gradients than a simple elastic model, but the displacement gradient still dies to zero at the fault tip (Figure 1.11) in contrast to observed displacement profiles. In fact many isolated (i.e. non-interacting) fault tips observed in the field have finite tip displacement gradients, do not end at a change in lithology, and show no evidence for a change in frictional properties along the fault.

Walsh and Watterson (1987) and Marret and Allmendinger (1991) suggest that fault displacement profiles are the sum of a number of discrete slip events, with each event having an elastic-type (elliptical) profile. During each slip event, the entire surface of the fault fails, and new fault surface is generated around the perimeter of the fault. Walsh and Watterson (1987) fixed the amount of incremental slip as proportional to the length of the fault. Marret and Allmendinger (1991) modified this geometrical model so that the difference between each slip event depends on the total number of slip events on the fault. This model predicts that the shape of the fault profile will

change with time such that faults have higher displacements for their length as they grow. This fails to account for the displacement length correlation seen in individual fault populations (Section 1.3.1). These models rely on simple relations between the size of each successive slip event. However the mechanism that would generate slip events proportional to either the size of the fault or the number of slip events on the fault is unclear. These models also do not replicate the observed linear fault displacement profiles at the fault tip.

1.5. Summary

1. Existing models of fault growth are inconsistent with observed triangular or flat-topped fault displacement profiles. Physical models based on linear elastic fracture mechanics models predict elliptical displacement profiles, and models incorporating an inelastic zone (process zone) at the fault tip predict bell-shaped profiles. Even simpler geometrical models incorporating summed slip events do not produce the scaling relations seen for natural fault populations.

2. The shape of the displacement profile at the tip of the fault is the key to distinguishing between the competing models, and should additionally provide information on the deformation mechanisms active at the fault tip. However, the small displacements that are seen at fault tips mean that they are often hard to recognise and quantify in the field. This thesis presents the results of very high resolution surveys at a fault tip, made possible by a detailed study of fault offset in a particularly well-exposed locality in Utah, USA.

3. Observations of structures associated with fault zones have highlighted the fact that many faults have a zone of deformation (off-fault deformation) concentrated around the main fault zone (fault core). Information on the history and mechanism of growth on the fault will be contained within the geometry and distribution of the off-fault deformation. However, prior to this study, a focused examination of off-fault deformation geometry and scaling has not previously been undertaken.

4. This thesis presents a systematic study of off-fault deformation architecture linked to the measured fault displacement profiles. The off-fault deformation is investigated at several scales and the structures are interpreted in terms of fault zone evolution.

2. GEOLOGICAL SETTING

2.1. Introduction

The first section of this chapter introduces the regional geology of the field area. The area was chosen because the well defined, relatively planar bedding provides an excellent constraint on the vertical fault displacement. In addition, deeply incised river canyons dissect the landscape, exposing the fault zones and their associated deformation. The deformation around the faults can therefore be examined in relation to the displacement on the faults. The arid desert climate of the area produces a sparsely vegetated landscape with very good exposure.

The faults in this study are exposed in a highly porous sandstone (~20%) which deforms in a characteristic way. The microstructure, geometry and petrophysical characteristics of faults in this rock type have been studied by previous workers. A summary of these observations, with appropriate references, is given in the second part of this chapter, using examples from the field area.

Two faults were selected for detailed study and are introduced in the final section of this chapter. The exposures along these faults are such that the deformation in the hangingwall and footwall of the faults could be related to the variation of displacement along the fault.

2.2. Geological setting

2.2.1. The San Rafael Swell

The San Rafael Swell (SRS) is located on the Colorado Plateau in east-central Utah. The SRS is a north-east trending asymmetric dome-shaped structure, approximately 120 km long and 50 km wide (Figure 2.1). Strata on the west flank of the SRS commonly dip 2-6° and on the east 45-85°. The centre of this dome has been eroded to expose the entire Triassic through to Cretaceous sedimentary sequence.

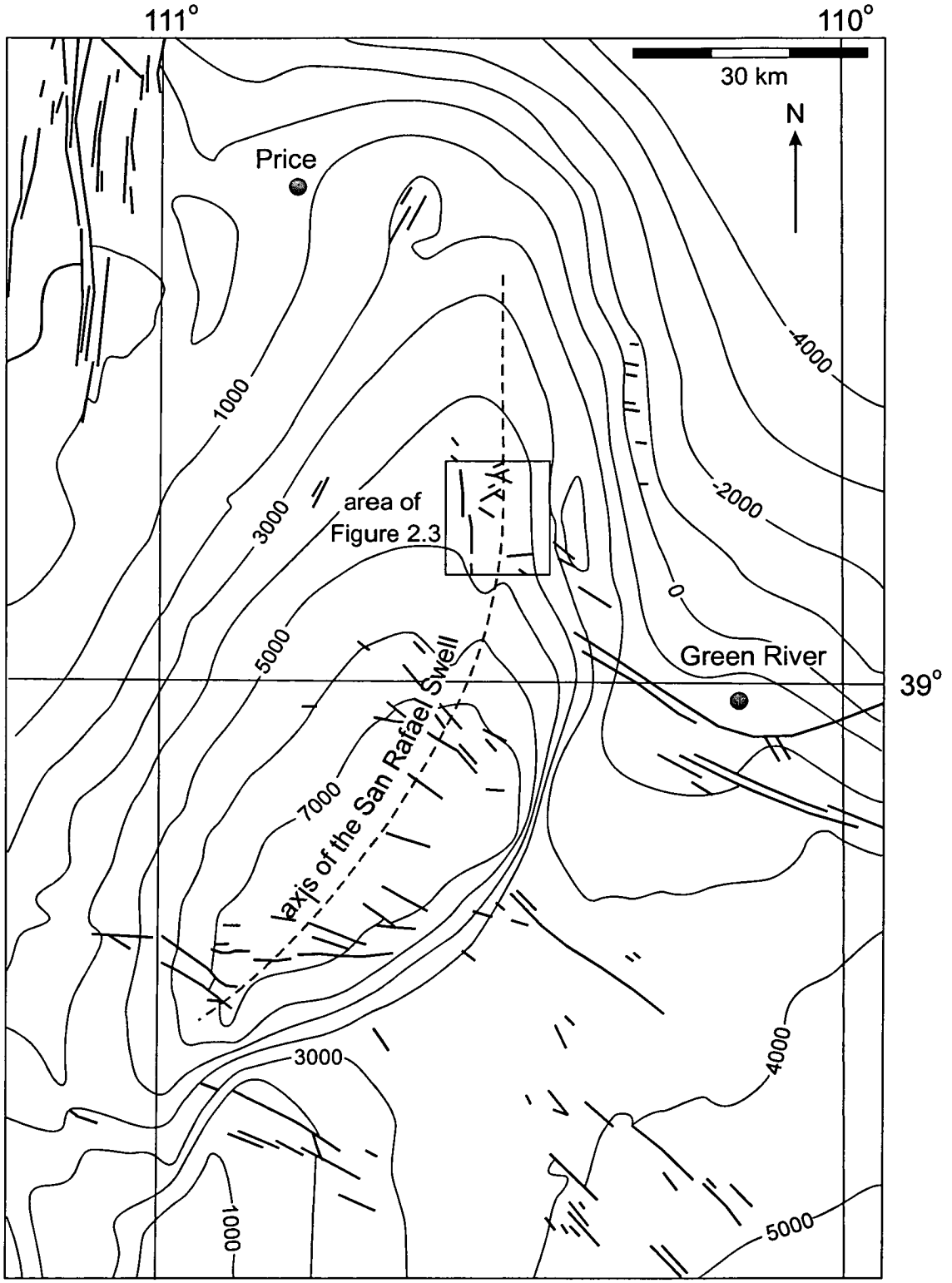

Figure 2.1. Structure contour map of the San Rafael Swell (top Chinle Formation ~ 1220 m below top Navajo Sandstone). Note that faults (bold lines) are concentrated along the axis of the Swell (dotted line). Contour intervals are feet above mean sea level. (after Krantz 1988b)

The SRS is one of a series of structures that formed within the Colorado Plateau during the Laramide Orogeny (80-50 Ma). Basement faults were reactivated in NE-SW horizontal compression resulting in the formation of forced monoclinal folds in the overlying sediments (Kelly 1955, Davies 1978) (Figure 2.2). Uplift of the SRS started in the late Campanian (74 Ma) as shown by changes in drainage patterns and onlapping stratal geometries (Lawton 1986). This onlapping and therefore the structural growth of the SRS had ceased by the late Palaeocene (56 Ma) (Lawton 1986). The postulated major basement fault beneath the SRS was not imaged by the COCORP (Consortium for Continental Reflection Profiling) profile, which runs through the field area (Allmendinger *et al.* 1986). This could be due to a near vertical fault geometry or alternatively to a low acoustic impedance contrast across the fault. The COCORP profile runs across the northern termination of the SRS where displacement is dying out to the north, making it harder in principle to image here.

2.2.2. The Chimney Rock fault array

The Chimney Rock fault array is situated on the north-east flank of the SRS. It is an array of normal faults ranging from 100 m to 6 km long with a maximum observed displacement of 33 m (Figure 2.3). The faults can often be traced for their entire length along strike so that one or both tips are exposed. Some of the faults in the array are relatively isolated whereas other faults intersect and cross-cut. The northern part of the area was mapped by Krantz (1988).

In the area shown on Figure 2.3, fault-line scarps strike both ENE-WSW and WNW-ESE and are clearly visible on aerial photographs (Figures 2.11a and 2.12c). The fault planes are highly polished and striated surfaces dipping at 65-85° both to the north and south. The striations indicate that movement on the faults was predominantly dip-slip. Larger undulations, up to one metre in wavelength, are oriented parallel to the direction of slip (Figure 2.4a). The fault zones are highly resistant compared to the host rock; therefore they tend to stand proud of the surface or form barriers across canyon floors. These fault "walls" can stand several metres

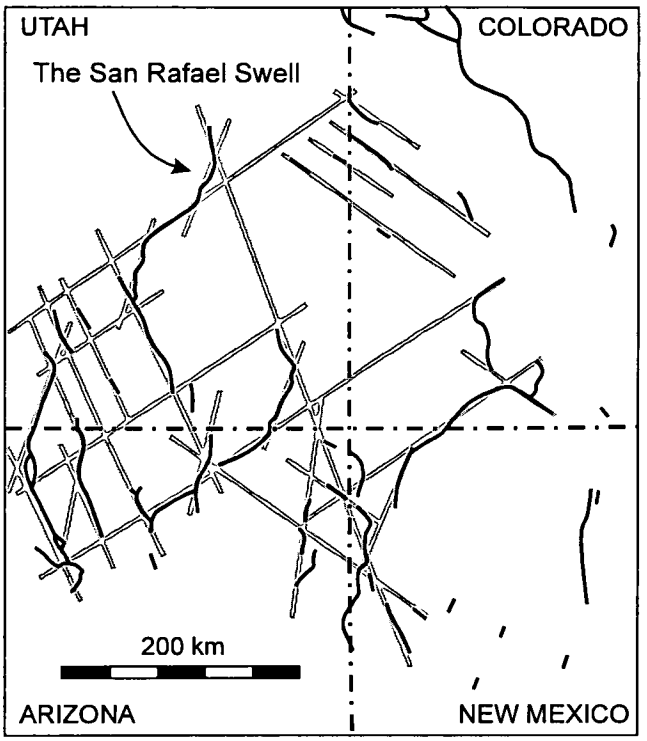

Figure 2.2. Location map of the San Rafael Swell within the Colorado Plateau. Black lines are the axes of the Colorado Plateau monoclines. Inferred basement-fracture zones are shown in grey. (after Davies 1978)

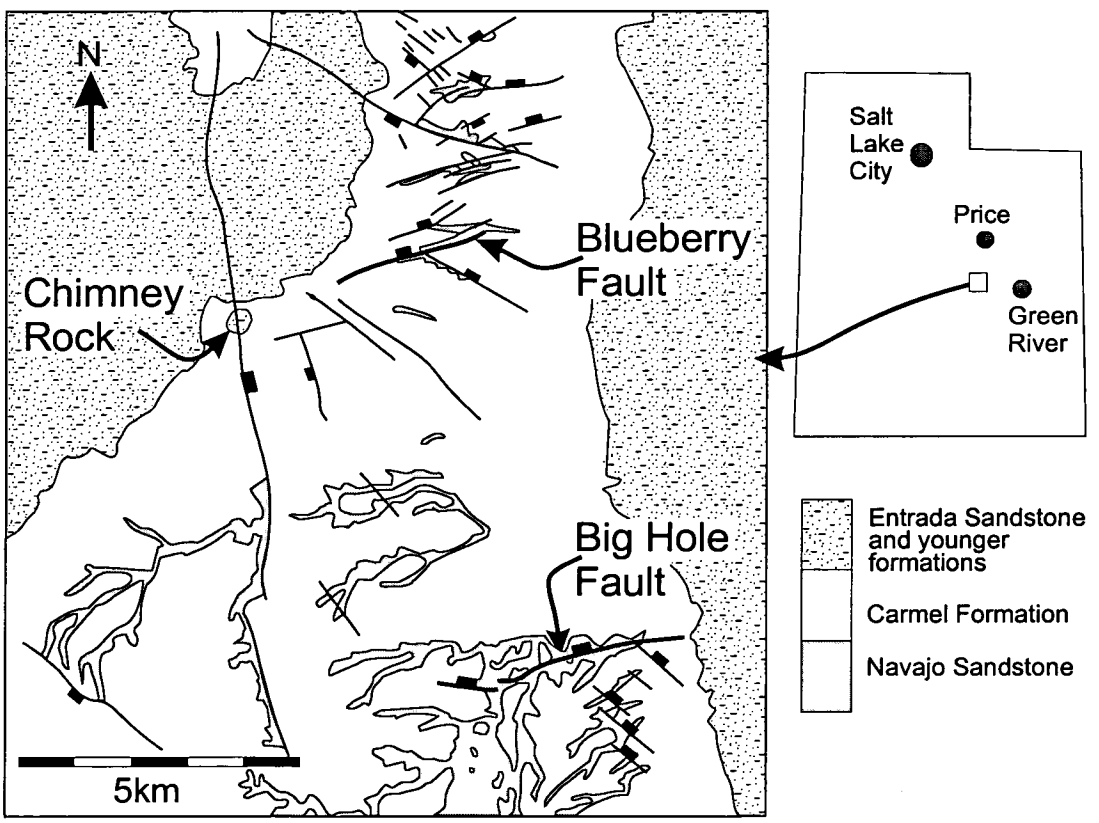

Figure 2.3. Map of the Chimney Rock fault array. (from the Huntingdon Quadrangle 1:100 000 geological map). The faults investigated in this study are indicated. The topographic maps of the study area are the Dry Mesa and Chimney Rock 1:24 000 maps.

high and are usually bounded by polished surfaces (Figure 2.4b). In cross-sectional outcrops the fault zone consists of a zone of densely packed anastomosing deformation bands and slip-surfaces (see Section 2.3.1). In places the faults bifurcate, both along strike and down dip.

The origin of the Chimney Rock fault array is uncertain. Witkind (1991) postulated that structures in this region that run east-west could result in principle from dissolution of the underlying Middle Pennsylvanian age Paradox Salt in the Eocene (56-35 Ma). However, the zero isopach of the Paradox basin is to the south of the field area (Witkind 1991), so this seems an unlikely origin for these faults. An alternative hypothesis is that the faults formed due to extension over the crest of the SRS as it developed (see Figure 2.1). In this case the faults would be between 74 Ma and 56 Ma.

Unfortunately, little evidence exists to constrain the date or depth of fault formation. A simple (i.e. not including correction for compaction) reconstruction of the sedimentary column suggests that the faults would have been at 2.5-4 km depth if they had formed in the Eocene, and 1.5-3 km depth if they had formed in the late Cretaceous. This would result in the rocks being at a temperature between 50-120 °C, and a lithostatic pressure between 20-50 MPa, at the time of faulting. There is some evidence that present-day drainage patterns in the area have been affected by the faults. This is more likely to be differential erosion of the weaker Carmel Formation in the hangingwall of the faults, than evidence for active contemporary fault growth at the surface. These faults are therefore considered to have been blind faults.

2.2.3. Orthorhombic Faults

There are four mutually cross-cutting (i.e. synchronous) fault sets in the Chimney Rock fault array: two strike sets, each with two dip directions. This type of orthorhombic fault geometry (Figure 2.5) has been interpreted as the result of growth in a three-dimensional strain field (Reches 1978, Aydin and Reches 1982, Krantz 1988, 1989). The angles between the four fault sets are dependent on the ratios

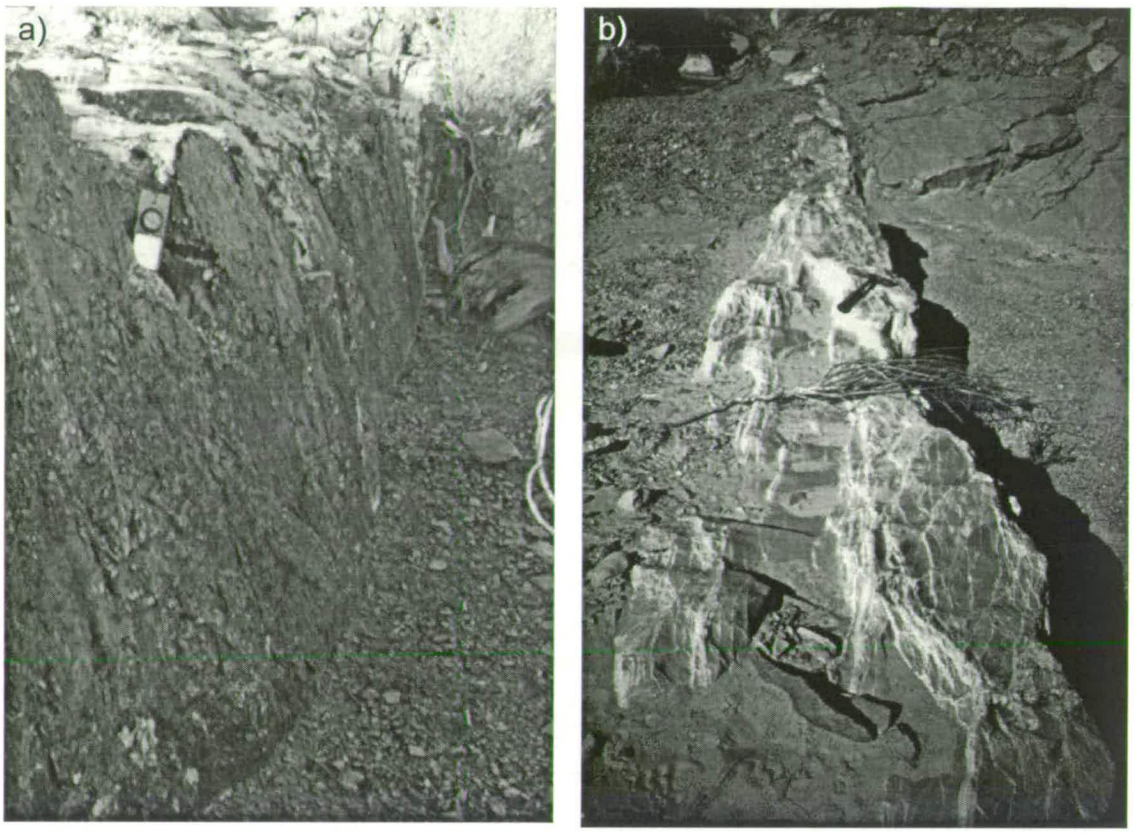

Figure 2.4. a) Undulating fault surface with dip-slip striations, compass for scale. b) Resistant fault "wall" standing proud of the base of the wash, hammer for scale.

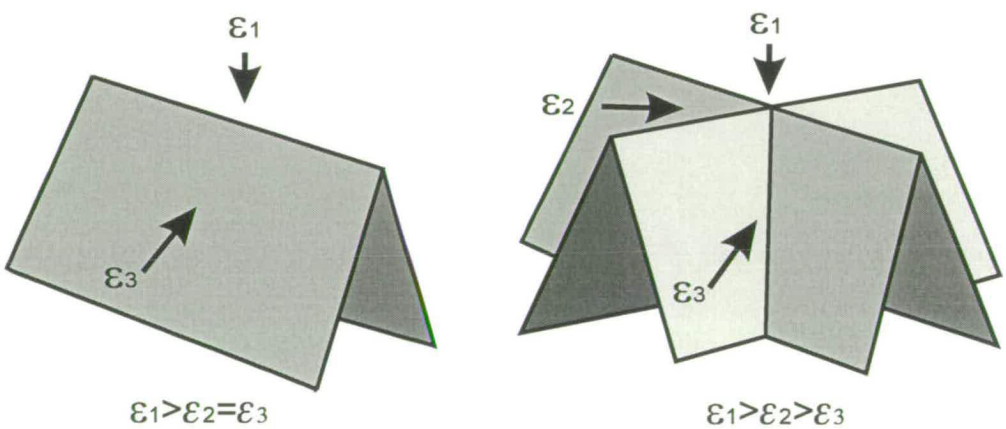

Figure 2.5. Illustration of conjugate and orthorhombic fault geometries. ε_1, ε_2, and ε_3 are the maximum, intermediate and minimum principle strains respectively. Two conjugate fault sets can potentially be developed in a two-dimensional strain field. Up to four orthorhombic fault sets can be developed in a three-dimensional strain

between the three principle strains (Krantz 1988). In this case, the Chimney Rock faults have developed in response to a maximum extensional strain oriented north-south and a minimum extensional strain oriented east-west, and a vertical compressive strain (Krantz 1988). The details of orthorhombic fault geometries are discussed further in Section 6.4.

A similar orthorhombic fault pattern has been documented in the New Red Sandstone of Arran (Woodcock and Underhill 1987). These faults have been interpreted as forming above an intruding granite batholith. In a similar fashion the growth of the dome-shaped SRS could have been responsible for the development of the orthorhombic geometry of the Chimney Rock fault array.

2.2.4. The Navajo Sandstone

The faults in this field area are exposed in the Lower Jurassic Navajo Sandstone. This is a thick unit of aeolian sandstone that outcrops over a large part of southern Utah and erodes to a characteristic topography of large domed cliffs (Figure 2.6). The Navajo Sandstone, and the correlative Aztec and Nugget Sandstones in Nevada and northern Utah respectively, were formed as deposits of a large erg complex that covered much of the western United States in the Early Jurassic (Saleeby and Busby-Spera 1992).

The Navajo is a fine to medium-grained, well-sorted quartzose sandstone. Large, well-developed aeolian cross-beds are interspersed with more massive beds. Towards the top of the unit, slumped horizons and other soft sedimentary deformation features are common. The Navajo varies in colour and cementation, but in this study area it contains a minor amount of syntaxial quartz overgrowths with occasional calcite cement and is stained with haematite, giving it a honey-brown colour.

Syn-sedimentary faults are often associated with the slumped horizons (Figure 2.7). They are slightly darker than the host rock, do not form a resistant seam on the outcrop, and show no grain size reduction in thin section (see section 2.3.1). They are

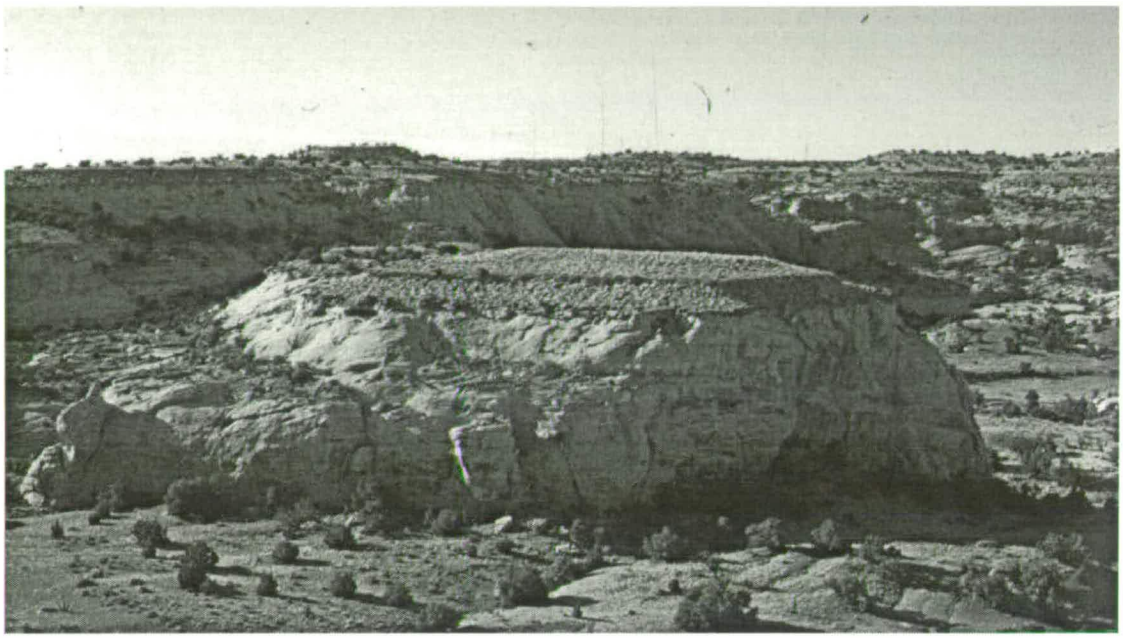

Figure 2.6. Photograph of the Big Hole Wash. The Carmel Formation forms the ledges capping the large cliff of Navajo Sandstone in the foreground. The Big Hole fault runs across the back of the photograph in shadow and the rock in the foreground has been dropped down in the hangingwall. The deep incision of the Big Hole Wash gives access to the fault both in cross section and plan view.

Figure 2.7 Syn-sedimentary folds and faults (white arrows) in the Navajo Sandstone.

not considered to be part of the deformation due to fault growth and are therefore not considered further in this study.

The top of the Navajo Sandstone is a regional sub-aerial erosion surface: the J-2 unconformity of Peterson & Pipringos (1979). This surface is represented by redder, more cemented beds with a rubbly appearance. The topmost tens of centimetres of the Navajo Sandstone has an extremely large grain size and relatively high porosity. Differential erosion of the top Navajo Sandstone created palaeotopography on this unconformity, but within the field area this relief is relatively small (less than 0.5 m) and the unconformity can be considered approximately planar (Figure 2.6).

2.2.5. The Carmel Formation

The Middle Jurassic Carmel Formation represents a marine incursion over the region. It consists of thin beds of harder, more resistant limestone interspersed with shaley marls. The limestone beds are highly fossiliferous and in places have well-formed ripple marks and raindrop pits. The limestone horizons cap benches on the eroded shale slopes above the tall Navajo cliffs (Figure 2.6). Bedding is laterally continuous and thus provides the marker horizons that, along with the top of the Navajo Sandstone, are used in this study to tightly constrain the fault displacement. Only the lower part of the Carmel Formation outcrops in the field area.

2.3. Deformation styles

2.3.1. Deformation in the Navajo Sandstone

The Navajo Sandstone deforms in a characteristic fashion, in common with other porous sandstones. Thin bands of cataclasis, each less than a few millimetres thick, form singly or as zones of bands. These structures are referred to as deformation bands (Aydin 1978, Aydin and Johnson 1978), granulation seams (Pittman 1981), microfaults or gouge zones (Jamison and Stearns 1982), cataclastic slip bands (Fowles and Burley 1994) or simply as faults (Underhill and Woodcock 1978). Surfaces with evidence of slip are referred to as slip-surfaces (Aydin 1978, Aydin

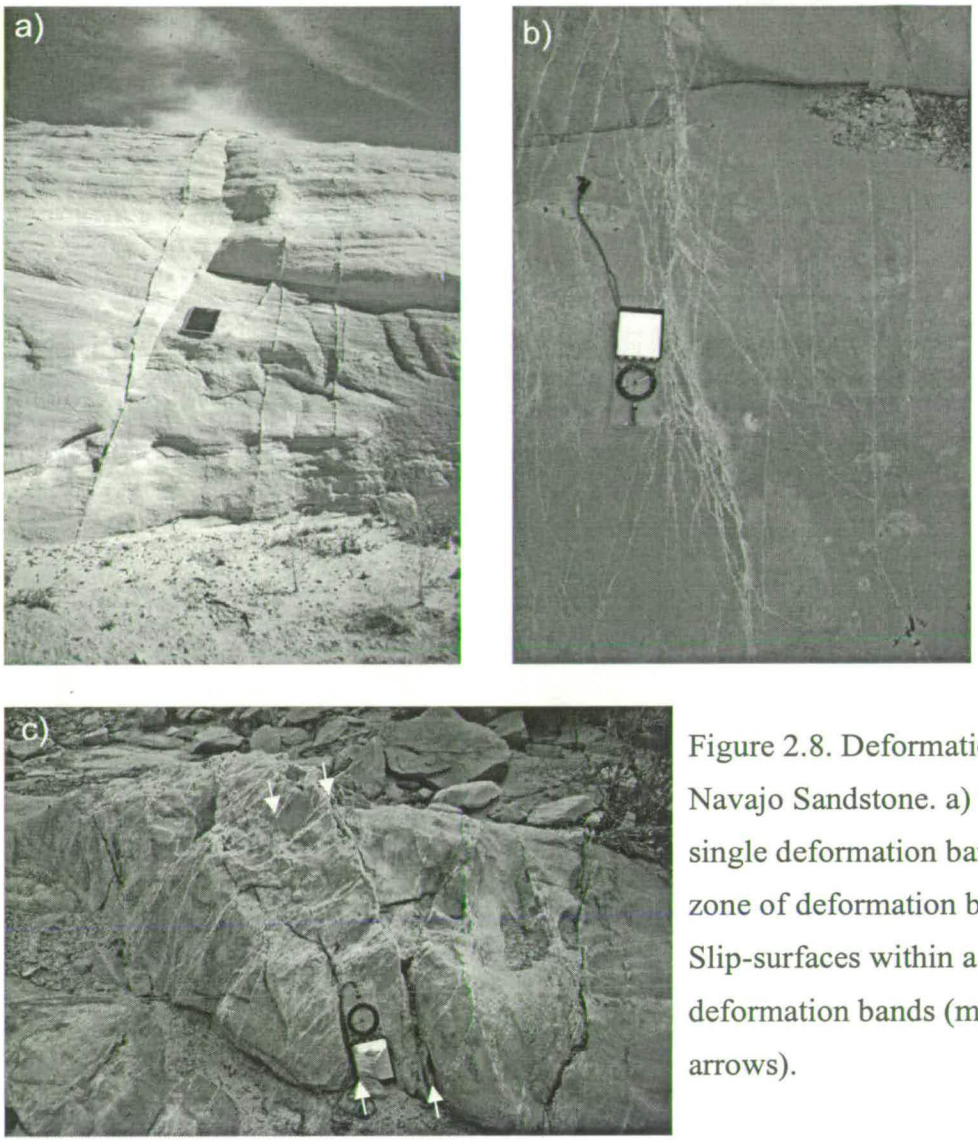

Figure 2.8. Deformation in the Navajo Sandstone. a) Several single deformation bands. b) A zone of deformation bands. c) Slip-surfaces within a zone of deformation bands (marked by arrows).

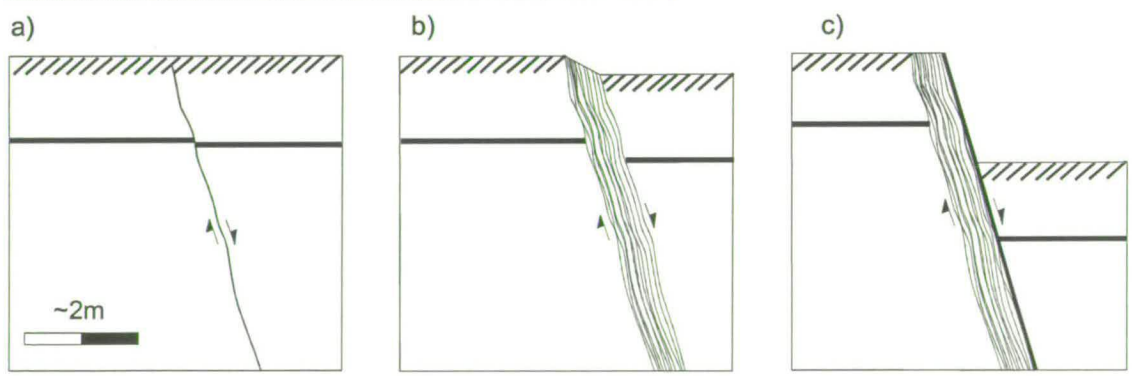

Figure 2.9. Schematic illustration of a model for the growth of faults in porous sandstones (after Antonellini and Aydin 1995). A hierarchical evolution is proposed from a) a single deformation band to b) a zone of deformation bands, and then into c) a slip-surface (thick solid line). Deformation bands have only small amounts of offset, whereas slip-surfaces accommodate large displacements (>0.5m).

and Johnson 1978) or shear fractures (Dunn *et al.*1973). *Deformation bands* and *slip-surfaces* are the preferred terms used in this thesis.

Single deformation bands are pale linear features extending for tens of metres, often standing slightly proud of the rock surface (Figure 2.8a). Each individual band is about 1 mm thick and accommodates up to a few millimetres of offset. In a few cases, the tips of these deformation bands end in an array of en echelon features. Larger displacements are taken up on zones of anastomosing deformation bands (Figure 2.8b). These zones are up to 0.5 m wide with displacements of up to tens of centimetres. Zones of deformation bands form clusters that trend sub-parallel to the main fault zones. Slip-surfaces appear as planes of parting within zones of deformation bands (Figure 2.8c). They accommodate larger amounts of displacement (over 0.5 m).

The association between deformation bands, zones of bands and slip-surfaces suggest that they develop sequentially (Figure 2.9). A mechanism for the origin of these bands is discussed in Aydin and Johnson (1978) and Antonellini *et al.* (1994), and is confirmed in the experiments of Mair (1997). They suggest that compaction and grain rotation produces stress concentrations at grain contacts that lead to the formation of fractures. Grain crushing and pore collapse create a band of fine cataclasite material which is more resistant to shear than the host rock (strain hardening). A new band then forms adjacent to the first one with continued deformation creating a zone of bands. The total displacement across the zone of deformation bands is proportional to the number of bands in the zone (Mair *et al.* 1999). Eventually a slip-surface is formed, with a smooth slickensided surface. The mechanism of the transition between zones of deformation bands and slip-surfaces has not previously been studied in detail.

Petrographic studies of the structure of individual bands show an inner zone of poorly sorted and crushed grains with much lower porosity than the host rock. This is surrounded by an outer zone with unfractured or slightly fractured grains and closer packing than the undeformed host rock (Aydin 1978). No chemical change is seen

between the band and host rock. The lighter colour seen in outcrop is due to the increase in light-reflecting surfaces accompanying grain crushing (Jamison and Stearns 1982).

Permeability within deformation bands is reduced by about 3 orders of magnitude with respect to the host rock (Antonellini and Aydin 1994). These structures therefore represent an important barrier to fluid flow, for example, in hydrocarbon reservoir rocks (Pittman 1981, Edwards *et al.* 1993). Edwards *et al.* (1993) found that compartmentalisation by sealing faults had concentrated post-tectonic cement near fault zones. Conversely it has been suggested that an increase in permeability will be created in the direction parallel to slip because of dilatancy and slip-surface generation (Antonellini and Aydin 1994).

2.3.2. Deformation in the Carmel Formation

The deformation style within the Carmel Formation is very different from that in the Navajo Sandstone. It includes complex veins, breccias and stylolites (Figure 2.10). Azurite and malachite mineralisation is often concentrated where the Carmel Formation and Navajo Sandstone are juxtaposed by movement on the faults. This suggests that fluid flow and the transport and deposition of solutes occur along the faults. This study concentrates on deformation within the Navajo Sandstone, so the deformation within the Carmel Formation is not discussed further in this thesis.

2.4. Study areas

2.4.1. The Big Hole fault

The Big Hole fault is exceptionally well exposed in a deeply incised canyon which exposes serial sections of the fault and its off-fault deformation (Figure 2.11a). The fault strikes 079° and dips 73° to the north and has a trace length of 4.1 km. The photograph in Figure 2.11b shows the displacement along the fault increasing from zero at the fault tip to its maximum displacement of 29 m at the centre of the mapped

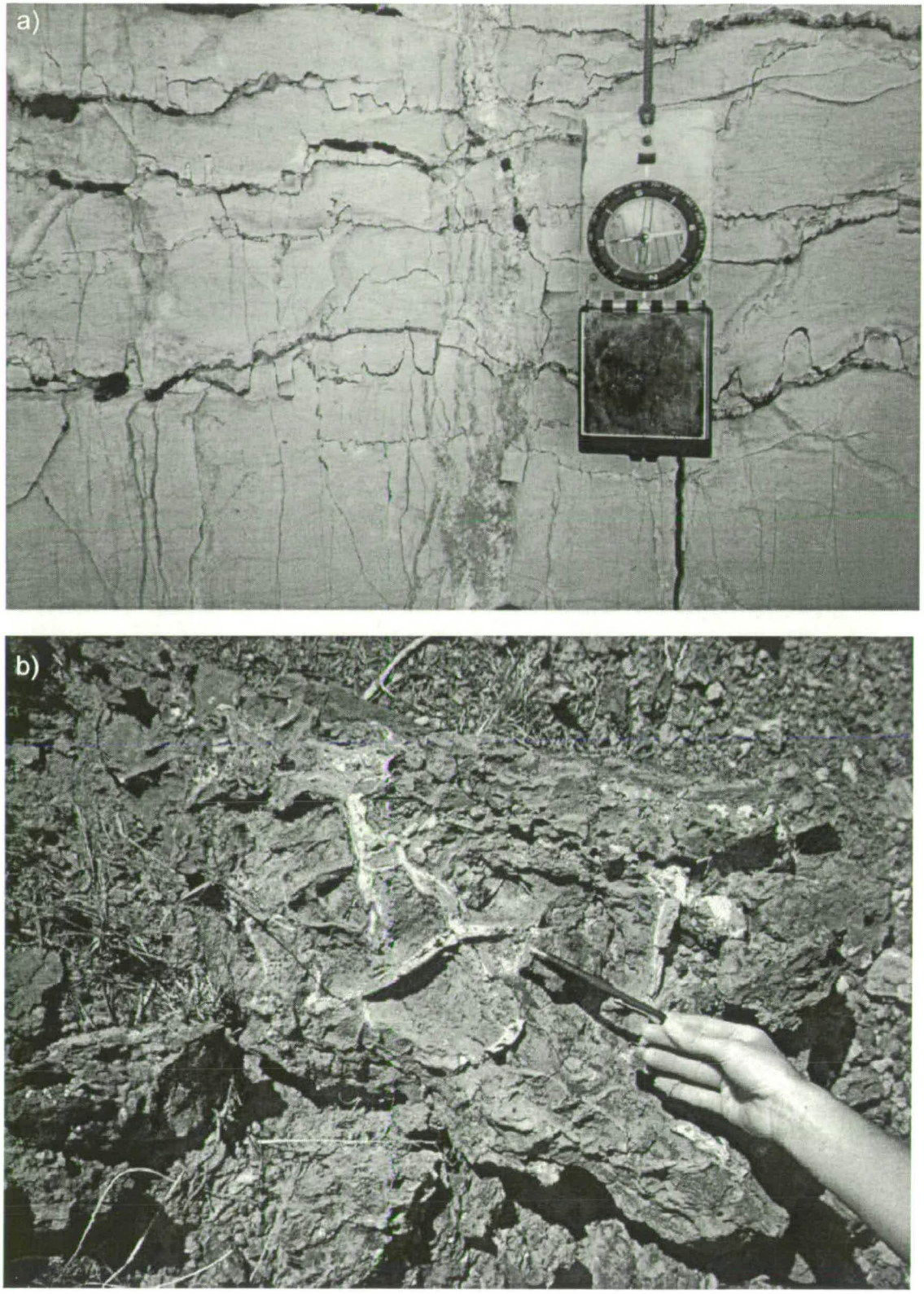

Figure 2.10. Deformation styles in the Carmel Formation a) Stylolites and calcite veins. b) Veined breccia in fault zone.

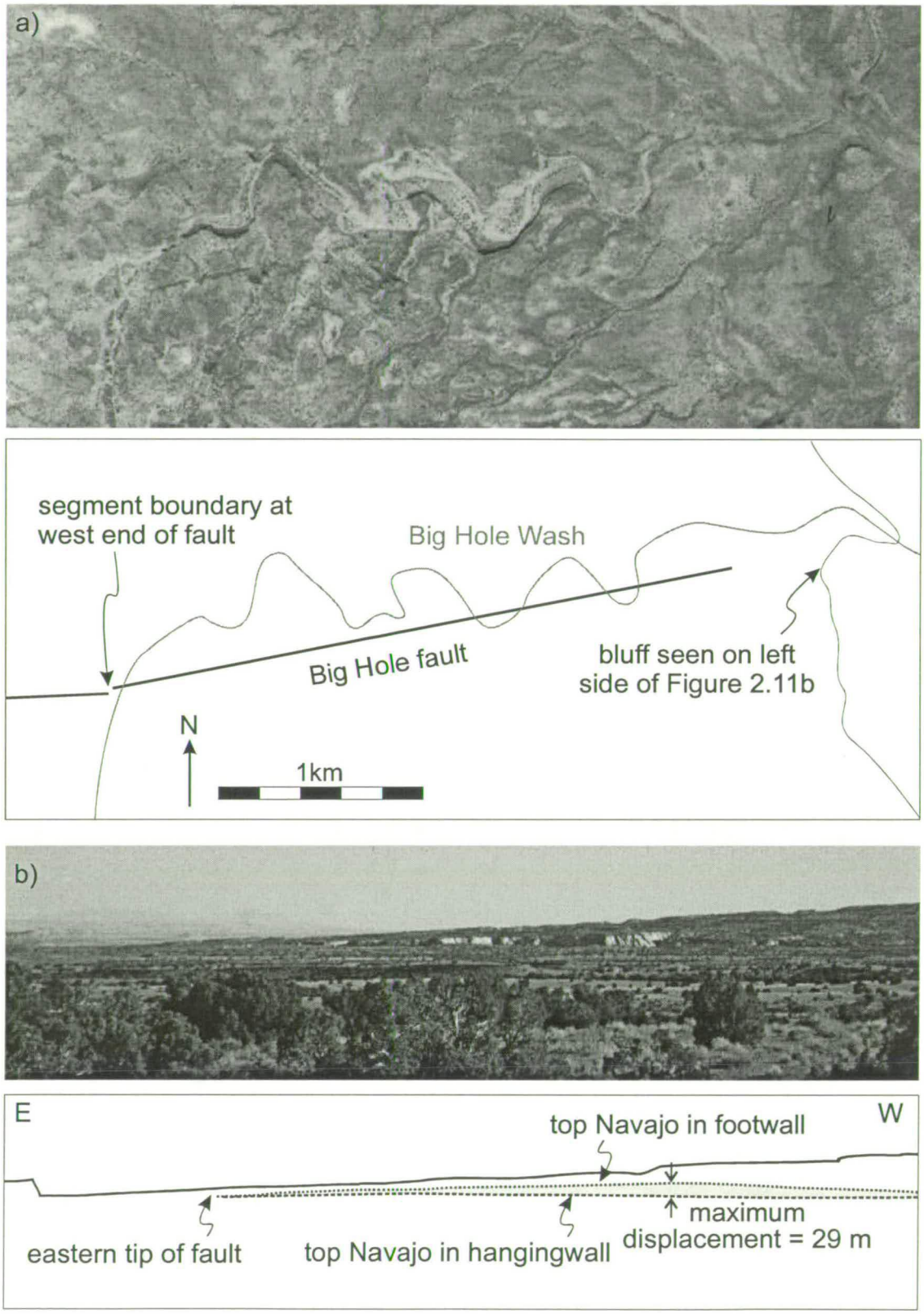

Figure 2.11. a) Aerial photograph of the Big Hole fault. b) Photograph of the Big Hole fault from the northeast. Cliffs of Navajo Sandstone are capped by the Carmel Formation and the displacement can be seen on the boundary.

fault trace. Striations on the fault surface indicate predominantly dip-slip movement (Figure 2.11c).

Both fault tips are hidden beneath Quaternary sediments, so neither tip can be investigated. This fault has not previously been mapped in detail, but does appear on the USGS 1:250 000 geological map (Witkind 1988). Two segments of the Big Hole fault with slightly different strikes meet near the western end of the fault (Figure 2.11a).

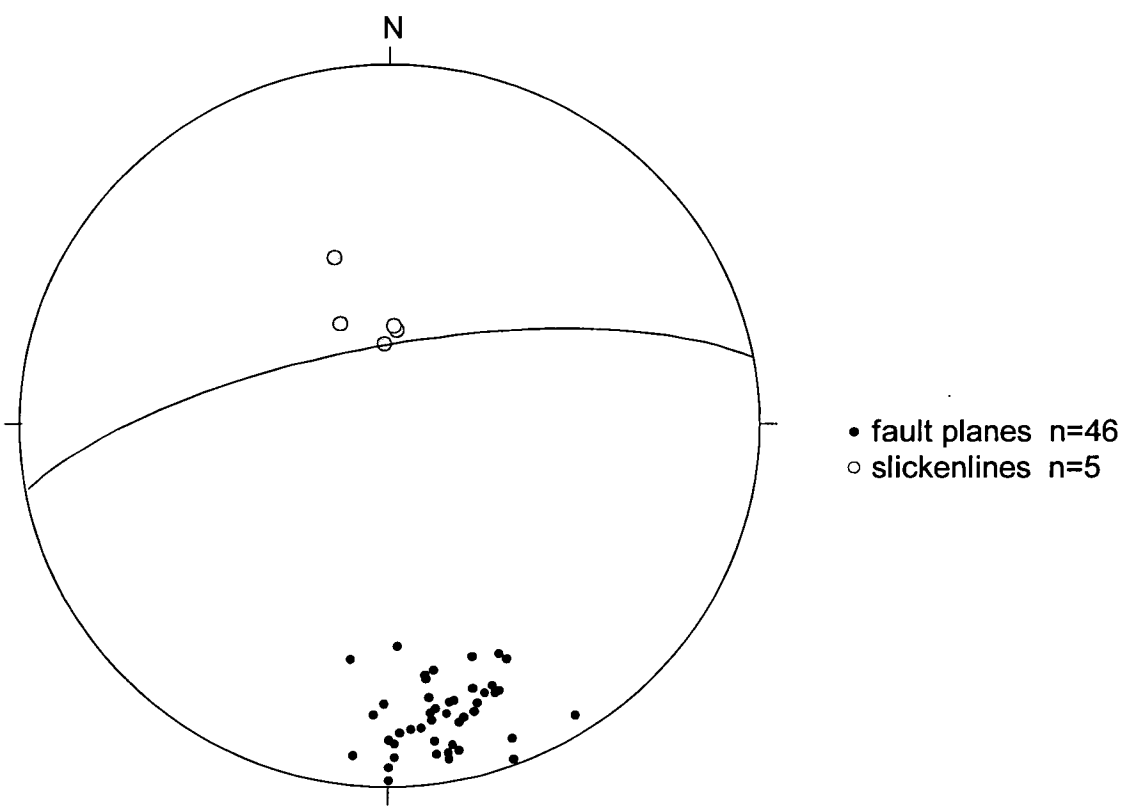

Figure 2.11. c) Stereonet of fault plane and slickenline orientations for the Big Hole fault. The great circle is the best fit to the fault planes.

2.4.2. The Blueberry fault

The eastern tip of the Blueberry fault is superbly exposed in a narrow canyon (Figure 2.12a). The Blueberry fault was named by Krantz (1988), presumably after the small botryoidal azurite concretions that are found close to the fault (Figure 2.12b).The fault is 3 km long and has a maximum displacement of 30 m. The fault strikes 076° and dips 76° to the north. Movement on the fault is predominately dip-slip, but towards the tip it has a small oblique component with slickenlines pitching 70° to the west of dip-slip (Figure 2.12d).

The Blueberry Wash has eroded down through the regional topographic surface (the top F horizon, see section 3.2.1) to expose the Navajo Sandstone. The fault scarp can be traced to the west, but the Navajo Sandstone (and hence the off-fault deformation) is not well exposed. The western tip outcrops in the badland topography of the Entrada Formation (Figure 2.12c). The Blueberry fault is obliquely linked near its mid-point to the La Sal fault. A small parallel fault to the north of the Blueberry fault was named the Bacon fault.

The Blueberry fault was previously studied by Krantz (1988). He collected some estimates of the displacement using basic surveying techniques at a few locations along the fault. His displacement values agree well with the more detailed data presented and discussed in this thesis (see Figure 3.11).

Figure 2.12. a) Photograph of the Blueberry fault tip exposed in the Blueberry Canyon. The photograph is taken looking directly down the fault trace. b) Azurite "blueberries" on the fault surface.

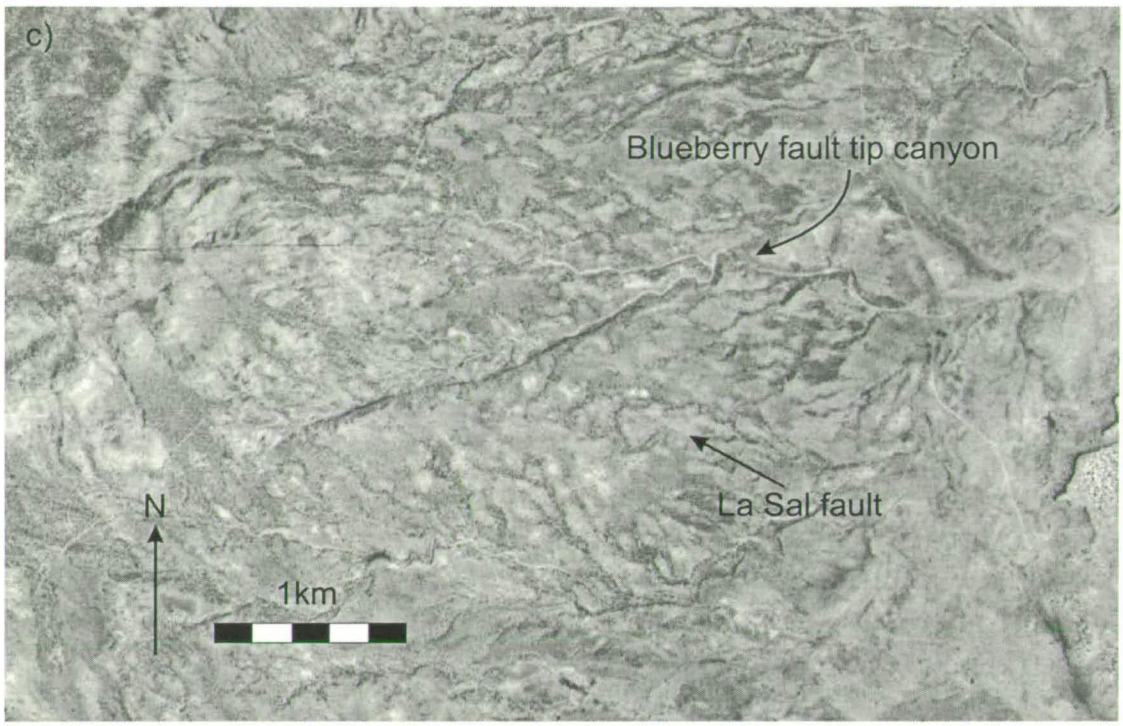

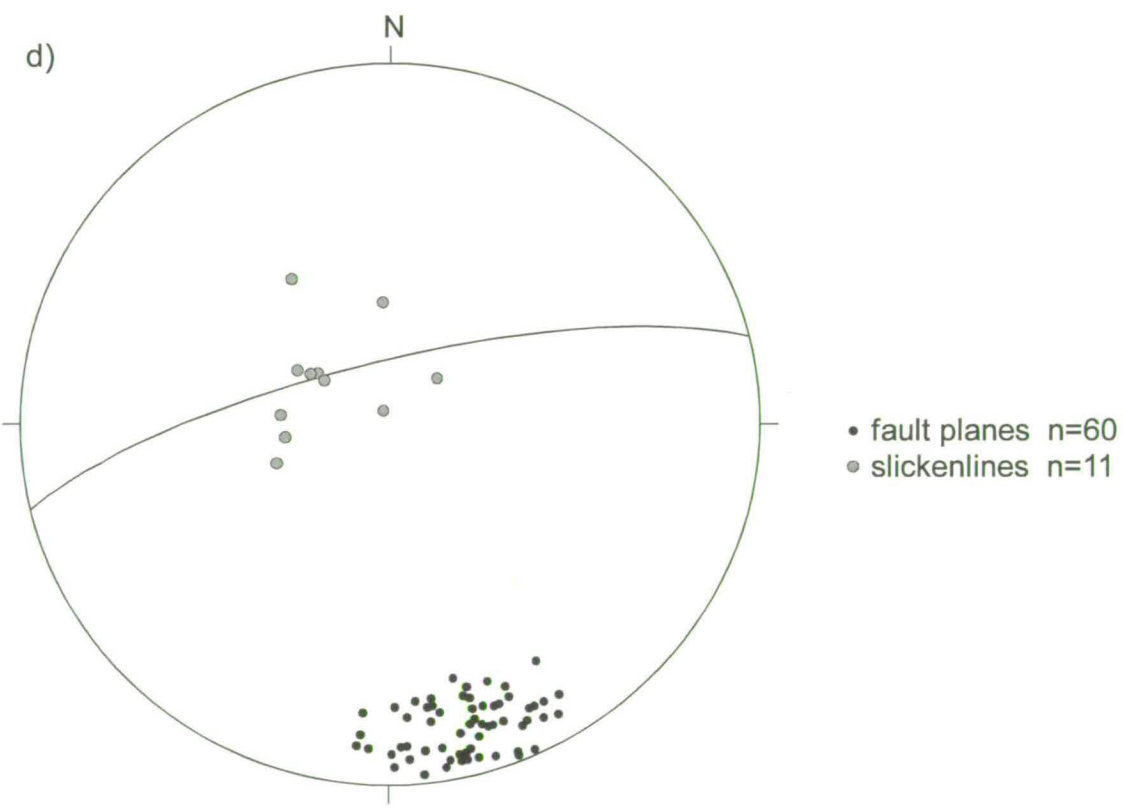

Figure 2.12. c) Aerial photograph of the Blueberry fault. d) Stereonet of fault plane and slickenline orientations for the Blueberry fault.

3. DISPLACEMENT PROFILES AND FAULT TIP GRADIENTS

3.1. Introduction

3.1.1. Rationale

The faults at Chimney Rock offer an opportunity to construct highly accurate displacement profiles: closely spaced horizons in the host sediments can be used as marker horizons to measure displacement. A total station surveying instrument was used to survey these horizons to build up geological maps, which were then used to construct displacement profiles. The Big Hole and Blueberry faults are of the same order of magnitude in size, so the Blueberry fault tip can be considered as a proxy for the unexposed tip of the Big Hole fault.

The region of low displacement near the tip of a fault is expected to correspond to an area where the fault surface is beginning to form, but where no through-going surface is yet developed. The majority of published displacement profiles do not concentrate on the tip area partly because a poorly developed fault surface with low displacement is difficult to resolve. Therefore a detailed, high resolution study of the end of a fault is needed to determine the geometry of fault displacement profiles at fault tips.

The principle aim of this chapter is to construct a detailed displacement profile concentrating on the tip zone of a real fault. This will be used to test the applicability of the mathematical models of fault growth described in Section 1.6, i.e. to distinguish linear from bell-shaped tip gradients. In addition the geological maps also form a framework for surveys of deformation in the volume surrounding the fault (Chapters 4 and 5).

3.1.2. Structure of this chapter

Section 3.2 presents the methods used to reconstruct the displacement profiles from the geological maps. The results for each of the three survey areas: the Blueberry fault, the western end of the Big Hole fault and the eastern end of the Big Hole fault

are described in Section 3.3. Section 3.4 compares the measured profiles to models discussed in Chapter 1. The results are summarised and discussed in Section 3.5.

3.2. Methodology

3.2.1. Marker horizons

Horizons in the lower Carmel Formation were originally assigned letters from A to F, with A being the top Navajo Sandstone unconformity and B to F being the tops or bases of resistant limestone layers. To be useful as a marker bed, a horizon has to be consistently recognisable in different locations, regardless of the present-day erosional state of the slope. The horizons chosen (top Navajo Sandstone, C, S, top and base F), and the criteria used to recognise them, are shown in Figure 3.1. There is some variation in the thickness of the sequence between the Blueberry and Big Hole faults, but it does not vary on the scale of individual surveys. Note that although the top of the Navajo Sandstone has some palaeotopography, it still acts as a good marker horizon (see Figures 3.5, 3.7 and 3.9).

Above horizon F, the Carmel Formation consists of loose friable limestones and marls that do not form easily identifiable beds. Hence surveys are constrained to the lowest part of the Carmel Formation. The regional land surface in this area is often the top of horizon F.

3.2.2. Surveying procedure

A total station is a highly accurate surveying instrument consisting of a theodolite, an electronic distance meter (EDM) and a telescope (Figure 3.2a). The telescope can rotate 360°in the vertical plane and the whole machine is mounted so that it can move 360° through a horizontal circle. Thus, the telescope can be focused on any point around the machine. To measure the position of a point, the telescope is focused on a corner-cube reflector fixed on a pole of known height located on the point of interest. The corner-cube reflector ensures that an incident light beam is reflected back along the same path regardless of its angle of incidence. The vertical and horizontal angles from the baseline that the theodolite must move through to

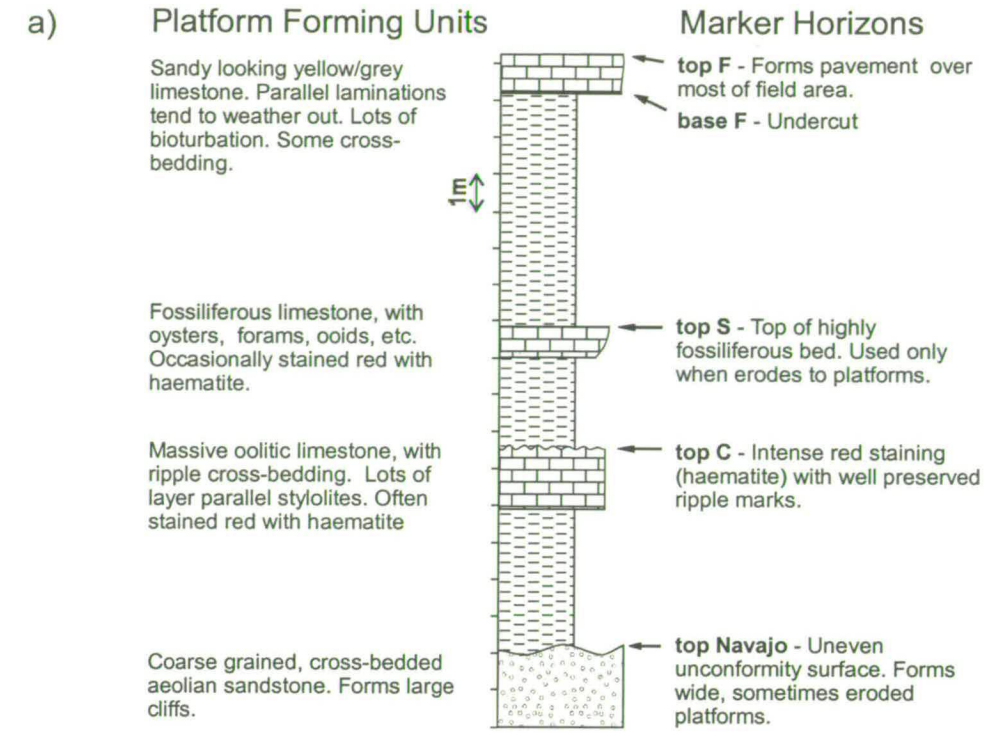

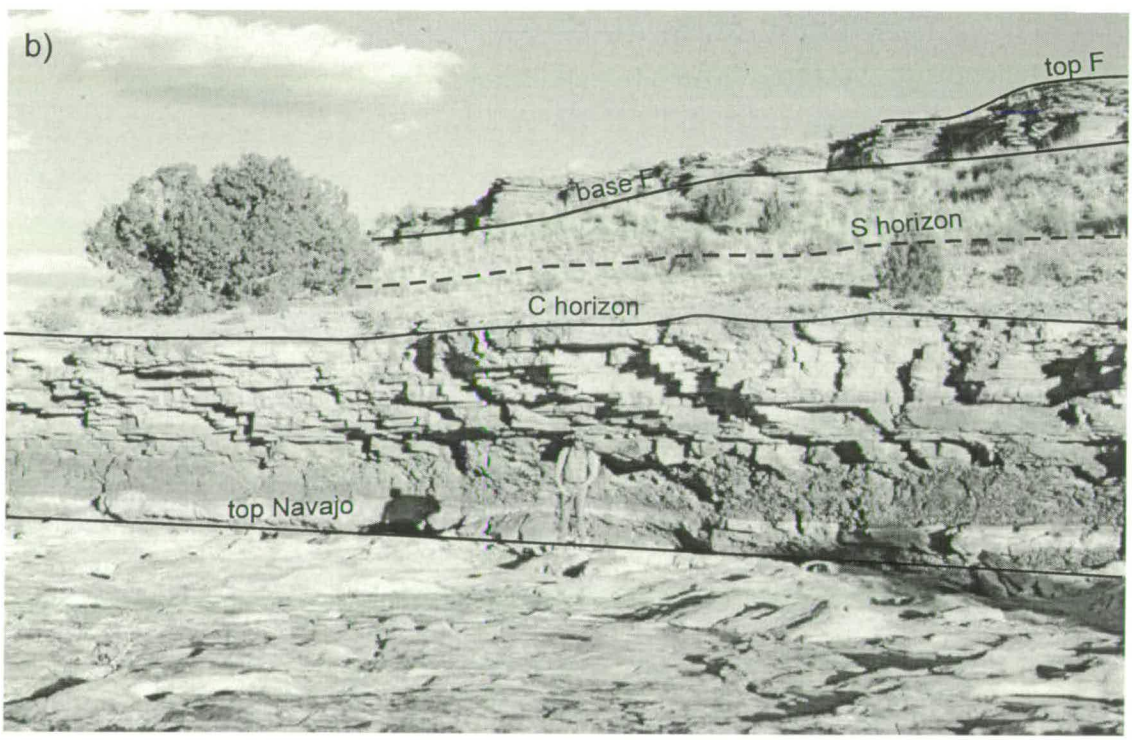

Figure 3.1. a) Schematic stratigraphic log of the lower Carmel Formation. Right-hand side: description of the more resistant rock units which outcrop in the field area. Left-hand side: description of the marker horizons used in the survey. b) Photo of the lower Carmel Formation showing the marker horizons used in these surveys.

focus on the reflector are recorded. The EDM sends out a laser pulse to the reflector and the travel time of the pulse is then converted into distance. The x, y, z co-ordinates of the point are then calculated using simple trigonometry (Figure 3.2b) and these are displayed on an LED screen and recorded in the field notebook. Theoretically the positional accuracy of the total station is ± 5 mm over distances up to 2 km. Although all the data points in these surveys were well within this distance from the theodolite, other errors are introduced through plotting the data.

To set up a survey, the total station is mounted on a tripod and levelled using three thumbscrews and a bubble level. The vertical circle is defined by rotating the telescope through 360°. The system of horizontal (x and y) co-ordinates is then defined by shooting a baseline in the x-direction (Figure 3.2b). For these surveys the baseline (x-axis) was chosen to be as close to compass north as possible to keep the co-ordinate systems consistent between surveys. In spite of this, the finite systematic error associated with compass measurements (2-3°) meant that a rotation of a few degrees had to be applied to connect two individual surveys together. To get true vertical (z) co-ordinates, the total station values must be corrected for the height of the instrument and the height of the mirror pole (true height = measured height + machine height - pole height). The former will remain constant throughout an individual survey, the latter is recorded for each individual measurement point.

For this study, the mirror was positioned above points on marker horizons in the footwall and hangingwall. To cover the entire fault along strike, several surveys were shot and then amalgamated into a global set of co-ordinates. To achieve this, two or more common reference points must be shot in neighbouring surveys. A network of cairns was built to act as common points. Surveys were combined by applying a matrix transformation to rotate and translate the co-ordinate axes of each survey to a common global origin. This was done using a FORTRAN program written for the purpose.

Using the x and y co-ordinates, data from the theodolite surveys were used to create geological maps of the tip areas. These were plotted in the field at a scale of 1:1000.

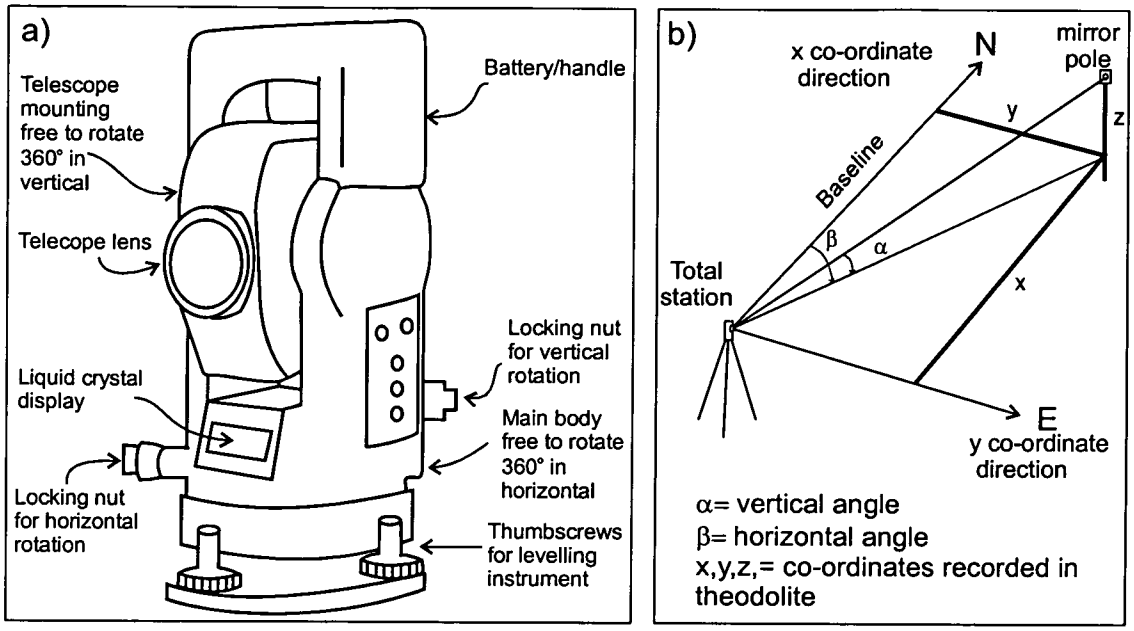

Figure 3.2. a) The Topcon GTS-3B total station used in this study b) Geometric configuration for the calculation of co-ordinates from distance and angle data.

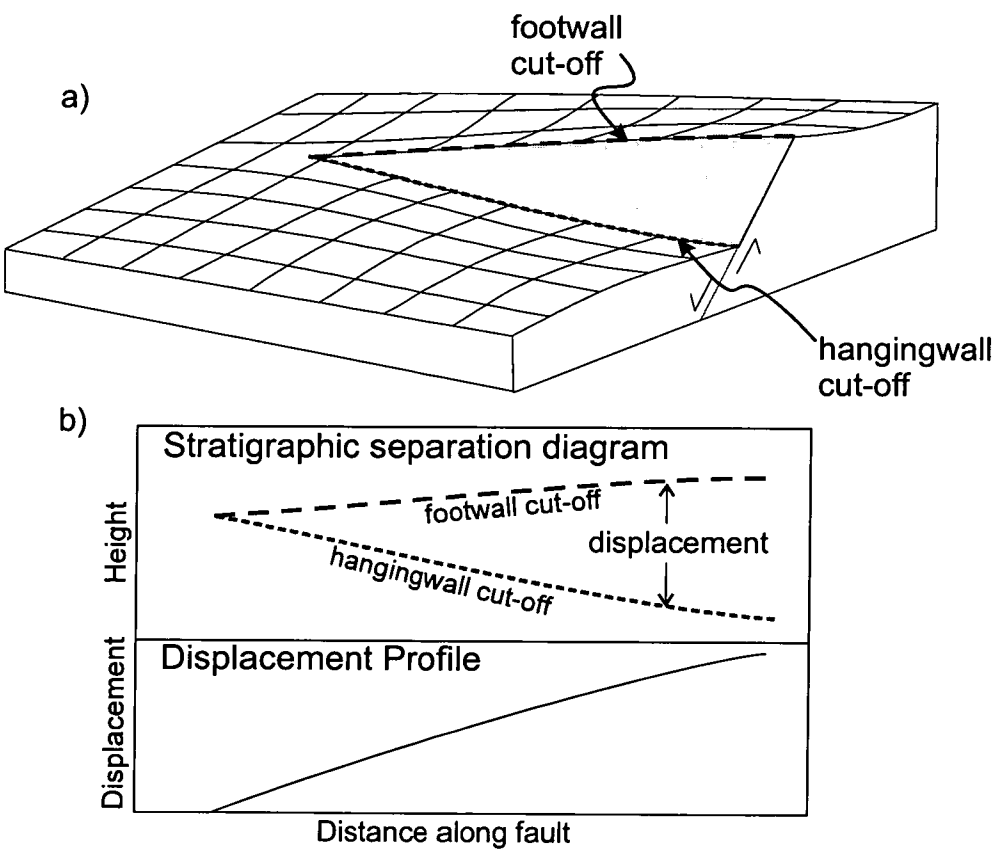

Figure 3.3. a) Cartoon of the plane of an individual marker bed offset by a fault. b) Stratigraphic separation diagram and displacement profile for that bed.

This allowed the data to be checked as it was being collected, and provided base maps for additional data collection (Chapter 4 and 5). The maps shown in section 3.3 below were plotted using Microsoft Excel from the transformed global dataset. The diamond symbols on these maps represent the position of actual data points, demonstrating the extensive coverage of the surveys.

3.2.3. Constructing displacement profiles

Stratigraphic separation diagrams show the hangingwall and footwall cut-offs of bedding on the fault surface. They are constructed by extrapolating strike lines into a vertical plane (Figure 3.3a). For steeply dipping faults, to a first approximation, the vertical displacement (throw) is then simply the height difference between the hangingwall and footwall cut-offs. The resulting displacement profile (Figure 3.3b) shows the change of displacement with distance along the fault. In this study throw is used as a proxy for displacement. This can be justified because (a) the fault surfaces dip steeply with negligible horizontal displacement, (b) there is no evidence for a significant change of dip or slip-direction along the faults, and (c) because it is the shape of the displacement profiles that is of interest rather than the amplitude of the displacement.

Stratigraphic separation diagrams can be calculated from the global dataset by finding the intersection of the two straight lines representing the strike line,

$$(y-y_o) = m_o\,(x-x_o), \tag{3.1}$$

and the fault plane,

$$(y-y_i) = m_i\,(x-x_i). \tag{3.2}$$

To calculate the intersection points subtract equation (3.1) from equation (3.2), giving

$$x = ((y_i-y_o) + m_o x_o - m_i x_i) / (m_o-m_i), \tag{3.3}$$

and then calculate y by substituting the value of x into equation (3.1). The position of the intersection points along the fault is then calculated as the distance from a known

point on the fault. Bedding cut-offs were linearly interpolated at 20 m intervals using mathematical software (Matlab), and displacement profiles calculated by subtracting the hangingwall cut-off from the footwall cut-off.

3.2.4. Bedding strike

Bedding in the area dips approximately to the east (Figure 3.4). Because the dip of the bedding is low (between 3.5° and 5°), the measured bedding strikes have a large range of directions. Each displacement profile has been plotted for three values of bedding strike; the best estimate, and the maximum and minimum reasonable strikes. The resulting plots show the errors that can reasonably be expected from measurement of bedding. The resultant propagated error can be up to 50 m in distance along the fault and 5 m in displacement, for the most extreme deviation. However in places where the bedding is much closer to the fault (e.g. the right-hand side of Figure 3.6) the errors are much smaller.

Figure 3.5 shows the geological map, stratigraphic separation diagram and displacement profile for the Blueberry fault tip area. As an example of the errors due to bedding, Figure 3.6 shows the stratigraphic separation diagrams and displacement profiles individually for each of the horizons in Figure 3.5b and c. This diagram illustrates the sensitivity of the displacement profile to uncertainties in the order of ± 5° in the bedding orientation. For the purposes of this study the errors are assumed to be represented by lines on the displacement profile graphs showing the variations in the calculated displacement profiles with respect to extreme values of bedding strike. A more detailed analysis of errors is not warranted, since all other sources of error are small compared to those associated with bedding orientation and a realistic variation in bedding direction does not drastically change the form of the measured displacement profiles.

3.2.5. Limitations of the technique

Displacement profiles were calculated assuming that strata are planar on either side of the fault. This is unrealistic because strata must be folded slightly to accommodate

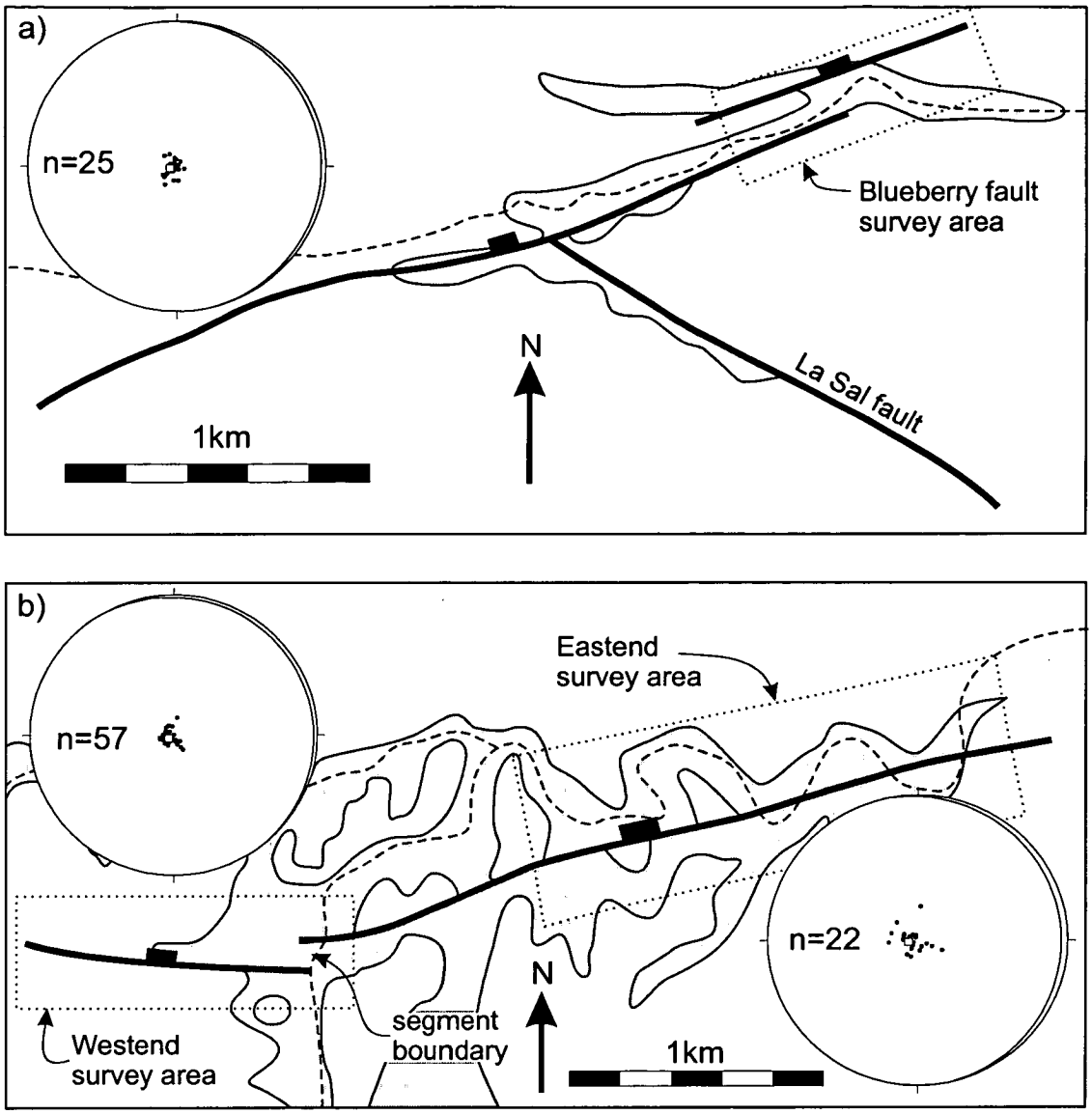

Figure 3.4. Location map of a) the Blueberry fault and b) the Big Hole fault displacement profile surveys (dotted lines). The faults are shown as bold lines with the bar on the downthrown side. The Navajo Sandstone is shown in grey. The courses of the Blueberry and Big Hole Washes are marked by dashed lines. Stereonets show the orientation of bedding around the faults. The average bedding is shown as a white square and a great circle.

displacement at the fault tip. Although the change in strike may only be a few degrees, the strike direction should vary systematically around the fault. This effect could not be resolved within the bedding data obtained here. Beds must also be folded to accommodate areas of local displacement minima, for instance segment boundaries.

These effects will be more important for readings at greater distances from the fault. The error in the orientation of the strike line also increases in proportion to the distance of the point away from the fault. This is illustrated well in the profiles for the top Navajo Sandstone at the Blueberry fault (Figure 3.6c). Where the fault cuts through a meander spur, the data points are closer to the fault plane and the deviation due to bedding is smaller. Where there is evidence on the stratigraphic separation diagrams for rollover of bedding in towards the fault, e.g. in the hangingwall of the Blueberry fault, the points closest to the fault have been used and those further away have been discarded.

3.3. Results

3.3.1. Blueberry fault eastern tip

Figure 3.5a shows the geological map resulting from five combined surveys made at the Blueberry fault tip. The western limit of the map is approximately the site of the first displacement measurement made by Krantz in 1988 (see Figure 3.12 for a comparison of Krantz's data with this survey). At this point the fault is well developed and forms a 2-4 m high fault scarp. The surveys extend east to well beyond the point where no deformation is apparent in the Navajo Sandstone or Carmel Formation.

The stratigraphic separation diagrams and displacement profiles for the Blueberry fault are shown in Figure 3.5b and 3.5c. The hangingwall and footwall cut-offs slope to the east because of the regional dip of the strata. Figure 3.6 shows the stratigraphic separation diagrams and the resulting displacement profiles for the individual horizons.

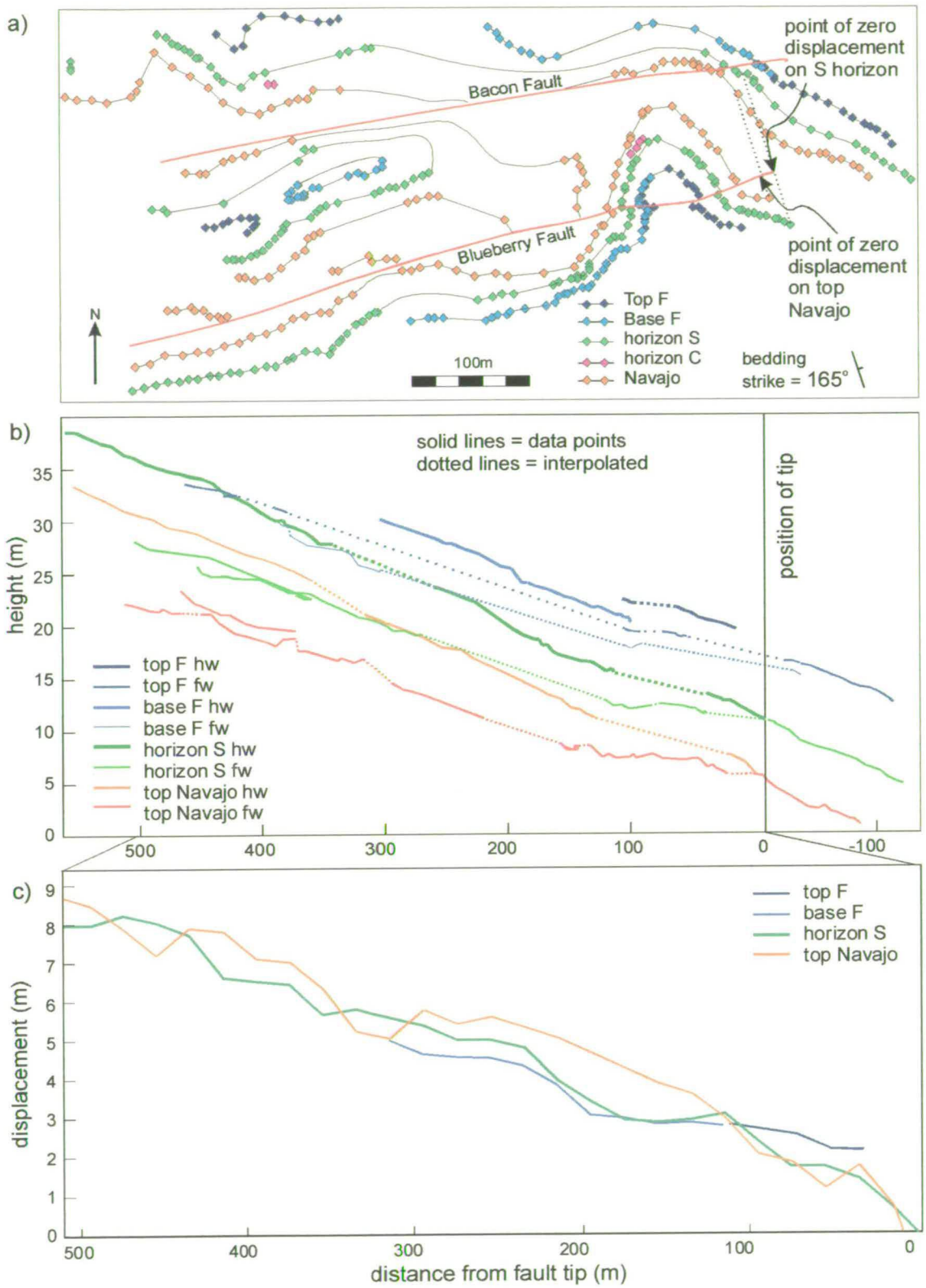

Figure 3.5. a) Geological map of the Blueberry fault tip area. b) Stratigraphic separation diagrams for the four marker units (hw = hangingwall, fw = footwall). c) The resulting displacement profiles calculated from the difference in elevation of the

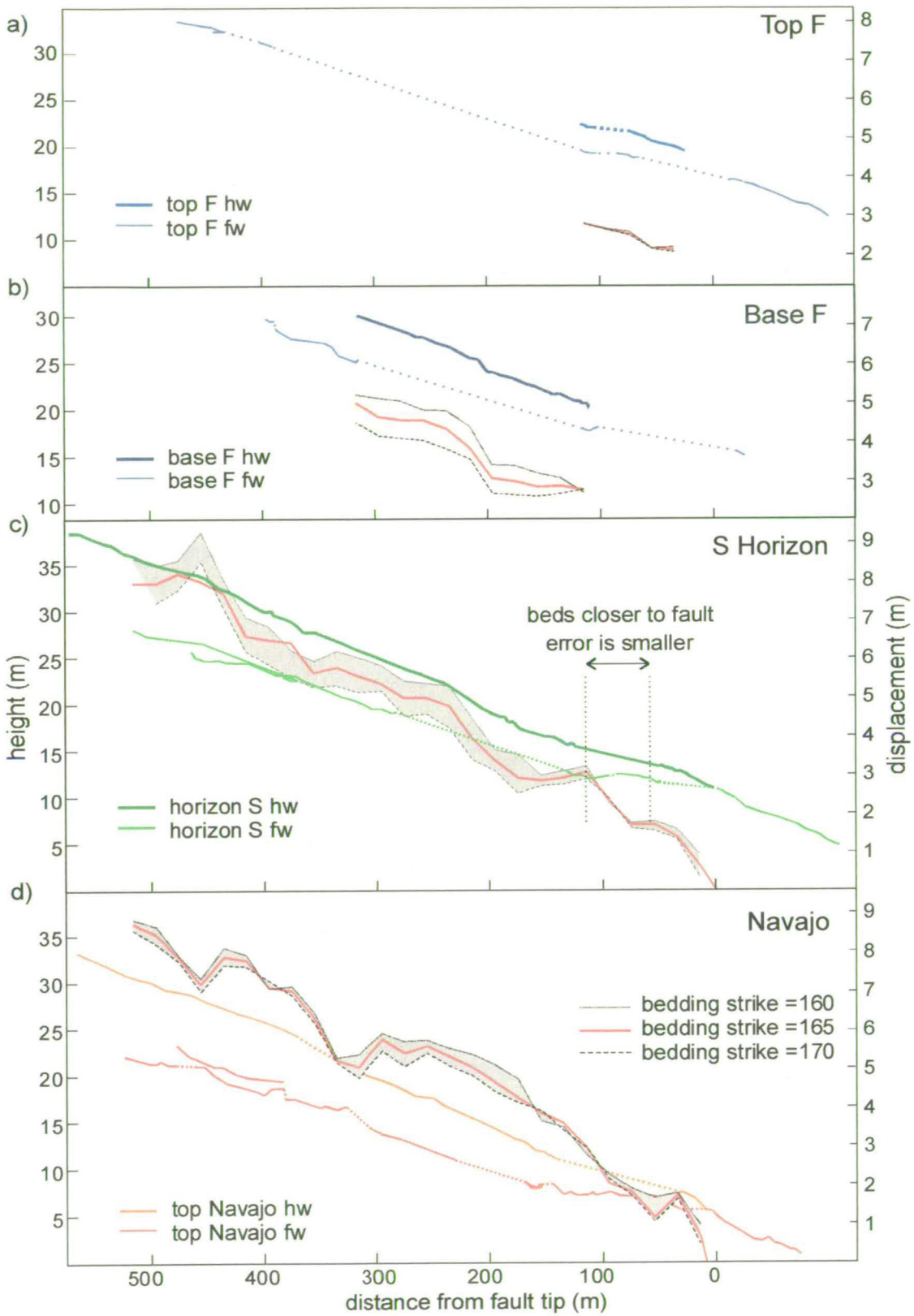

Figure 3.6. Stratigraphic separation diagrams and displacement profiles for individual horizons around the Blueberry fault tip. Displacement profiles are for three different values of bedding strike demonstrating the errors in displacement.

The displacement profiles are shown for three values of bedding strike: 160°, 165° and 170°. The deviation in displacement profile with bedding strike is largest where the points have been projected from a greater distance. The smallest deviation occurs where the fault cuts through the meander spur, e.g. at 75-150 m from the tip in the Navajo Sandstone.

All four measured horizons show a linear decrease of displacement with distance towards the tip of the fault (Figure 3.5c). The point where the displacement profile approaches zero is in the centre of the Blueberry Wash canyon. Although some deformation is seen in the rocks to the east, the fault plane no longer has a single well-defined slip-surface beyond this point (section 4.3.1). The tip defined by the Navajo Sandstone is 10 m further west of that defined by the S horizon (Figure 3.5a). However, this is within the error range defined by variations in bedding strike. The tip of this fault is defined as the zero displacement point on the S horizon.

3.3.2. Big Hole fault: eastern tip to centre of fault

Figure 3.7a shows the geological map constructed from eleven surveys of the Big Hole fault. Only the C horizon was measured over the majority of the area. The Big Hole Wash meanders across the fault zone, cutting a wide canyon, and as a result these surveys contain some of the largest distances measured in this study. Errors in this area due to uncertainties in bedding strike are therefore potentially much larger than those for the Blueberry fault or the western tip of the Big Hole fault.

Stratigraphic separation diagrams and displacement profiles for the east end and centre of the Big Hole fault are shown in Figure 3.7b and 3.7c. The displacement profiles are plotted for three values of bedding strike: 184°, 166° and 160°. Although the errors are larger than for the other two faults, the general form of the displacement profile is independent of the bedding strike direction (Figure 3.8c). The displacement profile shows a maximum at the centre of the fault and displacement decreasing towards the eastern tip.

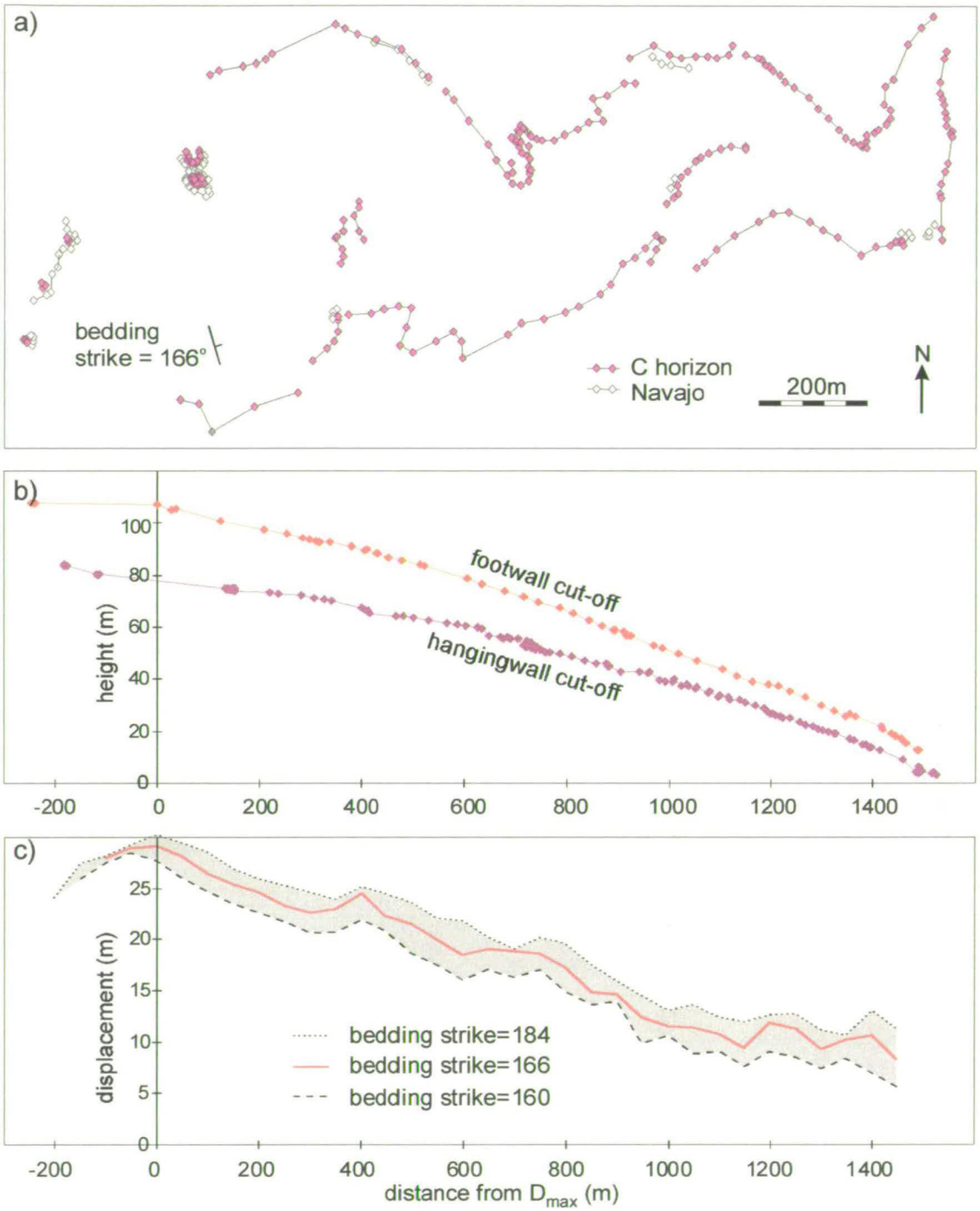

Figure 3.7. a) Geological map, b) stratigraphic separation diagram and c) displacement profile for the east end of the Big Hole fault. Displacement profiles are for three different values of bedding strike indicating errors in displacement.

For 350 m to the east of the last survey point a step in the ground surface runs parallel to the projected position of the fault. Beyond this point the fault is buried beneath Quaternary sediment. The position of the eastern tip is constrained by an outcrop of the Entrada Sandstone 900 m to the east in which there is no evidence of faulting. Three boreholes drilled by Evans *et al.* (1998) encountered the fault at 60 m depth at a site 300 m to the east of the last surveyed point.

3.3.3. Big Hole fault: western tip

Seven surveys were taken at the western end of the Big Hole fault near where a jeep track crosses the fault (Figure 3.8a). Exposure of the fault plane to the west of this track is poor, but offsets of the marker beds can be traced as far as 700 m to the west. The surveys extend 300 m beyond the segment boundary mapped by Witkind (1988) (Figure 3.4). The fault can be traced to the east as a topographic step in the land surface, but the marker horizons outcrop too far away from the fault, making further surveying beyond the segment boundary impractical.

Stratigraphic separation diagrams and displacement profiles for the west end of the Big Hole fault are shown in Figure 3.8b and 3.8c. The exact position of the fault tip is uncertain; therefore all distances are plotted relative to the point of maximum displacement (see Figure 3.13). The displacement profiles are plotted for three values of bedding strike: 138°, 142° and 150°.

There is a reasonable correlation between the displacements on all three horizons (Figure 3.8c). Anomalously large displacements are seen on horizon C at the west end of the profile. Some negative displacements are seen at the far west end of the profile. A close examination of the stratigraphic separation diagram shows that most of the negative displacements are a consequence of projecting between data points and hence are artefacts introduced by extrapolation.

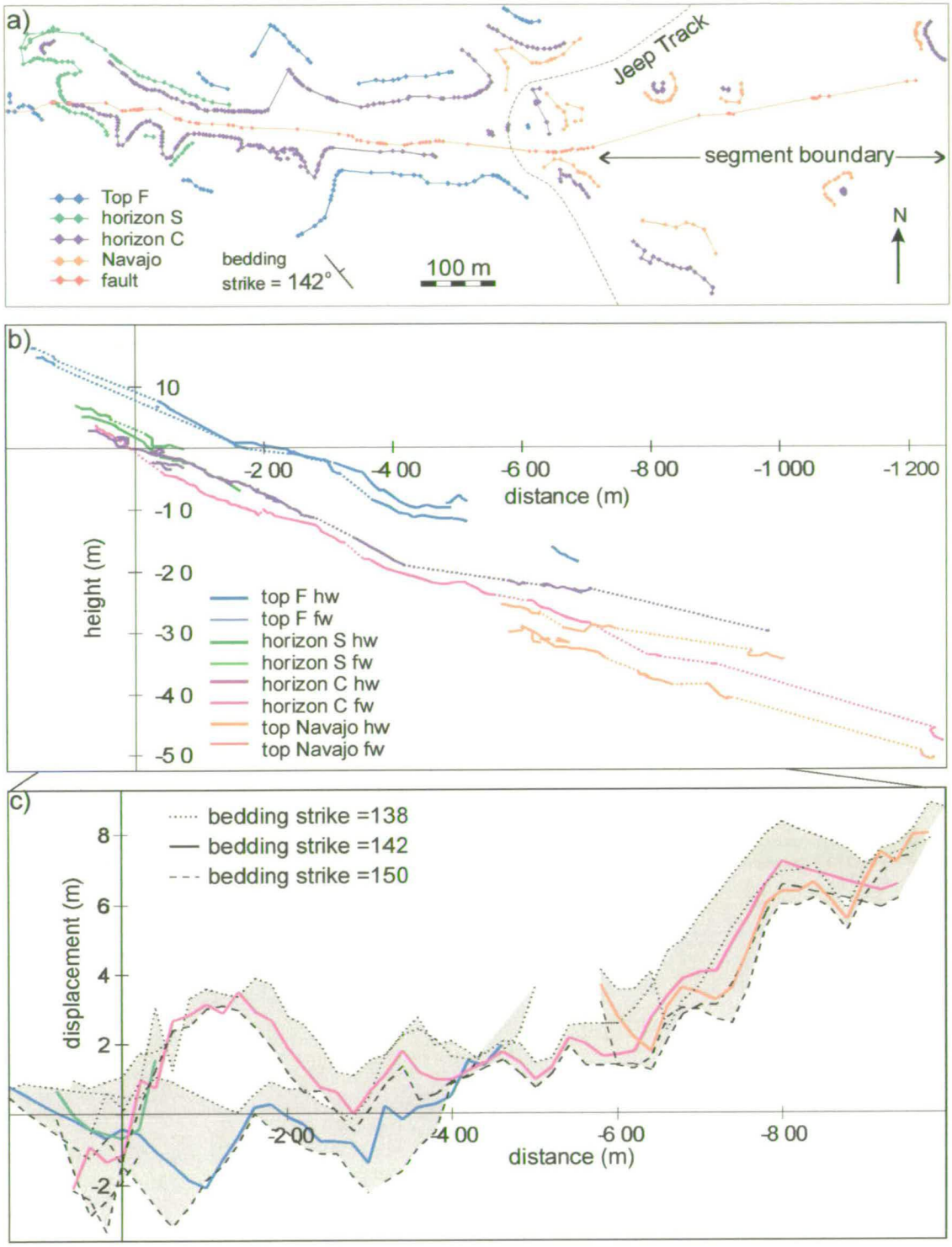

Figure 3.8. a) Geological map, b) stratigraphic separation diagram and c) displacement profile for the Big Hole fault western tip. Displacement profiles are for three different values of bedding strike indicating errors in displacement.

3.4. Interpretation

3.4.1. Blueberry fault tip

The displacement profile for the Blueberry fault tip is remarkably linear (Figure 3.9a). When the data for all four horizons are fitted with a straight line it has a slope of 0.015 with a correlation coefficient of 0.966 (Figure 3.9a). The best fit lines for individual beds are also very good (Figure 3.9b), especially those for the top Navajo Sandstone and S horizon, which are parallel to each other. The best fit lines for the base F and top F horizons are slightly shallower, but there are less data points on these horizons. The extrapolation of the best fit straight line to the data extends 58 m beyond the fault tip (as defined by the point where displacement on the S horizon is zero). This corresponds to the edge of the canyon where a few deformation band clusters are exposed but no slip surface is developed (Section 4.3.1).

As discussed in Section 1.4, fault tip gradients provide a means of constraining fault models. Bürgmann *et al.* (1994) invoke a lateral change in frictional properties along the fault plane as a way of eliminating the need for the bell-shaped profile predicted by Cowie and Scholz (1992a) and discussed in Section 1.4.2. However there is no evidence for a change in frictional properties on the Blueberry fault. The fault surface is consistently smooth and slickenlined up to the point where the tip is projected to be (Section 4.3.1).

Figure 3.9a shows the best fit line for the tip region compared to three theoretical model curves, constructed with the Cowie and Scholz (1992a) model. Reasonable values of the model parameters (yield strength, remote stress, shear modulus and Poisson's ratio) for the Navajo Sandstone are taken from Cowie and Scholz (1992a). The model parameters used are shown on Table 3.1 and have been chosen to give a range of s/L ratios from 0.1-0.3 (Section 1.4.2). The data is not convincingly fitted by any of these curves (Figure 3.9a).

Cowie and Scholz (1992a) predicted that the length of the convex-downward zone of the bell-shaped profile should be 10-20% of the total fault length (s/L=0.1-0.2).

Vermilye (1996), in a study of the distribution of microfractures around small strike slip faults, argued that this zone of microfracturing corresponded to the process zone. In Vermilye's case this was 1% of the fault length (s/L=0.01). However, even if the convex-downward region of the curve is this short, the remaining part of the fault profile should resemble a purely elastic profile (an ellipse) and the resolved displacement would be higher than that seen in this study. The straight lines seen in Figure 3.9b are not predicted either by an elastic fracture mechanics model (elliptical profile) or a model with a large process zone (bell-shaped), but they fit the data demonstrably better than either.

parameter	model 1	model 2	model3
υ	0.2	0.2	0.2
σ_v	130	140	166
σ_r	100	100	100
μ	4000	4000	4000
σ_f	30	40	50
s	1016	750	401
s/L	0.28	0.21	0.11
D_{max}	31	31	31

Table 3.1 Model parameters used to construct the models in Figures 3.9 and 3.12.

Displacement on the Navajo Sandstone seems to be consistently higher than on both the S horizon and base F horizon. This may be an indication of the position of this fault trace as a chord on the main fault ellipse (Section 1.4.1). That is, if the displacement is greater on lower horizons, then displacement is increasing downwards and this fault trace is above the centre of the fault ellipse.

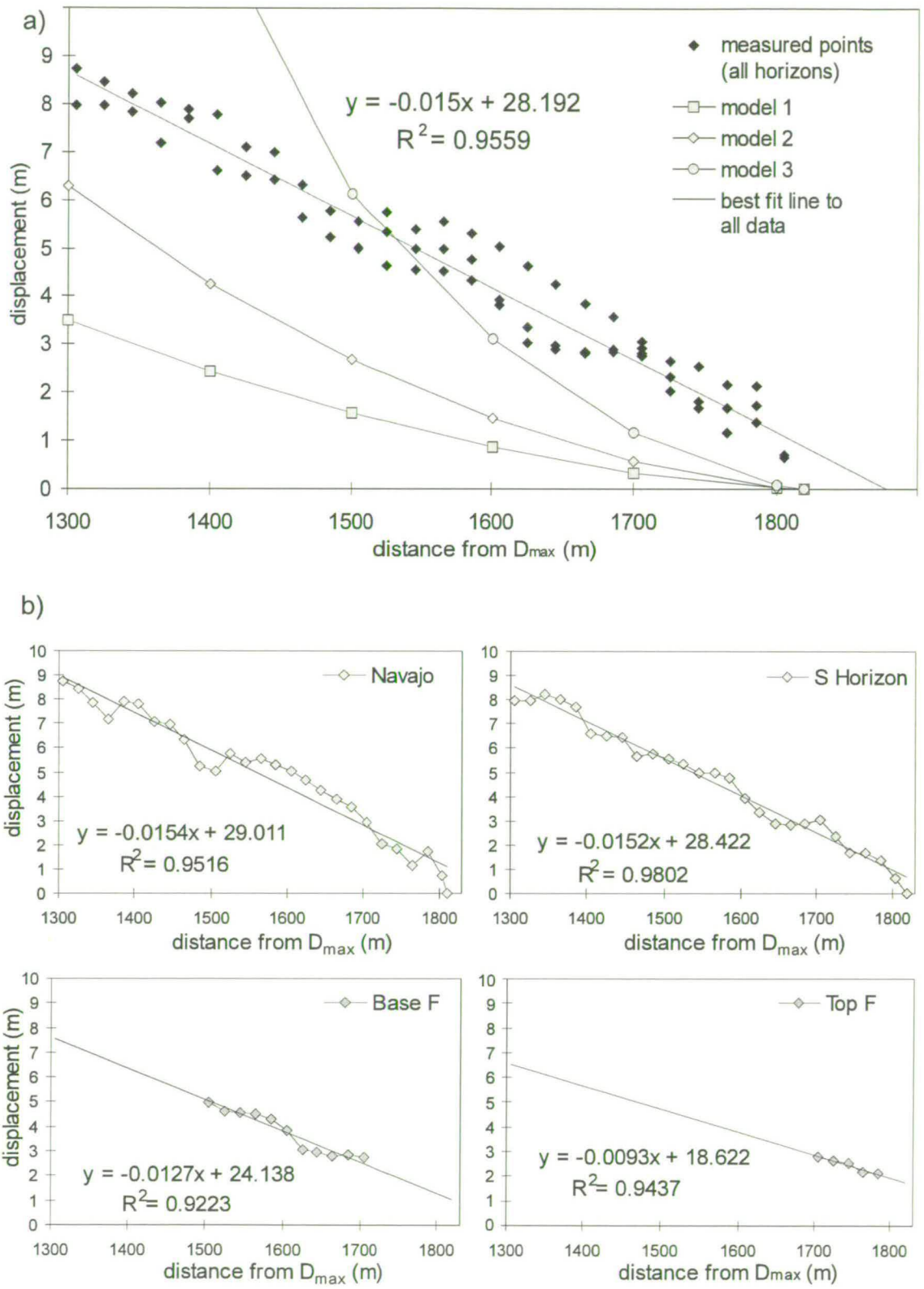

Figure 3.9. a) Comparison of measured displacement profile for the Blueberry fault with Cowie and Scholtz (1992a) model curves constructed using the parameters in Table 3.1. b) Displacement profiles and best fit lines for individual horizons.

3.4.2. Big Hole fault tips

When fitted with a straight line, the data at the west end of the Big Hole fault have a tip gradient of 0.007 (Figure 3.10). The points are reasonably well described by such a linear trend, with a correlation coefficient of 0.708. In this case, the data could conceivably be fitted with one of the bell-shaped model curves, but this uses rather low, and physically unrealistic, values of the input parameters (model 1). This results in an extremely high *s*/L ratio of around 30%. This is well above the ratio predicted by Cowie and Scholz (1992a) from considerations of realistic model parameters.

parameter	model 1	model 2	model 3
υ	0.2	0.2	0.2
σ_v	120	130	166
σ_r	100	100	100
μ	3500	3500	4000
σ_f	40	55	59
s	1250	835	356
s/L	0.31	0.21	0.09
D_{max}	29	29	29

Table 3.2 Model parameters used to construct the models in Figure 10, 11 and 13.

The best-fit lines for individual marker horizons are not as good as for the Blueberry fault tip (Figure 3.10b). This is because there is more scatter in the data for each bed in this location than there is at the Blueberry fault.

The data at the east end of the Big Hole fault is fitted very well by a linear displacement profile, with a gradient of 0.014 and a correlation coefficient of 0.961 (Figure 3.11). If this value of the displacement gradient is used to project the position of the eastern tip of the Big Hole fault, the approximate position of the tip is 2046 m from the maximum displacement. This agrees well with the position of the fault tip as inferred from field observations described in section 3.3.3.

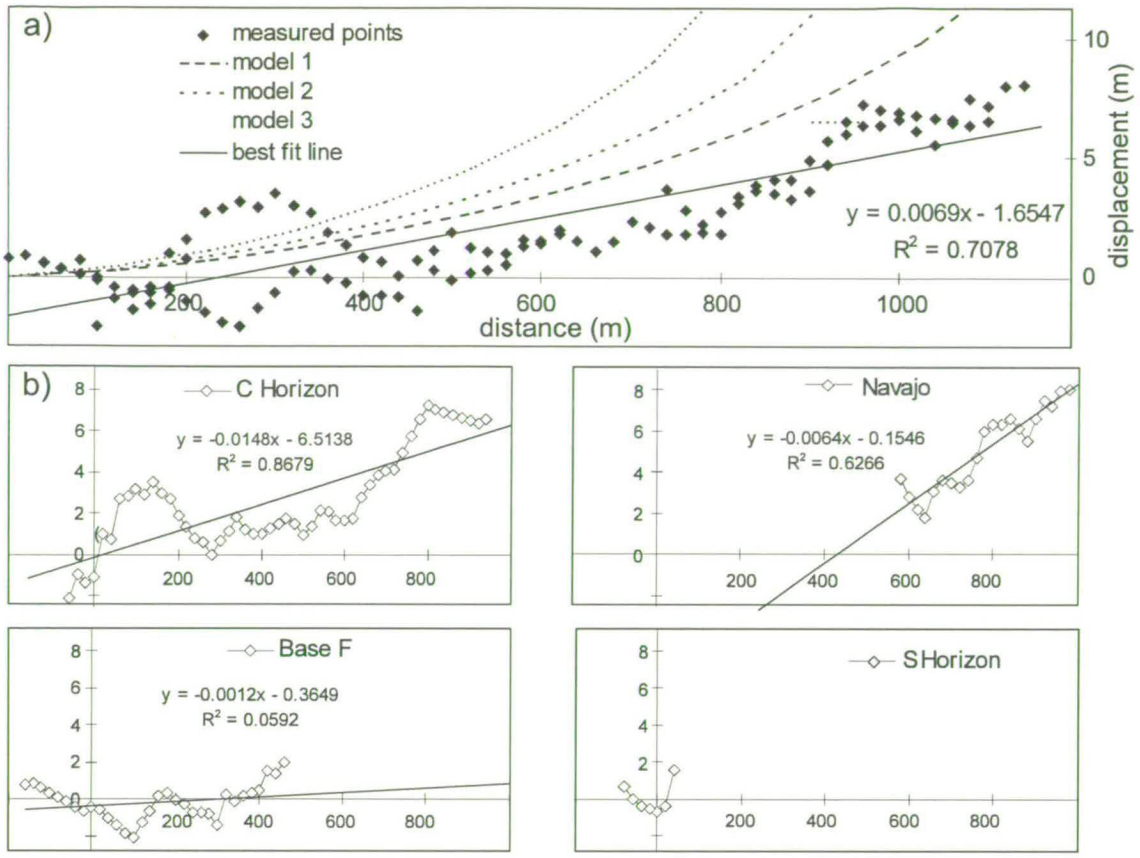

Figure 3.10. a) Comparison of measured displacement profile with model curves for the western end of the Big Hole fault. b) Displacement profiles and best fit lines for individual horizons.

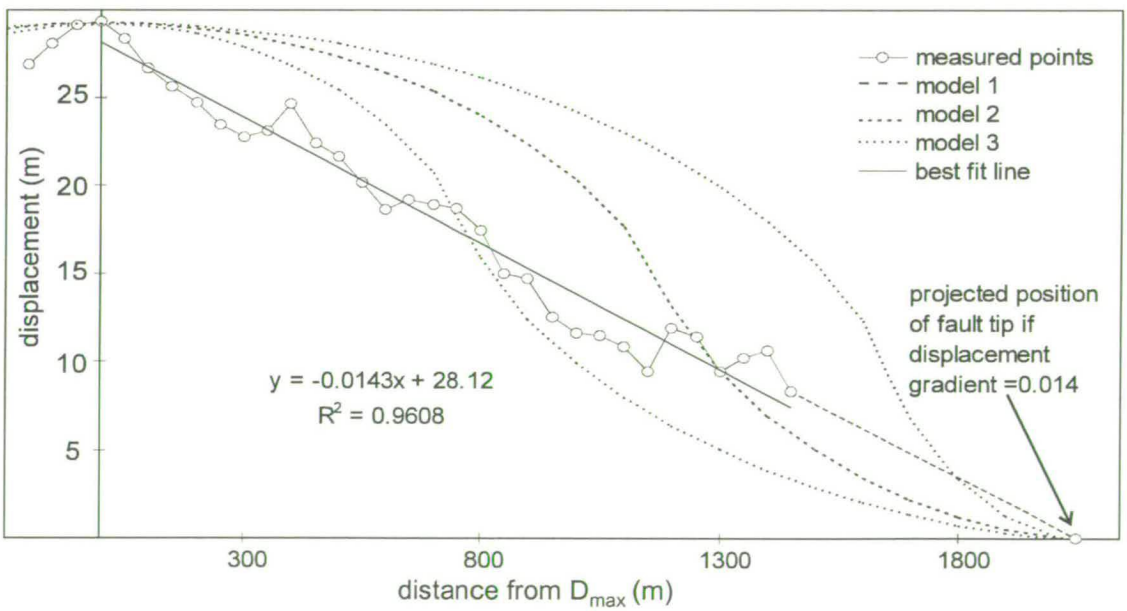

Figure 3.11. Comparison of measured displacement profile with model curves for the eastern end of the Big Hole fault. The best fit line is calculated for points to the east of the center of the fault only.

3.4.3. Whole fault displacement profiles

Figures 3.12 and 3.13 show the composite profiles for the two faults. These illustrate many features that have been found in other studies of fault displacement variation (Section 1.4.2). The faults have maxima in the centre with displacement decreasing to zero at the tips. The profiles are irregular, even with the smoothing that occurs when data is projected from points well into the footwall or hangingwall. This is a common feature of real fault profiles, and is discussed further in Chapter 7.

Displacement minima are seen where the faults link with other faults. This is very obvious on Krantz's (1988) profile for the Blueberry fault; displacement is low where the La Sal fault intersects the Blueberry fault. No obvious displacement minimum is associated with the segment boundary at the western end of the Big Hole fault, though there is an inflection in the displacement profile at this point (Figure 3.13). There is one point on the Big Hole fault where the fault has two main strands (Section 4.4.3). There is however no corresponding displacement minimum. This is discussed further in Section 4.6.2.

Triangular, peaked displacement profiles are characteristic of faults that have grown entirely within a layer (Dawers *et al.* 1993). The faults in Dawers *et al.* (1993) have a peaked profile up to a critical length controlled by the thickness of the faulted layer. Longer faults had flat-topped displacement profiles. Muraoka and Kamata (1983) also discuss this, where they refer to peaked displacement profiles as C-type and flat-topped profiles as M-type. The faults in Dawers *et al.* (1993) grew at the free surface. The faults in this study are more likely to have grown at depth (Section 2.2.2).

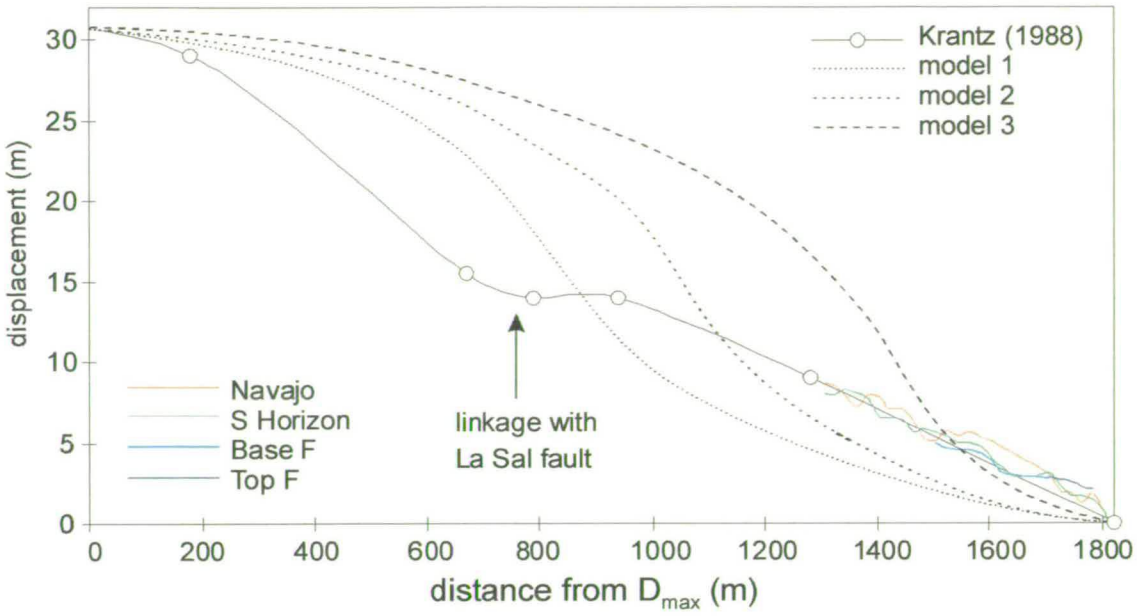

Figure 3.12. Comparison of measured displacement profile with Cowie and Scholtz (1992a) model curves (constructed using the parameters in Table 3.1) for the whole of the Blueberry fault. Measured points are from Krantz (1988).

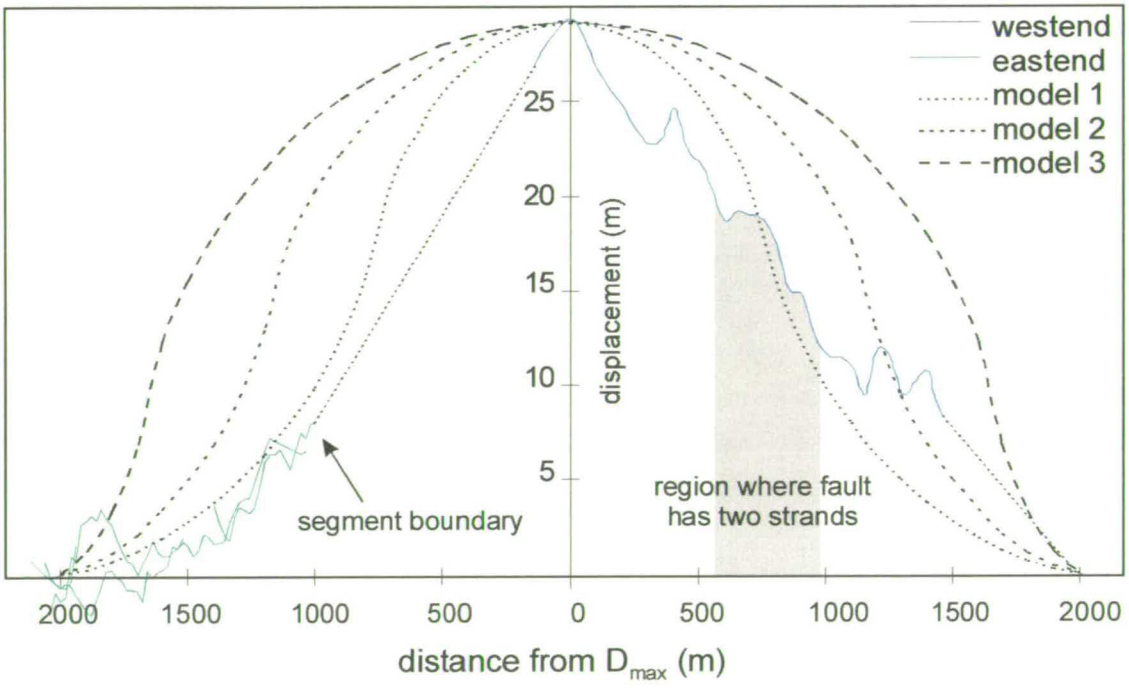

Figure 3.13. Comparison of measured displacement profile with Cowie and Scholtz (1992a) model curves (constructed using the parameters in Table 3.1) for the whole of the Big Hole fault.

3.5. Discussion

3.5.1. Comparison to other tip gradients

The data in this study is of a much higher resolution than that in other published surveys. It is not possible to find a bell-shaped curve with reasonable parameters that fits any of the three measured profiles. More importantly, all three fault tips are fitted well by linear displacement profiles. This confirms that the linear tip gradients seen in many lower resolution surveys are not in fact artefacts of sparse data points. The value of the displacement gradient at the Blueberry fault tip and the east end of the Big Hole fault are very similar, 0.014-0.015. The displacement gradient at the west end of the Big Hole fault is lower at 0.007, but is in the same order of magnitude. This would imply that a similar factor controls the fault tip displacement gradient at all three measured fault tips.

The lateral displacement gradient measured from the maximum displacement point is a value used widely in the literature to characterise displacement profiles (e.g. Dawers *et al.* 1993), but this does not take into account the irregular shape of the displacement profile. The problem of defining tip displacement gradients is explored in Cartwright and Mansfield (1998). They outlined four ways of defining the fault tip gradient; from the tip to the maximum displacement point of the fault, the first peak on the profile, the first inflection point on the profile and the first measured point. They concluded that the first point and first maximum methods were the best for most cases, and that there was less than 20% difference in the values achieved by using these two measurements.

Table 3.3 shows values for the displacement gradients at isolated fault tips found in previous studies. Where values for the tip gradient were not given, they were calculated using the first point method as described above. The two orders of magnitude scatter in these values appears to have no obvious correlation with rock type, size of fault or deformation style. The lowest values of tip displacement gradient were recorded along individual deformation bands measured in the high porosity Entrada Sandstone in southern Utah (Fossen and Hesthammer 1997). These

Source	tip gradients	lithology	fault type	mode	fault length
BB fault	0.017				
BH fault	0.007-0.014	sandstone	normal	III	3-4 km
CRFA	0.005-0.05**				
C+M 98	0.016-0.25	limestone, sandstone	normal	III	200-5000 m
F+H 97	0.001-0.01**	sandstone	normal	III	0.15-100 mm
M+K 83	0.002-0.1 **	silts, sandstone, tuff	normal	II	30-250 cm
P+S 96	0.025	limestone	strike-slip	II	>80 m
D et al. 93	0.015-0.06 **	tuff	normal	III	24-2210 m
W+W 89	0.0018-0.029	coalfield	normal	II, III	100-1200 m
S et al.96	0.05-0.2	siltstones	normal	III	10-100 cm

Table 3.3. Fault tip gradients from this study compared to examples from published literature. Values that have been calculated for this study using the first point method are indicated with a **. (BB fault = Blueberry fault, BH fault = Big Hole fault, CRFA = Chimney Rock fault array, C+M 98 = Cartwright and Mansfield 1998, F+H 97= Fossen and Hesthammer 1997, M+K 83 = Muraoka and Kamata 1983, P+S = Peacock and Sanderson 1996, D et al. 93 = Dawers *et al.* 1993, W+W 89 = Walsh and Watterson 1989, S et al. = Schlische *et al.* 1996)

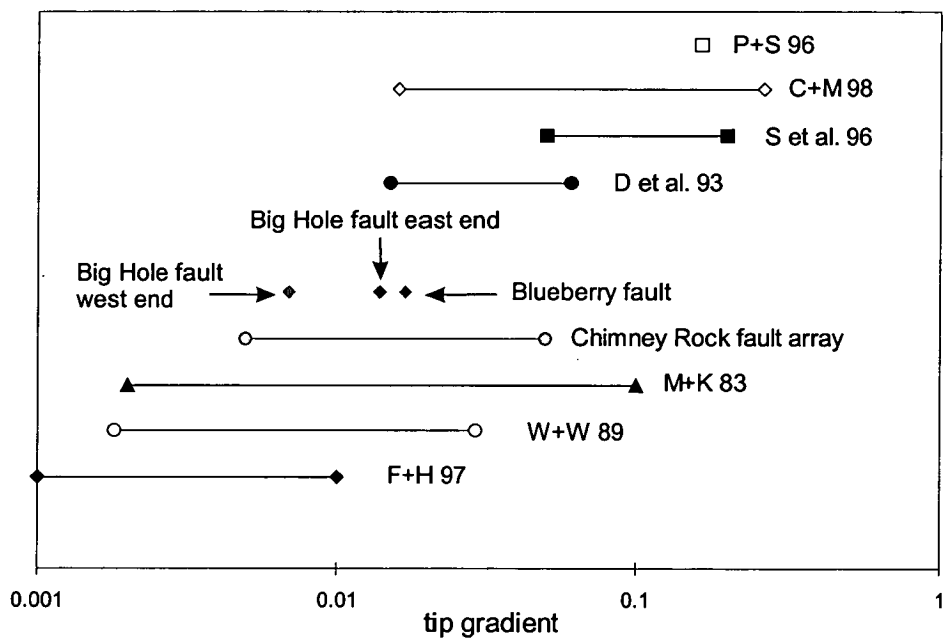

Figure 3.14. Variation of natural tip gradients from this study and published examples (from Table 3.3). The variation in tip gradient between the Big Hole and Blueberry Fault is less than that for other areas. Abbreviations as in Table 3.3.

ranged in length from 0.15 to 100 mm, and the lowest displacement gradients were seen in the longest deformation bands. This may be an effect of the specific deformation mechanism in the host sandstone of these faults (Section 5.5.4). Very low values (a minimum of 0.002) were also recorded in mixed lithologies (Muraoka and Kamata 1983) and in coalfield faults (Walsh and Watterson 1988, 1989). Conversely large values (a maximum of 0.25) have been found in the same localities as well as in limestone and sandstones (Cartwright and Mansfield 1998) and siltstones (Schlische *et al.* 1996).

A constant tip gradient has been cited as evidence for a critical taper at a propagating crack tip, due to a material control on the displacement distribution on a fault surface (Cowie and Scholz 1992a). There is a wide variation of tip gradients within individual lithologies (Figure 3.14), which would seem to indicate that the tip gradient is not simply dependent on lithology and hence the material properties of the host rock. The smallest faults (Schlische *et al.* 1996, Fossen and Hesthammer 1997), which could be presumed to have the simplest growth history, also have a range of finite tip gradients. Hence the tip gradient is also not necessarily dependent of the size, and therefore growth history, of the fault.

This study confirms that fault tip gradients are linear. This has important implications for predicting the distribution of sub-seismic faulting. Yielding *et al.* (1996) and Pickering *et al.* (1997) used linear tip gradients to extrapolate fault lengths to account for tip regions that are below seismic resolution. The high-resolution displacement profiles presented in this study validate this approach.

3.5.2. Tip lines in three dimensions

The displacement profiles in this study are approximately two-dimensional transects across a three-dimensional structure. As a consequence, these surveys may not be samples of the greatest displacement or length of the faults (Section 1.4.1). Thus the displacement profile gradients measured here are likely to be underestimates of the maximum profile (through the centre of the fault). Although there is relatively good

three-dimensional exposure of the fault, it is not of large enough vertical extent to pin down where on the fault surface the fault trace is. There is some evidence that displacement is increasing downwards (section 3.4.1), but there is no way of telling how far above the centre of the fault ellipse the fault trace is, without further data on the displacement at depth.

Displacement profiles have been shown to be influenced by the lithology of the host rock. Localised slip maxima are found within softer units (Muraoka and Kamata 1983), or at the boundary of stiffer units (Bürgmann *et al.* 1994). The profiles in this study are by necessity measured at a lithological boundary so the displacement is measured at a constant lithological level. There is little lateral change in lithology in this field area (section 2.2.4 and 2.2.5) so the displacement gradient is unlikely to have been affected by changes in the host rock lithology.

3.6. Summary

1. The displacement profiles of two normal faults in the Navajo Sandstone and Carmel Formation of Utah, have been measured using a total station surveying technique. The data in this study is of a much higher resolution than that in other published surveys. Because the faults are a similar order of magnitude in size, the Blueberry fault tip is assumed to be a proxy for the Big Hole fault tip that is not exposed.

2. The displacement profiles for the faults are approximately triangular with the maximum displacement in the centre of the fault and displacement tapering gradually towards the fault tips. Displacement minima correspond to regions where linkage can be seen to have taken place, either along strike or between faults of different strikes. In these respects these faults are very similar to those measured by other workers.

3. Neither of these faults could realistically be fitted with a curve that corresponds to a simple analytical model (either pure elastic or elastic-plastic). Instead, the fault

tip displacement profiles are linear. Existing analytical models for fault displacement do not account for the shape of even relatively simple isolated faults.

4. All three measured fault tips have similar fault tip gradients ranging from 0.007-0.015. This is within the range of tip gradients measured from previous, lower-resolution surveys. This implies that the controlling factor on the displacement gradient at the fault tip is constant for both faults.

4. MACROSCOPIC OFF-FAULT DEFORMATION

4.1. Introduction

4.1.1. Rationale

Off-fault deformation around fault planes results from the accommodation of strain due to fault propagation, accumulation of displacement and fault linking processes that occur during the time that the fault is active. The history of deformation on the fault will be recorded in the distribution, orientation and cross-cutting relationships of off-fault deformation structures. Hence an understanding of the formation of these structures allows the history of deformation on a fault to be deciphered.

The Big Hole and Blueberry Washes run both parallel to and across the faults, providing an ideal opportunity to investigate the off-fault deformation. This chapter presents detailed surveys of the distribution and orientation of deformation around the Big Hole and Blueberry faults, at scales from centimetres to kilometres. The geological maps created for the displacement profile surveys (Chapter 3) act as a base for these more detailed maps. The structures in the off-fault deformation zone have then been related to the displacement profiles along the fault, in order to quantify the development of the off-fault deformation with increasing displacement on the fault.

The faults in this study have displacements that are just at the resolution of the highest quality three-dimensional seismic survey (~12-20 m). Hence all the off-fault deformation would be sub-seismic in scale. Understanding the controls on the evolution of off-fault deformation would help to predict the distribution of sub-seismic deformation. Off-fault deformation can have potentially drastic implications for the flow of fluids through or across fault zones.

4.1.2. Structure of this chapter

Two-dimensional maps of the deformation around the Blueberry and Big Hole faults were created at two different scales: on the scale of the entire fault zone and at the scale of individual outcrops. One-dimensional samples of the off-fault deformation were also collected, in the form of transects. Section 4.2 discusses the methodologies used to create the maps and transects. Data is presented from three study areas: the Blueberry fault tip (Section 4.3); the eastern end of the Big Hole fault (Section 4.4); and the western end of the Big Hole fault (Section 4.5). Key outcrops are described and the maps and transects for each area are presented.

In Section 4.6 the map and transect data are interpreted. The distribution of deformation bands around the fault defines a zone of deformation around the main fault surface. The width of this zone is observed to correlate with the displacement on the fault. These interpretations are discussed in terms of fault growth and scaling in Chapter 7.

4.2. Methodology

4.2.1. Fault-scale maps

Off-fault deformation occurs as clusters of deformation bands and slip-surfaces. The distribution of these clusters was mapped using a total-station surveying instrument (Section 3.2.2). Clusters were mapped by defining the start and end of each cluster, points where clusters changed strike direction or bifurcated, and points where clusters emerge from under sand or soil. Where deformation is highly concentrated it can be difficult to distinguish separate clusters, though in general, trends can be picked out across complex zones.

Clusters were classified into three size classes: small, medium or large, depending on the number and size of deformation bands in the cluster. The number and type of bands in a cluster was recorded at several points in each survey. In this way the average number of bands for each size class can be defined (Table 4.1). Examples of

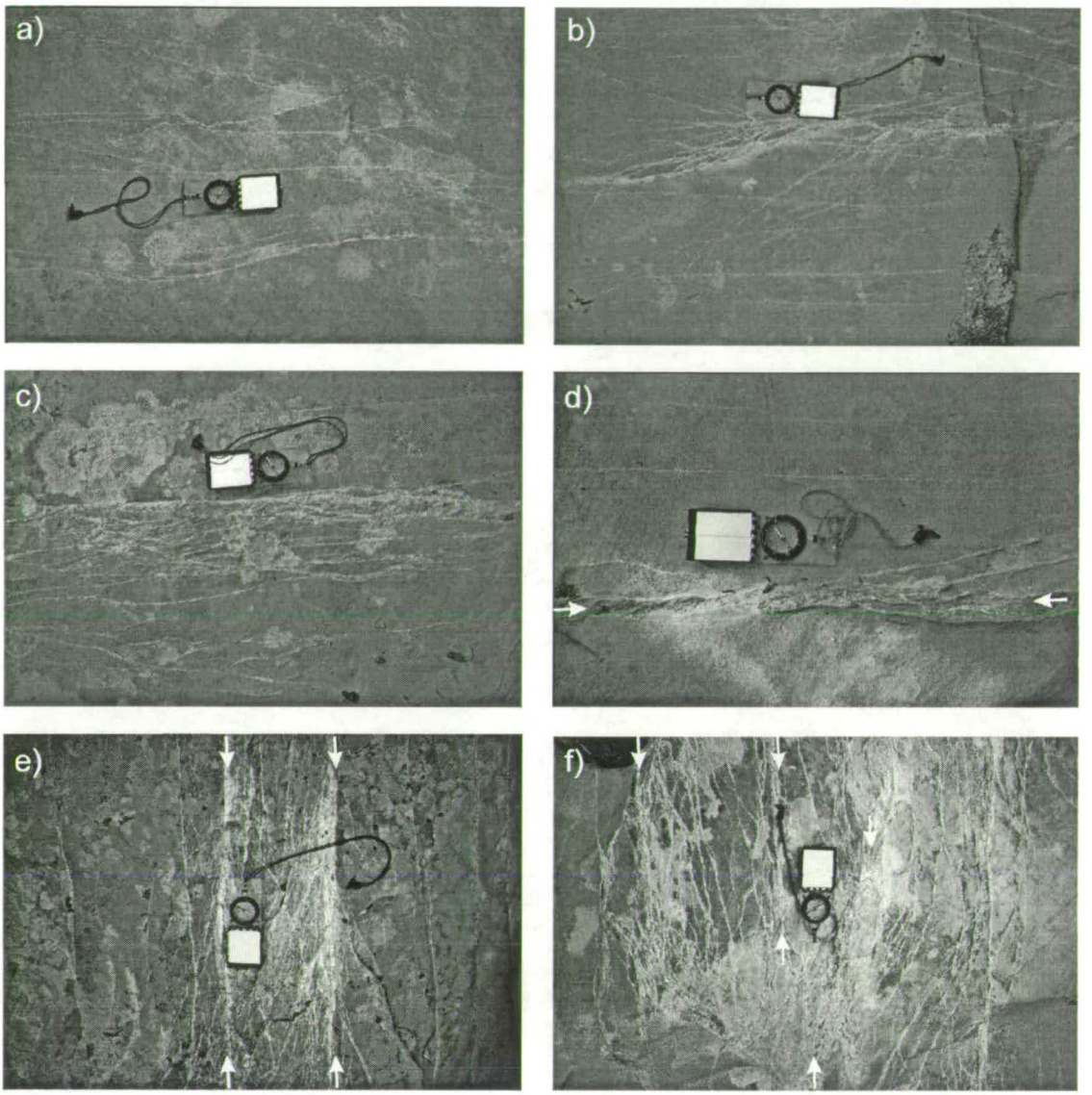

Figure 4.1. Examples of the three cluster classes used in creating the damage zone maps. a) and b) Class 1 clusters: a few single and multi-strand bands but no slip-surfaces. c) and d) Class 2 clusters: several single and multi-strand bands with a few relatively discreet slip-surfaces. e) and f) Class 3 clusters: many single and multi-strand bands and complex anasotomsing slip-surfaces. White arrows mark the position of slip-surfaces.

each cluster type are given in Figure 4.1. Within each individual cluster the majority of the deformation bands dip in the same direction. The overall dip direction of each cluster is indicated on the maps.

	Class 1	Class 2	Class 3
Map colour	orange	turquoise	green
Average width (m)	0.4	0.9	1.1
Average no. of singles	6.6	12.5	20.6
Average no. of multis	1.9	3.5	6.1
Avg. no. of slip-surfaces	0.2	1.2	2.8

Table 4.1. Average numbers of the different structures in the three cluster classes

Several surveys were needed to map the deformation around each fault. They were tied to the geological maps using the cairns built for the displacement profile surveys (Section 3.2.2). Fifteen surveys were required to cover the entire Big Hole fault and four surveys cover the area of the Blueberry fault Tip Canyon and the Bacon fault.

Although cliff sections often provide very good exposures of the structures, direct mapping of clusters in the steeper canyon walls is difficult. Structures were traced from photomontages of the canyon walls and then the cluster positions transferred onto the main map. Some areas in the base of the canyons have a covering of sand or soil and vegetation. Occasionally it is possible to trace the larger clusters through these areas. Figure 4.2 shows the outcrop style across the two survey areas, the location of each survey and the names of localities mentioned in the text.

4.2.2. Outcrop-scale maps

Large-scale maps of individual outcrops were also created. A metre-square grid was outlined on the outcrop, and the deformation bands were then traced directly onto graph paper at a scale of 1:25. On sub-horizontal surfaces, measuring tapes were used to mark the grid directly onto the outcrop with chalk. On sub-vertical cliff-faces the

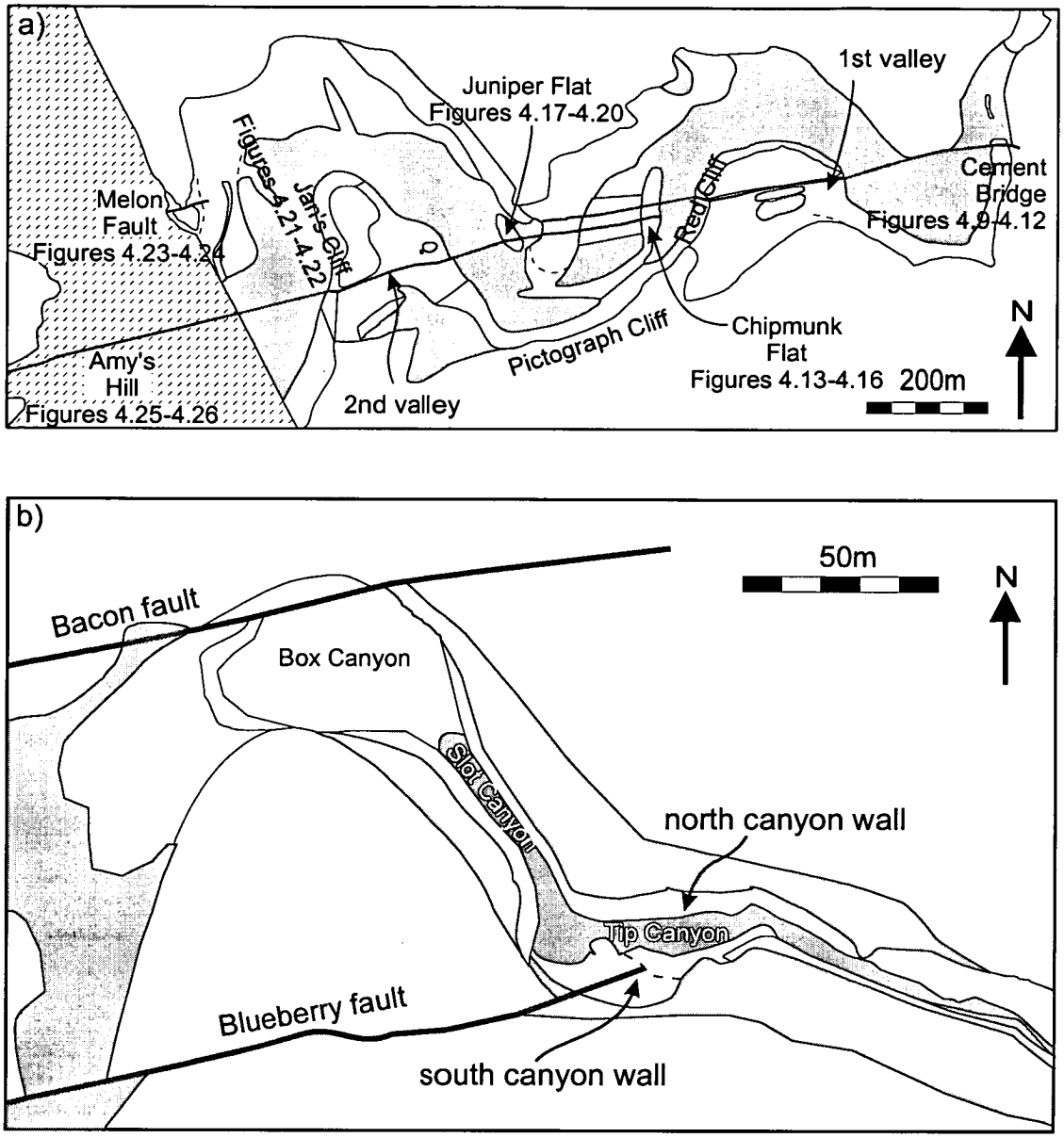

Figure 4.2. Locality map of a) the Big Hole fault and b) the Blueberry fault (Figures 4.4-4.7). The distribution of outcrop style is indicated by **white** - good quality easily accessable outcrop; **pale grey** - cliff outcrops mapped by photomontage; **medium grey** - poorer quality outcrop, large clusters can be traced, but individual bands cannot be seen; **dark grey** - outcrop covered by drift or inaccessable; **stipple** - outcrop not mapped. Dotted lines represent breaks in slope.

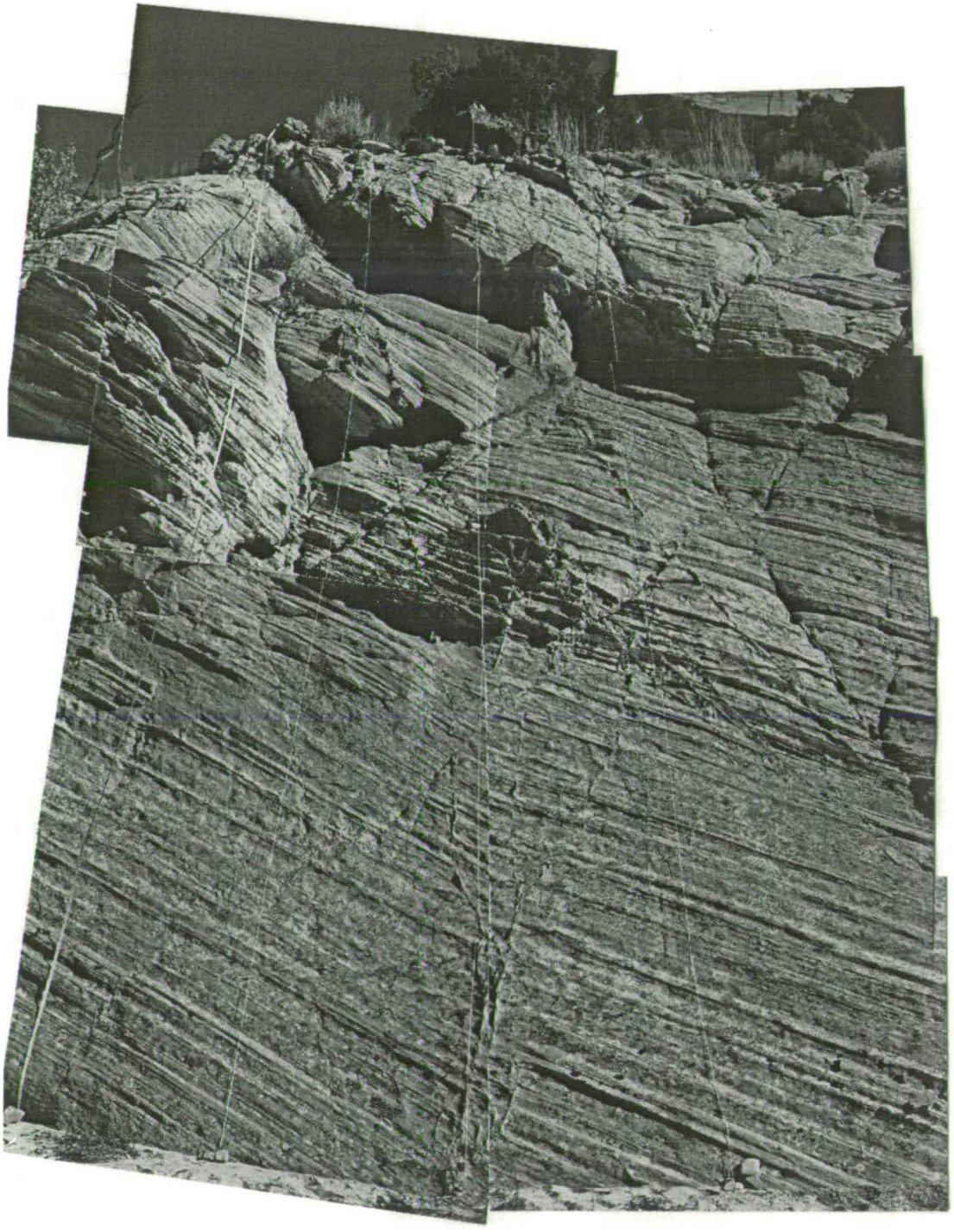

Figure 4.3. Method of creating outcrop-scale maps using tapes with markers (tassles) at meter intervals on cliff sections. The outcrop shown is the northern end of the footwall block at Cement Bridge (left-hand side of Figure 4.11).

grid was defined by hanging string from the top of the cliff at metre spacings, with markers at metre intervals along the string (Figure 4.3). In this way the pattern of deformation bands can be recorded quickly and relatively accurately.

Although care was taken to include all the structures within complex clusters, the maps under-represent the true number in densely deformed regions. Some very highly deformed areas are shaded in blue. Close to the fault zone there are regions where it is no longer possible to distinguish separate bands from one another. These regions have a glassy appearance and stand proud of the eroded surface. These are also coloured blue on the maps (see Figure 4.17a for an example). Single strand deformation bands often have small pods where the band is locally thicker. Although care was taken to include these structures on the maps, smaller ones may have been omitted. There are no fractures visible by eye smaller than a single deformation band so there is no lower resolution cut-off (censoring) in size of fault on these maps.

Outcrop-scale maps were created at the Juniper Flat, Chipmunk Flat and Cement Bridge outcrops on the Big Hole fault, and at the Blueberry fault Tip Canyon. The position of the outcrop maps is indicated on the maps of each location.

4.2.3. Transects

One-dimensional transects through the off-fault deformation were made at several locations along the fault. A tape was laid out as close to perpendicular to the fault zone as possible, and the location of each band that crossed the tape was noted. Where possible the width, orientation, and offset of each band was measured.

The positions of the transects are shown on location maps for each area. Transects were taken in seven locations on the Big Hole fault and one location in the Blueberry fault Tip Canyon. These were chosen to represent a variety of different displacements on the main fault. The transects were as long as possible given the outcrop pattern.

4.3. Blueberry fault

4.3.1. The Blueberry fault Tip Canyon

Figure 4.4 shows the map of the Blueberry fault tip and the Bacon fault exposed in the Blueberry fault Tip Canyon. Near the point where the Blueberry and Bacon washes converge, the Blueberry Wash has eroded a steep-sided box canyon. The Bacon fault, and its associated deformation, runs along the northern side of this box canyon. There is a large amount of deformation concentrated on the east end of this exposure of the Bacon fault, but very little is exposed at the western end of the outcrop. The wash then trends to the south-east through a narrow slot canyon. No deformation bands or clusters of bands are seen in the slot canyon.

The canyon widens out again where it intersects the Blueberry fault. The southern side of the canyon is shallowly-dipping, with patchy outcrop covered with some soil and vegetation. The sub-vertical northern wall is well exposed and it is possible to get a good view of the structures within it by scrambling up the southern wall. The top of this cliff-face is inaccessible due to the eroded nature of the sandstone at this point, but the outcrop extends back from the top of the cliff.

The Blueberry fault can be traced from the southern side of the canyon where it offsets the Navajo Sandstone. At this point the fault plane is a well-developed slip-surface with dip-slip and oblique-slip striations. The fault continues down the shallow southern slope and is buried in the sand at the base of the wash. Other deformation band clusters can be traced across the southern side of the canyon and are mostly synthetic or antithetic to the fault. Three clusters can be seen in the northern wall: two that dip to the south and one dipping to the north that is co-planar to the main Blueberry fault. At the top of the cliff, a single deformation band can be seen trending approximately co-planar to the fault.

The canyon narrows again to the east and trends west-south-west for 40 m. A series of clusters can be seen crossing the canyon at this point. These can be traced through the poor-quality outcrop in the slope above the canyon wall, and link to the main

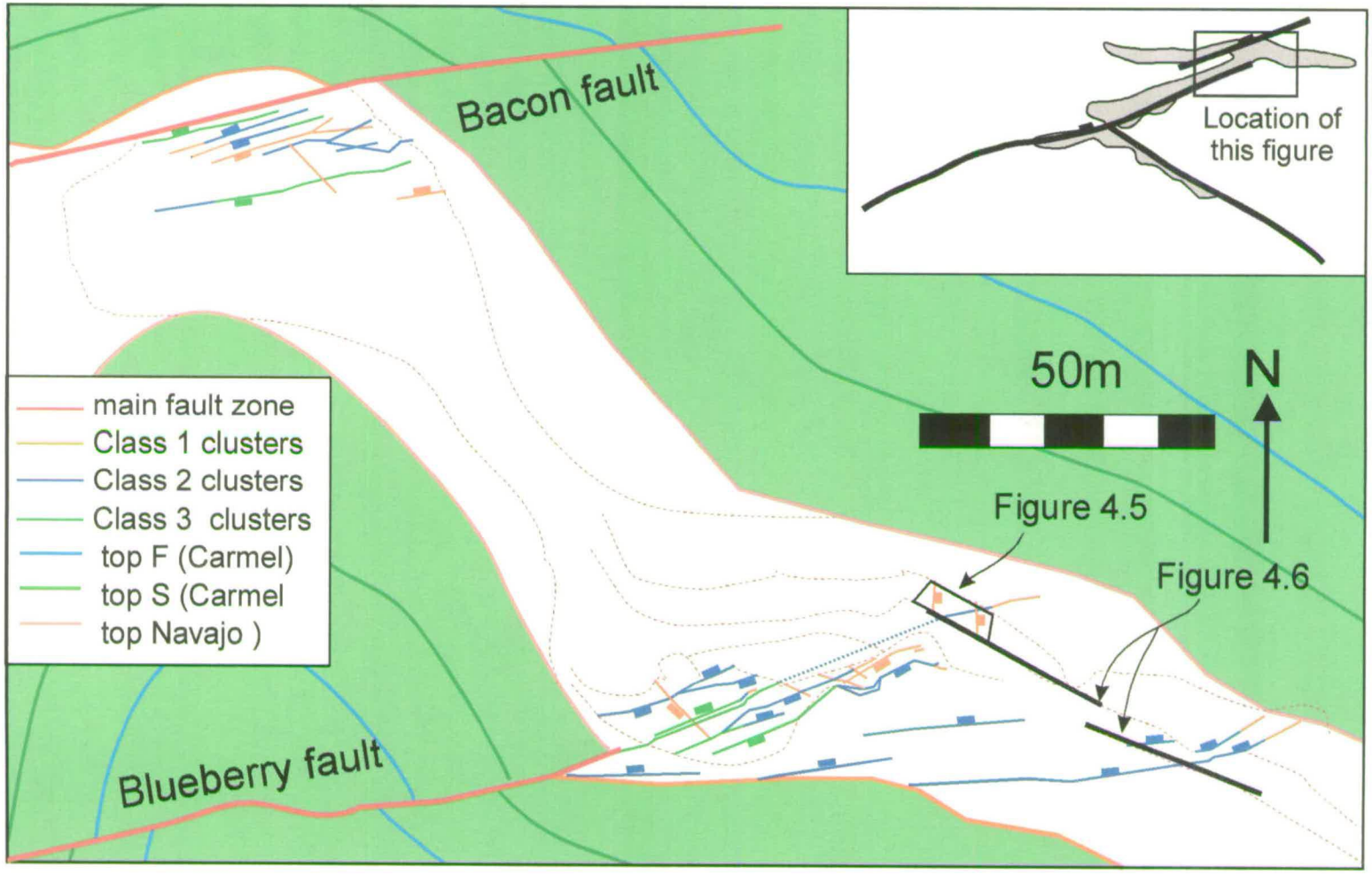

Figure 4.4. Map of deformation band clusters around the Blueberry and Bacon faults. The downthrown side of each cluster is marked by a tick. Dotted lines represent a change in the outcrop style (see Figure 4.2). The locations of the detailed sketch of off-fault deformation (Figure 4.5) and the transect (figure 4.6) are marked. The inset shows the location of this figure with respect to the rest of the fault.

fault strand. To the east of these structures, the canyon trends west-south-west for 25 m before opening out to a wider wash. The Navajo Sandstone is well exposed until the wash cuts up section into the Carmel Formation about 500 m downstream of the fault.

4.3.2. Blueberry fault outcrop map

The map of the sub-vertical northern canyon wall is 12 m by 9 m (Figure 4.5). The cluster which is co-planar to the main Blueberry fault consists of sub-parallel bands at the base of the canyon wall. Half way up the canyon wall, it takes on a cross-hatched pattern consisting of steeply-dipping synthetic segments and shallower dipping antithetic segments. A well developed slip-surface runs up through the centre of this cluster but is discontinuous towards the top and bottom of the outcrop map. This slip-surface and other bands in the cluster die out rapidly at the very top of the outcrop. Although there is no outcrop of Navajo Sandstone to the east of this point, there is no evidence for any deformation in the Carmel Formation above and to the east of this point. These observations confirm that this is the tip of the fault.

The southern cluster consists of a similar cross-hatched pattern with steeply-dipping synthetic segments and shallower dipping antithetic segments. A few short (<10 cm) slip-surfaces occur within these clusters. The northern cluster also has a cross-hatched pattern, but consists of more widely-spaced, longer segments. Only one of these segments has a well-developed, 1 metre long slip-surface. In places the deformation bands terminate at bedding planes. This is especially obvious in the hangingwall of the fault-parallel cluster, where many bands terminate at a very pronounced bedding plane. The main slip-surface, however, cuts through this bedding surface.

4.3.3. Blueberry fault transect

The transect taken at the base of the northern wall of the canyon extends from 7 m into the hangingwall to 90 m into the footwall (Figure 4.6). The three structures that are shown on the outcrop map can be seen. These define a zone of off-fault

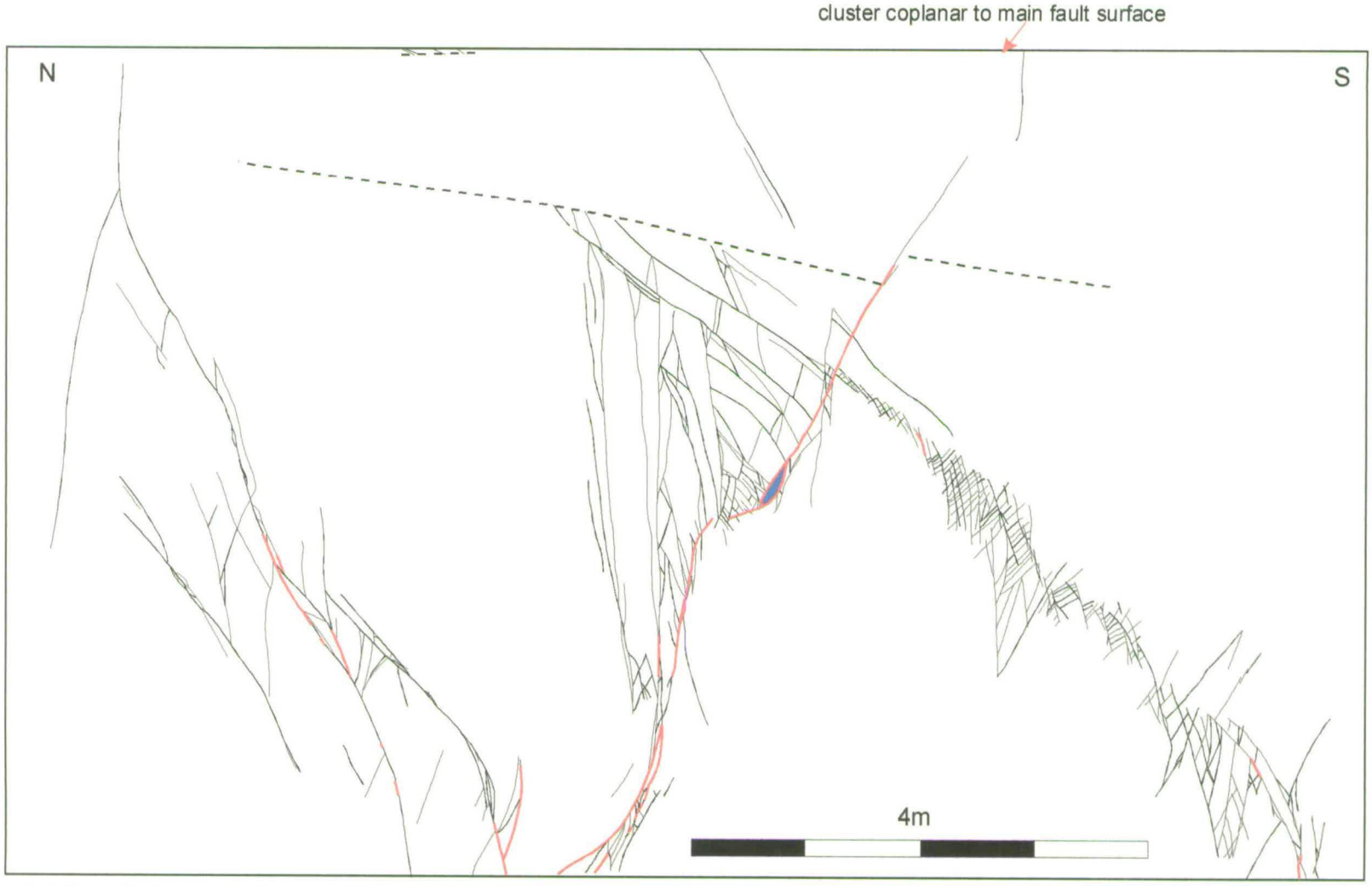

Figure 4.5. Detailed sketch of structures in the northern wall of the Blueberry fault tip canyon (sub-vertical face). Black lines are deformation bands, red lines are slip-surfaces, black dotted lines are major bedding surfaces, the blue area in the center is a slip surface.

deformation which extends for 6 m either side of the fault. The other structure at about 50 m from the fault zone can be seen. Most of the deformation band in these clusters are irregular and not well-developed. Between this cluster and the main fault there is a small number of widely distributed single strands. The canyon was walked out to the point where the wash cuts up into the Carmel Formation and no deformation bands were found beyond the end of the transect.

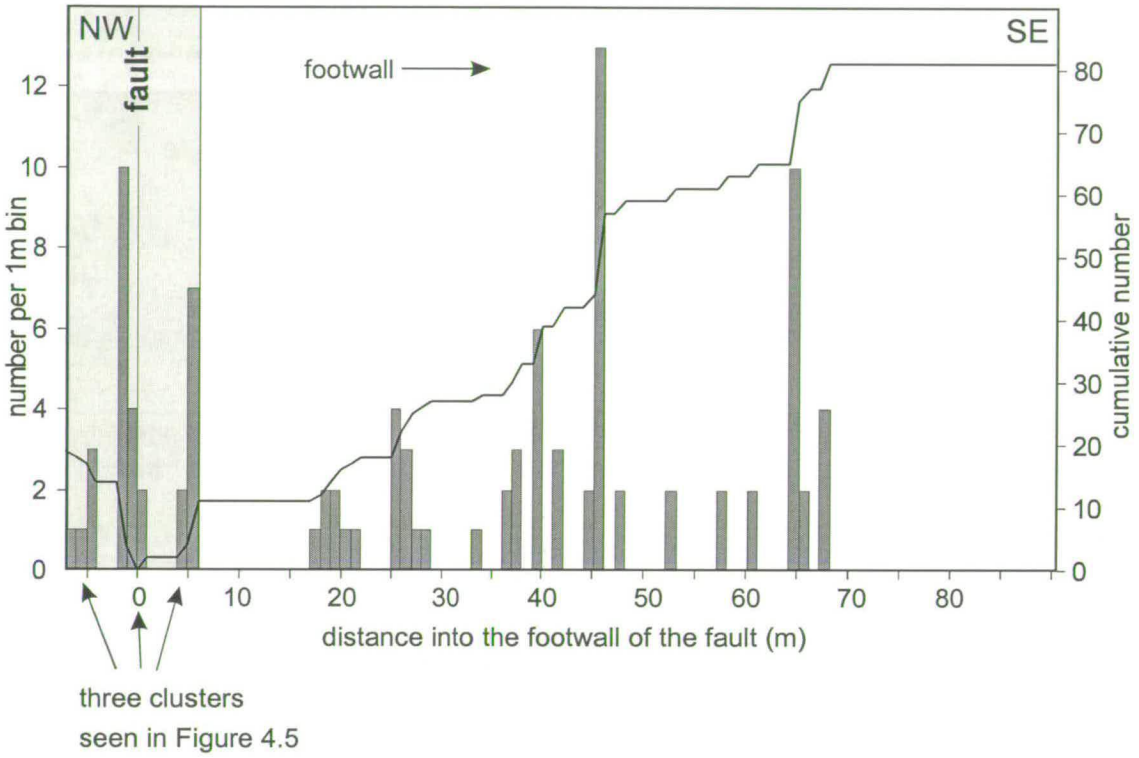

Figure 4.6. Transect across the Blueberry fault. The bars are the number of deformation bands per metre, the line is the cumulative number of deformation bands per metre. The grey box is the area that is considered to be the zone of off-fault deformation at this locality. The strand to the south east is poorly developed and is not considered to be part of the off-fault deformation for the Blueberry Fault.

4.3.4 Orientations

The orientations of structures away from the Blueberry and Bacon Faults are shown in Figure 4.7a. The majority of structures strike sub-parallel to the faults (striking 075-255 15). The structures that trend in the other regional strike direction (striking 120-300 15) consistently cross-cut the fault-parallel structures, and have a more indistinct appearance. Slip-surfaces within the off-fault deformation at this location have oblique striations (Figure 4.7b).

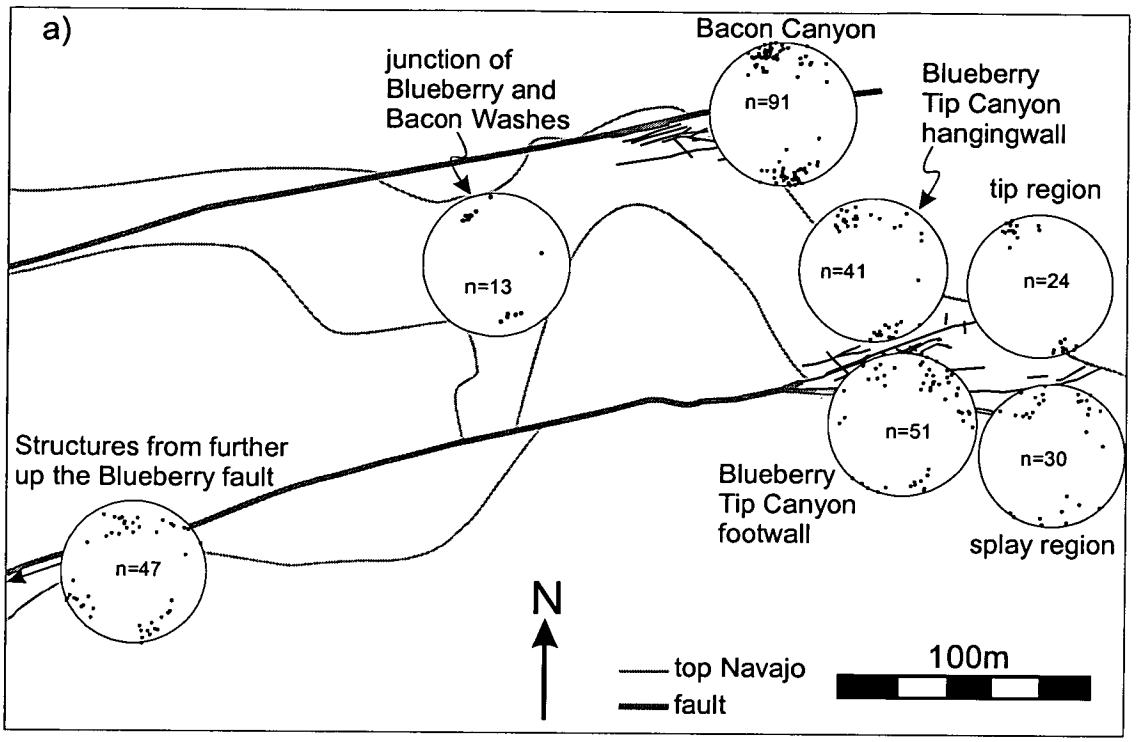

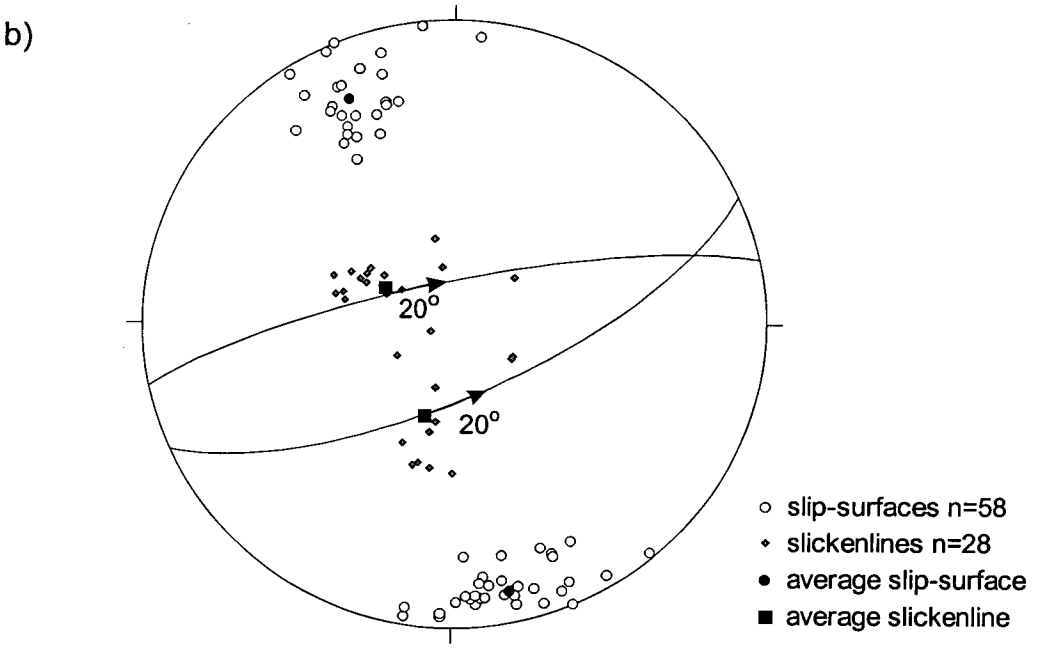

Figure 4.7. a) Poles to faults around the Blueberry fault. Each stereonet shows the orientation of structures for a small region of the area. See Figure 4.4 for the location of this figure. b) Orientation of slip-surfaces and slickenlines around the Blueberry fault. The great circles show the average slip-surface. The average slickenlines fall on these surfaces but are oblique. The arrows show the 20° pitch difference between the slip vectors and down-dip slip.

4.4. Big Hole fault east end

4.4.1. The Big Hole fault cluster map

Figure 4.8 shows the result of fifteen surveys of deformation band clusters around the Big Hole fault. The vast majority of off-fault structures are sub-parallel to the main fault strand, and dip either antithetically or synthetically to the main fault zone. Only a few structures strike in a non-fault-parallel direction (parallel to the second strike set of the main Chimney Rock fault array, Section 2.2.3). Only a few of the clusters in this strike direction are sufficiently well developed to appear as clusters on this map. These consistently cross-cut the fault-parallel structures.

A separate zone of bands is often observed from 150-200 m into the hangingwall. No displacement of the top Navajo Sandstone is associated with this cluster, except at the Melon fault (section 4.4.5).

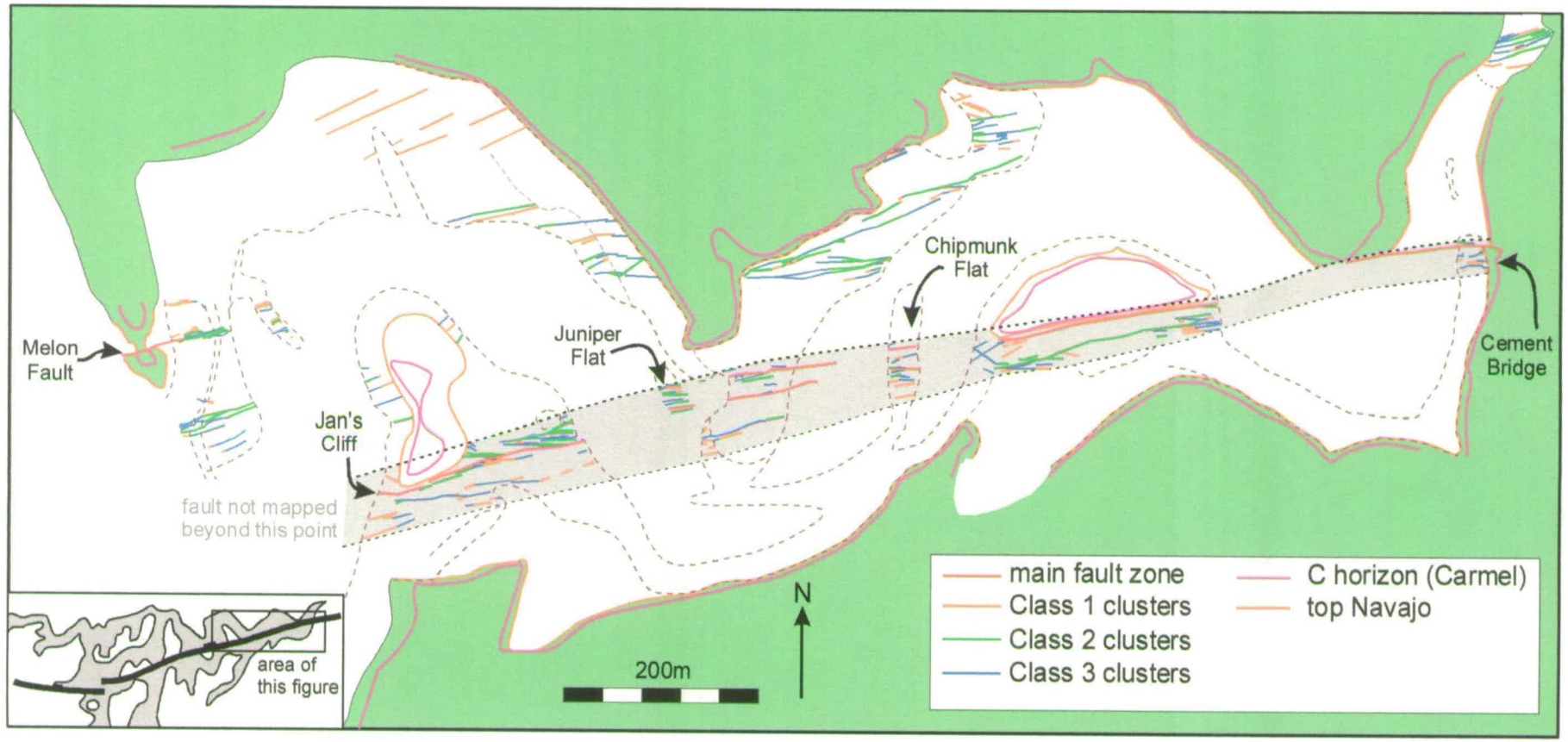

Figure 4.8. Map of deformation band clusters around the Big Hole fault. Dotted lines represent breaks in slope or change in outcrop style (see Figure 4.2). A description of individual locations is given in the text. The inset show the location of this figure with respect to the rest of the fault. The grey area represents the zone of off-fault deformation for the Big Hole fault.

4.4.2. Cement Bridge

This is the easternmost outcrop where the deformation around the Big Hole fault can be seen in the Navajo Sandstone (Figure 4.9a). The top of the Navajo Sandstone forms the base of the wash in the hangingwall, and is nine metres higher in the footwall, where it is exposed as a large block-shaped cliff (Figure 4.9b). Some clusters can be seen through the sand in the base of the wash. At this location the fault zone is a single main strand. The gently undulating fault surface stands proud of the more eroded Carmel Formation, and in places contains azurite and malachite mineralisation. Where it crosses the wash, the fault forms a raised wall and consists of two to three main slip-surfaces bounding a complex structure of bands. Two orientations can be picked out within the fault zone (Figure 4.10a).

The footwall block is well exposed and gently sloping (between 40 and 80° towards the west). It is therefore possible to scramble up the cliff to examine the structures in detail. The resulting outcrop map extends 15 m by 10 m (Figure 4.11). The outcrop close to the fault is obscured by a tree, so the structures immediately adjacent to the fault were not mapped. One main cluster is synthetic to the fault. One smaller synthetic cluster, and three antithetic clusters can also be seen. The main antithetic cluster contains many anastomosing but discontinuous slip-surfaces. The two other antithetic clusters to the south contain short segments of slip-surfaces. The short segments of slip-surfaces in the southernmost cluster are usually associated with local thickening of single deformation bands (Figure 4.10b). This is a relationship that is seen throughout the off-fault deformation. The two sets of faults define lozenge-shaped blocks of relatively undeformed host sediment. Within the clusters, smaller lozenge-shaped blocks are preserved between individual deformation bands.

A transect was taken along the base of the cliff in the footwall (Figure 4.12). The main clusters can be picked out on the transect, and the edge of the off-fault deformation is very well defined at 22 m from the fault. The section beyond the transect has been walked out and contains no more deformation bands. The total width of off-fault deformation including the hangingwall is 27 m.

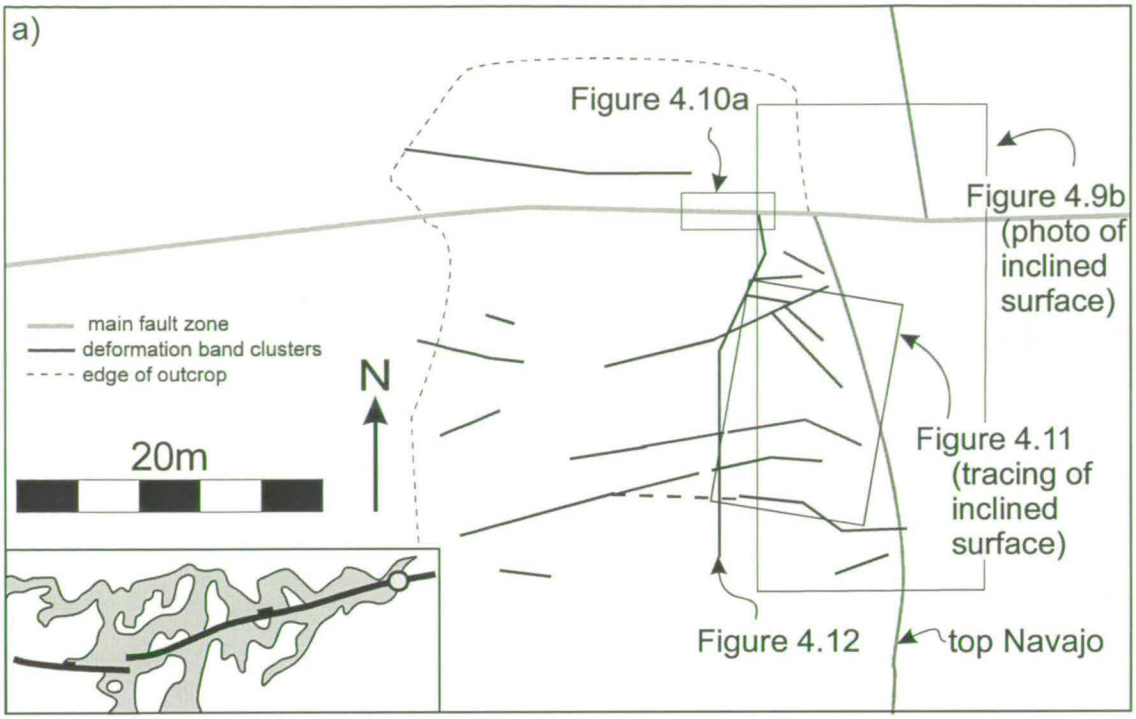

Figure 4.9. a) Map of the Cement Bridge locality. The position and outline of other figures is marked. The dot on the inset shows the position of this outcrop with respect to the rest of the fault. b) Photograph of the Cement Bridge outcrop. The fault runs down the center of the picture separating the Carmel Formation in the hangingwall from the Navajo Sandstone in the footwall. The block of Navajo Sandstone in the footwall forms a gently sloping cliff.

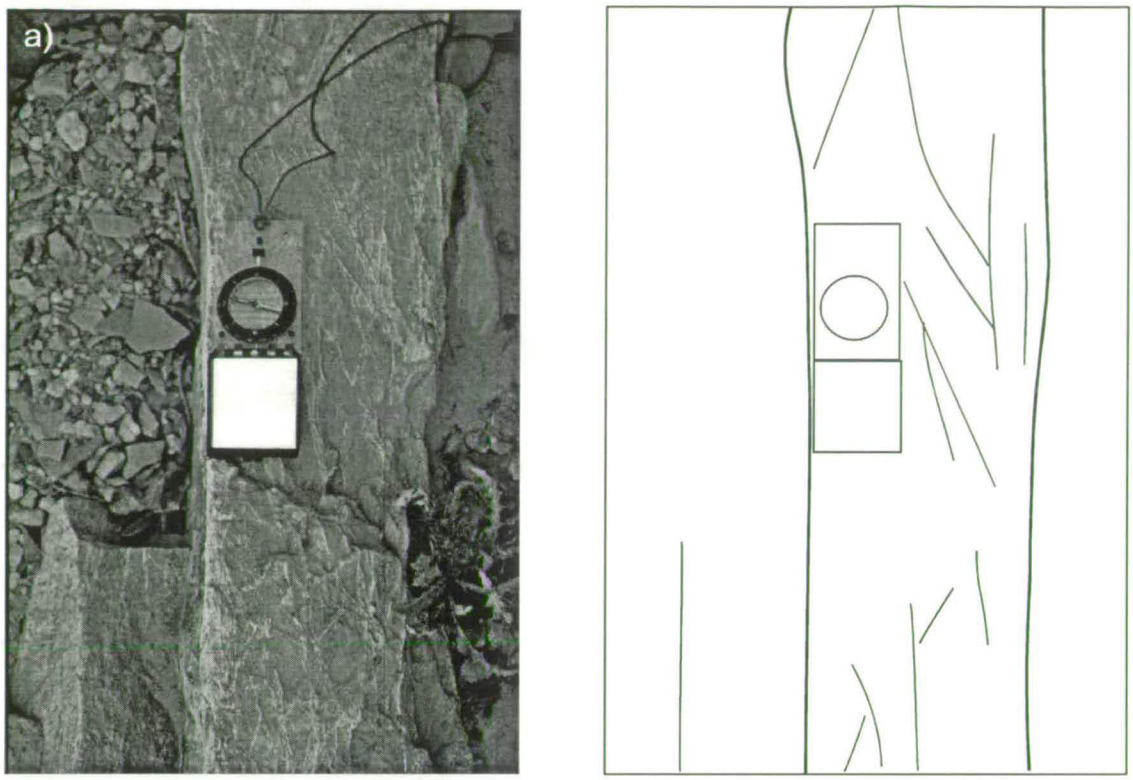

Figure 4.10. a) Photograph and line drawing interpretation of the fault at Cement Bridge. Two deformation band trends can be seen between the two main bounding slip-surfaces. b) Photograph of a cluster of deformation bands with pods of local thickening marked by arrows. Slip-surfaces are often seen within these pods. The square marked on the outcrop is 1 m x 1 m.

Figure 4.11. Detailed sketch of structures in the Cement Bridge footwall block (face dipping 40-80° to the west). Black lines are deformation bands, and red lines are slip-surfaces. Grey fill is sand at the base of the outcrop. The dotted line on the right-hand side of the diagram is a bedding surface along which the deformation bands have been offset.

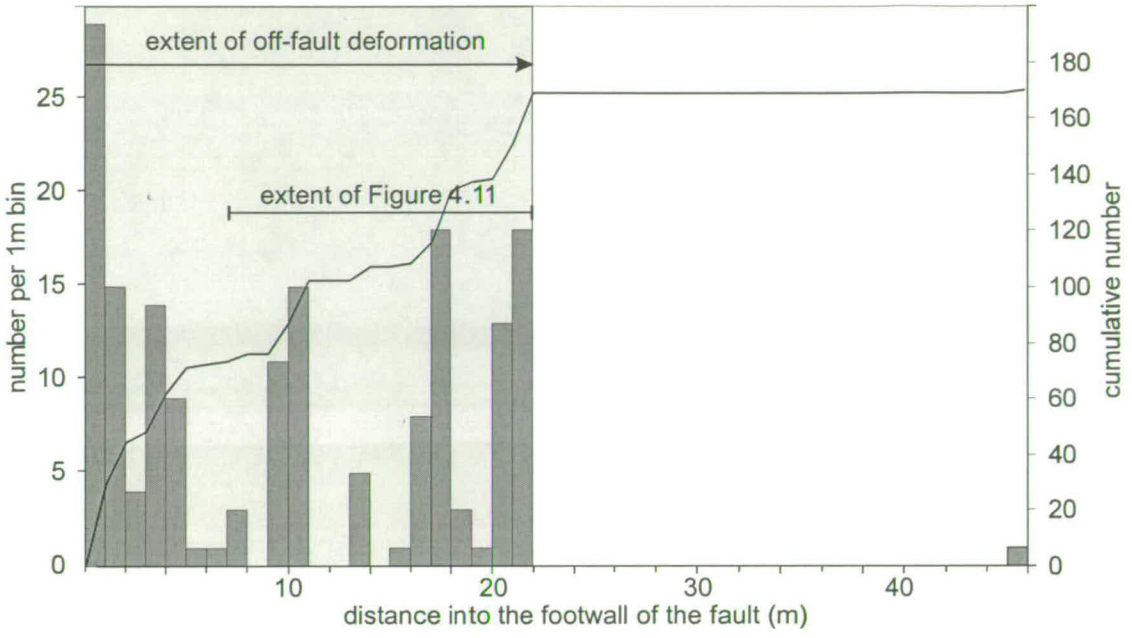

Figure 4.12. Transect across the Big Hole fault at Cement Bridge. The fault is on the left hand side of the graph. The bars are the number of deformation bands per 1m wide bin; the line is the cumulative number of deformation bands per metre.

4.4.3 Chipmunk Flat

Chipmunk Flat is a large flat outcrop exposed in the base of the wash (Figure 4.13a). At this locality, the Big Hole fault consists of two main strands. The displacement on each strand can be estimated from the cliff to the east. The top of the Navajo Sandstone has been eroded from between the two strands, but the northern strand must have more than 3 m of displacement and the southern strand must have less than 14 m (Figure 4.14). Two outcrop-scale maps were made at Chipmunk Flat, one at each strand.

The northern outcrop map is 9 m by 7 m (Figure 4.15a). A single slip-surface can be traced through the centre of the fault zone. Other slip-surfaces anastomose around this main one defining a zone of concentrated deformation (marked as blue on Figure 4.15a). The width of this zone is highly variable, ranging from just a single slip-surface up to 30 cm wide. In the western half of the map the deformation around the fault extends for about 1-1.5 m symmetrically around the fault. In the eastern half of the map the deformation around the fault is mostly within the footwall. To the north there are no clusters of deformation. The outcrop to the south is rather patchy due to sand trapped between the two upstanding fault strands.

The southern outcrop map is 5 m by 18 m (Figure 4.15b). The southern strand has many anastomosing slip-surfaces. Intense arrays of deformation occur close to the fault mostly within the footwall. Complex clusters of single and multi-strand deformation bands can be traced up to 14 m to the south. Clusters of deformation bands can be identified by groups of bands with local thickening (Section 4.2.2), though it is hard to pick out individual clusters on the map. In both maps, the structures trend sub-parallel to the fault zone and define blocks of undeformed host rock between them.

The Chipmunk Flat transect (Figure 4.16) extends from 48 m into the footwall to 52 m into the hangingwall of the northern strand. The density of deformation is higher around the southern strand than the northern strand. The southern strand has therefore been defined as the main fault at this location. Off-fault deformation extends for 55 m across both strands.

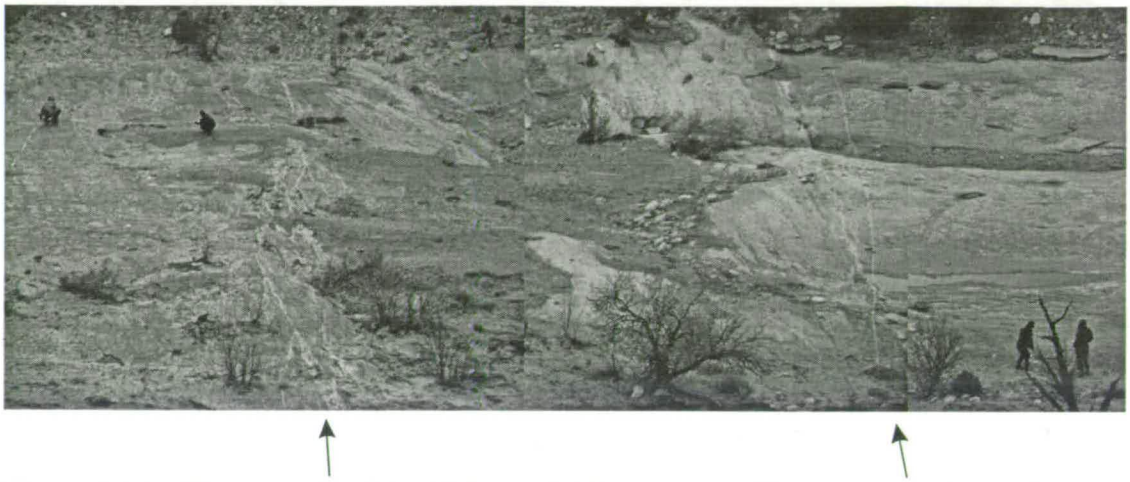

Figure 4.13a. Photograph of the Chipmunk Flat outcrop. The arrows point to the two strands of the fault. Photo is taken facing west.

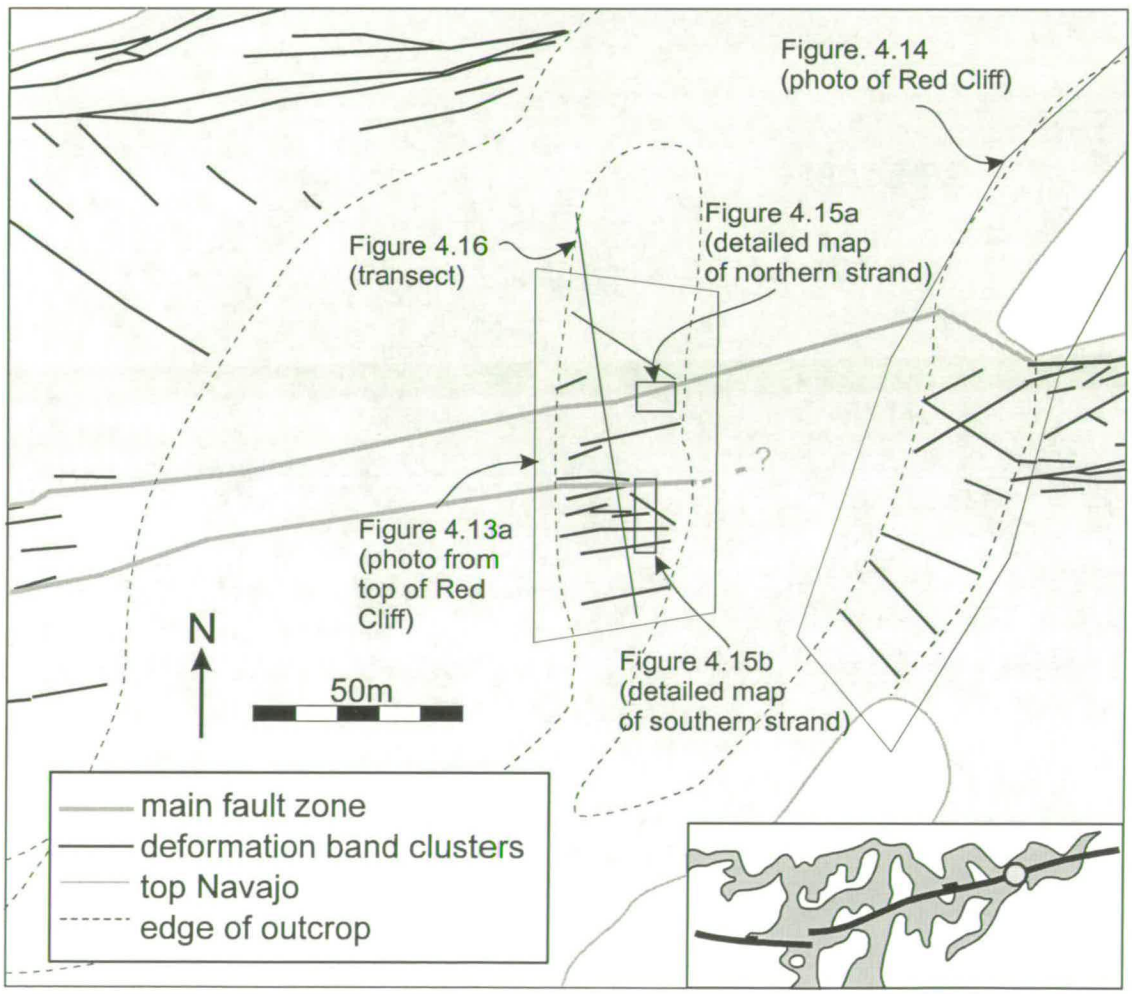

Figure 4.13b. Map of the Chipmunk Flat locality. The position of other figures at this locality are marked. The dot on the inset shows the position of this locality with respect to the rest of the fault.

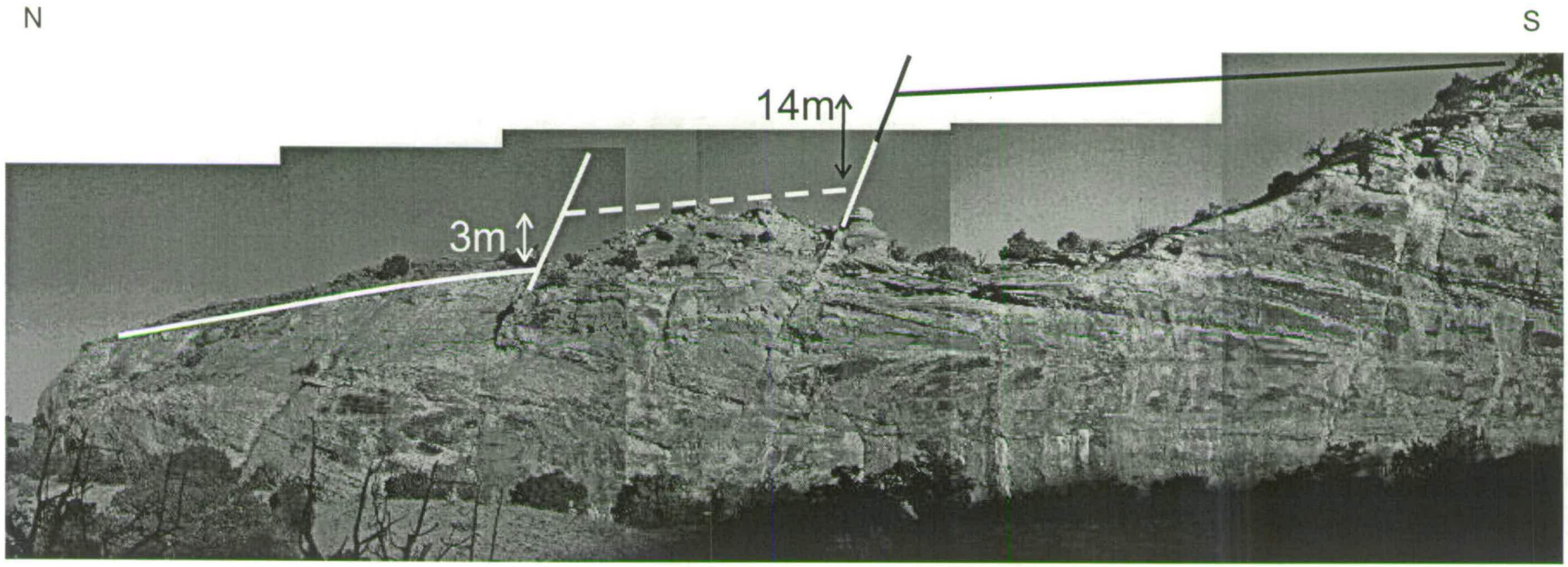

Figure 4.14. Photograph of the Red Cliff looking east from Chipmunk Flat. The two strands of the fault and position of the top Navajo Sandstone are marked. The position of the top Navajo Sandstone between the two strands cannot be defined, but the displacement can be limited to greater than 3 m on the northern strand and less than 14m on the southern strand.

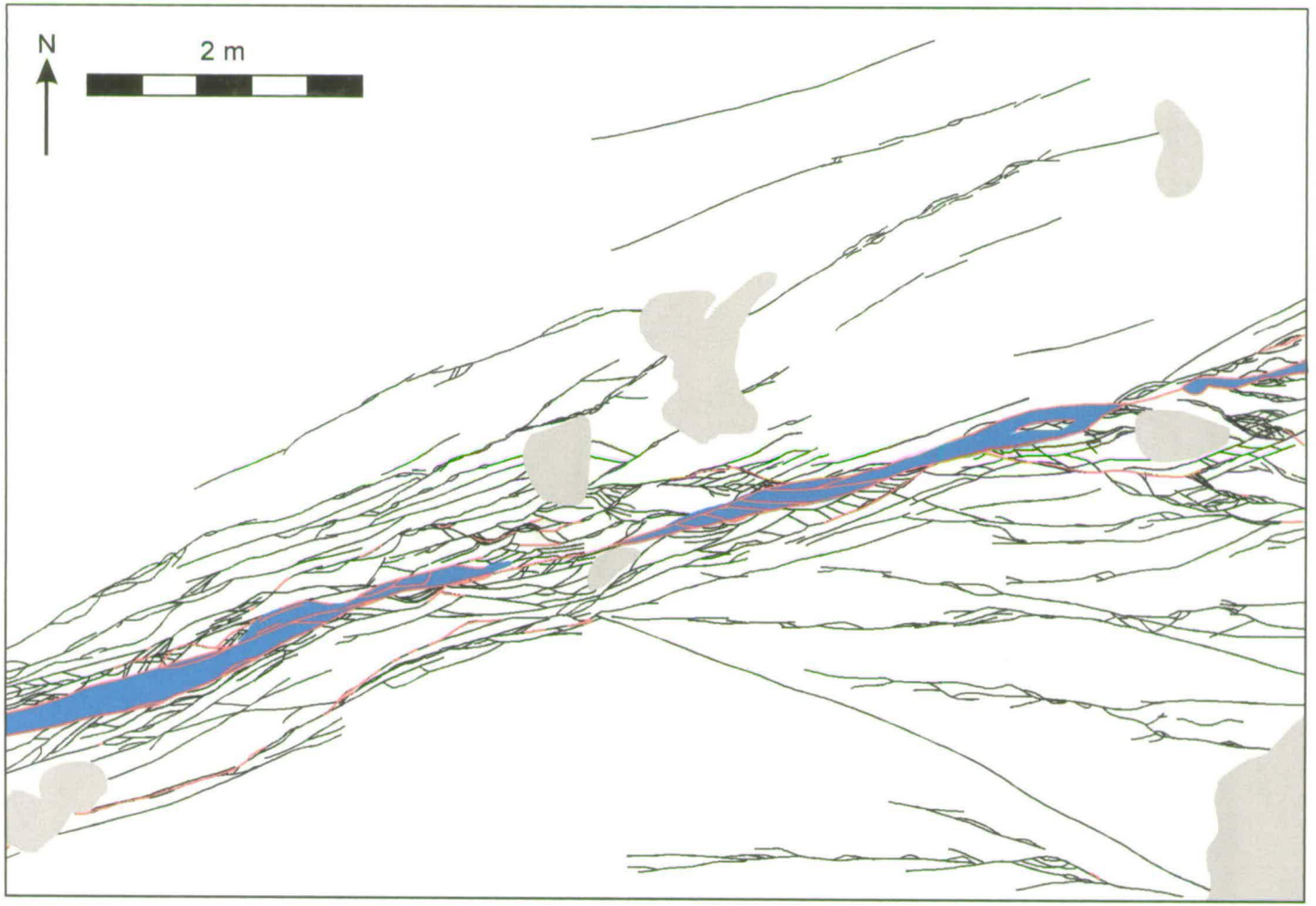

Figure 4.15 a) Outcrop map of the northern strand of the Big Hole fault at Chipmunk Flat. Black lines are deformation bands; the red lines are slip-surfaces. Blue areas are complex, tightly packed zones of bands in which it is difficult to distinguish individual bands. Grey areas are covered with sand. The plane of this map is approximately horizontal.

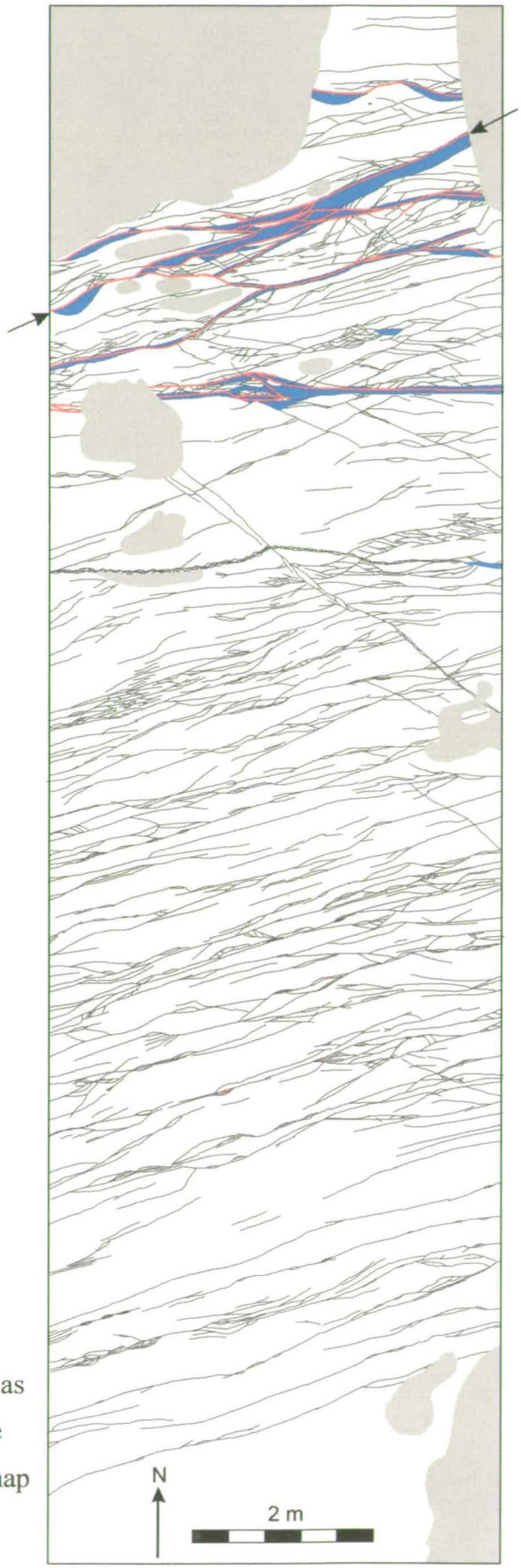

Figure 4.15 b) Southern strand of the Big Hole fault at Chipmunk Flat. Key as in Figure 4.15 a). The arrows mark the main fault surface. The plane of this map is approximately horizontal.

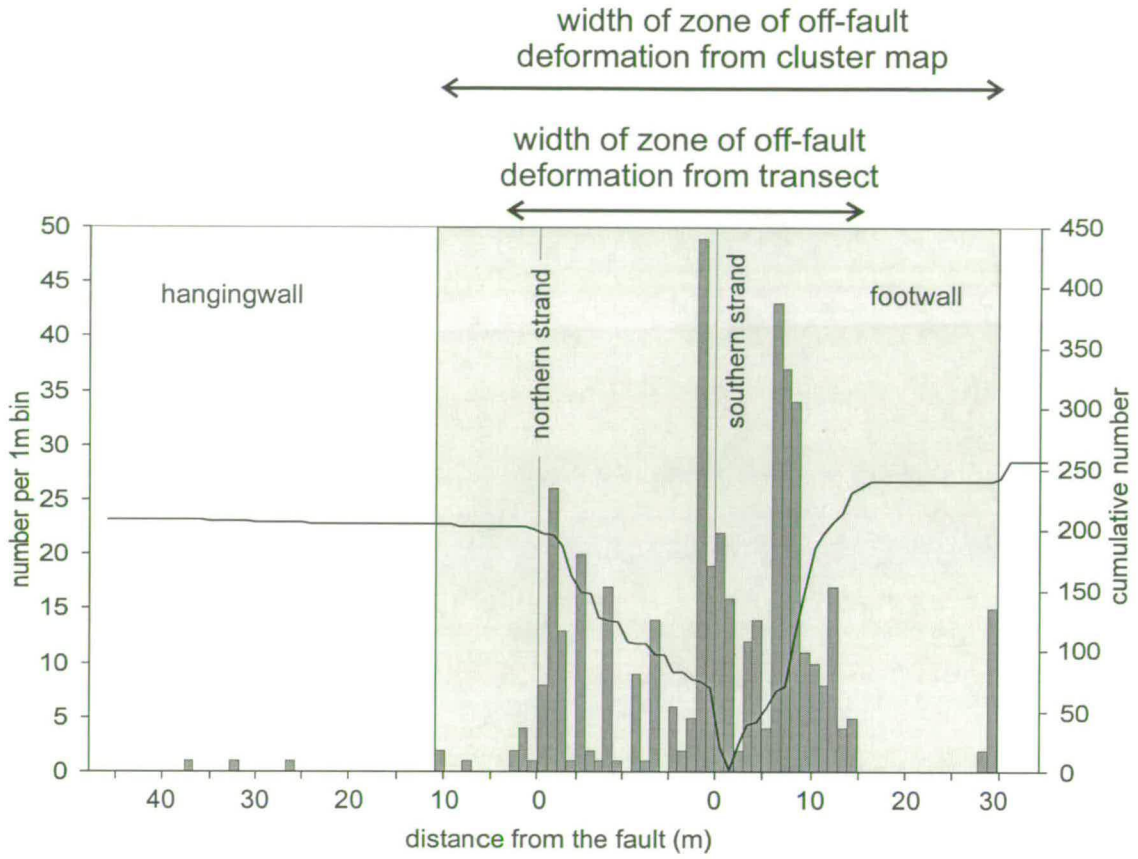

Figure 4.16. Transect across the Big Hole fault at Chipmunk Flat. The bars are the number of deformation bands per metre, the line is the cumulative number of deformation bands per metre distance from the southern strand. The shaded region is the area considered to be the zone of off-fault deformation from the cluster map (Figure 4.8). Note that this transect defines a narrower zone of off-fault deformation than that taken from the map. This illustrates that one-dimensional transects are not always the most useful way of defining a two-dimensional (map) off-fault deformation zone width.

4.4.4. Juniper Flat

This is another outcrop exposed in the base of the wash. The fault here has one main strand which forms a large step in the outcrop (Figure 4.17a). At this location the fault has 24 m of displacement. The outcrop map is 5 m by 28 m (Figure 4.18). Almost all the deformation is concentrated on a single strand of the fault zone. Other discontinuous slip-surfaces anastomose around the main surface. This defines a zone of concentrated deformation about the main fault (coloured blue on Figure 4.18) of varying width along strike of between 10-30 cm. Within the main fault is a small pod of pale green glassy material about 1 m in length and 3 cm wide (see Section 5.3.5).

To the south of the main fault there is one large antithetic cluster which also forms a step in the outcrop. Good quality outcrop extends southwards as far as Pictograph Cliff (180 m) and there are no more large clusters up to this point. To the north of the fault, several large clusters are seen up to 26 m from the fault. Only one of these clusters has a significant number of slip-surfaces in it. A wide variety of widths and numbers of bands can be seen in the clusters. Beyond the map the outcrop is mostly covered in sand, but no more deformation bands can be seen in the sand-free patches.

The Juniper Flat transect extends for 240 m into the hangingwall (Figure 4.19) along the base of a large cliff. At 150 m from the fault, a large cluster can be seen, followed by several small clusters. Although the exposure is not good, the cliff face to the east shows that there are no deformation bands in the gap between the two clusters. The large cluster at 150 m from the fault contains some of the highest numbers of deformation band per metre seen in these transects, but is not associated with any displacement of the top Navajo Sandstone (Figure 4.20). This cluster appears to be another fault system (the Melon fault) and is not included in the off-fault deformation for the Big Hole fault.

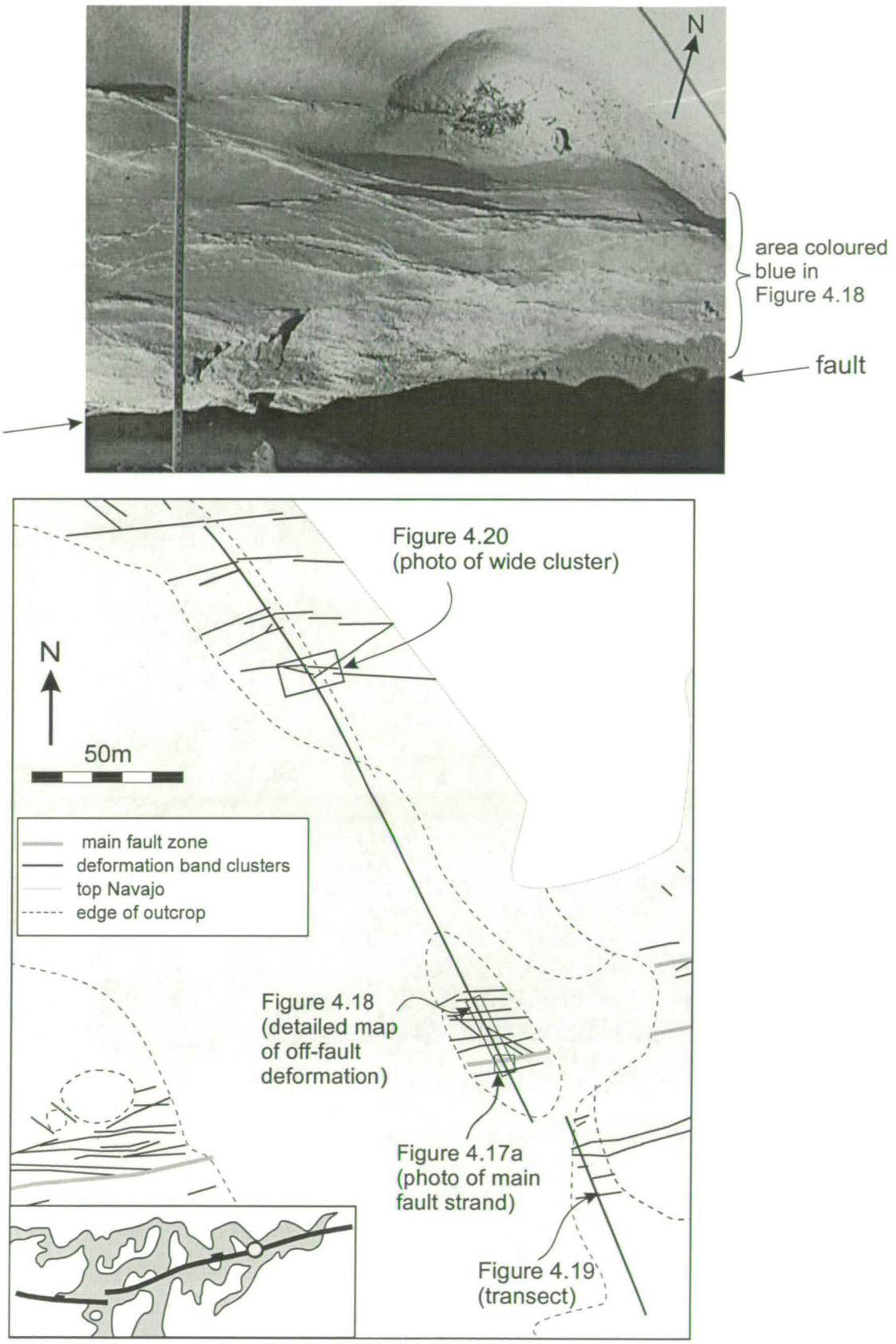

Figure 4.17 a) Photograph of the Big Hole fault at Juniper Flat. The fault forms a large step in the outcrop so the lower part of the photograph is in shadow. b) Map of the Juniper Flat locality. The position and outline of other figures are marked. The dot on the inset shows the position of this outcrop with respect to the rest of the fault.

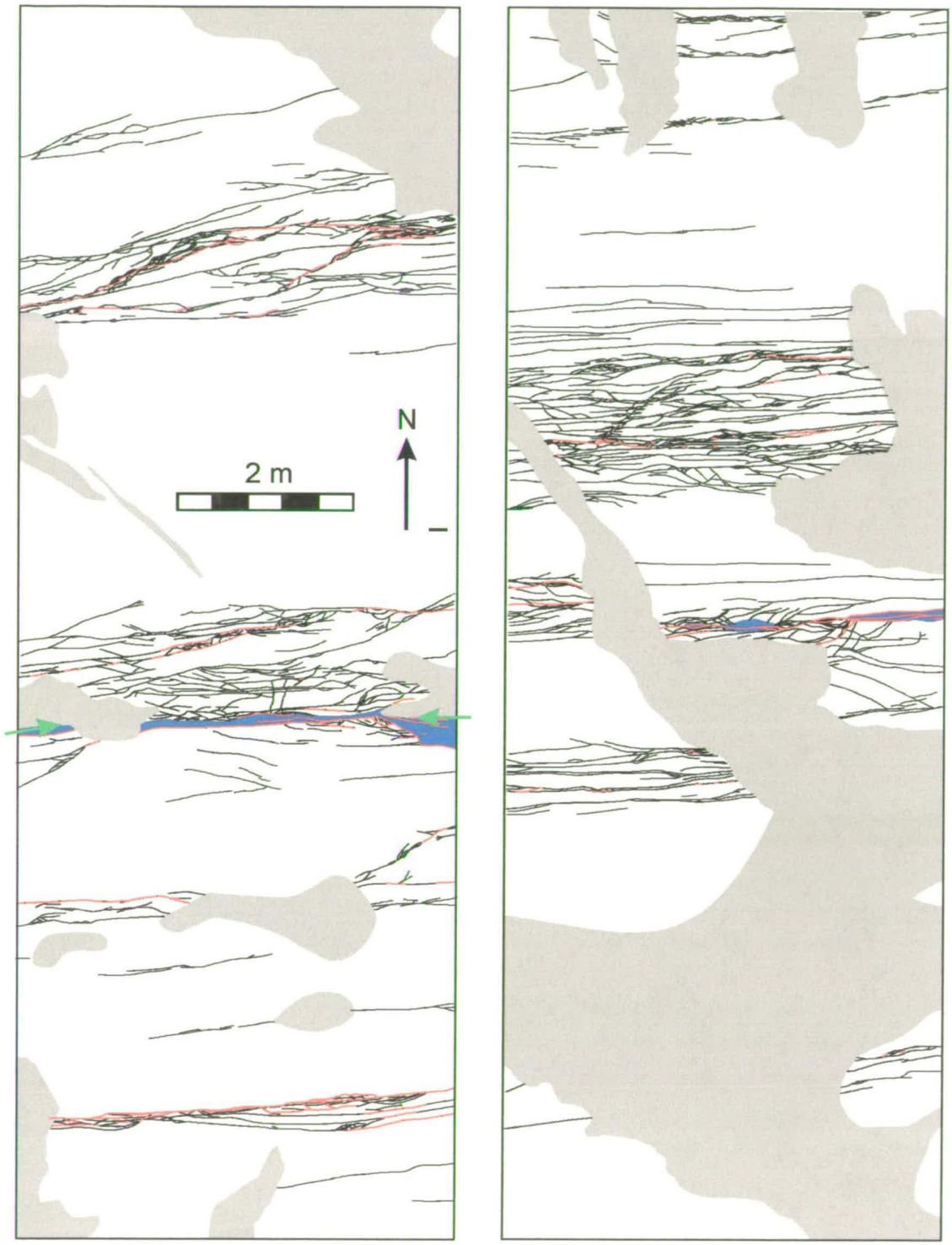

Figure 4.18. Outcrop map of the Big Hole fault at Juniper Flat. Black lines are deformation bands, and red lines are slip-surfaces. Blue blocks are zones where individual bands are hard to distinguish from one another. Grey fill is areas of sand on the outcrop. Green arrows mark the position of the main fault surface. The right-hand map fits onto the bottom of the left-hand map.

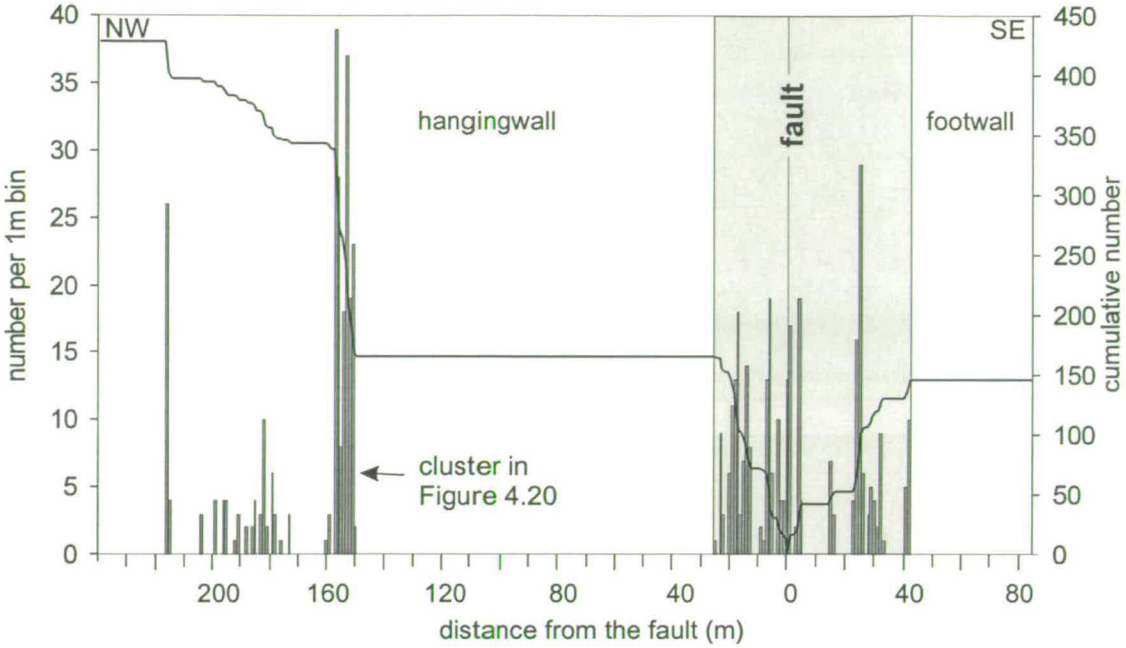

Figure 4.19. Transect across the Big Hole fault at Juniper Flat. The bars are the number of deformation bands per 1m wide bin, the line is the cumulative number of deformation bands per metre. The cluster at 150 m is a separate fault system.

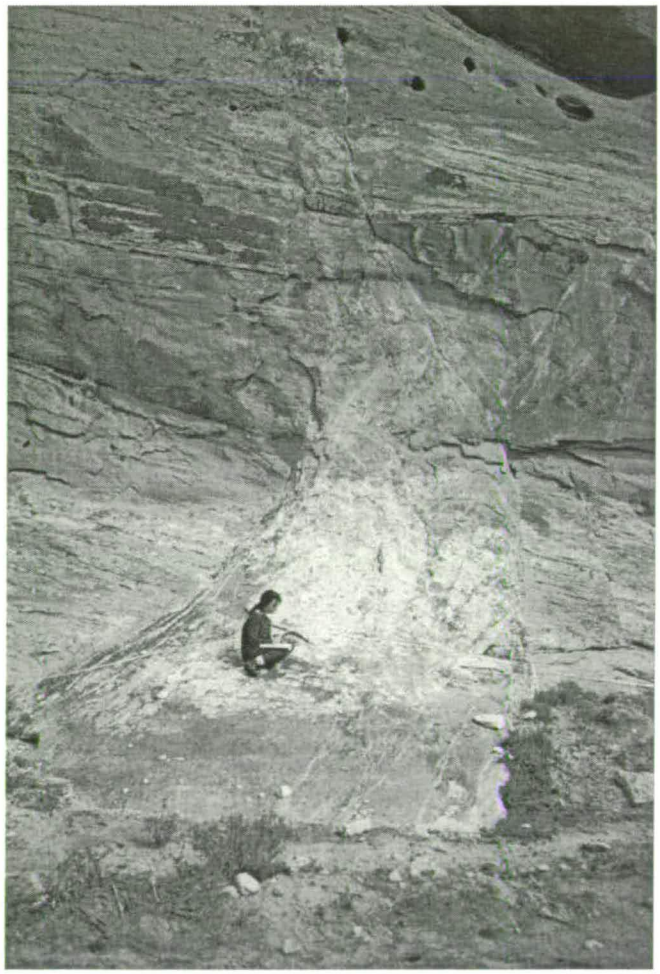

Figure 4.20. Photograph of the large cluster at 150-160 m from the Big Hole fault along the Juniper Flat transect.

4.4.5 Jan's cliffs

This good-quality cross-sectional outcrop of the fault is the closest exposure to its maximum displacement. The fault is exposed in a long cliff approximately 30 m high. The cliff runs to the north for 140 m where it ends at the tip of the meander spur (Figure 4.21a). In the footwall, the cliff runs 230 m to the back of the meander bend. The fault in Figure 4.21b has 23.5 m of displacement.

The transect runs along the base of the cliff (Figure 4.22). It is not obvious from the transect alone where the edge to the off-fault deformation is at this location. Many of the deformation bands recorded on this transect are those of the non-fault-parallel regional strike direction. The majority of the structures in the footwall strike in this direction.

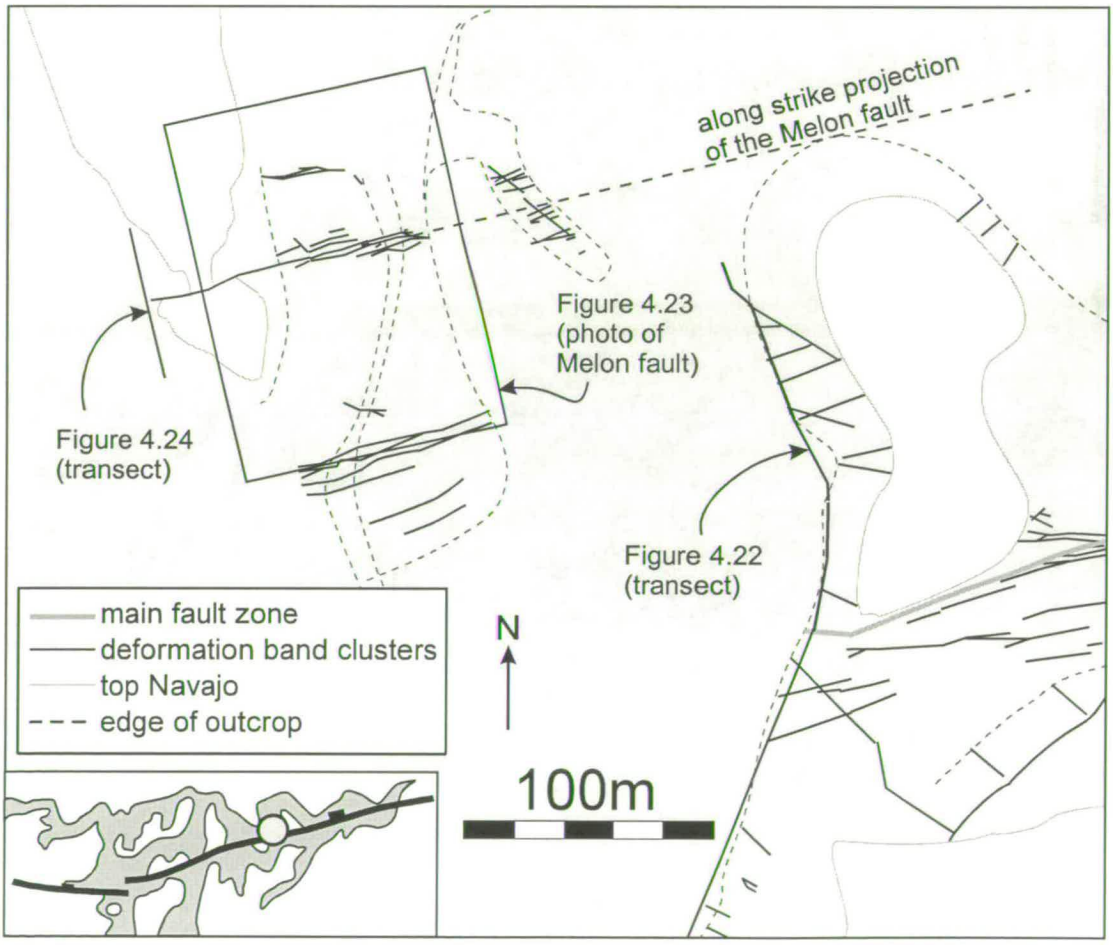

Figure 4. 21 a) Map of the Jan's Cliff and Melon fault localities. The position of other figures are marked. Inset shows position of this outcrop with respect to the rest of the fault.

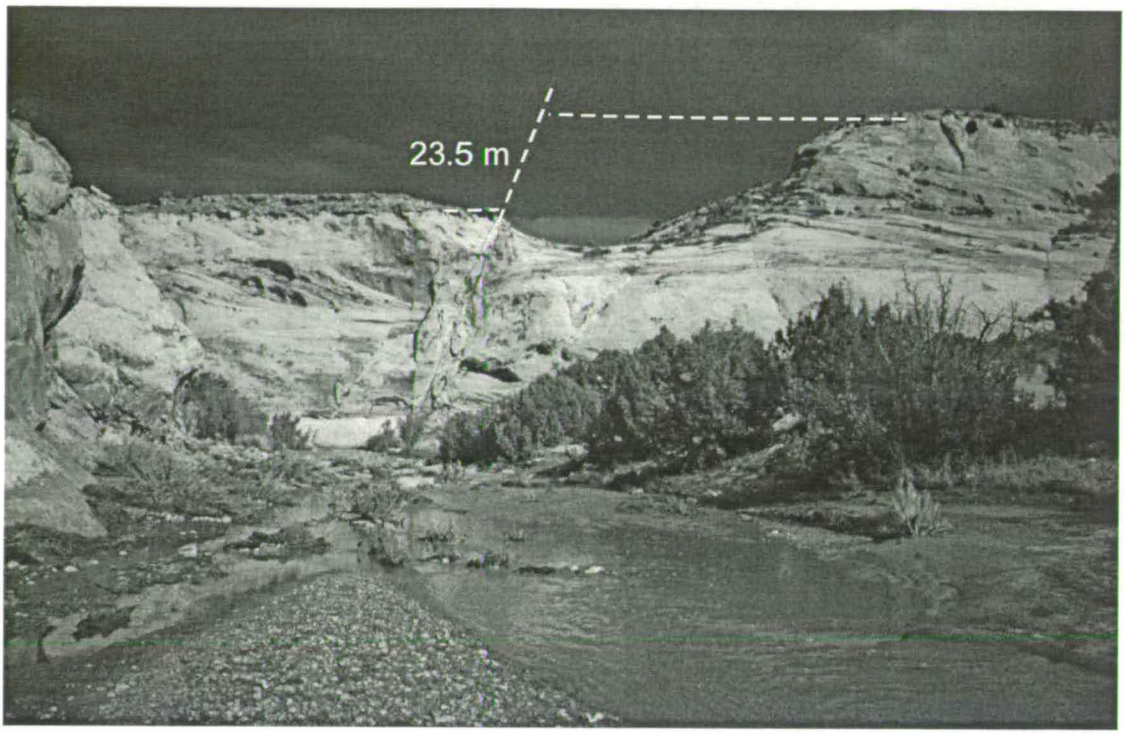

Figure 4.21 b) Photo facing east towards Jans cliff. The Big Hole fault has a displacement of 23.5 m at this locality.

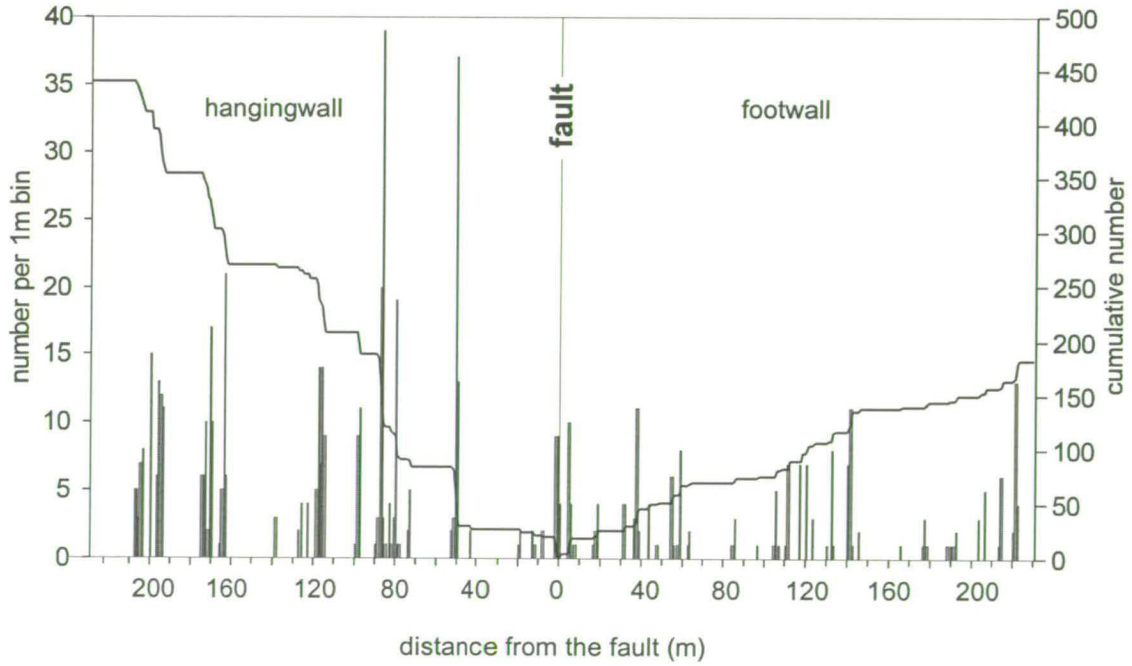

Figure 4.22. Transect across the Big Hole fault at Jan's Cliff. The fault is in the centre and the footwall is to the right. The bars are the number of deformation bands per 1m wide bin; the line is the cumulative number of deformation bands per metre.

4.4.6. Melon fault

The Melon fault is a small antithetic fault in the hangingwall of the Big Hole fault. Figure 4.23 shows this fault displacing the top Navajo Sandstone by 3m. The deformation that is concentrated around this fault can be traced down into the wash below (Figure 4.23), and probably controls the end of the large meander spur running across the meander bend.

The transect extends 30 m into the footwall and hangingwall (Figure 4.24). Deformation is tightly clustered around the fault defining a zone 15 m wide with the fault in the centre.

4.4.7. Amy's Hill

This outcrop is at the opposite side of the meander bend from Jan's Cliff. The fault here has 25 m displacement. Figure 4.25 shows the outcrop of the fault at this point. The transect (Figure 4.26) shows off-fault deformation 64 m wide with the fault towards the hangingwall side of the off-fault deformation. There is a gap in the data from 5-40 m.

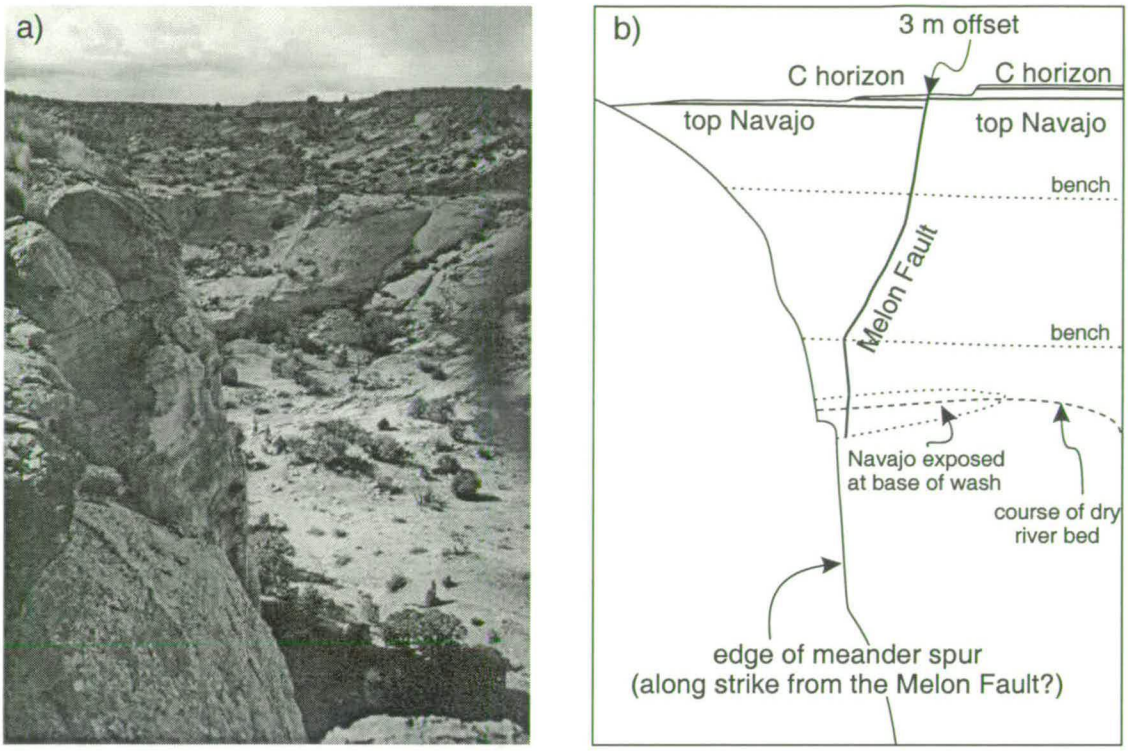

Figure 4.23. a) Photograph looking west towards the Melon fault. Taken from the meander spur to the east of Jan's Cliff. b) Line drawing interpretation showing the fault offsetting the top Navajo Sandstone.

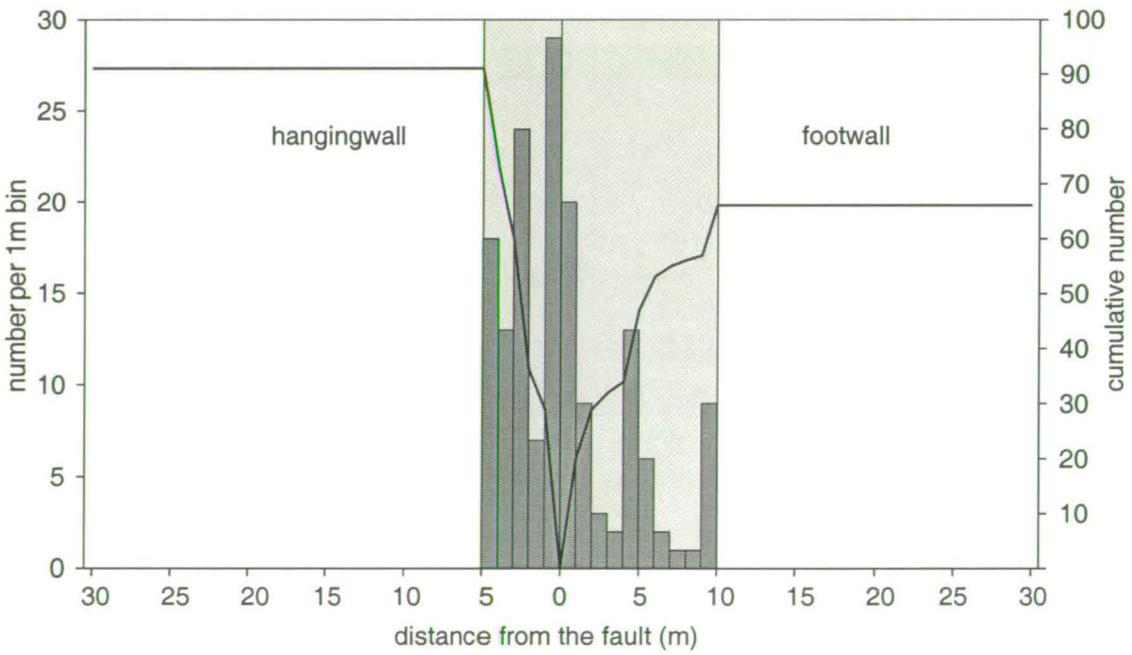

Figure 4.24. Transect across the Melon fault. The bars are the number of deformation bands per metre, the line is the cumulative number of deformation bands per metre.

Figure 4.25. Photograph of antithetic structures in the hangingwall of the Big Hole fault at Amy's Hill. Photo is taken facing west.

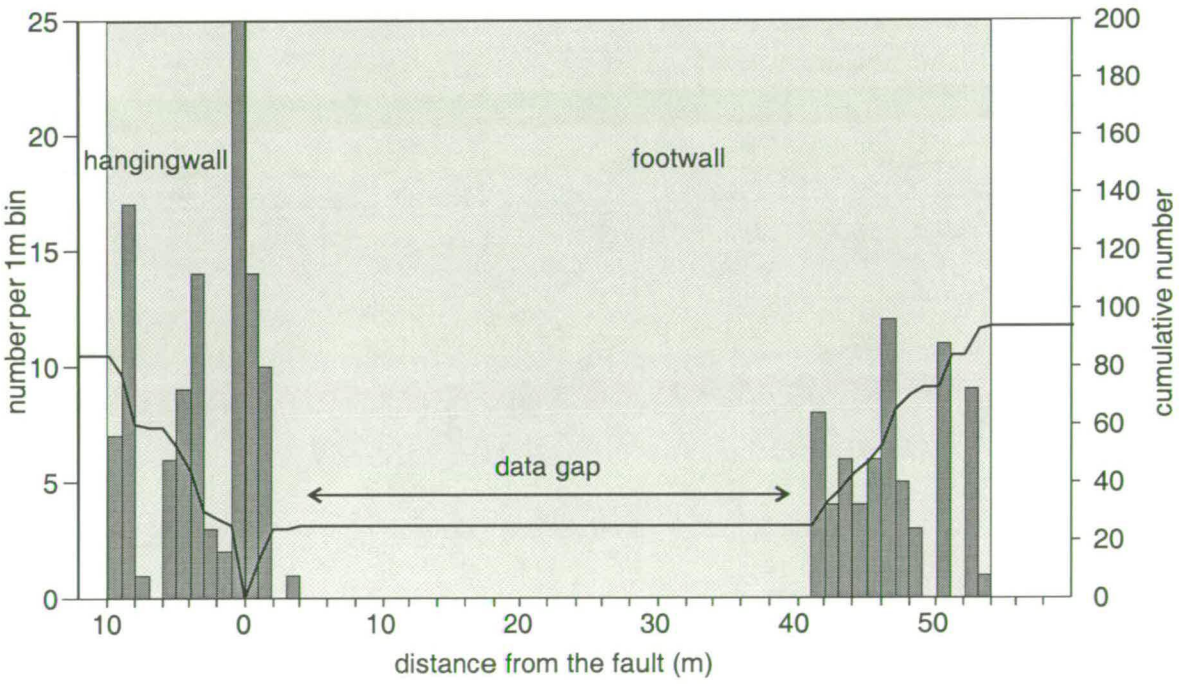

Figure 4.26. Transect across the Big Hole fault at Amy's Hill. The fault is near to the left of the graph, the footwall is to the right. The bars are the number of deformation bands per 1m wide bin, the line is the cumulative number of deformation bands per m.

4.4.8. Orientation of structures around the Big Hole fault

Figure 4.27a shows the orientations of the structures in various locations around the Big Hole fault. The majority of the structures are strike-parallel to the fault (striking 080-260° ± 10°) with equal proportions of synthetic and antithetic faults. At the top of Figure 4.27a the orientation of the structures seen at two localities a substantial distance from the fault (> 500 m) are shown. Very little deformation is seen away from the fault and the majority of it is in the non-fault-parallel regional strike direction (striking 125-305° ± 10°). Structures striking in this direction consistently cross-cut the fault-parallel structures, and are less well-developed. Figure 4.27b shows all the data for the hangingwall and footwall of this fault. There is no difference in the orientation of off-fault structures between the footwall and hangingwall.

The orientation of slickenlines on slip-surfaces around the Big Hole fault is shown in Figure 4.27c. The square shows the average slickenlines and the star shows down-dip on the average slip-surface great circles. On average, all of the slickenlines on slip-surfaces around the Big Hole fault are pure dip-slip.

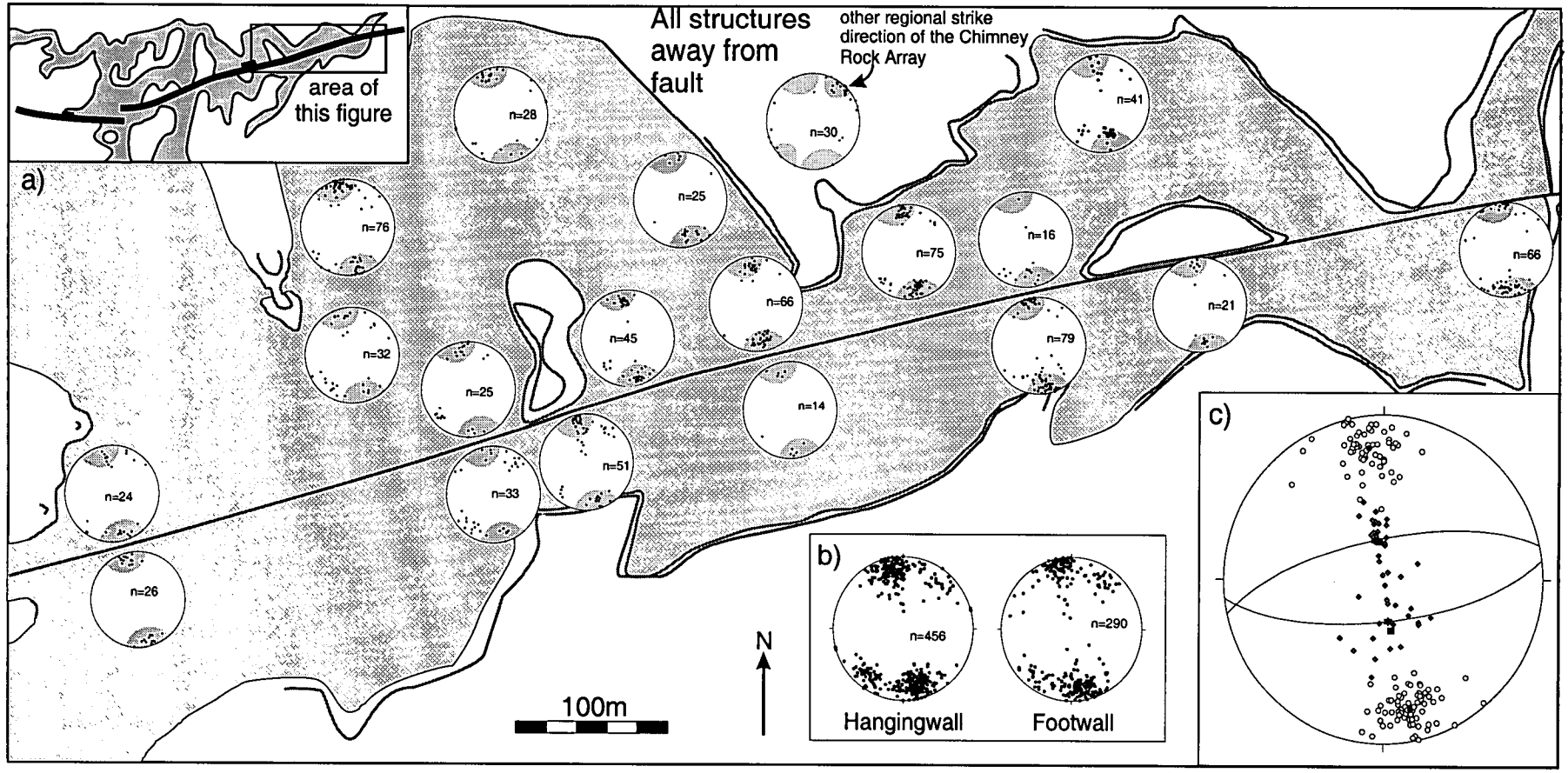

Figure 4.27. a) Poles to deformation bands around the Big Hole fault. Each stereonet is for the hangingwall or footwall of an individual location. Shaded regions show the average synthetic and antithetic cluster orientation. The inset shows the location of this figure with respect to the rest of the fault. b) Stereonets of all structures in the hangingwall and footwall of the fault. c) Slip-surfaces (n=132) and slickenlines (n=43) around the fault. Symbols are the same as figure 4.7b.

4.4.9. Big Hole fault west end

At this locality, two differently-trending segments link together (see Figure 3.4). The structures within the segment boundary have been mapped, though the outcrop quality is poor (Figure 4.28a). The clusters on the map have not been assigned to classes. The clusters antithetic to the fault are shallower dipping than the synthetic structures (Figure 4.28b).

The transect in Figure 4.29 runs along on the east side of the Big Hole Wash, which cuts a shallow canyon at this point. This location is beyond the detailed displacement surveys, so the displacement is extrapolated from the nearest survey and is in the order of 9 m. The deformation is tightly clustered and approximately symmetrical for 16 m on either side of the fault.

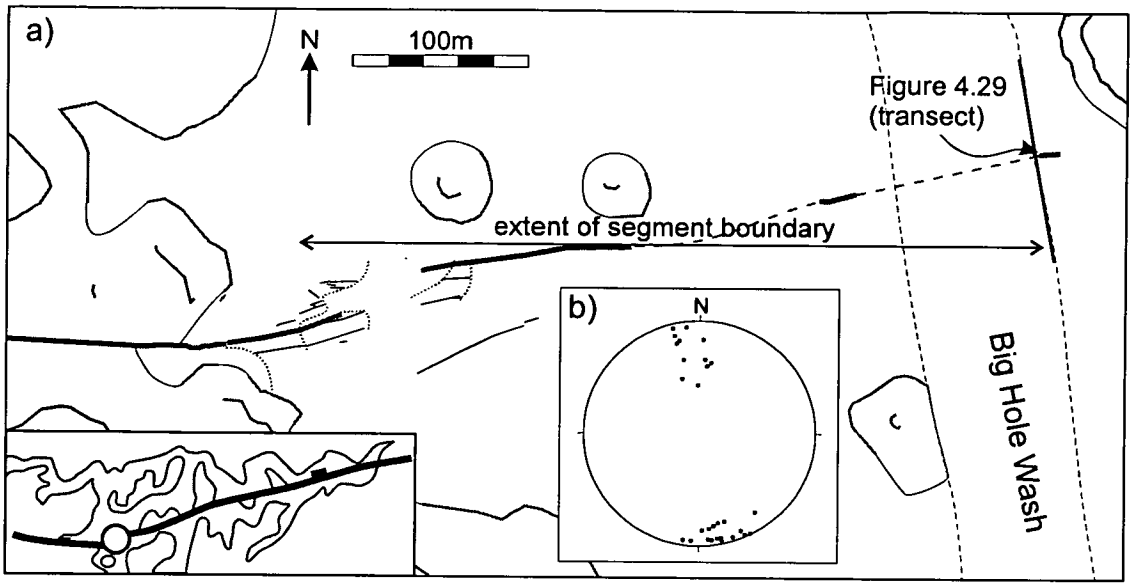

Figure 4.28. a) Map of the segment boundary at the west end of the Big Hole fault. The Navajo Sandstone is white, the Carmel Formation is grey. The dot on the inset shows the location of the segment boundary. b) Poles to deformation bands within this zone.

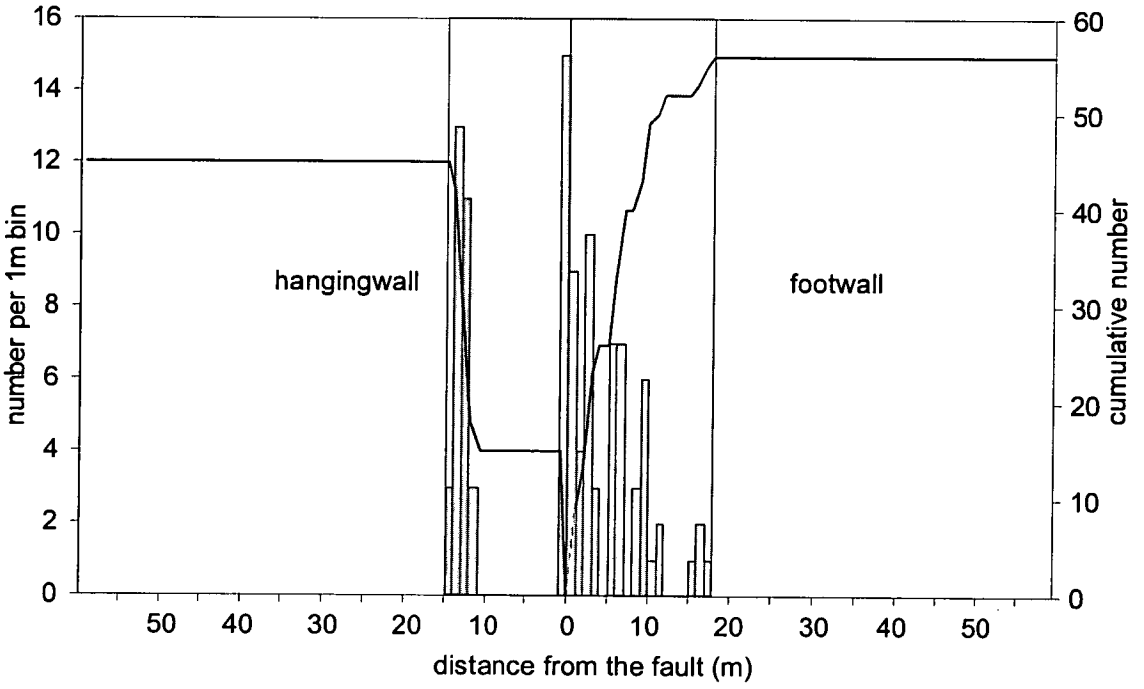

Figure 4.29. Transect across the Big Hole fault at the west end segment boundary. The fault is in the centre and the footwall is to the right. The bars are the number of deformation bands per 1m wide bin, the line is the cumulative number of deformation bands per metre.

4.5. Interpretation

4.5.1. Defining the width of off-fault deformation

As discussed in Section 1.3.3, the edge of the zone of off-fault deformation that is associated with a particular fault can be defined in a variety of different ways. However, it is relatively straightforward to define off-fault deformation width for the Big Hole and Blueberry faults; deformation bands are clustered around the fault, and beyond a certain distance there is essentially no deformation (envelope on Figure 4.8). This distance defines the edge of the off-fault deformation zone. Structures trending in the non-fault-parallel regional strike direction consistently cross-cut the fault-parallel clusters and appear to belong to a later stage of deformation. Hence these structures are not considered to be part of the off-fault deformation associated with the Big Hole and Blueberry faults.

A subsidiary zone of clusters is observed between 150 and 200 m into the hangingwall of the Big Hole fault. It is conceivable that these structures could be linked along strike to form a continuous cluster. None of these structures are associated with any displacement of the top Navajo Sandstone, except the Melon fault.

It is interesting to note that of the two strands at Chipmunk Flat, the southern strand is surrounded by more deformation than the northern strand. The southern strand also has a larger displacement. This implies that the density of deformation correlates with fault displacement. This is investigated further in Section 6.3, where the distribution of off-fault deformation is discussed in terms of strain around the fault.

4.5.2. Off-fault deformation scaling

The tip of the Blueberry fault, as defined by displacement profile mapping, outcrops in the centre of the Blueberry Canyon (Figure 3.4a). The off-fault deformation at this point has a finite width of 12 m. Deformation band clusters extend for another 45 m up to the point where no further deformation is seen beyond the fault tip. The off-

fault deformation around the Big Hole fault extends up to a maximum of 80 m from the fault. Thus the off-fault deformation appears to be wider where the displacement on the fault is larger. Table 4.2 shows the values of displacement and off-fault deformation width at each locality. The errors in displacement in Table 4.2 are taken from Figures 3.6-8. The errors in off-fault deformation width are due to the accuracy of measuring this from the cluster maps.

location	distance from fault centre (m)	displacement from measured profiles (m)	errors	off-fault deformation width (m)	errors
Blueberry fault					
top of N. canyon wall	1865.5	0	-	0	+/- 0.25m
base of N. canyon wall	1849.5	0	-	5.25	
tip defined in Chapter 3	1820	0	0.154	12.00	
1/2 way up S. canyon wall	1815	0.214	0.069	11.50	
top of S. wall (S horizon)	1797	0.937	0.221	11.75	
top of S. wall (N horizon)	1797	1.114	0.173	11.75	
Big Hole fault					
Cement Bridge	1450	9.414	1.742	27	+/- 1m
1st valley	1150	11.595	1.793	25	
top of Redcliff	950	17.437	1.596	31	
Chipmunk Flat	830	19.059	2.485	49	
Platform	653	18.881	1.544	64	
Juniper Flat	596	24.337	2.333	76	
bottom of 2nd valley	475	22.924	1.233	54	
middle of 2nd valley	373	24.028	1.881	79	

Table 4.2. Measured values of displacement and off-fault deformation width used in Figure 4.29. Localities are marked on Figure 4.2.

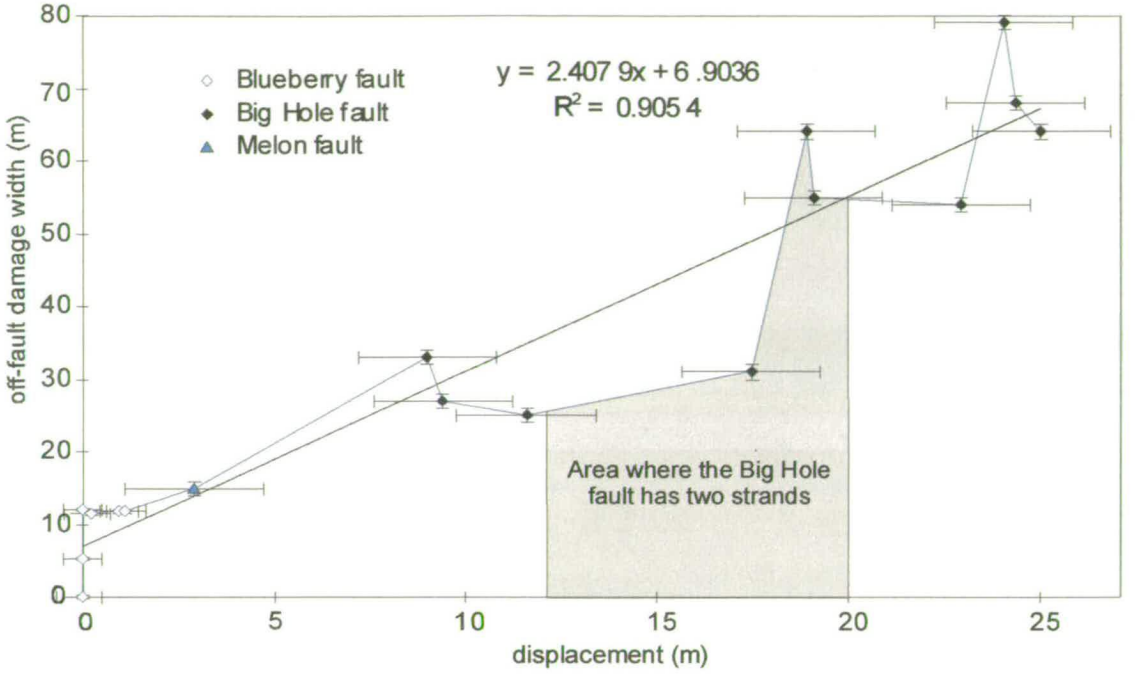

Figure 4.30. Scaling of off-fault damage width with displacement. The best fit line is for all the data. Error in displacement is calculated from the extreme values of bedding strike in chapter three, and is in the order of +/-1 m for the Blueberry fault and +/-1.5 m for the Big Hole and Melon faults. The errors in off-fault damage width are +/-0.25 m for the Blueberry fault and +/-1 m for the Big Hole and Melon

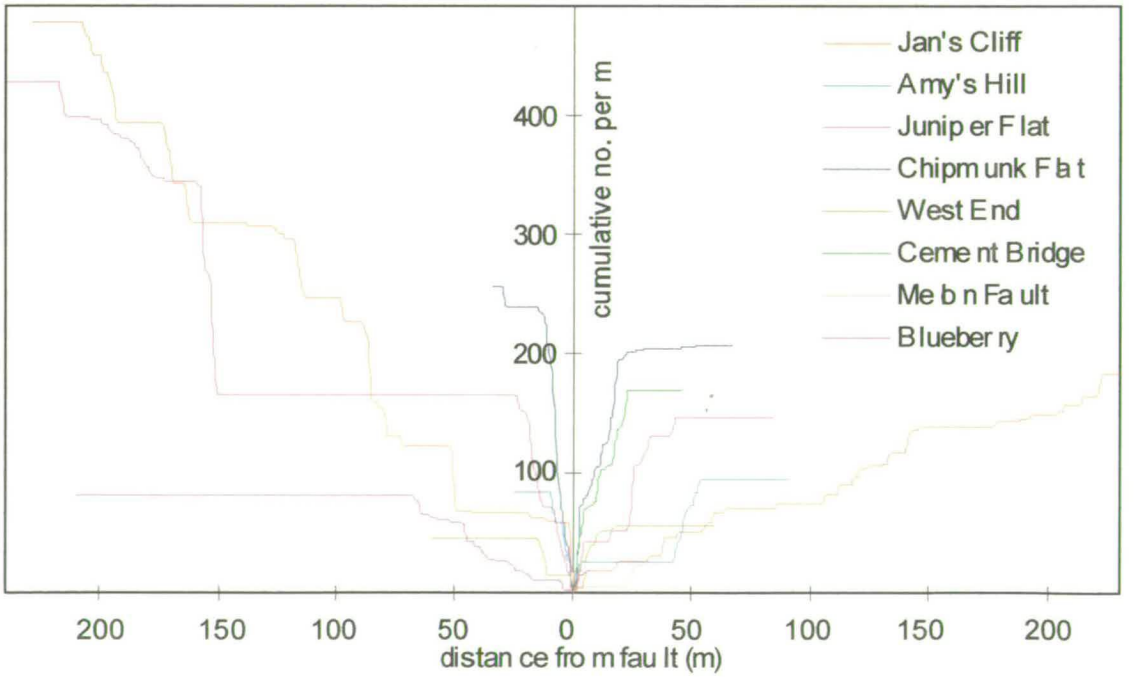

Figure 4.31. Comparison of the cumulative deformation curves for all transects. The key shows the localities in order of decreasing displacement.

When the off-fault deformation width is plotted against displacement (Figure 4.30), the data is reasonably well fit by a straight line, $y = 2.4 x + 7.0$. The best fitting straight line implies that off-fault deformation width is approximately two and a half times the displacement. The finite intercept of 7.0 m implies that the width needs to have a critical value before a significant offset (slip-surface) can occur. This is consistent with the model of Antonellini *et al.* (1994).

The region where the off-fault deformation width is anomalously low can tentatively be correlated with the area where the displacement is accommodated on two main fault strands rather than one. However, no anomaly in the displacement profile is seen at this point (see Figure 3.13). This would suggest that more of the displacement can be taken up on two strands rather than on a single strand, and that less strain is transferred to the off-fault deformation. Because the displacement measurement points are outside the entire fault zone, the displacement profiles are actually those of all of the off-fault deformation in addition to the main fault surface.

The zone of off-fault deformation has a distinct edge on most of the transects, but they can often be more ambiguous to interpret than the maps of off-fault deformation. There is considerable lateral variability in the number and connectivity of the deformation band clusters and therefore a transect taken a few metres along the same outcrop could have a significantly different form. There seems to be no consistent variability in the slope of the cumulative number of deformation bands with displacement (Figure 4.31). Although there is a positive relationship between the spacing of clusters and the distance from the fault, it is very weak (Figure 4.32). There is, however, an increase in the variability of cluster spacing with distance from the fault. There is no obvious decay in the of the number of deformation bands with distance from the fault. This contrasts with the logarithmic decay in microfracture densities observed around fault in other studies (Anders and Wiltschko 1994, Vermilye and Scholz 1998).

The relationship between width of off-fault deformation and displacement could be very useful for the prediction of the distribution of sub-seismic features around faults.

However the error bars on Figure 4.30 show that the predicted off-fault deformation width could vary by about as much as 10-20% of the displacement at a point. Tentative relationships between off-fault deformation width and displacement have been found by other workers. Knott et al. (1996) found that the half-width of the off-fault deformation scaled with displacement according to a power-law, but they found that the hangingwall and footwall had different distributions, which is not the case in this study. However the data is not abundant enough to form a definite rule applying to all faults, that could be used with certainty to predict the distribution of sub-seismic faults, and many other factors may be important (see Section 7.3.3).

4.5.3. The fault core

Slip-surfaces often form the edges of concentrated zones of deformation which are usually between 30 and 50 cm wide. The width of these zones appears to be independent of the displacement on the fault, and in fact significant variation is seen locally along strike (see Figure 4.15a). In the terminology of Caine *et al.* (1996), these zones would be termed the fault core. It has been argued that a scaling between the fault core width and displacement exists (Hull 1988, Evans 1990a). However, in the light of the observations made here, this seems unlikely for the Big Hole and Blueberry faults.

Slip-surfaces can be identified running through the entire length of individual Big Hole fault outcrop maps. These are presumably the surfaces upon which most of the displacement has been localised, and therefore represent the main slip-plane of the fault itself. The discontinuous nature of slip-surfaces in the Tip Canyon clusters is consistent with the observation that these structures represent deformation ahead of the fault tip. If no slip-surface can be traced through a cluster, then no significant localisation of displacement can have taken place. This provides a criterion for defining fault core clusters from clusters within the off-fault deformation.

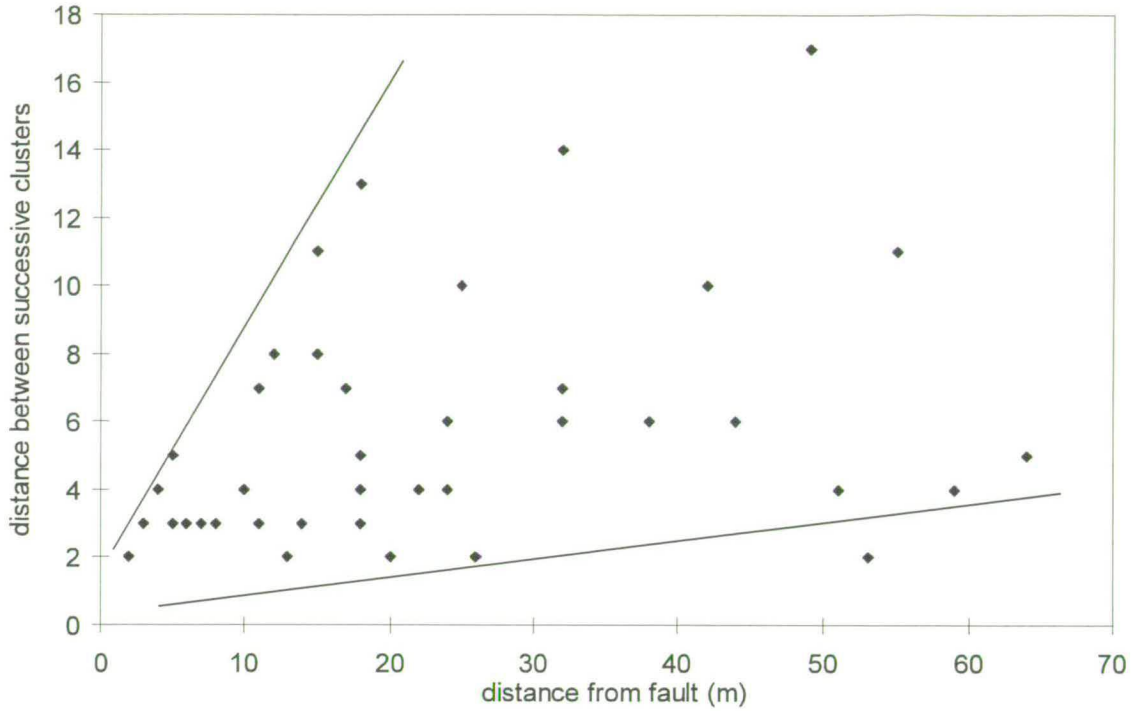

Figure 4.32. Increase of spacing of deformation band clusters with distance from the fault.

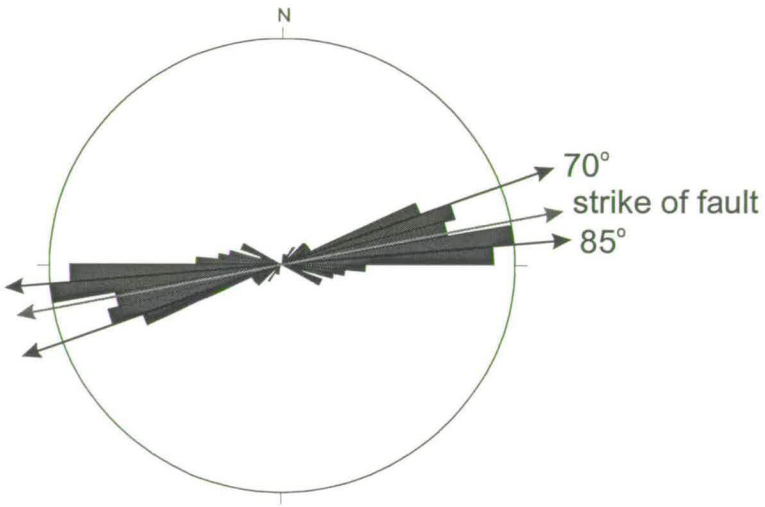

Figure 4.33. Rose diagram of the strike direction of off-fault structures around the Big Hole Fault. Two main strike directions can be seen which are symmetrical around the main fault.

4.5.4. Slip-surfaces

Slip-surfaces are always associated with deformation band clusters. However, small slip-surfaces are often associated with zones of local thickening on single deformation bands. This contradicts the model of Aydin and Johnson (1978) and Antonellini *et al.* (1994). This model implies that a certain amount of strain is required across a zone of deformation bands before the nucleation of a slip-surface occurs. However, the observation above suggests that slip-surfaces can form relatively early on in the development of a zone of deformation bands. This is discussed further in Section 5.5.2 where the microstructure of slip-surfaces is investigated.

Unfortunately the transect data were collected before the importance of slip-surfaces was appreciated and therefore the location of slip-surfaces is not always marked on the transects. However, it can be observed qualitatively that slip-surfaces are concentrated within the clusters closest to the fault and that the number and continuity of slip-surfaces decreases away from the fault. The number of slip-surfaces were counted from the outcrop sketches. Four slip-surfaces cut the base of the Blueberry fault Tip Canyon outcrop, three cut the Cement Bridge outcrop, ten cut both the Chipmunk Flats outcrop maps and eleven cut the Juniper Flats outcrop. These results point towards a positive correlation of the number of slip-surfaces with the displacement on the main fault surface, but more data would need to be collected to confirm this.

4.5.5. Orientations of off-fault deformation features

An important difference is seen between slip-surfaces at the fault tip and those around the well-developed fault plane. Slip-surfaces at the tip have oblique slickenlines and near the well-developed fault surface the slickenlines are dip-slip. The almost total lack of oblique-slip slickenlines on the Big Hole fault surface suggests that repeated slip on the fault obliterates evidence of early oblique slip. Oblique-slip slickenlines occur throughout the Blueberry fault Tip Canyon outcrop (0-23 m from tip, from 0 to 1.1 m of displacement). However, dip-slip slickenlines

are dominant at the Cement Bridge outcrop (500 m from tip, 9 m of displacement). The oblique-slip slickenlines must be obliterated at some point between 1 and 9 m of displacement. In cases of limited exposure the presence of oblique-slip slickenlines could be a useful indicator of the proximity of a fault tip.

The majority of deformation bands and clusters of bands are synthetic or antithetic to the main fault. In plan view the deformation bands are not strictly parallel to one another. The low angle between bands means that they often define thin lozenge-shaped blocks between faults. This pattern can be seen on a plot of orientations of the deformation bands within the off-fault deformation (Figure 4.33). In cross-section the clusters surround lozenge-shaped blocks with a lower aspect ratio. This describes an orthorhombic pattern of faulting with a low angle between strike sets. The orthorhombic geometry within the off-fault deformation is discussed further in Section 6.4.

At the western end of the Big Hole fault is a zone where two non-parallel fault strands are obviously linking. A stereonet of the structures within this zone of linking shows an interesting pattern of steeply dipping synthetic structures and shallower dipping antithetic structures (Figure 4.34a). Intriguingly, the same relationship is seen for the structures within the fault core (Figure 4.34b), and also for the structures within an individual cross-hatched deformation band cluster (Figure 4.34c, pictured in Figure 4.35a). These cross hatched patterns are seen in the Blueberry fault Tip Canyon and Cement Bridge outcrop maps (see Figure 4.5 and 4.11) and are ubiquitous in cross-sections of deformation band clusters. Cross-hatched patterns are also seen on horizontal surfaces (e.g. Figure 4.15b). Regions of cross-hatched deformation bands are often bounded on one or both sides by slip-surfaces (e.g. Figure 4.35a). Slickenlines on these surfaces are mostly dip-slip. A cartoon of the three-dimensional structure is shown on Figure 4.35b.

It is possible that this pattern is characteristic of structures that form where two fault segments or deformation band clusters are in the process of linking together. If this is the case then the presence of this pattern of structures in the fault core is evidence

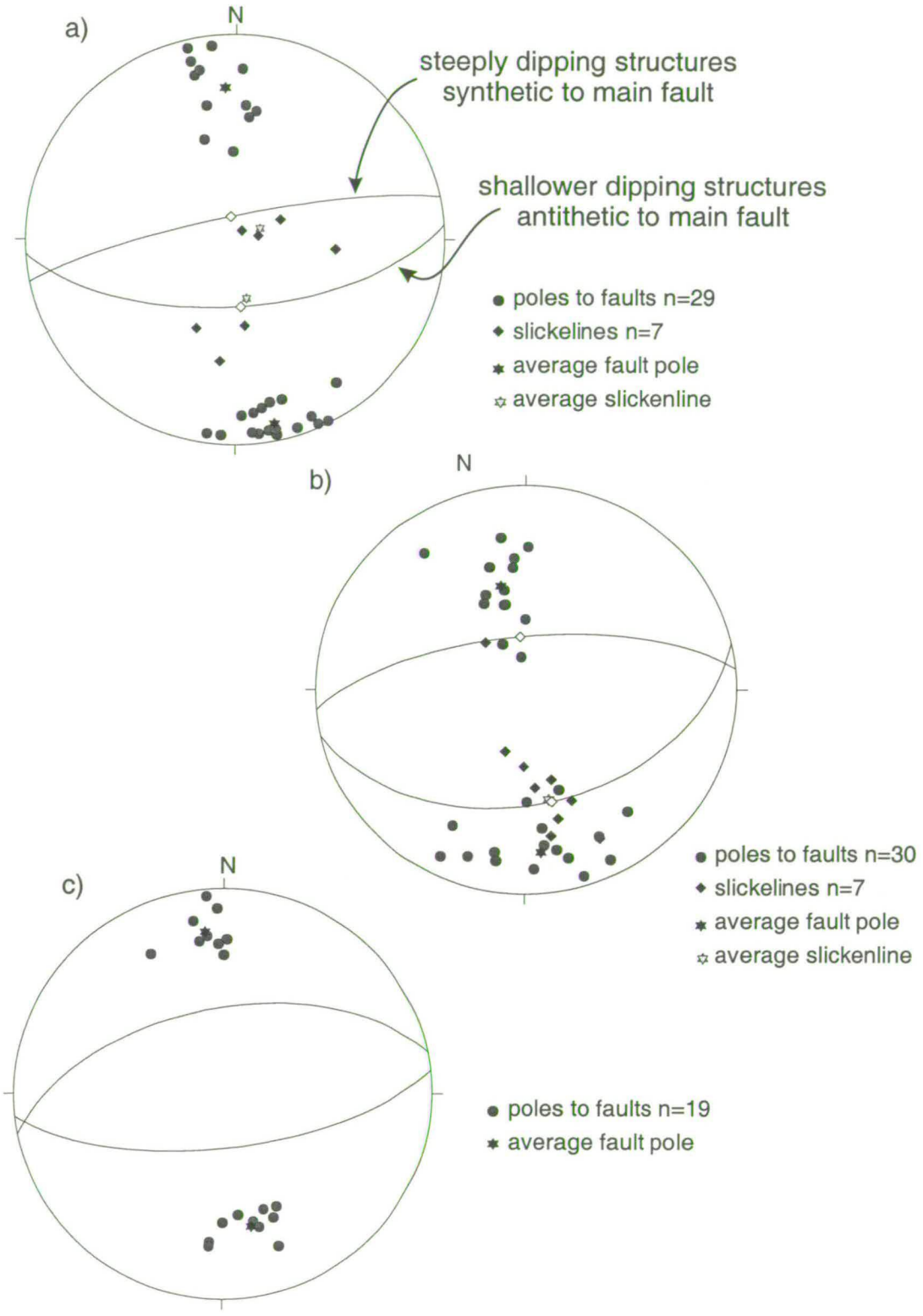

Figure 4.34. Stereonets of poles to slip surfaces and deformation bands within a) the link area at the west end of the Big Hole fault, b) the fault core of the Big Hole fault, and c) deformation bands within one cluster of the Big Hole fault damage zone at Juniper Flat (photo in Figure 4.35a).

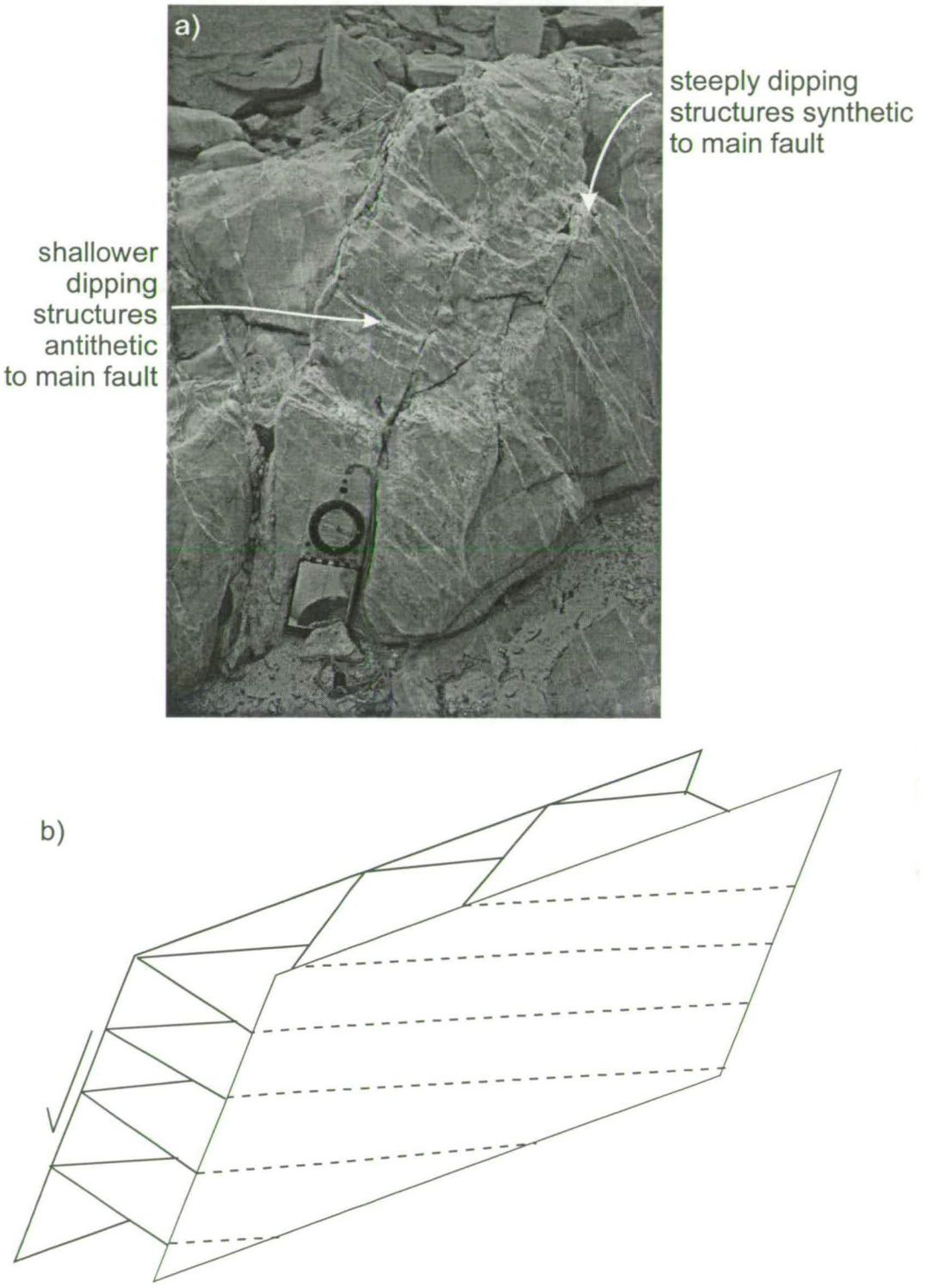

Figure 4.35. a) Example of a cluster with a cross hatched pattern, bounded on both sides by slip-surfaces. (stereonet in Figure 4.34c) b) Three-dimensional cartoon of the cross hatched structures in Figures 4.34 and 4.35a.

that this evolves at least partly by the linkage of along-strike structures. Likewise the structures seen within the off-fault deformation at Blueberry fault and Cement Bridge may have this type of origin. These are just preliminary observations and further research is warranted.

4.6. Summary

1. The distribution of clusters of deformation bands around two fault zones has been mapped using a total station surveying instrument. Outcrop-scale maps of individual deformation bands have been created in selected areas of interest, and one-dimensional transects of the deformation have been made.

2. Clusters of deformation bands and slip-surfaces are concentrated around the main fault plane. Beyond a certain distance from the fault the rock is essentially undeformed. This distance defines the edge of the off-fault deformation. Within the off-fault deformation there is no decay of number of deformation bands with distance, rather the deformation is clustered. There is some evidence for an increase of cluster spacing with distance from the fault.

3. Close to the fault, a zone of concentrated deformation exists which is often bounded by slip-surfaces. This represents the fault core. The width of the fault core is highly variable and does not scale with the displacement on the fault. An uninterrupted slip-surface can usually be traced that runs through the fault core. This is the main fault plane upon which the majority of deformation is localised.

4. The Blueberry fault can be traced, as a well-developed slip-surface with slickenlines, to the Tip Canyon locality. Slip-surfaces in the northern wall of the Tip Canyon are discontinuous. This confirms the observation in Chapter 3 that the tip of the fault is situated in the centre of this canyon.

5. The off-fault deformation is narrow around the Blueberry fault tip, but has a finite width at the point where the point of zero displacement is defined by the surveys in Chapter 3. The off-fault deformation around the Big Hole fault is wider than that around the Blueberry fault. The width of the off-fault deformation is positively correlated with the displacement on the fault with a slope of around 2.5 and an intercept of 7.0 m. The relationship between off-fault deformation width and displacement is a potentially useful predictive tool, but the precise form of the relationship must be investigated further.

6. A pattern of steeply-dipping synthetic and shallowly-dipping antithetic structures is commonly observed. This pattern is seen at the segment boundary at the West end of the Big Hole fault and is associated with the fault core and some of the larger clusters within the off-fault deformation. It is possible that this pattern of structures is evidence for the linkage of segments.

5. MICROSCOPIC OFF-FAULT DEFORMATION

5.1. Introduction

5.1.1. Rationale

Although the process of deformation band initiation from undeformed rock has been described in detail in the literature, little attention has been paid to the transition from the strain-hardening process of deformation band formation to the strain-softening movement on a slip-surface (see Section 2.3.1). The formation of deformation bands and slip-surfaces is the main deformation mechanism in the Navajo Sandstone. Therefore an appreciation of the evolution of deformation bands and slip-surfaces with increasing displacement is crucial to the understanding of off-fault deformation development around these faults.

This chapter presents studies of the distribution of microstructures around the Big Hole and Blueberry faults. Samples of deformation bands at different stages of evolution have been studied with an emphasis on the stage of evolution when slip-surfaces form from zones of deformation bands. In places, the aeolian cross bedding provides markers to constrain the displacement on individual deformation bands. This enables the development of deformation bands with increasing displacement to be quantified.

Samples from the apparently undeformed rock between deformation band clusters were collected along transects away from the fault to investigate the decay of microfracture density with distance. Transects were made at localities with a range of displacements on the main fault, to investigate the influence of the variation of fault displacement on the microfracture population. The samples were collected along the same transects as the deformation bands to look at the relationship between microfracturing and deformation band growth.

5.1.2. Structure of this chapter

Oriented samples of the deformation around the Blueberry and Big Hole faults have been examined in thin section. Section 5.2 discusses the methodologies used to collect and analyse these samples. The samples have been divided into five deformation types based on their microstructure: host rock; single-strand deformation bands; zones of deformation bands; slip-surfaces and fault planes. The microstructural data from the five deformation types is presented in Section 5.3. The data are interpreted in Section 5.4, and these interpretations are discussed in terms of deformation band growth in Section 5.5.

5.2. Methodology

5.2.1. Deformation band microstructure

Oriented samples were collected from outcrops with a rock drill. Five localities were targeted: Blueberry fault Tip Canyon (BB1, BBA), Cement Bridge (BH3, BH7), Juniper Flat (BH5, BH8), and Jan's Cliff (BH1, BH10, BHB) (Table 5.1). Figure 5.2 shows the location of these samples. The rock was impregnated with epoxy before sectioning. Thin sections were cut perpendicular to the deformation bands in order to get the best cross-section of the internal structure. Thin sections were examined under an optical microscope and with cathodoluminescence (CL) and backscatter (BSEM) modes on an electron microscope.

Single-strand deformation bands are simple linear features about 1 mm thick accommodating up to a few millimetres of offset. Zones of deformation bands are formed of several anastomosing single-strand bands. Pods of relatively undeformed Navajo Sandstone are often preserved between these strands. Slip-surfaces occur as very planar features, often with a white powdery appearance in outcrop. They often form partings in the rock and it was found to be very difficult to sample a slip-surface without the sample falling apart along the slip plane. Therefore many of the slip-surfaces run along the edge of the sample (e.g. BH3.6) or have been glued back

together during the process of impregnating the sample (e.g. BH1.3/4). Fault planes are slip-surfaces that are considered to be the main slip-surface within a fault zone.

Point counts of deformation bands at different stages of evolution were taken to characterise the deformation style. A device was attached to the microscope stage that advances the sample a set distance across the field of view. The type of grain (or pore), its long axis orientation, and the number of microfractures, were measured for each grain seen under the cross hair, each time the sample is advanced across the stage. An eyepiece containing a graticule was used to measure the long and short axis of each grain. In this way the particle size distribution, preferred orientation of grains and porosity can be calculated for each sample.

The porosity of small regions within the samples was also calculated by image analysis of BSEM images using two packages: Erdas Imagine and Optimas. The greyscale of BSEM images is proportional to the atomic number of the grains, quartz grains can be seen as dark grey, feldspar grains are pale grey, and epoxy-filled pores are black. The image analysis software represents the number of pixels that are each colour on a histogram. Portions of the histogram can then be highlighted in a different colour until the sub-set of pixels that represent the mineral or porosity of interest is selected (Figure 5.1). The number of selected pixels is then counted and presented as a percentage of the total number of pixels in the image. In this way the percentage porosity or quartz, feldspar or any other mineral can be counted.

This method has an advantage over traditional point counting methods because large numbers of measurements can be made relatively quickly. The advantage of using BSEM images is that optical images do not have such a strong contrast between the grains and the epoxy (Antonellini *et al.* 1994). In addition, each mineral has the same grey level across the image, so that no problem occurs with identifying minerals or distinguishing them from the epoxy.

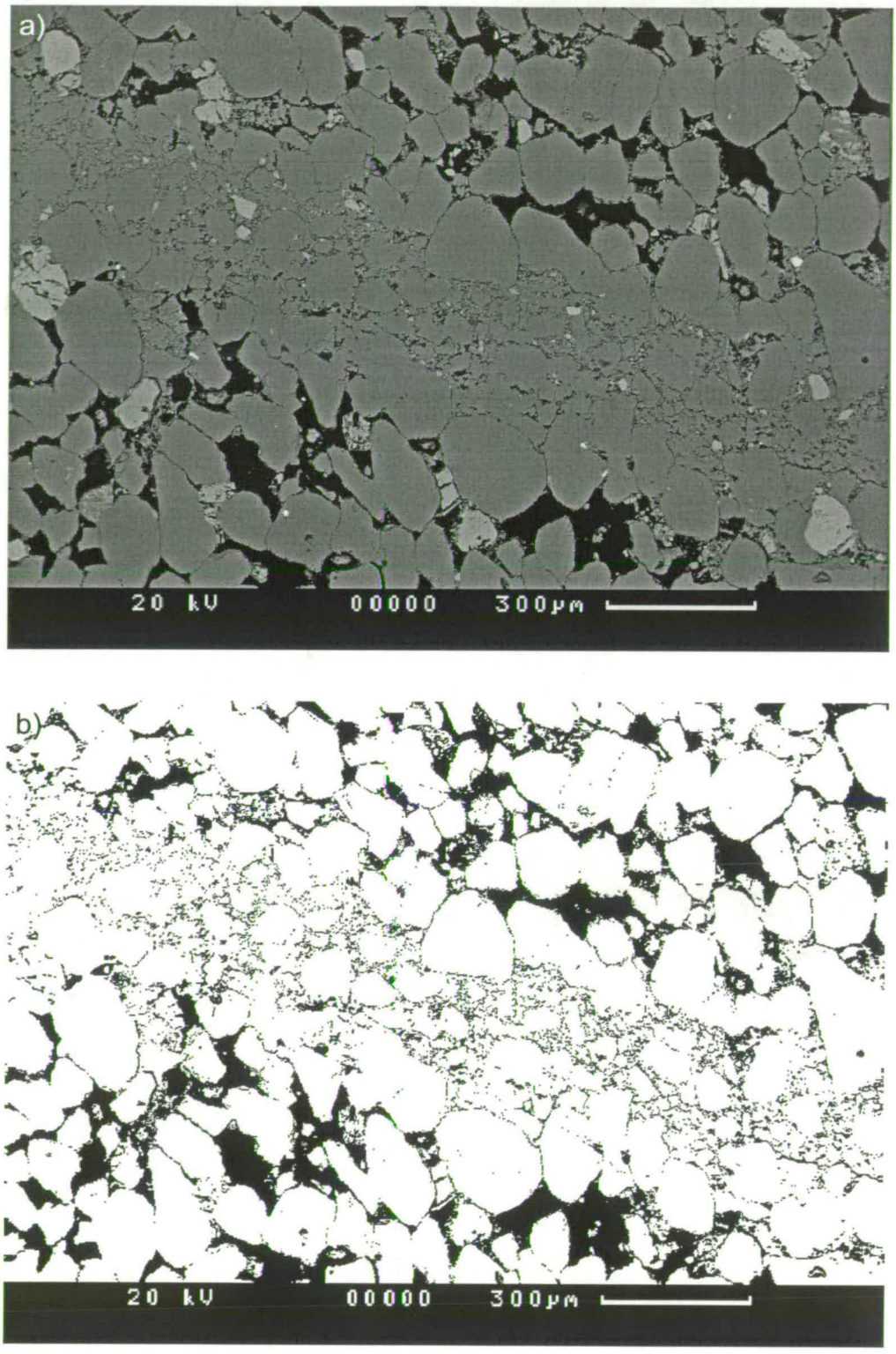

Figure 5.1. a) BSEM image of a single strand deformation band. Pores are black, quartz is grey and feldspar is pale grey. b) The same image adjusted so that pores are black and quartz and feldspar grains are white. The percentage of black pixels can be calculated to give percentage porosity.

5.2.2. Microfracture density

Oriented cores were collected with a rock drill from four localities: The Blueberry fault tip canyon (BBA, BG2), Jan's Cliff (BH1, BHA), Penguin Mesa (BHB) and the west end of the Big Hole fault (BH2). Figure 5.2 shows the locations of these samples. The samples were collected at increasing distances from the fault along the line of the deformation band transects described in Chapter 4. The BG2 samples were collected to represent the background level of deformation in the area and were not associated with any macroscopic deformation. The BHB samples are from pods of relatively undeformed host rock within the fault zone. Microfracture densities were also calculated for the rock adjacent to, and within, deformation bands during point counting.

The plane normal to the fault surface and parallel to the slip vector has been shown to contain the maximum number of microfractures (Engelder 1974, Vermilye 1996). The second set of thin sections (BBA, BHA, BHB, BG2) were cut along this plane. The first set of thin sections (BH1, BH2) were cut before the significance of section orientation was appreciated, and are therefore in random orientations.

The method used to determine microfracture density is similar to that of Anders and Wiltschko (1994) and Vermilye (1996). The number of microfractures crossing a 0.15 mm transect line (one half of the cross hair under a magnification of x40) is recorded. Grains smaller than half a cross hair are not counted. The number of microfractures in twenty grains were counted across each sample. Two perpendicular transects were measured across each thin section in order to eliminate the effects of any anisotropy in the samples. The number of microfractures per millimetre is then averaged for each transect.

Microfractures are most visible when viewed end-on and become invisible at low angles to the plane of the thin section (Anders and Wiltschko 1994). A U-stage (used to detect microfractures at lower angles to the thin section plane) was not used in this study so the true number of microfractures will be underestimated. However the

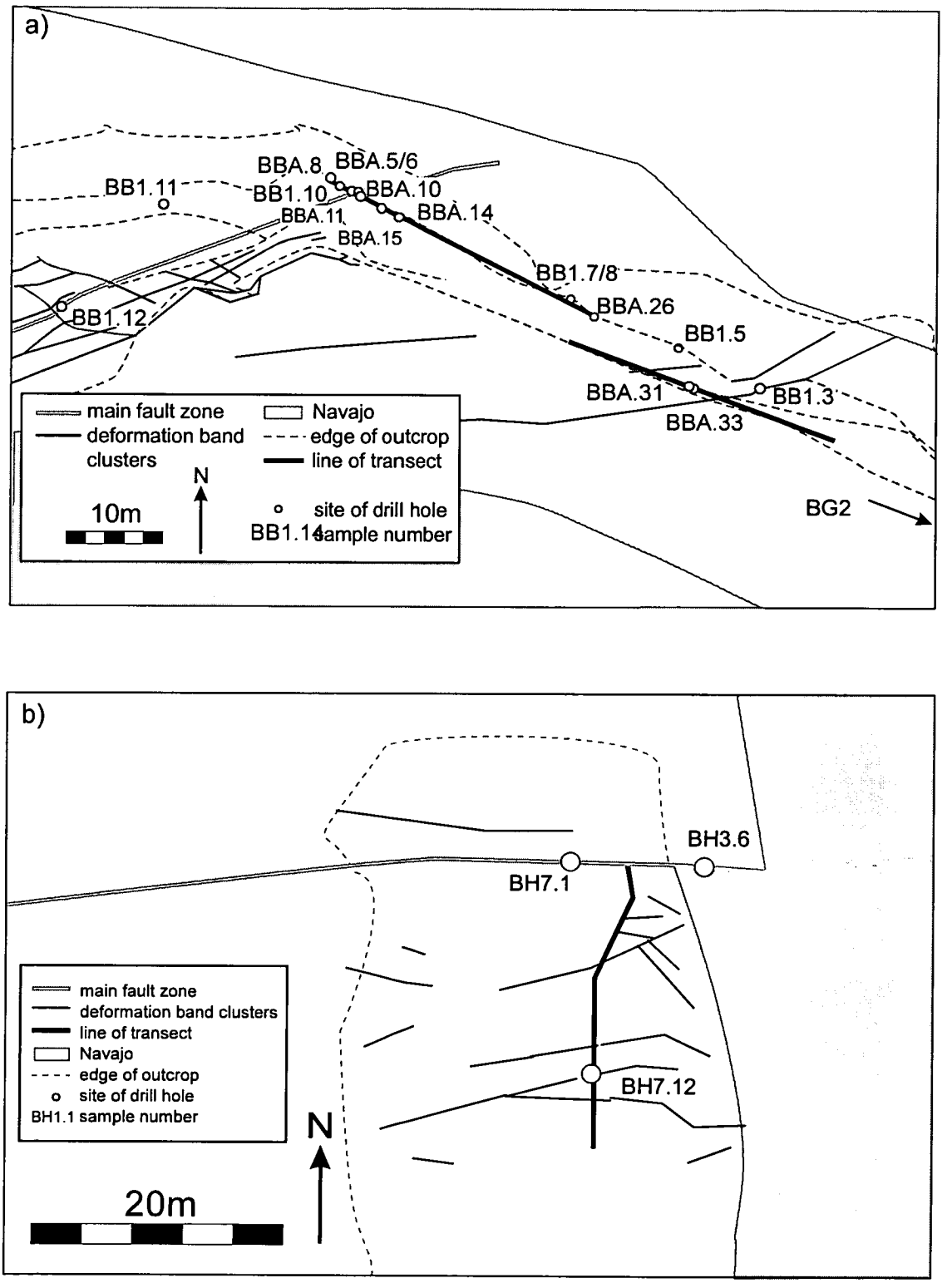

Figure 5.2. Location of samples for microstructure analysis and microfracture counts at a) the Blueberry fault Tip Canyon and b) the Cement Bridge locality. The line of the transects are shown.

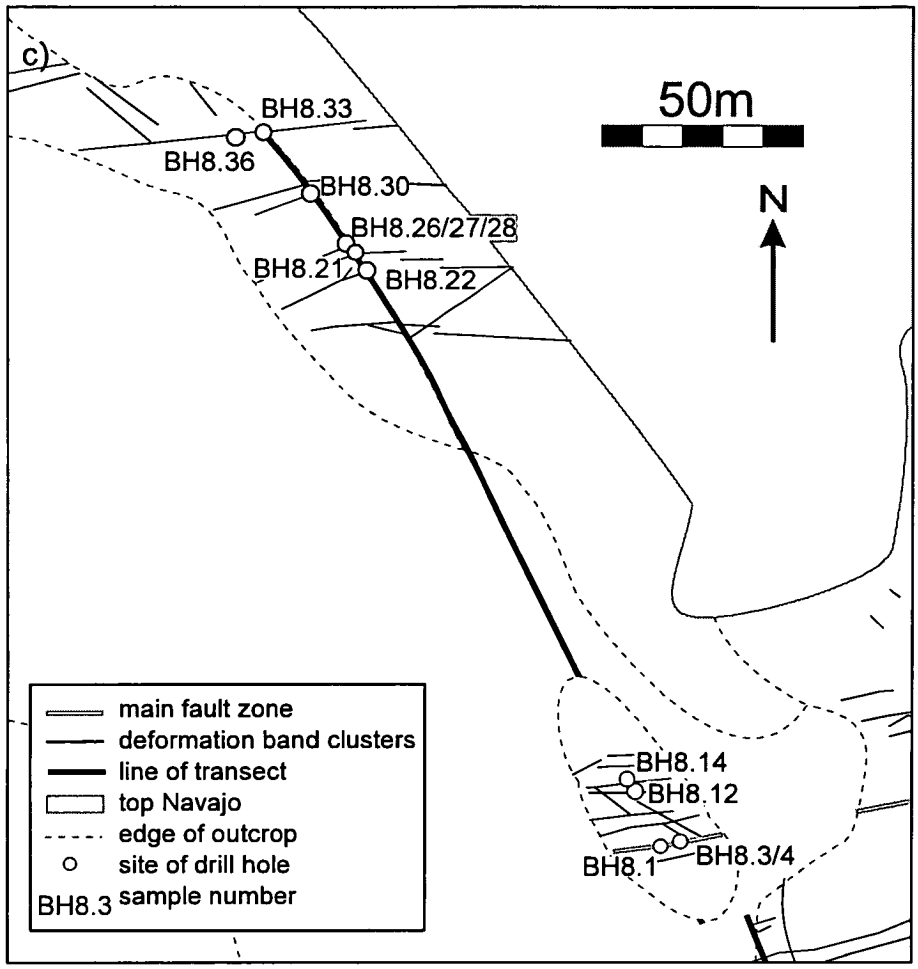

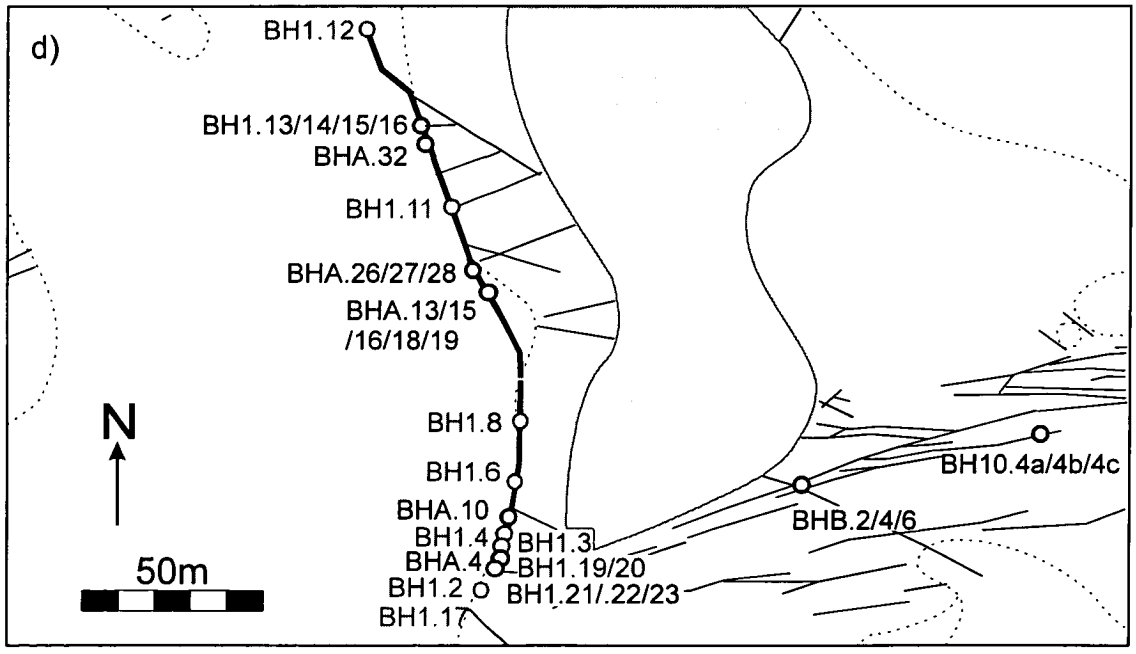

Figure 5.2. (cont.) Location of samples for microstructure analysis and microfracture counts at c) Juniper Flat and d) Jan's Cliff. Key to symbols is in 5.2c.

locality	sample no.	description	displacement	dist. from fault	
Tip Canyon	BB1.3	single	1 mm	50	fw
d=0 m	BB1.5	brown staining	30 mm	41	fw
	BB1.7	single	62 mm	26	fw
	BB1.10a	slip surface		0	
	BB1.10b	slip surface		0	
	BB1.11	tip of single	0 mm	6	hw
	BB1.12	slip-surface		0	
	BB3.4	no def		-	hw
Cement Bridge	BH3.6	fault zone	9 m	0	
d=9.4 m	BH7.1	fault zone	9 m	0	
	BH7.5	tip	0 mm	1.7	fw
	BH7.12	single	34 mm	16.7	fw
Juniper Flat	BH5.1	single		15	hw
d=24.3 m	BH5.1a	single		15	hw
	BH5.2	no def		35	fw
	BH5.4	zone of bands		0	fw
	BH8.1	pod in fault zone	24 m?	0	
	BH8.3	into fault plane	24 m?	0	
	BH8.4	into fault plane	24 m?	0	
	BH8.12	zone of bands		20.6	hw
	BH8.14	single		20.3	hw
	BH8.17	zone of bands		22.9	hw
	BH8.21	wide part of single	53 mm	147	hw
	BH8.22	single	53 mm	147	hw
	BH8.26	single	3 mm	148	hw
	BH8.27	zone of bands	650 mm	150	hw
	BH8.28	single	15 mm	150	hw
	BH8.30	tip of single	0 mm	169	hw
	BH8.33	zone of bands	1.21 m	177	hw
	BH8.36	slip-surface	1.21 m	177	hw
Jan's Cliff	BH1.13	wide single		89	hw
d=23.5 m	BH1.14	thin single		89	hw
	BH1.15	zone of bands		91	hw
	BH1.16	zone of bands		91	hw
	BH1.21	within fault zone		0	
	BH1.22	within fault zone		0	
	BH1.23	within fault zone		0	
Penguin Mesa	BH10.4a	fault		-	
d=22.9 m	BH10.4b	slip-surface		-	
	BH10.4c	wall rock		-	
	BHB.2	in fault zone		0	
	BHB.4	in fault zone		0	
	BHB.6	in fault zone		0	

Table 5.1. Samples used for analysis of deformation band microstructure. Samples are arranged into localities and the description, displacement on the deformation band and the distance into the hangingwall (hw) or footwall (fw) for each deformation band is given. The displacement at each locality is indicated.

underestimate will be consistent for all samples and it is the form of the decay of microfracture densities away from the fault that is of interest in this case, rather than the absolute densities. In any case, different observers will have different criteria for recognising microfractures, so that a direct comparison between studies is difficult. However, the microfracture densities in this study compare well with data from the same rock type presented in Anders and Wiltschko (1994) using a U-stage (see Figure 5.25).

5.3. Results

5.3.1. Host rock

A range of grain size, shape and lithology is seen in the undeformed host rock (Figure 5.3a and 5.3b). From point counting, the average host rock consists of 76% quartz, 5% feldspar and 19% porosity. In general, the host rock at the Blueberry fault is characterised by larger, rounder grains, more lithic fragments, and more obvious stratification than the host rock of the Big Hole fault. The porosity in the host rock ranges from 13.5-25%. Much of this variation is due to differences between the microfacies of the aeolian sandstone. Calcite cement is common in the Navajo Sandstone, and is especially well developed at the Juniper Flat and Cement Bridge outcrops. Very little quartz cementation is seen in the Navajo Sandstone in this field area. This is possibly due to the clay rims on the grains, which would inhibit the development of quartz overgrowth cements.

Microfractures can be seen under an optical microscope or BSEM as lines of fluid inclusions (Figure 5.4b). These have a purple or greenish tinge and often contain bubbles or even small crystals. When the microscope is focused in and out, the lines of bubbles that are in focus shift sideways, defining a plane. These fluid inclusions, or bubble planes, are characteristic of healed microfractures (a review of crack healing structures is given in Smith and Evans 1984). Under CL they can be seen as lines of dimmer luminescence (Figure 5.4b). This is because the microfractures have been healed by authigenic quartz; the brighter luminescence reflects a change in the

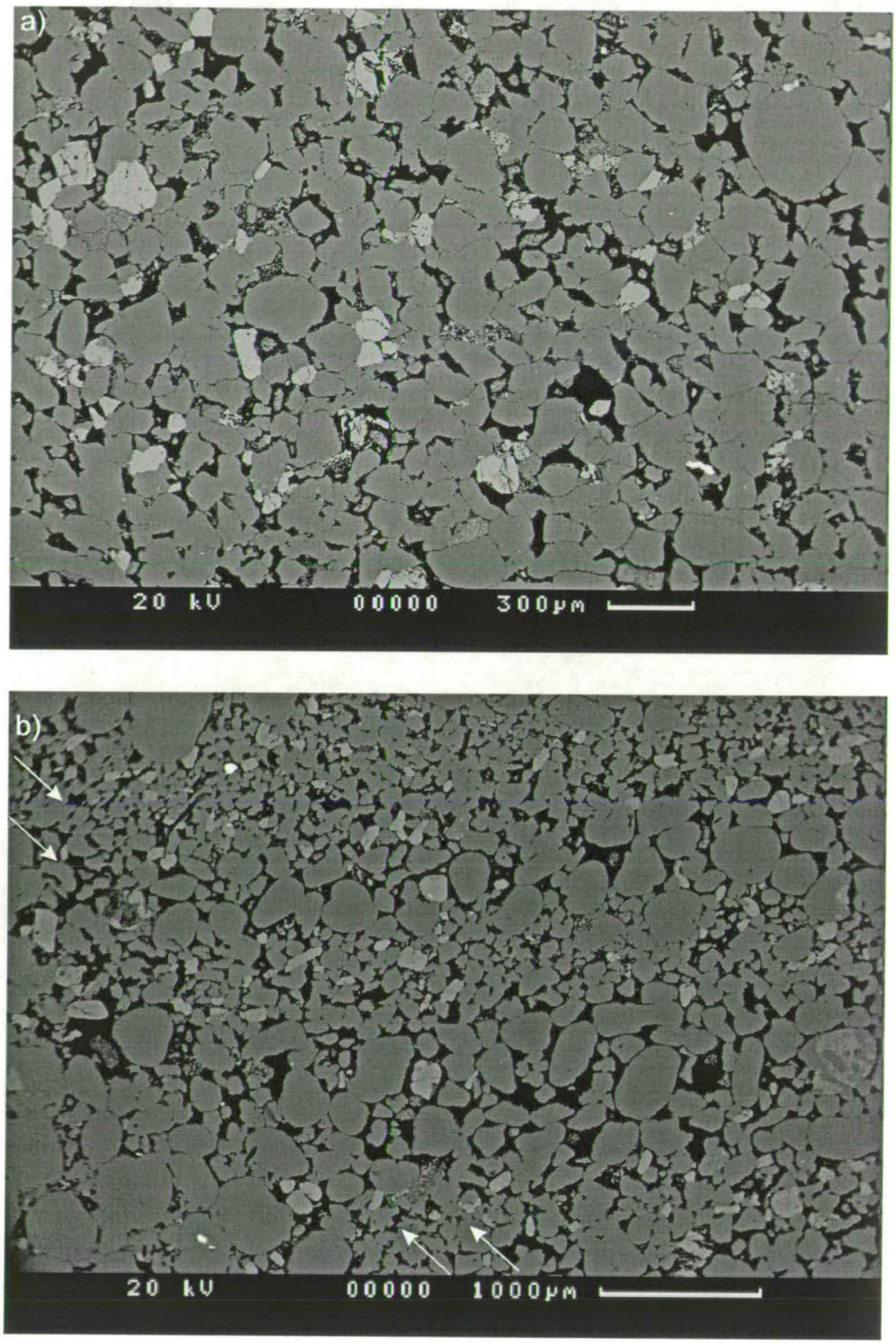

Figure 5.3. a) BSEM image of the host rock (sample BH8.12) at the Big Hole fault. b) BSEM image of the host rock at the Blueberry fault (sample BB3.1). Note the band of compaction with no grain crushing on the left-hand side of the image (arrows). Note the larger grain size at Blueberry fault.

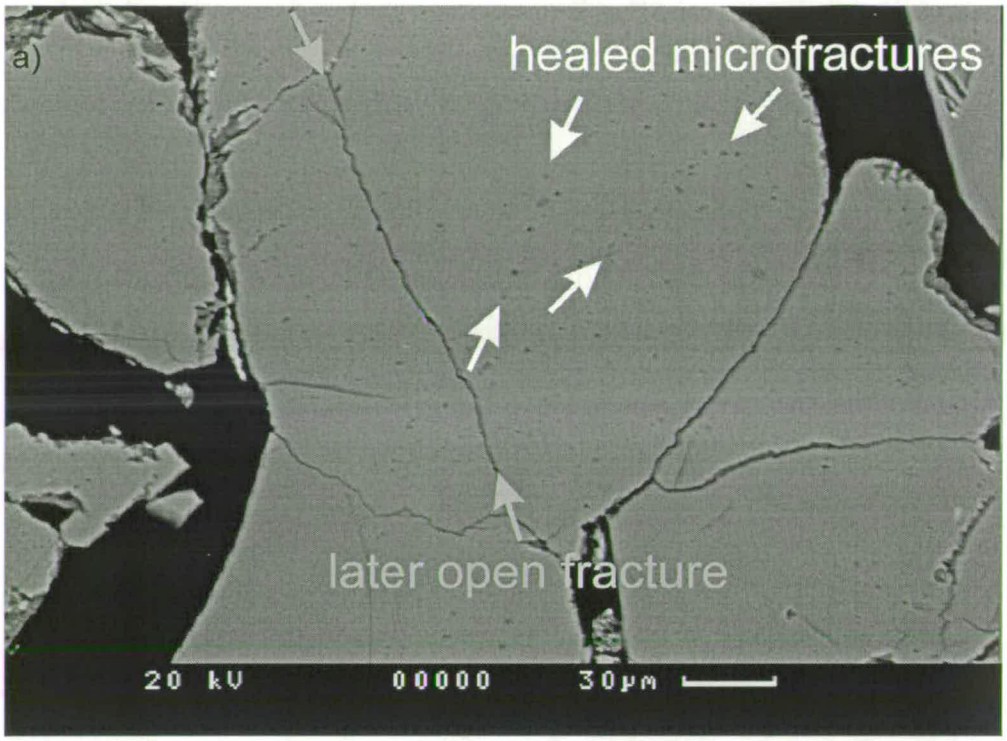

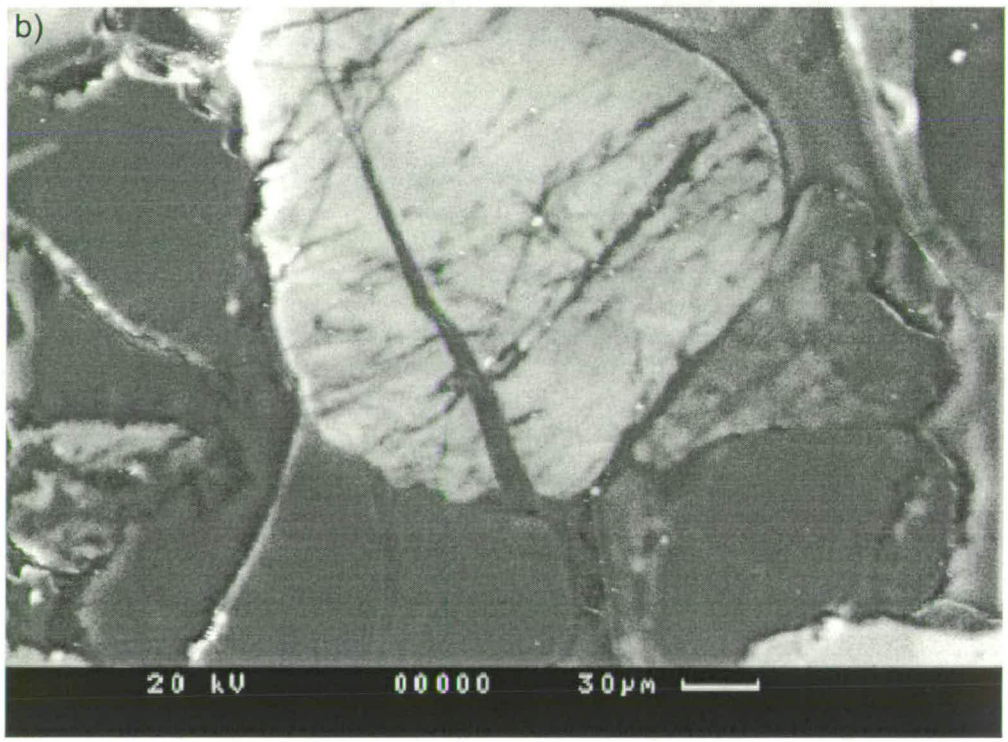

Figure 5.4. a) BSEM image of microfractures in a quartz grain (sample BH8.12). Healed microfractures (lines of fluid inclusions) are cross-cut by newer non-healed fractures. b) CL image of the same grain. Healed fractures have a different trace element composition from the original quartz grain, therefore a different degree of luminescence.

trace element composition of the quartz. Figure 5.4b shows healed bubble planes being cross-cut by a later open fracture.

The majority of microfractures are within the grains and do not cross between grains. The majority are straight, and do not appear to be controlled by the position of grain boundaries. In the few grains that have quartz overgrowths the microfractures can be seen to stop at the original grain boundaries and do not extend into the overgrowths (Figure 5.5) implying that diagenesis occurred later than the formation of these microfractures. All of these observations suggest that these are inherited microfractures.

Sample BB3.4 is an example of the type of deformation band that is always associated with soft-sediment deformation in this field area. Figure 5.3b shows this structure running top left to bottom right. The deformation band has little grain crushing and is mostly defined by a collapse of the available pore space.

5.3.2. Single-strand deformation bands

Single-strand deformation bands consist of broken, angular, grain fragments supporting relatively unbroken host-sized grains, in a narrow band approximately 1 mm wide. Figure 5.6 is a BSEM image showing a single-strand deformation band running from top left to bottom right. Feldspar grains in single-strand deformation bands are fractured, but the fragments do not appear to have moved a significant distance with respect to each other (Figure 5.7).

Single-strand deformation bands have reduced grain size and have a wider range of grain sizes. The reduced sorting means that the grains are more tightly packed than the host rock so that the deformation band has reduced porosity. The porosity in single-strand deformation bands varies from 2-12%. The lowest porosity seen in a single strand deformation band was in BH5.1. Some single-strand bands have zones of brown (hematite) cement restricted to the edge of the band. This cement may have been concentrated by fluid flow adjacent to these low porosity structures (Section 2.3.1).

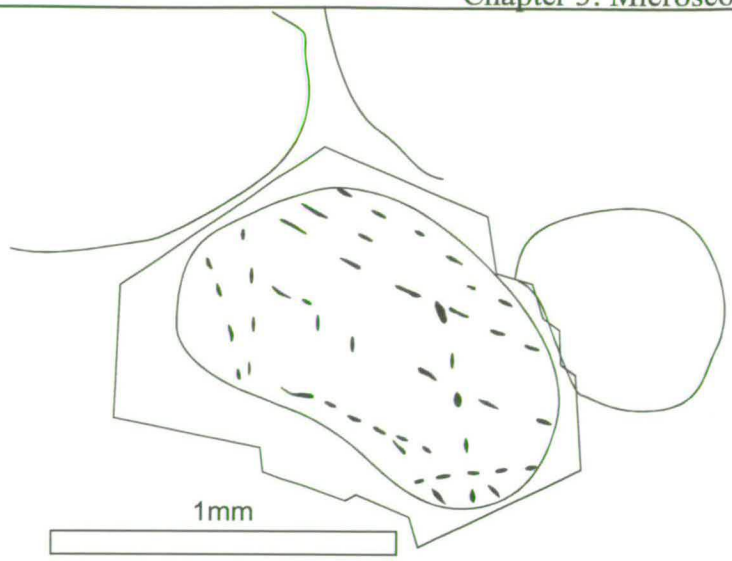

Figure 5.5. Sketch of a quartz grain with authigenic overgrowth from sample BH1.19. Healed microfractures are marked by lines of bubbles but do not extend into the overgrowth.

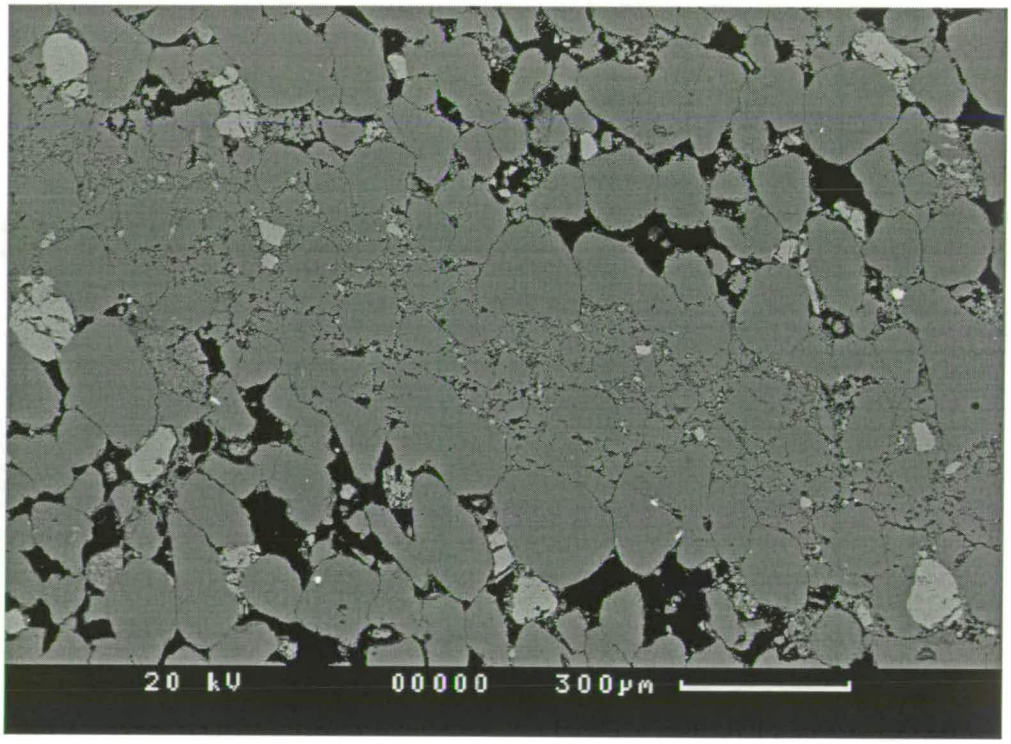

Figure 5.6. BSEM image of a single strand deformation band (sample BH5.1).

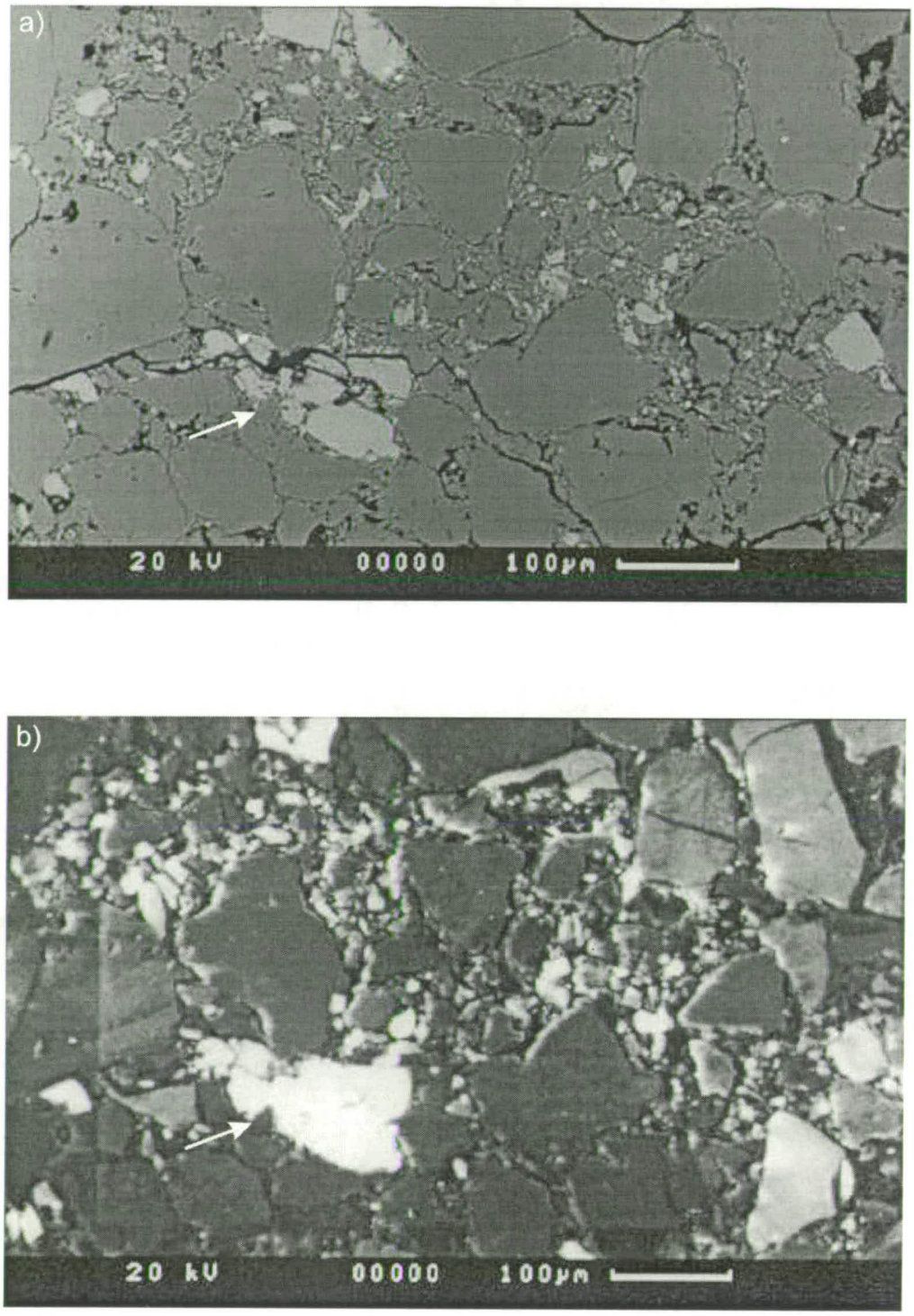

Figure 5.7. a) BSEM and b) CL images of grains in a single-strand deformation band. The CL image shows that few microfractures are seen within these bands. Some feldspar grains have been disaggregated, but the fragments have not moved a significant distance with respect to each other (example arrowed).

5.3.3. Zones of deformation bands

Zones of deformation bands consist of several anastomosing bands of angular, crushed grains. In Figure 5.8 two strands can be seen with undeformed rock between them. Large grains are often supported in a matrix of much smaller grains (Figure 5.9). Feldspars within these bands have been intensively deformed and appear as elongate groups of feldspar fragments (Figure 5.10). Porosity in zones of deformation bands varies from 2-10.8%.

The porosity of relatively undeformed pods of host rock between the strands in zones of deformation bands is 7-14%. These pods have little or no grain crushing so the majority of the porosity loss must occur by compaction and re-organisation of the grains.

Figure 5.11 is a close up of a grain in Figure 5.9. In BSEM it looks like a single grain with very uneven boundaries. In CL however, original grain fragments (pale grey) can be distinguished from authigenic quartz cement (dark grey). It appears that this grain has been crushed and then healed in situ. This indicates that some fluids must have been moving through these structures as they formed. Figure 5.12 shows that these healed, crushed grains are often confined to the outer parts of deformation bands.

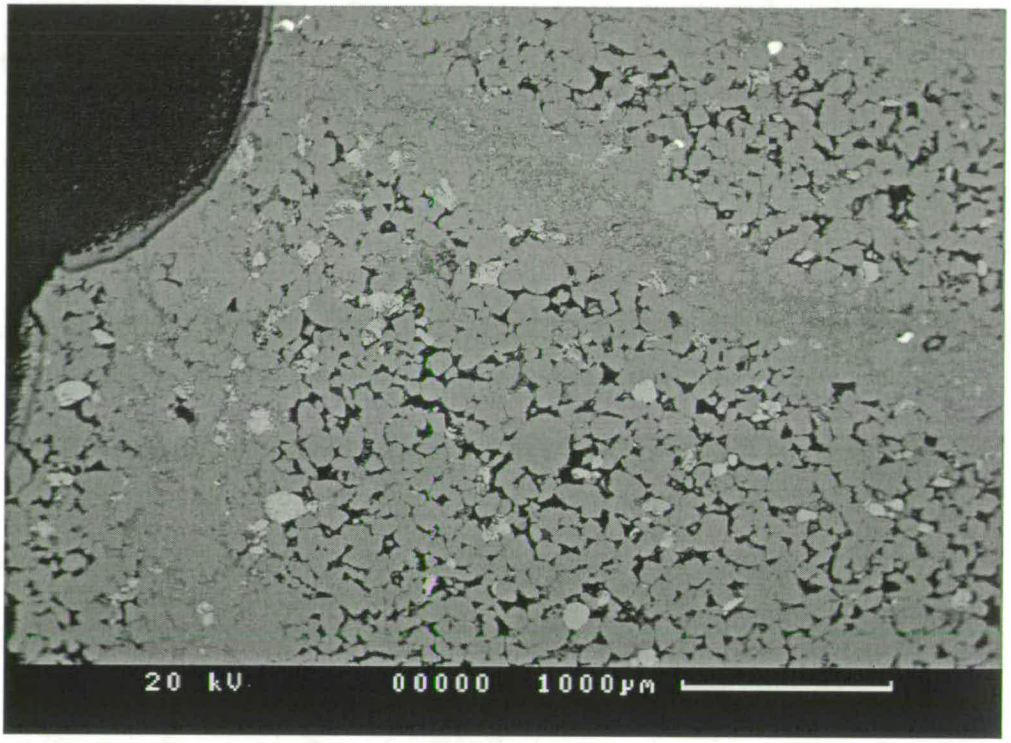

Figure 5.8. BSEM image of two strands within a zone of deformation bands (sample BH8.36).

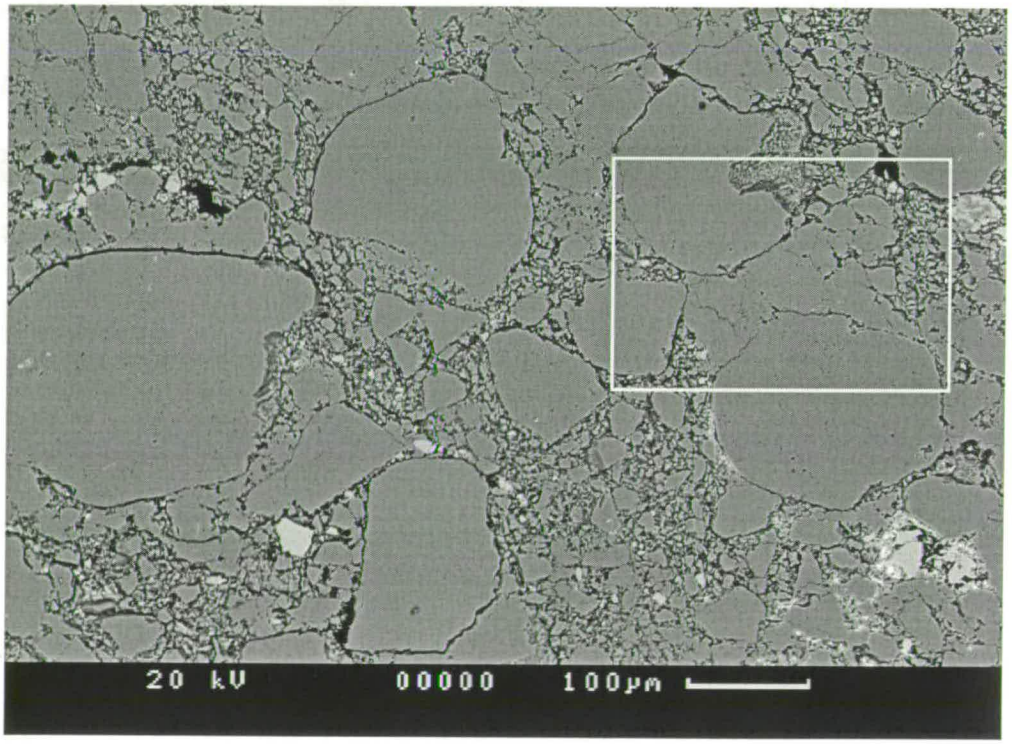

Figure 5.9. BSEM image of the structure of a strand within a zone of deformation bands (sample BH8.12). Larger, unbroken, grains are supported by smaller, crushed, grains. The rectangle shows the area of Figure 5.11.

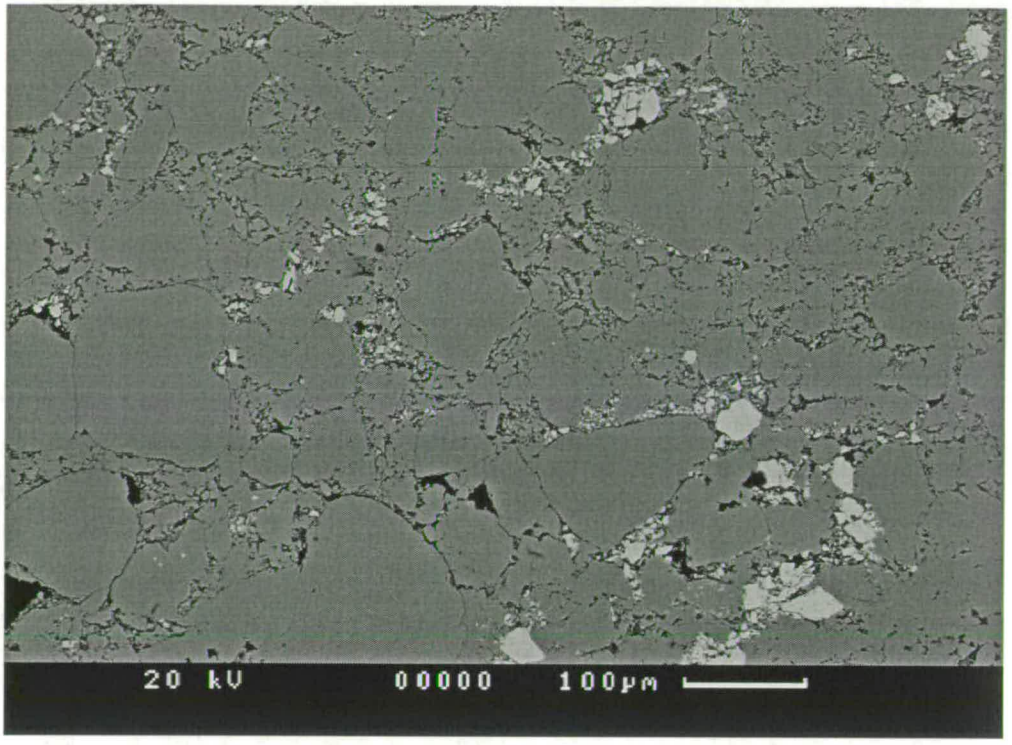

Figure 5.10. BSEM image of a strand within a zone of deformation bands (sample BH5.4). Note the strung out pale grey feldspar grains.

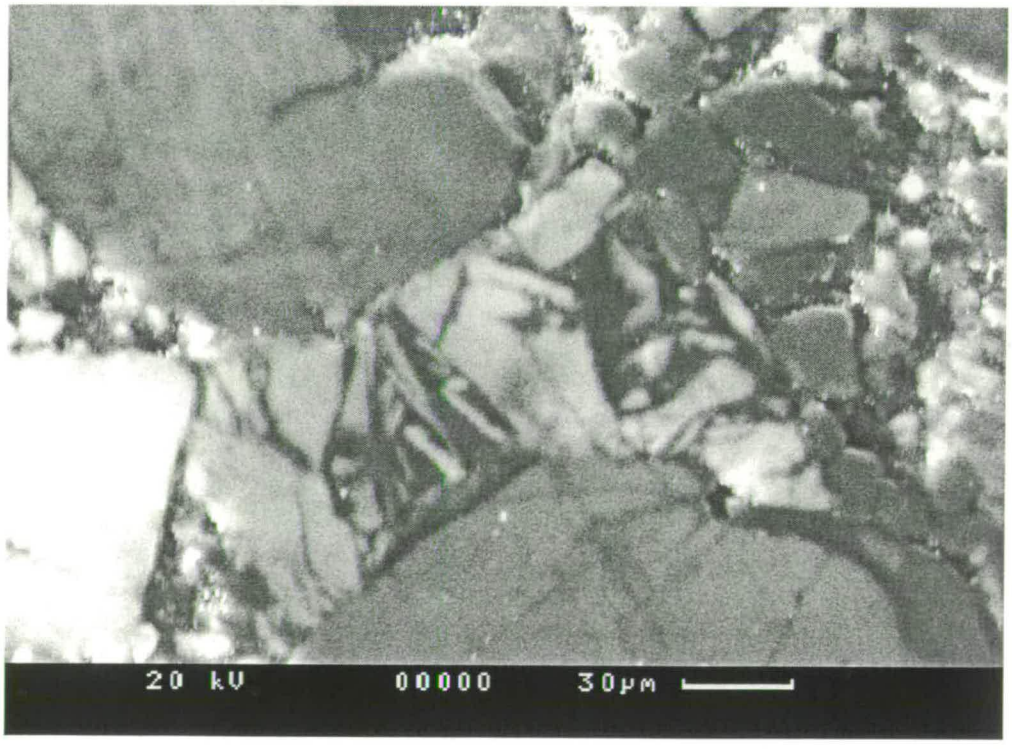

Figure 5.11. CL image of the square area in Figure 5.9. The pale quartz grain in the centre of the image has been crushed, and healed in-situ by the dark authigenic quartz cement.

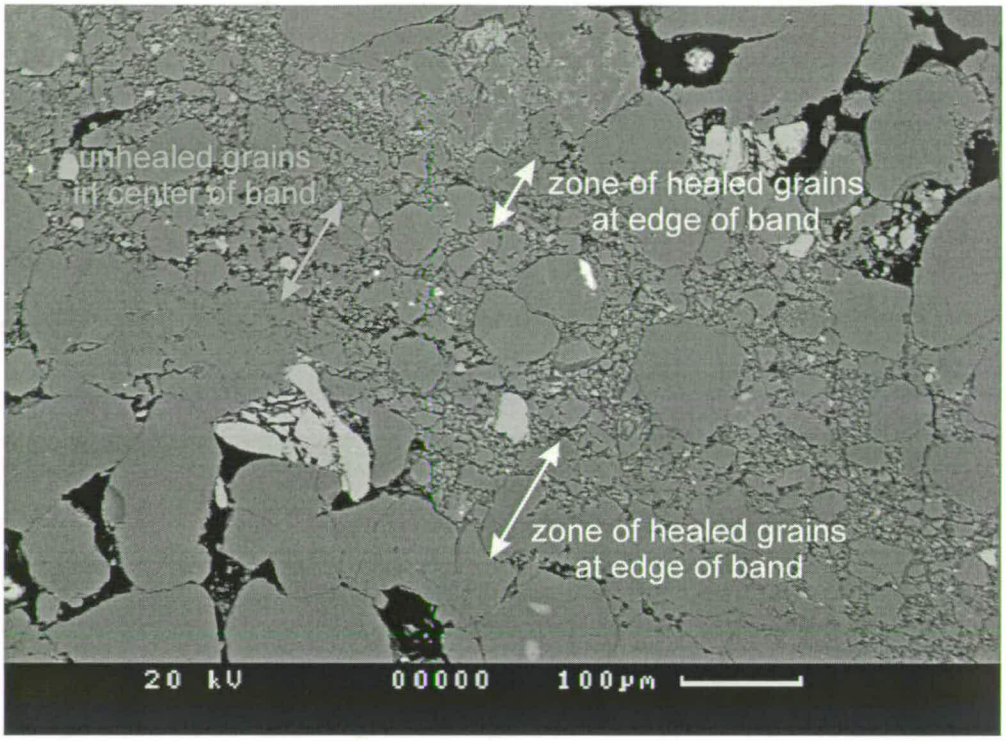

Figure 5.12. BSEM image of a strand within a zone of deformation bands (sample BH8.36). Crushed grains that have been healed are confined to the edge of the band.

5.3.4. Slip surfaces

Slip-surfaces are always located within highly crushed zones (Figure 5.13). These zones are usually between 1 and 2 mm wide. Within these zones large apparently undeformed grains are preserved. Porosity adjacent to slip-surfaces varies from 0.5-3.8%. Crushed feldspar grains deformed into elongate groups of feldspar fragments within these zones (Figure 5.14). This implies that these grains have been sheared out after they were crushed.

The smallest offset band that contains a slip-surface is BB1.10a/b. Figure 5.15 shows this slip-surface within the crushed zone. The amount of grain crushing looks to be similar in both of these samples even though the sample in Figure 5.13 has substantially more slip across it than that in Figure 5.15 (see Section 5.5.1).

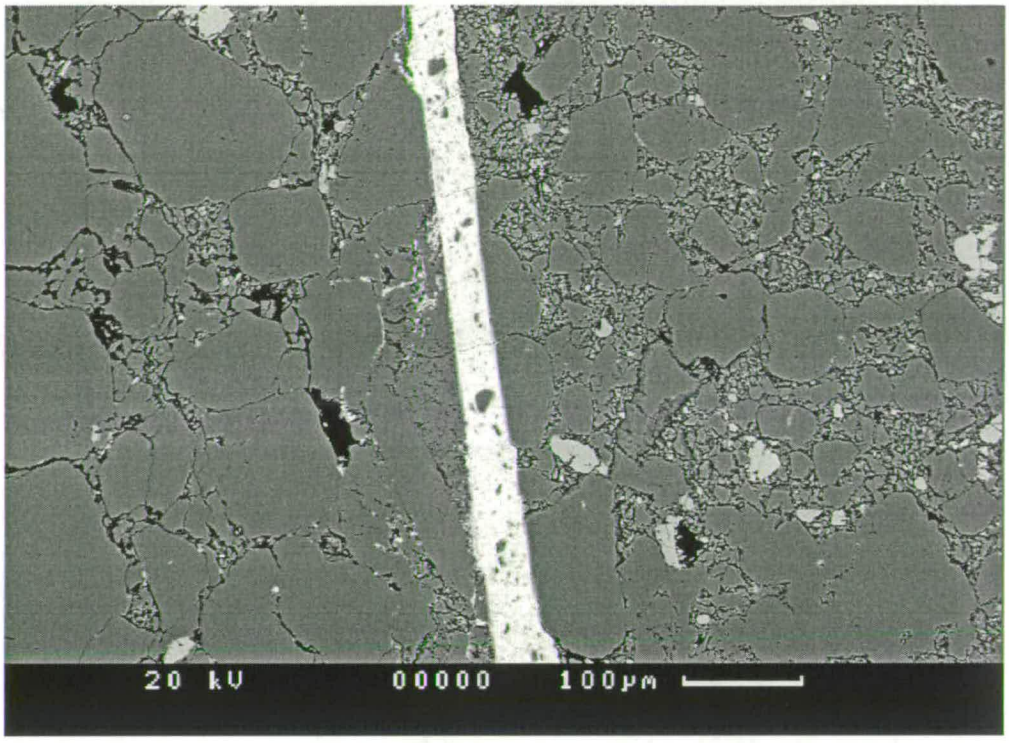

Figure 5.13. BSEM image of a cemented (white) slip-surface in sample BH8.4. Slip-surfaces always occur within zones of intense comminution.

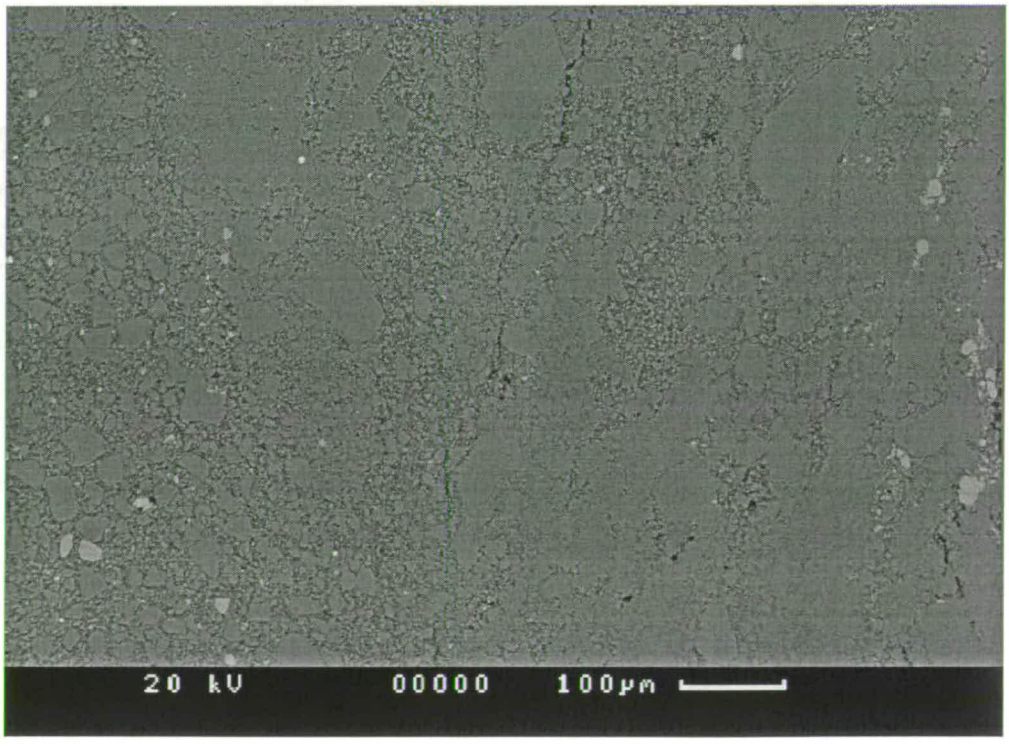

Figure 5.14. BSEM image of a slip-surface within a zone of intense comminution (sample BB1.10). Note the strung out pale grey feldspar grains at the right-hand side of the image.

5.3.5. Fault planes

BH8.3 and BH8.4 are samples through the fault plane that is assumed to have accommodated the majority of the 24 m displacement at the Juniper Flat outcrop. Both the samples cut through the green glassy material described in Section 4.4.4. Despite the proximity to a major slip surface, intact grains are still seen. It can be seen that individual grains have been planed off as displacement was accommodated along this surface (Figure 5.16). The fault plane occurs within a zone of bands and is surrounded by a highly crushed zone about 2 mm thick. Porosity in this zone is 2.6%.

More microfractured grains are seen adjacent to the faults than in zones of deformation bands with less displacement (Figure 5.17) and many of these are unhealed microfractures. Unhealed microfractures immediately adjacent to the fault in the hangingwall are at an angle of 36° to the downwards pointing slip vector. Bands of highly comminuted grains occur at angle of 15° to the main fault within the this zone of cataclasis (Figure 5.18).

At this locality the fault contains some cement. This looks brown in hand specimen and appears pale grey on BSEM images (to the left-hand side of Figure 5.16a). The composition of this cement is unclear, but a preliminary analysis indicates that it contains sulphur, phosphorous and aluminium. The cement does not appear to be deformed, though as the sample split along the fault when it was collected this is difficult to determine.

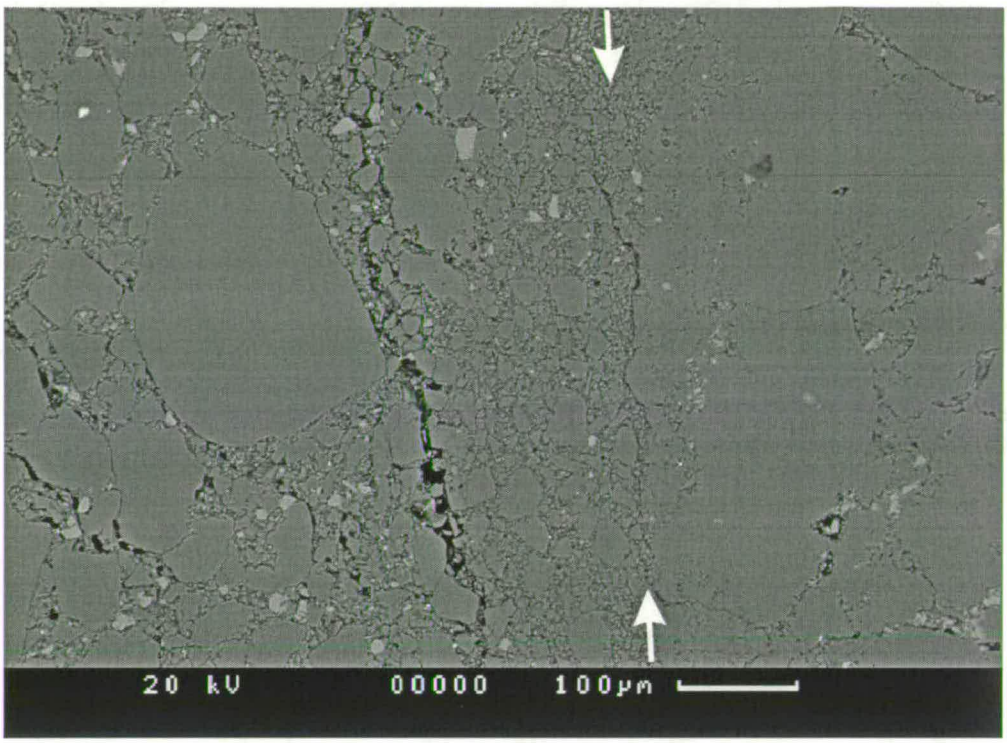

Figure 5.15. BSEM image of the slip-surface at the tip of the Blueberry fault marked by arrows (sample BB1.10).

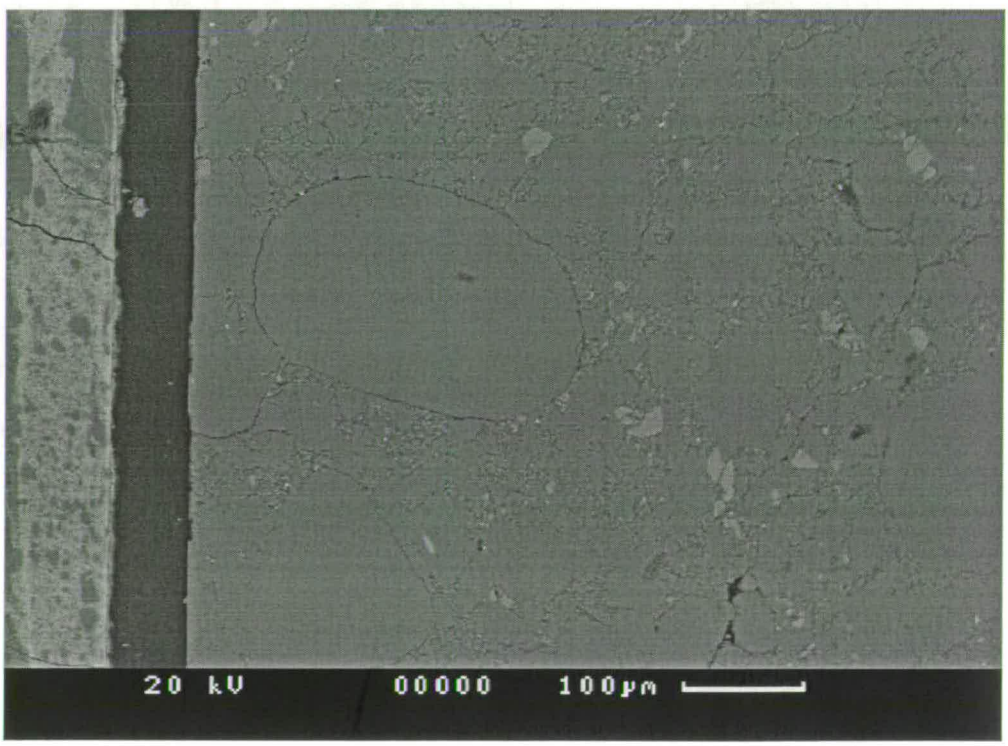

Figure 5.16. BSEM image of the fault plane at Juniper Flat (sample BH8.3, displacement = 24 m). The sample broke along the fault surface; the black stripe is the epoxy where the sample has been glued together.

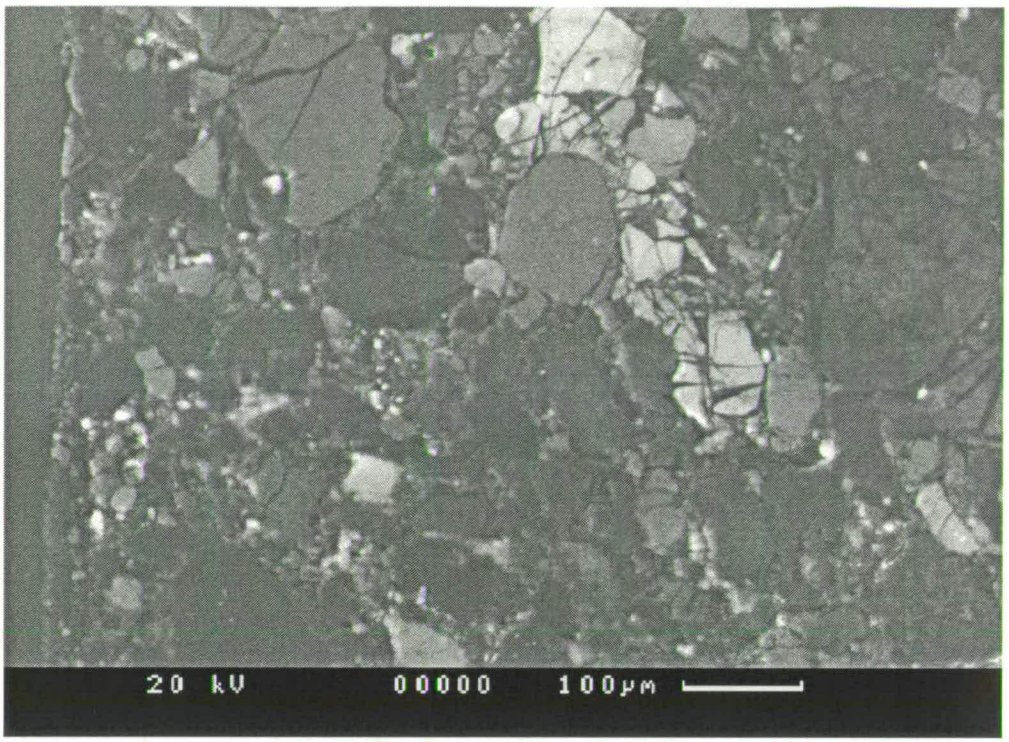

Figure 5.17. CL image of microfractures in the crushed zone adjacent to the fault plane at Juniper Flat (sample BH8.3).

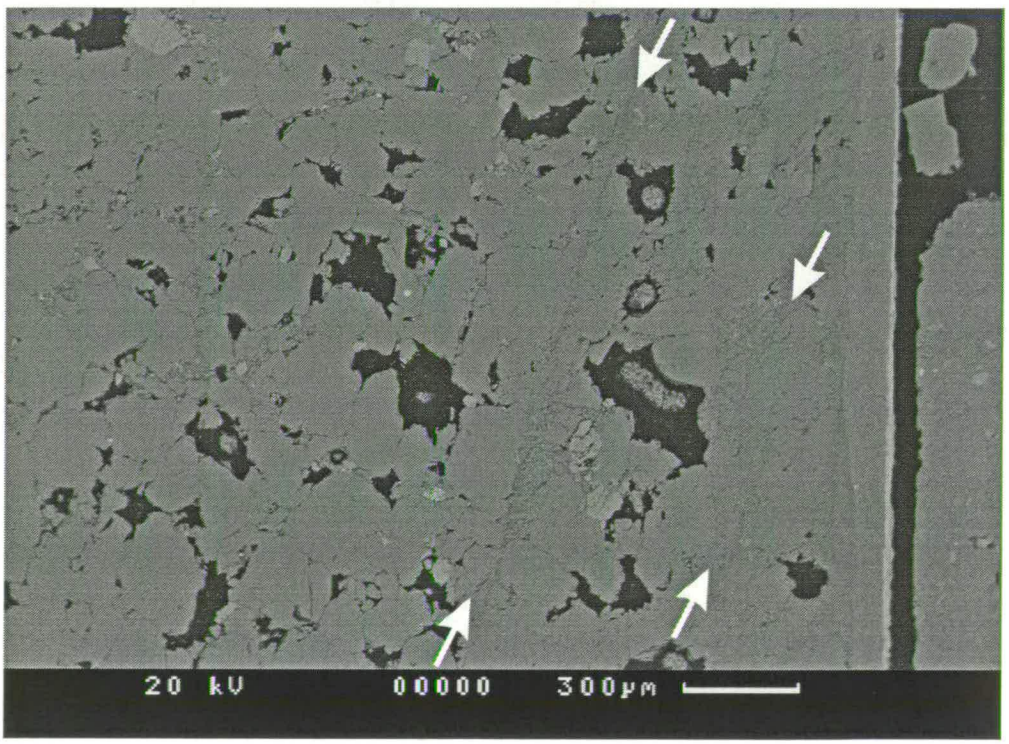

Figure 5.18. BSEM image of subsidiary (Reidel?) shear structures (arrows) in the crushed zone adjacent to the fault plane at Juniper Flat (sample BH8.3).

5.3.6. Microfracture density

The results of the density counts for all six sample suites are presented in Table 5.2. The average microfracture density defined by all the samples is 9.65 mm^{-1} with a standard deviation of 2.10. No significant difference was seen between the numbers and densities of microfractures in the samples that were oriented correctly and those that were oriented randomly. This indicates that the orientation of the sample has little effect on the microfracture count.

Microfracture densities for samples adjacent to deformation bands (0.5 - 1 cm from deformation bands) are shown in Table 5.3. The average microfracture density for all the samples is 12.47 mm^{-1} with a standard deviation of 3.33.

sample no.	description	short	long	average
BH8.3	host to fault	-	-	13.60
BH8.3	host to fault	-	-	14.05
BB1.10	zone of bands	-	-	12.54
BH8.12	zone of bands	9.22	5.83	7.52
BH8.22	within single	-	-	5.11
BH8.22	next to single	10.72	17.71	14.22
BB1.3	single	11.72	17.71	14.72
BH5.1	single	16.52	15.26	15.89
BH8.30	host (tip)	13.91	16.32	15.11

Table 5.3 Results of microfracture counts for samples adjacent to deformation bands around the Big Hole and Blueberry faults. If only an average is given, only one count was taken.

sample no.	distance (m)	short	long	average
Samples normal to fault surface and parallel to slip vector				
BHA.4	3	13.33	11.67	12.50
10	15	9.67	9.67	9.67
13	77.9	11.33	11.00	11.17
15	79.05	8.33	9.33	8.83
16	79.2	9.33	12.33	10.83
18	79.55	9.67	7.33	8.50
19	79.8	10.67	8.00	9.33
26a	85	12.33	10.00	11.17
26b	85.9	12.67	7.67	10.17
27	86.35	9.67	9.00	9.33
28	86.85	10.33	12.00	11.17
32	123.2	7.67	9.33	8.50
BG2.1	465	10.67	9.00	9.83
2	448	9.33	8.00	8.67
4	269	9.67	9.67	9.67
5	218	9.00	8.33	8.67
BHB.2	0	12.67	7.67	10.17
4	0	6.33	11.33	8.83
6	0	12.00	11.67	11.83
BBA.5	1.93	16.33	11.67	14.00
6	2.1	9.00	8.67	8.83
8	2.7	13.33	18.33	15.83
10	0.23	10.33	12.00	11.17
11	0.5	11.00	10.33	10.67
14	3.45	13.33	13.00	13.17
15	5.75	10.00	9.67	9.83
26	30	9.33	7.33	8.33
31	44	10.67	14.67	12.67
33	44.45	11.00	13.00	12.00
Randomly oriented samples				
BH1.20	0.02	10.67	7.67	9.17
19	0.495	7.67	12.00	9.83
2	0.96	6.33	9.33	7.83
17	5.52	7.67	7.67	7.67
3	6.96	6.00	7.00	6.50
4	9.96	8.00	9.67	8.83
6	25.02	6.00	10.00	8.00
8	42.35	7.00	10.00	8.50
11	106.15	10.67	9.00	9.83
12	155.6	6.00	7.33	6.67
BH2.1	42.6	6.00	8.00	7.00
3	12.17	8.00	4.33	6.17
8	2.85	7.67	6.00	6.83
9	0.1	5.33	8.00	6.67

Table 5.2. Results of microfracture counts for 43 samples of the host rock around the Big Hole and Blueberry Faults. Two transects of each slide were made, one parallel to the long axis of the slide and one parallel to the short axis. The average microfracture density for all samples is 9.65 mm^{-1} with a standard deviation of 2.10.

5.4. Interpretation

5.4.1. Porosity and grain size reduction

A correlation between the porosity and the amount of grain crushing can be observed in many studies of deformation band microstructure (Fowles and Burley 1994, Mair 1997). Grain size reduction will not result in a reduction of porosity unless the shape, sorting and packing also change, but it can be seen from the photomicrographs that this is the case. From the reduction of porosity in the pods between deformation bands it can be seen that some pore collapse has occurred by shear along grain boundaries, possibly enhanced by clay coatings on the grains (Figure 5.9). However the detailed point counts of deformation band microstructure show that the reduction of sorting in deformation bands is linked to a reduction of porosity. Therefore the porosity, which is easier to quantify, is taken as a proxy for grain crushing.

Figure 5.19 shows the porosity of samples arranged according to the deformation type. The average porosity for each deformation type is shown as a shaded bar. The average host rock porosity is 19.2%. This is typical of the Navajo Sandstone (Dunn *et al.* 1973). The average porosity for single-strand deformation bands (7.9%), zones of deformation bands (7.4%) and slip-surfaces (1.5%) successively decreases. Rock from between two bands in a zone of deformation bands, which looks apparently undeformed in hand specimen (Figure 5.9), has a porosity of 11.9%. This is significantly lower than for the host rock. Mair (1997) also observed qualitatively that the porosity was lower in pods of host rock between bands, than for the host rock away from deformation bands.

Rock in the wall of slip-surfaces had the lowest porosity; however this does not correlate with the displacement on the slip-surface. The lowest porosity (0.5%) was seen on the slip-surface at the Blueberry fault tip, which has negligible displacement, and the rock adjacent to the slip-surface at Juniper Flat, which has in the order of 24 m slip, has 2.6% porosity. This can be see qualitatively in Figures 5.15 and 5.16. This indicates that increased displacement on a slip-surface does not necessarily result in a reduction of grain size adjacent to that surface.

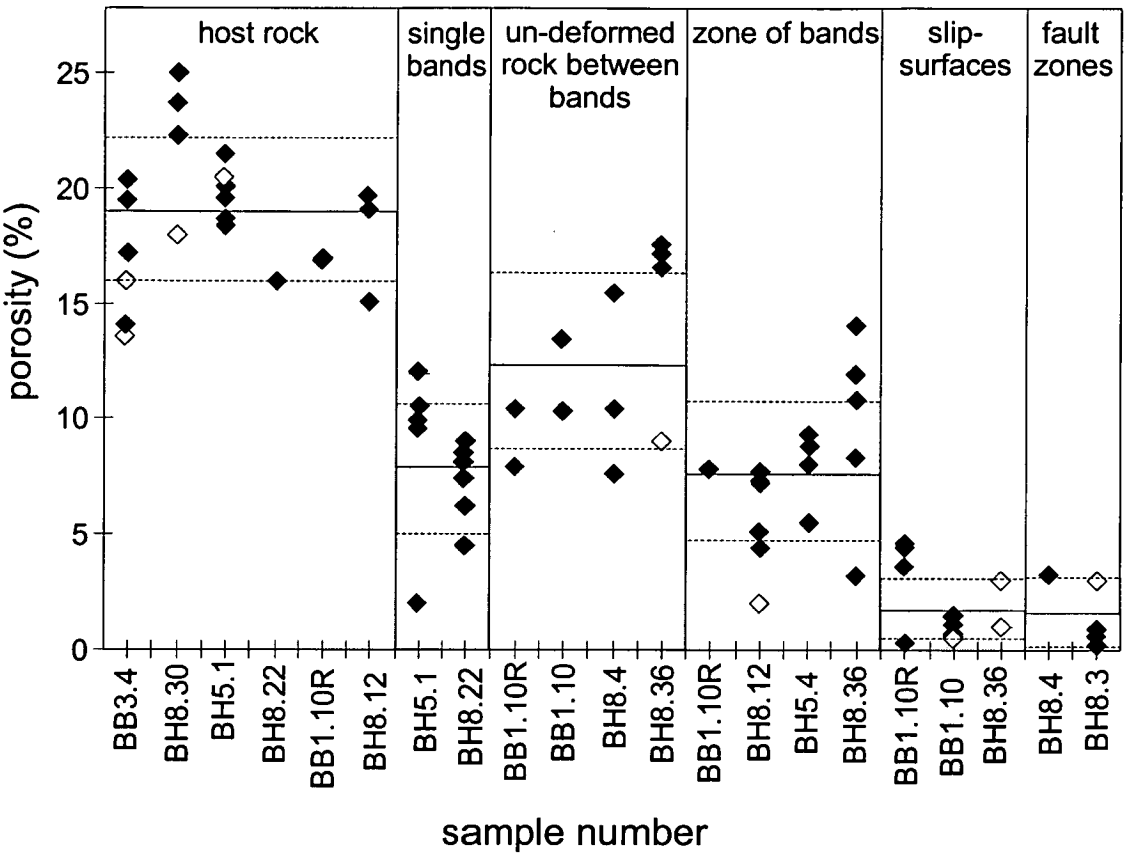

Figure 5.19. Porosity as a function of deformation band evolution. The samples are arranged according to deformation type. The column for each deformation type is shaded up to the value of the average porosity. The dashed lines represent one standard deviation either side of the average. Filled symbols are measurements made with Erdas Imagine, unfilled symbols are measurements made with Optimas.

5.4.2. Microfracture density

Figure 5.20a shows the average microfracture density for each location plotted against distance from the fault. The least squares best fit line is also shown but, given the extremely low value of the correlation coefficient, this is a poor representation of the data. The data is better represented by a constant microfracture density with distance from the fault. Figure 5.20b shows the microfracture density measured immediately adjacent to, and within, deformation bands during point counting compared to the host rock samples. The average microfracture density for each of the sample suites is shown. The average density for the deformation bands is higher than those in the host rock, though the two populations can not be distinguished at 95% confidence.

There is no consistent decrease in microfracture density with the value of the displacement on the fault at each site. Figure 5.21 shows the maximum, minimum and average values at each site plotted against displacement. The best fit line for the average microfracture density is essentially flat implying that the displacement on the fault has no correlation with the microfracture density.

The microfracture density does not correlate with the number of macroscopic deformation bands. Figure 5.22 shows the microfracture density profiles for the Blueberry fault tip canyon and Jan's cliff compared to the deformation band transects at those locations. The dotted lines on the graph show the standard deviation of all the sample values. The distribution of deformation bands seems to have little effect on the host rock microfracture density.

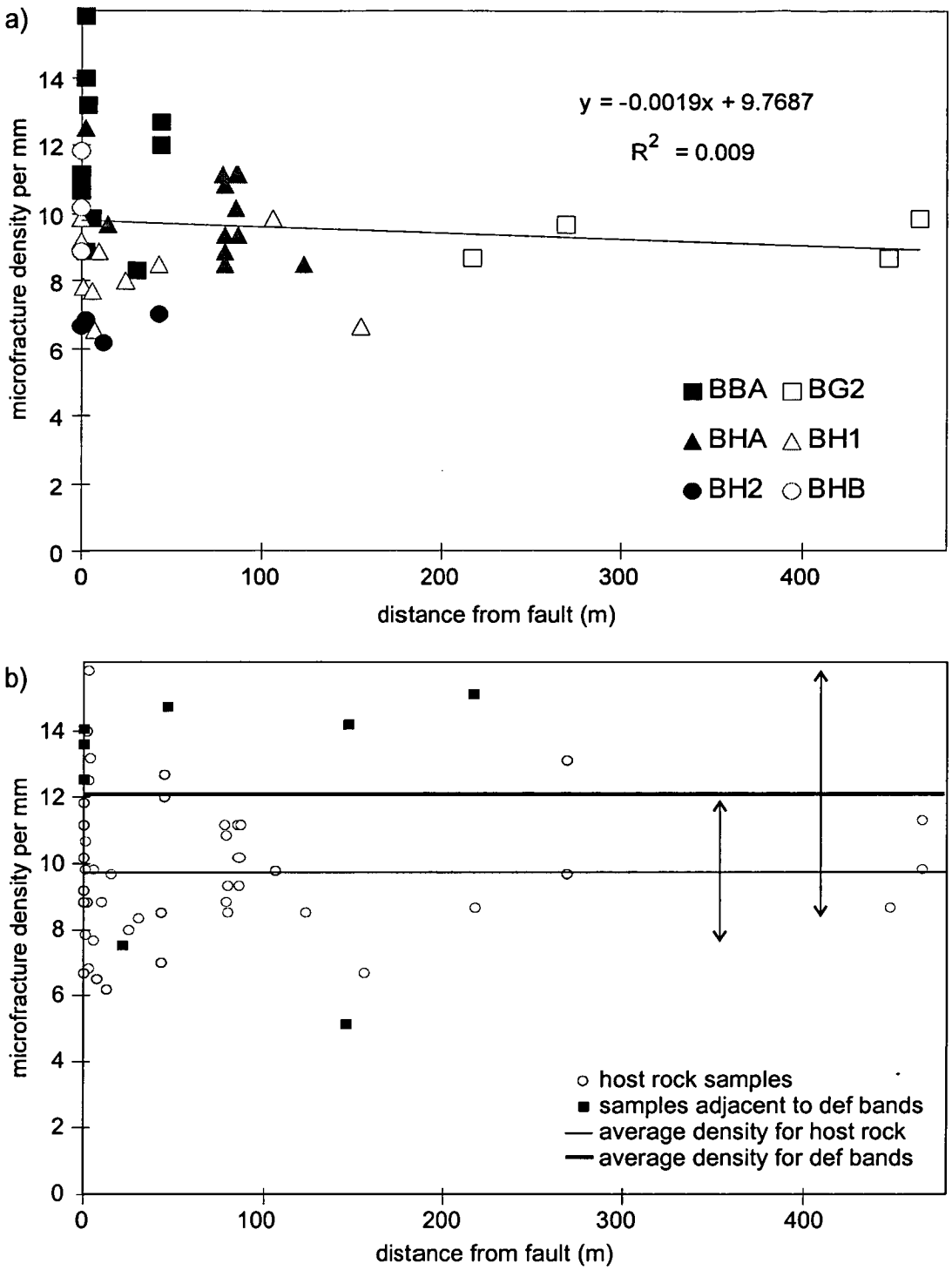

Figure 5.20. a) Microfracture densities per mm against distance from the main fault plane for the six host rock sample suites. The best fit line shows a very weak correlation, with poor statistical significance. b) Comparison of microfracture densities in the host rock and those adjacent to deformation bands (within 0.5-1 cm). The average microfracture density for the host rock and deformation bands are shown. The arrows indicate one standard deviation.

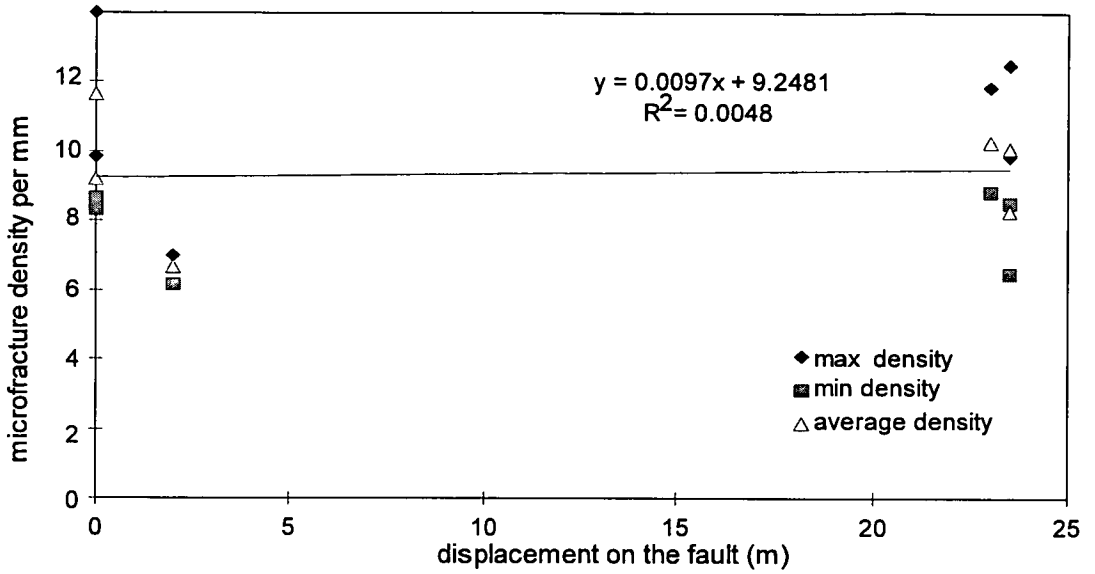

Figure 5.21. Maximum, minimum and average microfracture densities per mm against the displacement on the fault for the six sample suites. There is no significant change of microfracture density with the displacement on the fault.

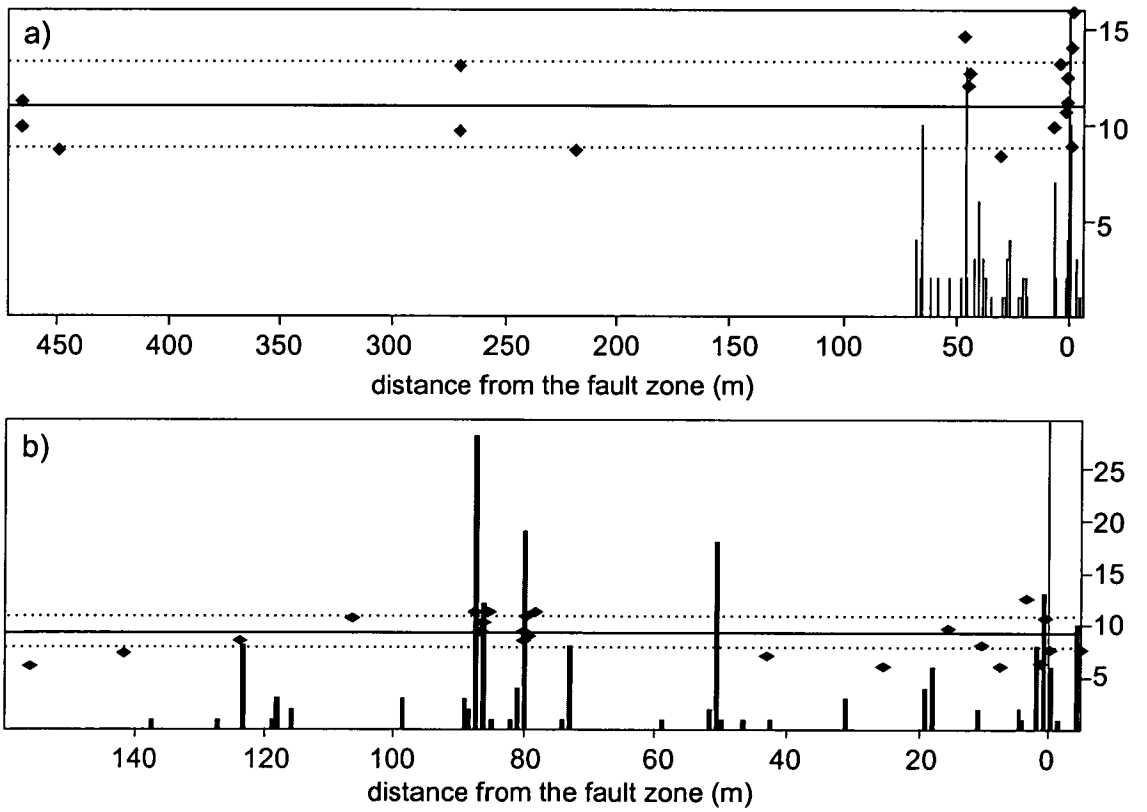

Figure 5.22. Comparison of microfracture density (diamonds) with the number of deformation bands per meter (bars) for two locations, a) the Blueberry fault tip and b) Jans Cliff. The solid line is the mean value for the data at each location and the dotted lines are at one standard deviation either side of the mean.

5.5. Discussion

5.5.1. Growth of deformation band clusters

The development of deformation bands from single-strands into zones of bands has been well documented (Section 2.3.1). The observations in this study confirm that the increase of displacement across zones of deformation bands is accommodated by the addition of new single bands with small increments of slip. The porosity of single bands and strands within zones of bands is essentially the same, showing that a finite amount of grain size reduction occurs in each strand of a zone of deformation bands. This agrees with well-documented relations between the displacement across a zone of bands and the number of strands within the zone (Aydin and Johnson 1978, Mair 1997). Mair (1997) also found that the mean grain size within deformation band strands was similar regardless of the bulk strain across the sample. This supports the observations made above and the correlation of porosity reduction with grain size reduction.

The distribution of fragments of fractured feldspar grains indicates that there is very little shear movement within single bands. Shear movement in cataclastic zones has been documented to produce rotation in the grain fragments (e.g. Engelder 1974, Cladouhos 1999). The grain fragments within the deformation bands in this study show no evidence of significant rotation. Feldspars in zones of bands and slip-surfaces appear to be more strung out than those in single bands. This could be evidence for a larger amount of shear movement along the bands, or could be an indication of the higher degree of grain crushing across these structures. Further work is required to investigate these relationships.

5.5.2. Slip-surface initiation

The model for the initiation of slip-surfaces put forward in Aydin and Johnson (1983) (Figure 2.8), did not distinguish if the increased amount of crushing around slip-surfaces was a precursor to slip-surface formation or occurred as displacement was accumulated. Sample BH8.27 contains a highly crushed zone that is not apparently

associated with a slip-surface. This indicates that some localised increase of granulation does occur within zones of deformation bands before slip-surface initiation. From the outcrop maps, it appears that slip-surfaces localise in small sections, usually associated with local thickening of deformation bands (e.g. Figure 4.11). In Section 4.5.4 it is suggested that slip-surfaces may form at a relatively early stage in the growth of a zone of deformation bands. This is backed up by the work of Mair (1997) who found slickenlines on the surface of experimentally generated deformation bands, at low values of axial strain. From outcrop-scale observations and microstructures, it would appear that slip-surfaces can nucleate in small patches and then propagate and link up to form an inosculating network of slip-surfaces. This interpretation is substantially different from previous models for deformation band and slip-surface evolution, which have tended to focus on the two-dimensional evolution of structures up to the point of slip-surface nucleation (Aydin and Johnson 1978, Antonellini *et al.* 1994).

There is no significant increase in the degree of granulation with continued displacement on a slip-surface. Engender (1974) found a similar result from experimental studies of saw-cut samples with simulated gouge. Initially the gouge between the faces of the samples deformed by cataclastic reduction in grain size and sorting. Beyond a certain point there is no further increase in grain crushing. Mair (1997) found a constant mean grain size in experimentally produced deformation bands, regardless of the total bulk strain applied to the sample. She invoked a steady state grinding limit where a favourable grain size distribution is reached, and further displacement is accommodated solely by rolling and movement of the grains. The highly crushed bands running at angles to the fault are in the correct orientation to be Riedel Shears formed within the progressively deforming crushed zone (Figure 5.23c) (Logan *et al.* 1992).

The open microfractures adjacent to the main fault zone in this study (Figure 5.23a) are not in the correct orientation to have been formed by shearing within the crushed zone due to repeated slip along the slip-plane (Figure 5.23b). It is possible that these have occurred in response to rupture of a small part of the fault surface. A similar

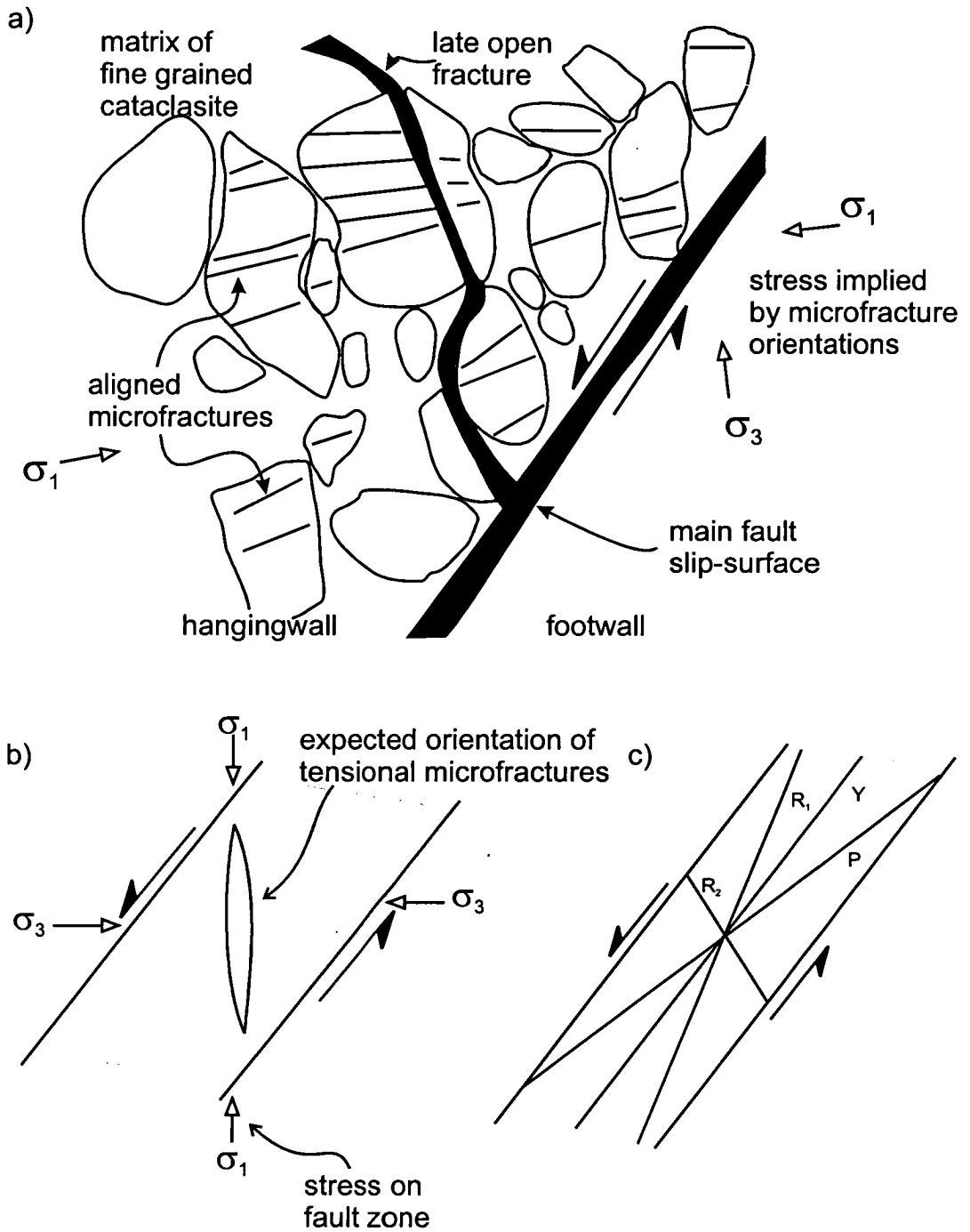

Figure 5.23. a) Sketch of microfractures in the highly crushed zone adjacent to the fault in sample BH8.3. b) Cartoon of the stress around a normal fault zone. The fault is initiated by vertical σ1 and horizontal σ3, but within the fault zone, σ1 is sub-horizontal and σ3 sub-vertical. This would not produce the microfractures seen in the sample above. c) The orientation of Reidel shears in the fault gouge. The structures seen in Figure 5.18 would correspond to the P shears.

effect has been seen by Vermilye and Scholz (1998). They studied the orientation of microfractures in detail and related these to the predicted stress orientation around a propagating fault. They found that cross cutting sets of microfractures were seen in different orientation, each of which could be related to a rupture propagating in a different direction along the fault surface.

The lack of any relationship between the offset on a slip-surface and the amount of grain crushing implies that the displacement on a slip-surface can not be estimated from its microstructural properties. The amount of grain crushing adjacent to the surfaces in Figures 5.15 and 5.16 is essentially indistinguishable, even though one has a very small amount of slip and the other has up to 24 m. Sammis *et al.* (1987) and Draper (1976) predicted from experimental work and theoretical models that the strain in a fault zone could be estimated from the particle size distribution. This study, and the results of Mair (1997), show that the sequential development of shear bands precludes such a possibility and confirms the observations of Draper (1976), who pointed out that discrete slip planes may accommodate displacements in excess of those indicated by the particle size distribution. This has important implications for studies of faults in porous sandstones where the outcrop size is limited, specifically in core studies. Specifically, if the offset of marker beds is greater than the borehole size, no estimate of offset can be made from the microstructural properties.

5.5.3. Fluid flow through deformation bands

The presence of authigenic quartz cement within deformation bands indicates that fluid was present in the band at some point. Large amounts of fluid are unlikely to have flowed through these structures given the large reduction of porosity (and hence permeability) that they represent. It is possible that the quartz is locally derived; the presence of fresh grain surfaces would make quartz available to solution whereas previously the grain boundaries had clay coatings. In addition, nucleation sites on freshly broken grains are energetically more favourable than on host rock grains. If this was the case then a high permeability is not necessary as the quartz would not

have to move far through the deformation band. The concentration of hematite cements adjacent to deformation bands would suggest that fluid flow has been concentrated at the margins of these structures. This would occur because of the reduced permeability of the deformation bands, and possibly because of a zone of increased permeability parallel to the bands due to early dilatancy (Antonellini *et al.*1994).

The evolution of slip-surfaces as described above results in anastomosing networks of slip-surfaces within the off-fault deformation which will potentially have an important influence on fluid flow. Slip-surfaces are often found as open fractures at the surface. Deformation bands have previously been modelled as having a reduced permeability perpendicular to slip-surfaces due to grain crushing, but an increased permeability in the plane of the slip-surface (Edwards *et al.* 1993, Antonellini *et al.* 1994, Antonellini and Aydin 1995). This effect would be enhanced where slip-surfaces are interconnected along-strike and down-dip. Samples from cores through the faults in this field area (Evans *et al.* 1999) have indicated that these structures are cemented at depth, consistent with the cement fills shown in Figure 5.13. However, it remains unclear to what extent these structures were once open fractures, and at which stage in the evolution of the fault zone the cement may have been deposited. There is no evidence for deformation of the fracture filling cements seen here, which would imply that they were introduced either during or after the deformation, but that no significant deformation has subsequently taken place.

Pods of relatively undeformed rock between strands of a zone of deformation bands have a reduced porosity. This will have an important effect on fluid flow. It has been suggested that the presence of these pods could result in a high permeability parallel to deformation band clusters (Antonellini and Aydin 1994). However these results indicate that, even ignoring the effects of along-strike linkage of deformation bands within an inosculating network, the reduced porosity within these pods would result in a retarded permeability parallel to deformation band clusters. The anastomosing nature of deformation band clusters results in the formation of compartments of relatively undeformed rock. This is illustrated by the difference in degree and colour

of staining in the small compartments within even a small zone of bands (Figure 5.24). That this fault type can form compartments at a larger scale is illustrated by Edwards *et al.* (1993) in the Hopeman Sandstone in Scotland. Here the faults control the distribution of quartz, calcite and fluorite cements, and secondary porosity is much decreased towards the fault due to the concentration of these cements.

5.5.4. Microfracture density

The poor correlation between microfracture density and distance from the fault suggests that these microfractures are not formed due to slip on the fault surface. Microfractures due to deformation of porous sandstones are often curvilinear in shape and radiate from grain boundaries, and are called Herztian microfractures (Wong 1990). The majority of the healed microfractures in this study are straight, and where quartz overgrowths are present they are often not fractured. This suggests that these microfractures are inherited features from the original protolith of the detrital grains (i.e. a granite, mylonite or vein quartz), and are not associated with deformation of the Navajo Sandstone. This would explain why no logarithmic decay of microfractures is seen with distance from the fault. It would also explain why the orientation of the sample had no effect on the number of microfractures counted. Inherited microfractures would be expected to have a random orientation.

Experimental studies report large numbers of acoustic emissions (AE) occurring throughout high-porosity sandstones before failure (Lockner *et al.* 1992). Thin section analysis of these experimentally deformed sandstones has shown that grain crushing caused by enhanced stress at grain contacts causes this lithology to fail and form deformation bands without the production of a dense population of intra-grain microfractures (Lockner *et al.* 1992). The AEs have therefore been interpreted as the rupture of grain boundary microfractures. The AE activity was also used to locate events interpreted as distributed microfracturing, grain crushing and grain boundary sliding. Fracture localisation occurred earlier in Berea Sandstone (18% porosity) samples, and 10-30 times more AE events occurred pre-failure in than granites (Lockner *et al.* 1992). The locus of fault nucleation in the granites was apparently

controlled by the large modulus change at the sample edge. Conversely, the faults nucleated within the sample for the sandstones. The transition from grain crushing to localisation of new bands and shear along a slip-surface will correspond to a transition from dilatant hardening to strain softening (Mair 1997).

The identification, and hence quantification, of grain boundary microfractures is extremely difficult, if not impossible, in mature sandstones such as the Navajo Sandstone. In the absence of any pre-faulting cements which could act as a marker for failure, it is very hard to identify grain boundaries that have fractured. It would be interesting to see if grain angularity and preferred orientation changed across the fault. Spalling of overgrowths and re-orientation of grains may occur during grain boundary movement which could potentially produce a preferred orientation (Cladouhos 1999). The strength of the grain boundary cement may also be a factor, though this has not been investigated.

The low microfracture densities seen in this study contrast with the large numbers of fault-related microfractures described by Vermilye and Scholz (1998) in very well indurated quartz sandstone and by Anders and Wiltschko (1994) in calcite and silica cemented sandstones (Figure 5.25). These data, for low porosity sandstones (porosity $< 10\%$), describe a logarithmic decrease in microfracture density with distance from the fault. Anders and Wiltschko's (1994) data for the Navajo Sandstone and Entrada sandstones, however, shows a poor correlation with distance from the fault with no data above nine microfractures per millimetre. These studies and that of Lockner *et al.* (1992) highlight the difference between the behaviour of high-porosity sandstones, and low-porosity sandstones and granites. The porosity of the host rock has a strong effect on the microfracture population, presumably because dilatancy and hence grain fracturing can occur more easily where porosity is lower. This effect has been noted in previous studies (e.g. Dunn et al. 1973), however this study indicates that host rock lithology may be an important factor in the style of microfracture populations away from faults, which has not been previously been discussed.

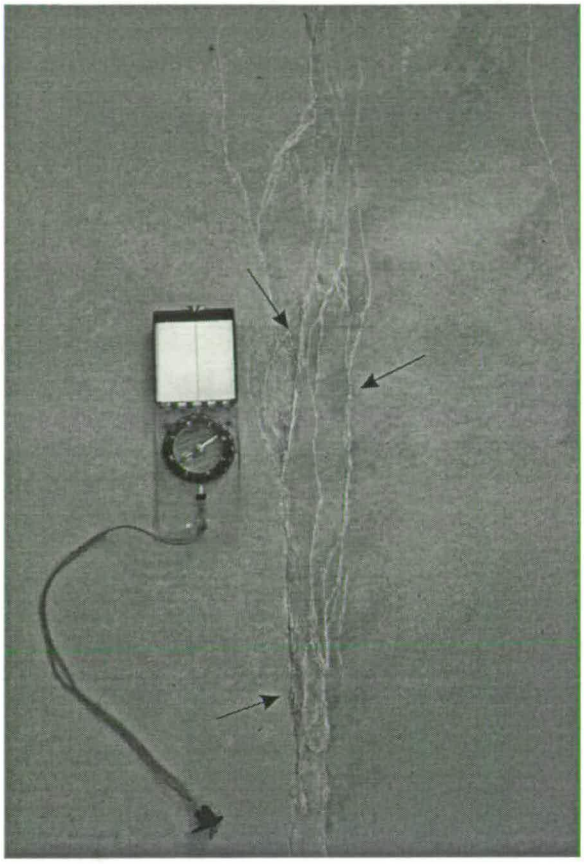

Figure 5.24. Photograph of deformation band cluster with mineral staining (slightly darker colour, highlighted by arrows). Note that staining is restricted to only a few of the compatments that are defined by the deformation bands. This indicates that deformation bands are a good barrier to fluid flow.

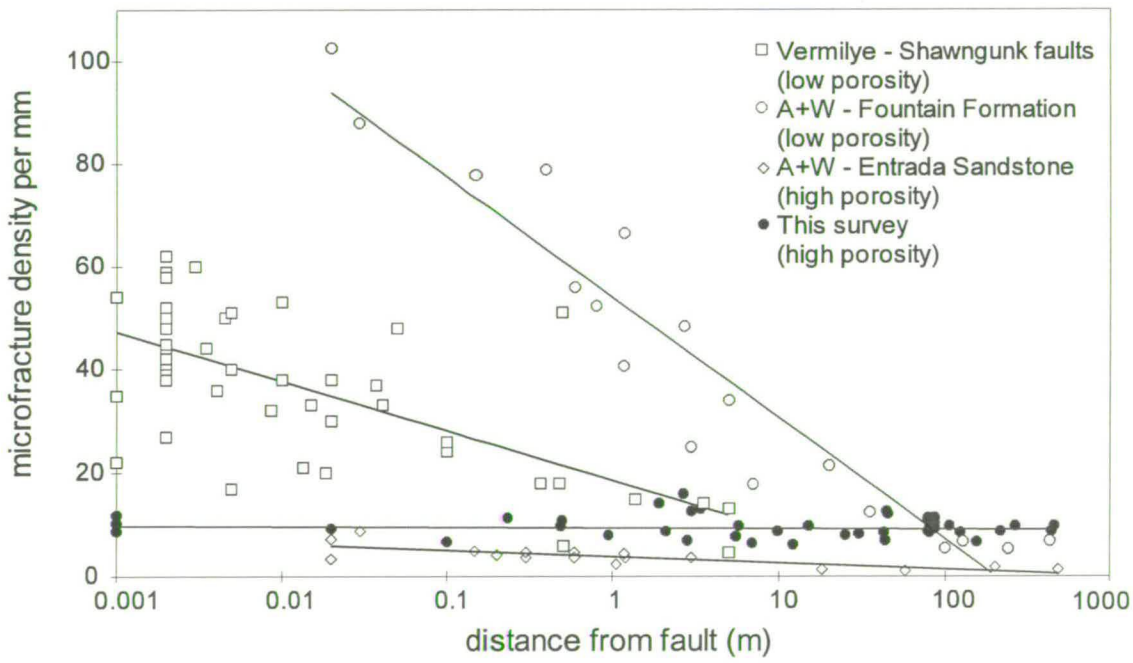

Figure 5.25. Comparison of data from this study (filled circles) with that of Anders and Wiltschko (1994) and Vermilye (1996) (empty symbols). The best fit line for each dataset is shown. Note that low porosity sandstones (<10%) behave differently from high porosity sandstones.

5.5.5. Scaling of off-fault deformation

Most discussions of process zones ahead of propagating fault tips (Section 1.2.2) have concentrated on microscopic deformation (Scholz *et al.* 1993, Vermilye and Scholz 1998). However, there is no signal of the fault in the microfracture population and in any case the amount of grain boundary deformation is unquantifiable in this rock type. The finite width of the macroscopic off-fault deformation at the fault tip (Section 4.3.1), indicates that the process zone is not simply a microscopic feature in this case. It is suggested, that in the light of the discussion in Section 5.5.4, that a macroscopic process zone should be expected in a high porosity sandstone.

If the deformation at the fault tip consists of 12 m width of macroscopic deformation bands and an unquantifiable amount of grain boundary fractures, then the scaling relation for process zone width and fault length proposed by Cowie and Scholz (1992a) does not hold. They predicted that the process zone length would be 10-20% of the length of the fault. Although their model only applies strictly to in-plane fractures, Scholz *et al.* (1993) have argued that the same scaling will apply to the width of the process zone at the fault tip. If this relation applied then this width would be in the order of 30-60 m, for the Blueberry fault (with a length of 3 km). This discrepancy is discussed further in Section 7.3.4.

5.6. Summary

1. The microstructure of deformation bands and the host rock in the off-fault deformation around the Blueberry and Big Hole faults has been systematically sampled and characterised in order to investigate processes active along the fault and within the off-fault deformation during fault evolution.

2. Single-strand deformation bands have a reduced grain size and porosity within them. Displacement across single deformation bands is limited to a few millimetres. Displacement accumulation across zones of deformation bands is accommodated almost solely by the addition of new strands. Essentially no increase in grain crushing (decrease in porosity) is seen between single-strand

deformation bands and zones of bands. Pods of relatively undeformed rock between strands in deformation band clusters have a reduced porosity with respect to the host rock.

3. At some point a zone of increased grain crushing nucleates, and a slip-surface forms within this zone. The precise mechanism of slip-surface nucleation is still unclear, but there is evidence that slip-surfaces can nucleate in small patches and propagate together to form an anastomosing network. Displacement accumulation on the slip surface has little effect on the grain size (porosity) of the adjacent rock. This means that the grain size distribution cannot be used to distinguish slip-surfaces formed in small off-fault deformation clusters from major fault planes.

4. Late stage microfractures are seen only immediately adjacent to the fault (within a few millimetres). These are not in an orientation consistent with shear across a zone of gouge and may have occurred due to rupture of a small part of the fault surface. Riedel shear structures consistent with shear across a zone of gouge are found adjacent to the fault surface. These structures indicate that some reactivation of the fault gouge adjacent to the main fault slip-plane occurs, even though no grain size reduction is seen.

5. Microfractures are distributed around the fault, but the density of microfractures does not seem to be related either to the distance away from the fault or to the displacement on the fault at the point measured. Therefore they are unrelated to movement on the fault surface and are probably inherited microfractures.

6. Deformation at the Blueberry fault tip (the process zone) is composed of an unquantifiable amount of grain boundary microfracturing, and macroscopic deformation in the form of deformation bands. The deformation bands extend for 12 m either side of the fault. This is substantially smaller than the process zone width expected from theoretical scaling relations, which for this fault would be in the order of 30-60 m. Microstructural measurements from this study confirm

experimental observations that deformation is significantly different in high porosity sandstones than in other rock types.

6. OFF-FAULT STRAIN

6.1. Introduction

6.1.1. Rationale

In Chapters 4 and 5, the distribution and orientation of off-fault deformation around the Blueberry and Big Hole Faults have been quantified. The positive correlation of off-fault deformation width with displacement suggests that this deformation formed in response to increasing displacement on the main fault zone (Section 4.6.2). The orientation of structures around the faults suggest that they formed in a stress field locally controlled by the orientation of the main fault rather than that of the regional strain field (Section 4.6.5). Given the scaling of off-fault deformation width and displacement, the deformation density might be expected to increase where the displacement is greater. The orientations of structures may also be expected to vary between the deformation alongside the well-developed fault and deformation ahead of the tip fault.

In order to investigate these possibilities, strain and deformation density have been calculated for the off-fault deformation, both across and along the strike of the main fault planes. The orientations of the off-fault structures have been analysed using a model for three-dimensional strain. These results are then interpreted in terms of the growth of the Big Hole and Blueberry faults.

6.1.2. Structure of this chapter

Section 6.2 discusses the total strain across the off-fault deformation represented by each of the transects perpendicular to the main fault surface. Section 6.3 investigates the variation of deformation density within the off-fault deformation using an image analysis package. In Section 6.4 the possibility of three-dimensional strain within the off-fault deformation is tested using the theory of orthorhombic faulting introduced in Section 2.2.3. These findings are interpreted in terms of the evolution of the off-fault deformation around the Blueberry and Big Hole Faults in Section 6.5.

6.2. Variation of strain along fault strike

6.2.1. Methodology

Strictly speaking, the quantitative measurement of strain in a faulted rock volume would require measurement of the sense and magnitude of displacement on all the faults in that volume. However, it is possible to approximate this strain if some assumptions are made about the population of structures. Transects through the off-fault deformation in this study logged the position and width of every deformation band encountered. The aeolian cross-bedding provided markers to measure offset on individual bands. Therefore in the more massive beds it was not always possible to measure the sense and magnitude of displacement on all the deformation bands. An estimate of the strain across the deformation band can be made, however, if the relationship between the structure width and offset is assumed.

Aydin and Johnson (1978) observed that the total displacement across a zone of deformation bands was proportional to the number of bands in the zone. This was a key observation in the development of their model of deformation band growth (Section 2.3.1). They noted that each individual band had in the order of 1 mm offset and that zones of bands had up to 30 cm offset. However they did not present any quantitative data to evaluate this correlation. Mair (1997) found a very good positive relationship between the number of gouge strands and the applied axial strain in experimentally formed deformation bands. This corresponds to a correlation between the horizontal (extensional) offset in millimetres, d, and individual deformation band thickness in millimetres, w, of

$$d = 0.91\ w + 1.22 \qquad (6.1)$$

with a correlation coefficient, R^2, of 0.96 (Figure 6.1). In this study, the porosity (amount of grain size reduction) is essentially the same in single bands and strands within zones of bands (Section 5.5.1). This indicates that a correlation between deformation band width and offset should be expected in this field area. However, only a crude positive correlation is seen for the deformation bands where both offset and deformation band width were measured (Figure 6.1). The poor correlation

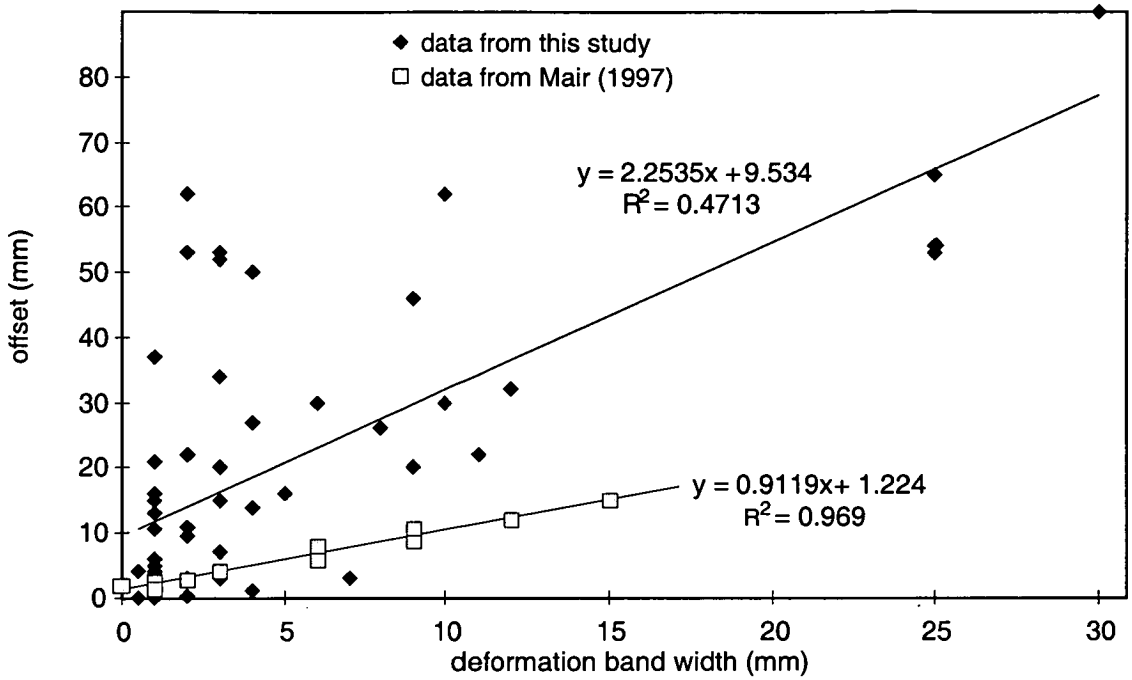

Figure 6.1. Plot of deformation band width and offset for deformation bands from this study and from experimentally generated bands (Mair 1997).

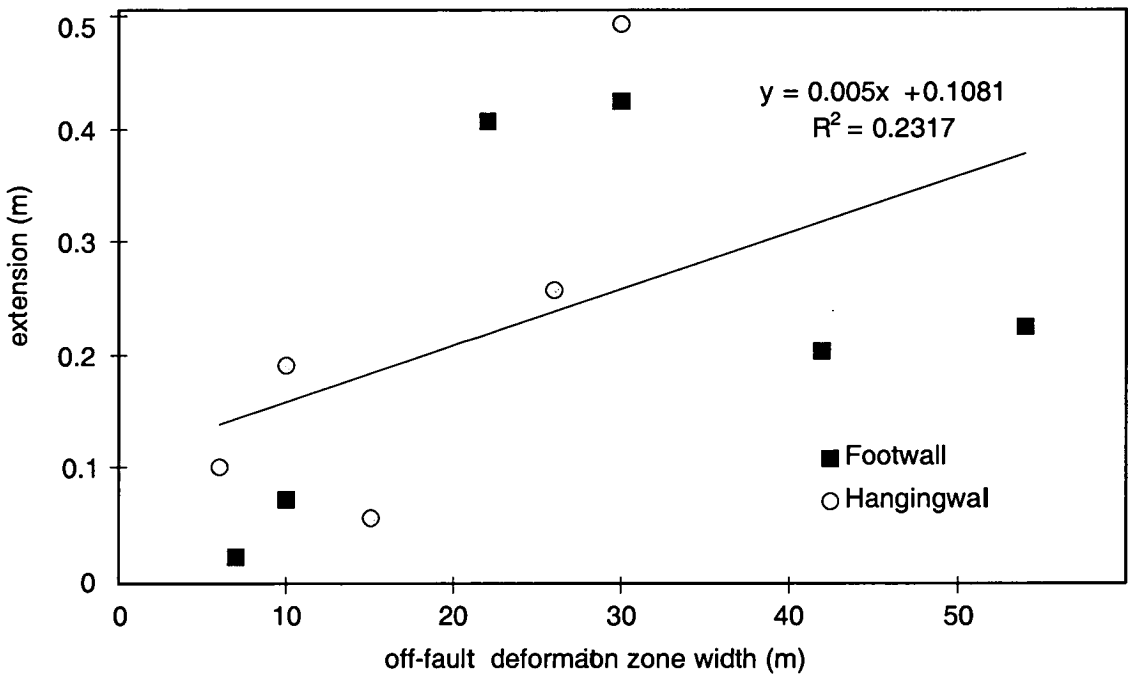

Figure 6.2. Plot of the extension across the off-fault deformation zone vs. the off-fault deformation zone width. The hangingwall and footwall are shown in different symbols, showing that there is no asymmetry between the hangingwall and footwall. The amount of extension is approximately proportional to the damage zone width supporting the observation that the total strain across the off-fault deformation zone is constant.

($R^2 = 0.47$) could be due to an undersampling of very small offset bands, which are hard to measure accurately. Measurement of a greater number of wider zones of deformation bands would also improve the correlation.

Strain, ε, is defined as

$$\varepsilon = \Delta l / l_o = \Delta l / (l_f - \Delta l), \quad (6.2)$$

where l_o is the original length, Δl is the increase in length, or extension, and l_f is the final length of a marker. In this case l_f is the final width of the off-fault deformation. The extension, Δl, along each of the transects is the sum of the component of slip parallel to the transect direction for all the structures on a transect. The horizontal component of slip was either measured in situ or, for structures where no offset was measured, estimated from the empirical relationship of Mair (1997) as discussed above.

When the transect data were collected, the significance of the slip-surfaces was not fully appreciated. As a result, the position of slip-surfaces was not always recorded on the transects. An individual slip-surface can theoretically have any amount of displacement, but usually forms when the vertical offset on a zone of deformation bands exceeds 10-50 cm (Aydin and Johnson 1978). Very few of the off-fault slip-surfaces offset the top Navajo Sandstone; most have only a few centimetres of slip and none have more than 1-2 m slip. Although these offsets are small relative to the main fault they may contribute significant extension within the off-fault deformation. There is no simple relationship between slip-surface structure and displacement (see Section 5.5.2), so if there is no offset marker it is not possible to assign a value of displacement to a given slip-surface. In order to estimate the contribution of the slip-surfaces to the total strain, an arbitrary vertical offset of 10 cm per slip-surface has been assigned to each slip-surface on the transects where the number of slip-surfaces could be counted from the outcrop maps (Section 4.6.4). The strain has been calculated for the entire width of the off-fault deformation at Blueberry tip, Chipmunk Flats and Juniper Flats and for the footwall only at Cement Bridge. Two

values are calculated, the strain for the deformation bands only and the strain including the contribution from slip-surfaces.

6.2.2. Results

Table 6.1 shows the strain calculated for each of the transects presented in Sections 4.3 and 4.4. The empirical relationship of (Mair 1997) is used to estimate Δl (Equation 6.1). The localities in Table 6.1 are in ascending order of displacement showing that the strain does not vary in a systematic way with the displacement on the fault. The average strain is 8.7×10^{-3} with a standard deviation of 5.2×10^{-3}. If the off-fault strain is constant then the extension, Δl, must be linearly related to the width of the off-fault deformation. This is plotted in Figure 6.2, and a weak positive correlation is seen. No systematic asymmetry in the amount of strain is seen between the hangingwall and footwall.

The calculation of strain for the outcrops where the number of slip-surfaces was recorded is shown in table 6.2. The average strain including slip-surfaces is 16.1×10^{-3}. This contrasts with an average strain of 10.1×10^{-3} for the deformation bands only. The value of strain is consistently higher when the slip-surfaces are included. Although this is a very simplified calculation, it indicates that the strain remains constant along the strike of the main fault.

	off-fault deformation width , l_f (m)	cumulative width of deformation bands, w (m)	extension, $\Delta l = 0.91w + 0.00122$ (m)	calculated strain, $\varepsilon = \Delta l/(l_f - \Delta l)$
hangingwall				
Blueberry	6	0.088	0.0815	0.0138
Westend	15	0.048	0.0450	0.0030
Chipmunk	30	0.429	0.3924	0.0133
Juniper	26	0.224	0.2055	0.0080
Amy's Hill	10	0.166	0.1526	0.0155
Jan's Cliff	50	0.056	0.1043	0.0020
footwall				
Blueberry	7	0.019	0.0186	0.0027
Westend	10	0.062	0.0578	0.0058
Cement	22	0.345	0.3240	0.0149
Chipmunk	30	0.369	0.3377	0.0114
Juniper	42	0.176	0.1617	0.0039
Amy's Hill	54	0.195	0.1790	0.0033
Jan's Cliff	50	0.081	0.0924	0.0014

Table 6.1. Calculation of the strain due to off-fault deformation.

	total l_f (m)	deformation band extension Δl (m)	slip-surface extension Δl (m)	strain due to deformation bands	strain including slip-surfaces
Blueberry	13	0.1001	0.120	0.0078	0.0172
Cement fw	22	0.3240	0.090	0.0149	0.0192
Chipmunk	60	0.7301	0.300	0.0123	0.0175
Juniper	68	0.3672	0.330	0.0054	0.0104

Table 6.2. Calculation of the strain due to off-fault deformation including an estimate of slip-surface strain (assuming 10 cm vertical offset on each slip-surface).

An analysis of the dip direction of deformation bands within the off-fault deformation shows that there are approximately equal numbers of synthetic and antithetic structures (Table 6.2). There tend to be more synthetic single deformation bands, but these contribute only a small proportion to the total strain. Slip-surfaces, which contribute a larger proportion to the strain, are almost equally synthetic and antithetic. If numbers of synthetic and antithetic structures are equal, the strain within the off-fault deformation is coaxial. Therefore, in cross-section, the strain due to the off-fault deformation can be approximated by pure horizontal stretching with very little overall vertical shear of bedding either in the hangingwall or footwall (Figure 6.3). This indicates that the off-fault deformation is not accommodating flexure of the bedding perpendicular to the fault surface (i.e. non-coaxial strain) as is sometimes the case (e.g. Jamison and Stearns 1982).

	Synthetic	Antithetic	% Synthetic	% Antithetic
Location				
Hangingwall	185	184	50	50
Footwall	140	93	60	40
Big Hole fault	281	202	42	58
Blueberry fault	98	109	47	53
Structure type				
single deformation bands	114	55	67	33
zones of def. bands	147	145	50	50
slip-surfaces	118	111	49	51

Table 6.3. Relative numbers of synthetic and antithetic structures for different locations around the faults and for different structure types.

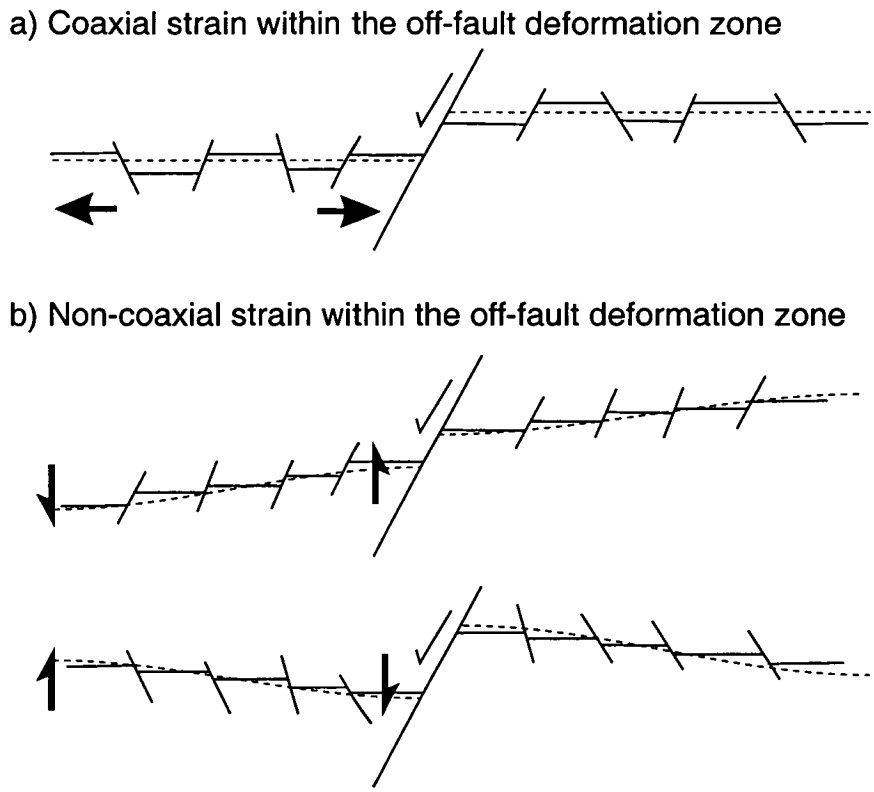

Figure 6.3. Cartoon showing the effect of the relative proportions of synthetic and antithetic faults in the off-fault deformation zone. a) Equal proportions of synthetic and antithetic faults results in overall extension across the off-fault deformation zone. b) Mostly synthetic or mostly antithetic results in shear across the off-fault deformation zone, but in opposite directions.

6.3. Variation of strain within the off-fault deformation zone

6.3.1. Methodology

The variation of the density of deformation throughout the off-fault deformation zone is a convenient way of looking at local variations in strain (Jamison and Stearns 1982). Deformation density is defined as the number of features per square meter. Using an image analysis package (Erdas Imagine), the off-fault deformation maps presented in Sections 4.3 and 4.4 have been contoured for deformation density. Line drawings of the individual outcrops were scanned and digitised. The widths of the lines are the correct width for deformation bands at the scale of the image. Each pixel in the image is given a colour value corresponding to the percentage deformation that the pixel is considered to contain: a black or red pixel contains a deformation band or slip-surface and is assigned the value 100; a white pixel contains no deformation bands and is assigned the value 0; a grey pixel contains a data gap due to cover and is assigned the value 101; a blue pixel is an area of concentrated deformation (see Section 4.4.2) which is assigned the value 100. The area over which density is to be calculated is called the focal window. This is a matrix defined as x by y pixels wide, which can be varied in size as the user decides. The size of the focal window is calibrated to meters by checking the number of pixels in the image. All the outcrop scale maps have the focal window scaled to 0.5 x 0.5 m wide.

The program then calculates the focal mean for every pixel in the image. This is the mean of the values assigned to each pixel in the focal window excluding pixels with 'no data' values. For example, for a focal window of 5 x 5 pixels containing 6 grey pixels (no data=101), 5 black pixels (deformation bands=100) and 15 white pixels (no deformation bands=0), the focal mean is 26.3% (Figure 6.4). This is equivalent to the deformation density: the area of uncovered outcrop within the focal window that contains deformation bands, or deformation band clusters, divided by the area of the

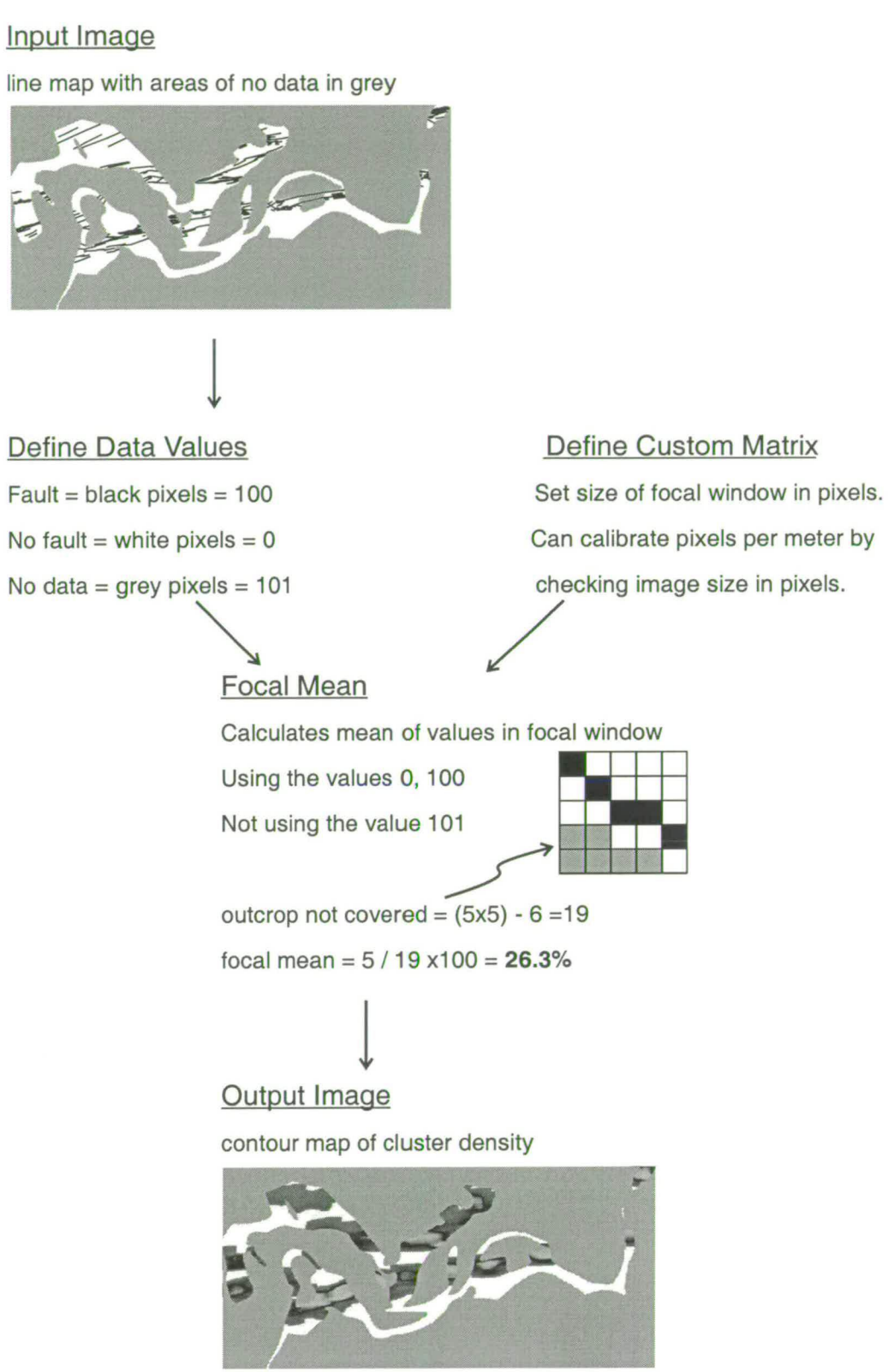

Figure 6.4. Calculating fault density from line maps using the Erdas Imagine image analysis software.

focal window. The output image is a map of the focal mean for a focal window centred over each pixel in the image.

The same procedure is followed for the cluster maps. To calculate the deformation density, each cluster class was assigned the value 100. The extension across the average cluster in each class (see Section 6.2.1) was calculated in the same fashion as for the off-fault deformation transects according to the number and type of deformation bands in each class. The width of each cluster was then scaled accordingly: Class 1 (orange) clusters were assigned a width of 0.4 m; Class 2 (blue) clusters were assigned a width of 0.9 m; Class 3 (green) clusters were assigned a width of 1.1 m. The focal window is set to 5 m x 5 m for the Blueberry fault tip canyon map and 50 m x 50 m for the Big Hole fault map. The different focal window size reflects the different scales that the maps were created on.

The maps of deformation density are presented in Figures 6.5-11. The same colour scale is used for all the maps: white is 0% deformation; pink through red is 1 - 100% deformation. Some local maxima are edge effects (e.g. high values at bottom right-hand side of Figure 6.9). This occurs where the focal window contains a large proportion of "no data" points. The faults in the remaining area take up a larger proportion of the focal window, and hence the focal mean returns artificially higher values of density.

6.3.2. Results: Outcrop-scale maps

Figure 6.5 shows the density map for the Blueberry fault tip canyon outcrop (displacement = 0 m). The highest density of deformation bands at the fault tip is 27% per 0.5 m^2 on the northern antithetic structure. This structure has the cross-hatched pattern that has been previously described (Section 4.3.2). The deformation map of the same outcrop (Figure 6.5a) shows that more slip-surfaces are seen along the fault parallel structure. Thus the greatest deformation density is not coincident with the greatest number of slip-surfaces. This backs up the observation that slip-surfaces are often seen within relatively narrow clusters of deformation (Figure 4.10b). This map seems to shows that the greatest deformation density is towards the

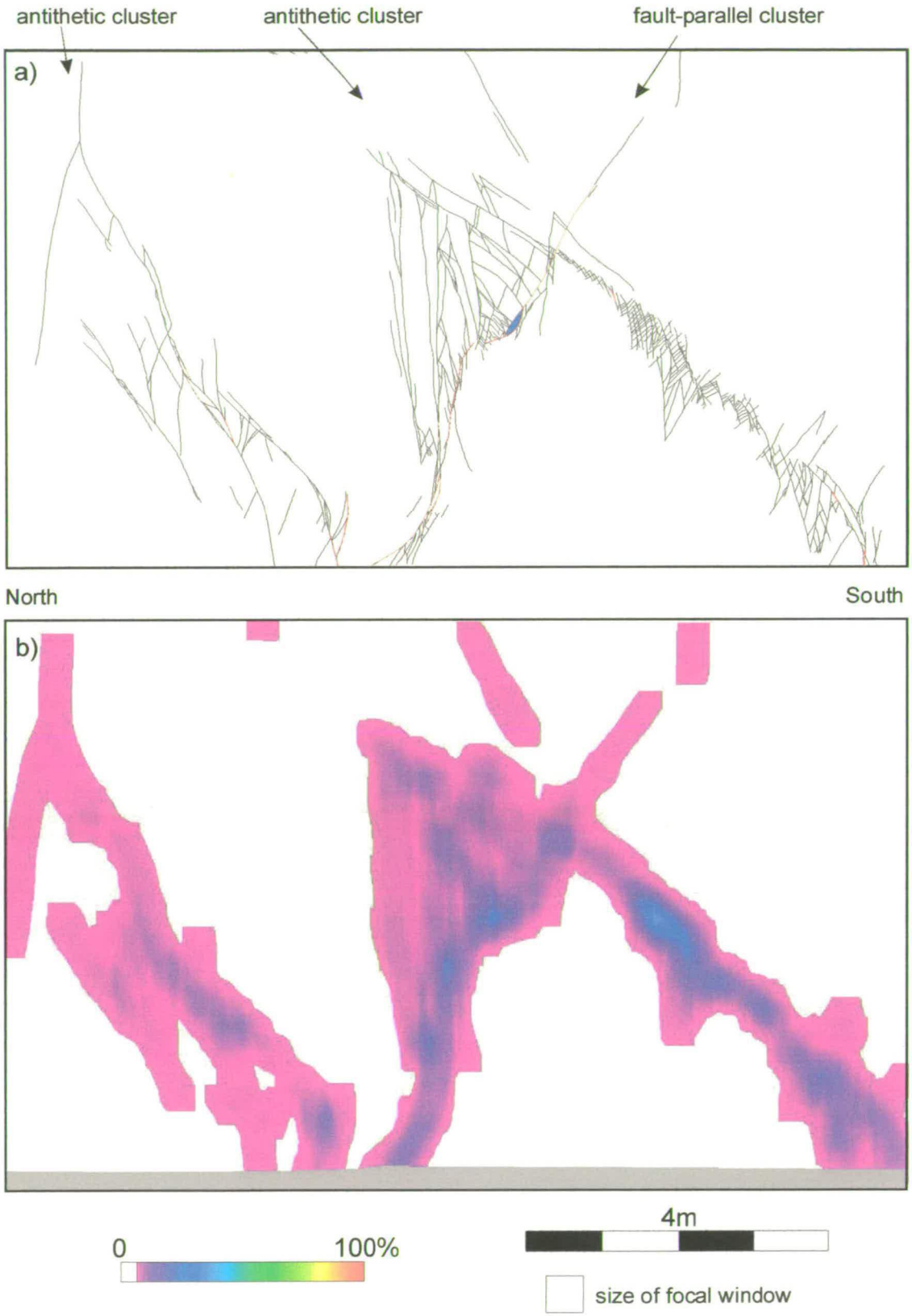

Figure 6.5. a) Deformation map (on a sub-vertical surface) with slip-surfaces in red, and b) deformation density map of the Blueberry fault tip outcrop.

base of the outcrop. This may be a consequence of the displacement on the fault increasing downwards (Section 3.3.1).

Figure 6.6 shows the density map for the Big Hole fault Cement Bridge outcrop (displacement = 9.4 m). The large cluster that runs antithetic to the fault has the highest deformation density of 33% per 0.5 m^2. This cluster is also associated with the cross-hatched pattern which is notably very concentrated at the bottom left-hand-side of the image. The maximum density on this map correlates well with the position of the slip surfaces. Both the deformation density and the number of slip-surfaces are higher here than at the Blueberry fault tip.

Figures 6.7 and 6.8 shows the density maps for the Big Hole fault Chipmunk Flats northern and southern strands (displacement = 19.1 m). As noted in Section 4.6.3, the southern strand is surrounded by higher deformation densities (76% per 0.5 m^2) than the northern fault strand (62%), possibly reflecting larger displacement on this strand of the fault. The northern strand could have up to 14 m of displacement whereas the southern strand has more than 3 m (Section 4.4.3). Away from the fault strands the maximum deformation density is fairly uniform (in the order of 30% per 0.5 m^2). For both of these maps there are no slip-surfaces at distances greater than 2 m from the main fault surface. Close to the fault (<1 m) the maximum density seems to be associated with the high number of slip-surfaces immediately adjacent to the fault.

Figure 6.9 shows the density map for the Big Hole fault Juniper Flats outcrop (displacement = 24.3 m). This map has the some of highest deformation densities of all the outcrop-scale maps (95% per 0.5 m^2), but most of these are edge effects (e.g. at the eastern end of the main fault strand). If these local maxima are ignored, the maximum deformation band density is 77% per 0.5 m^2. The high deformation densities away from the fault zone (i.e. at 15 m from the fault) are always associated with deformation band clusters containing slip-surfaces.

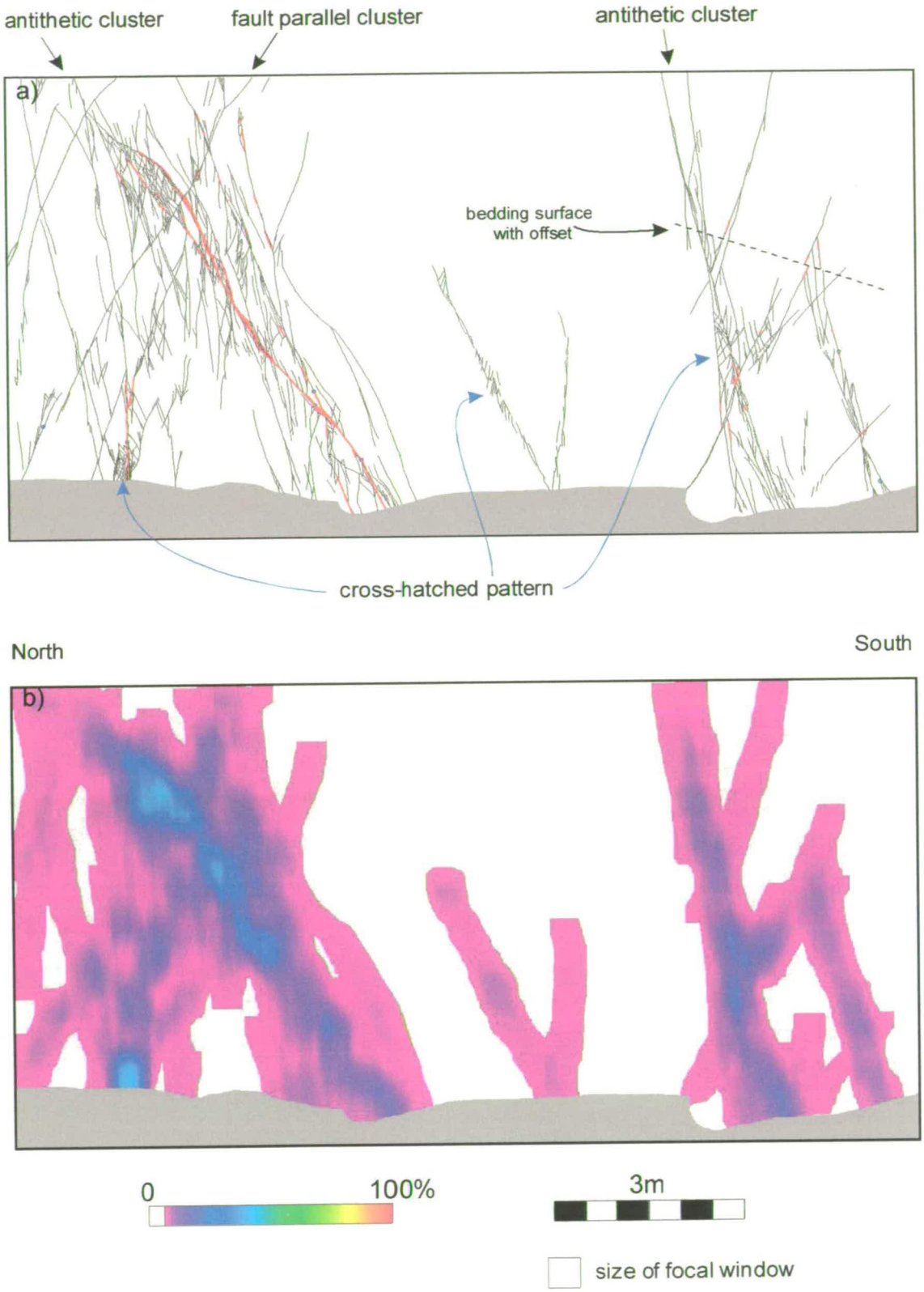

Figure 6.6. a) Deformation map (on 40-80^{o} dipping surface) of the Big Hole fault Cement Bridge outcrop with slip-surfaces in red. The main fault surface is off the diagram to the left. b) Deformation density map.

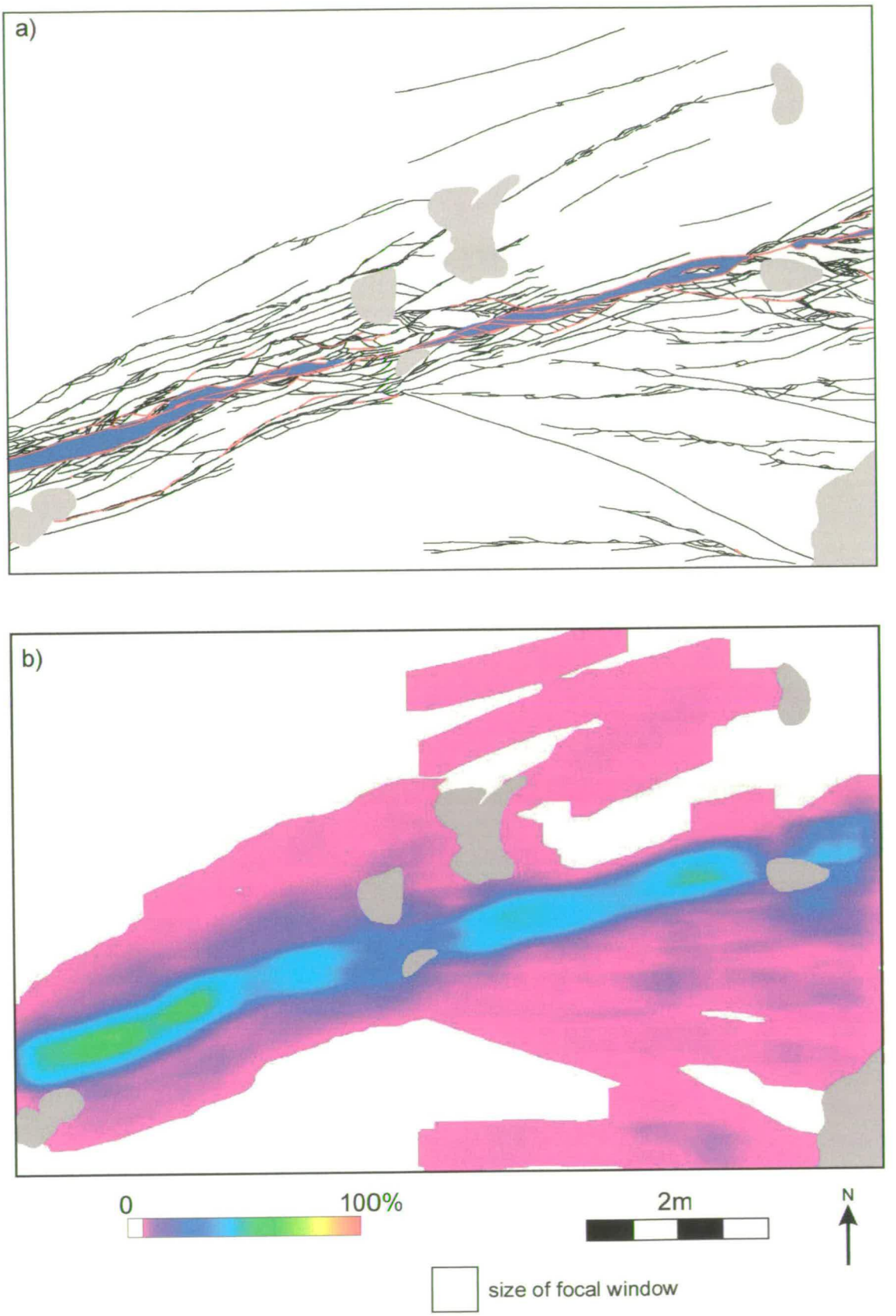

Figure 6.7. a) Deformation density map with slip-surfaces in red and b) deformation density map of the Big Hole fault Chipmunk Flats northern strand outcrop.

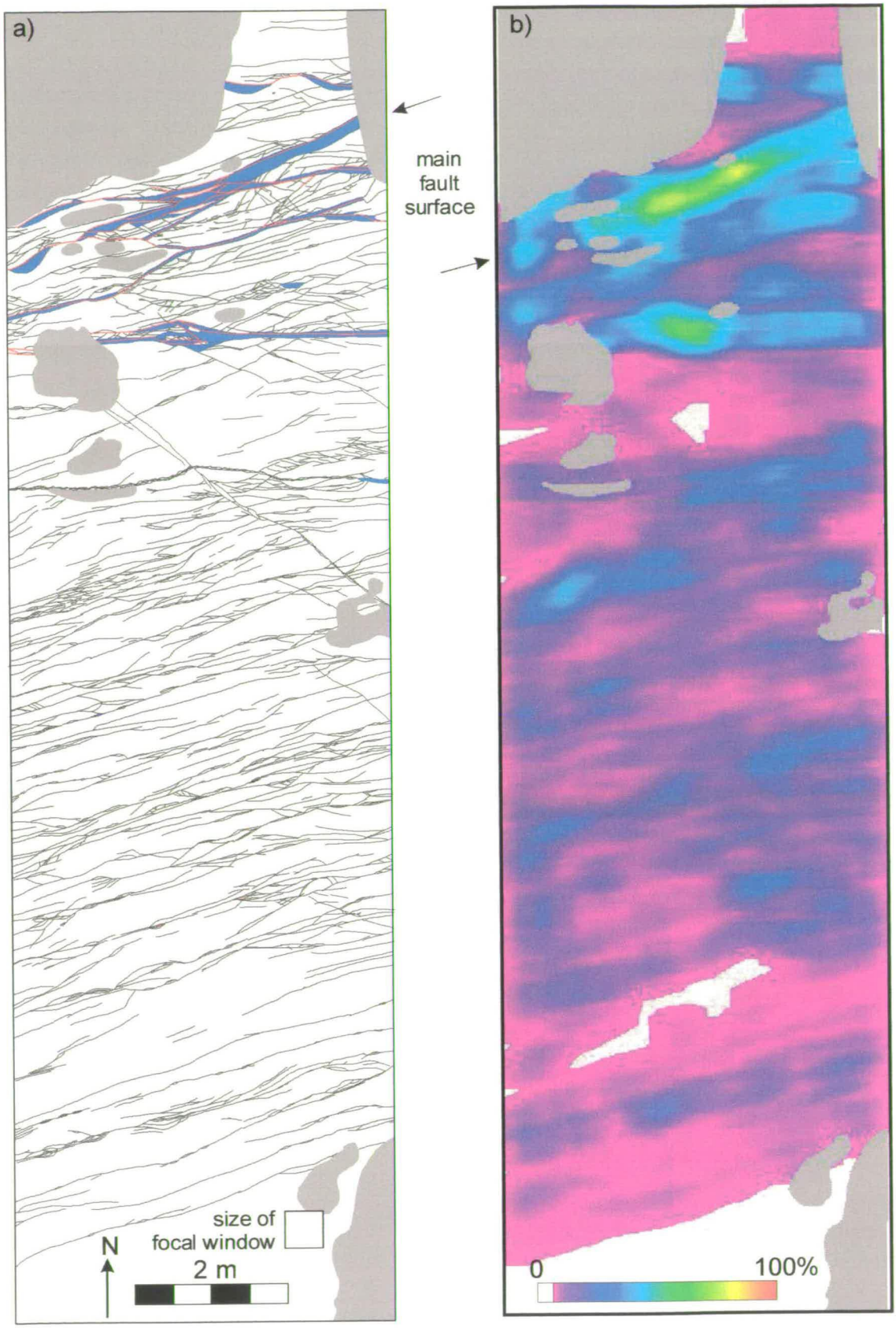

Figure 6.8. a) Deformation map with slip-surfaces in red, and b) deformation density map of the Big Hole fault Chipmunk Flats southern strand outcrop (planar surface).

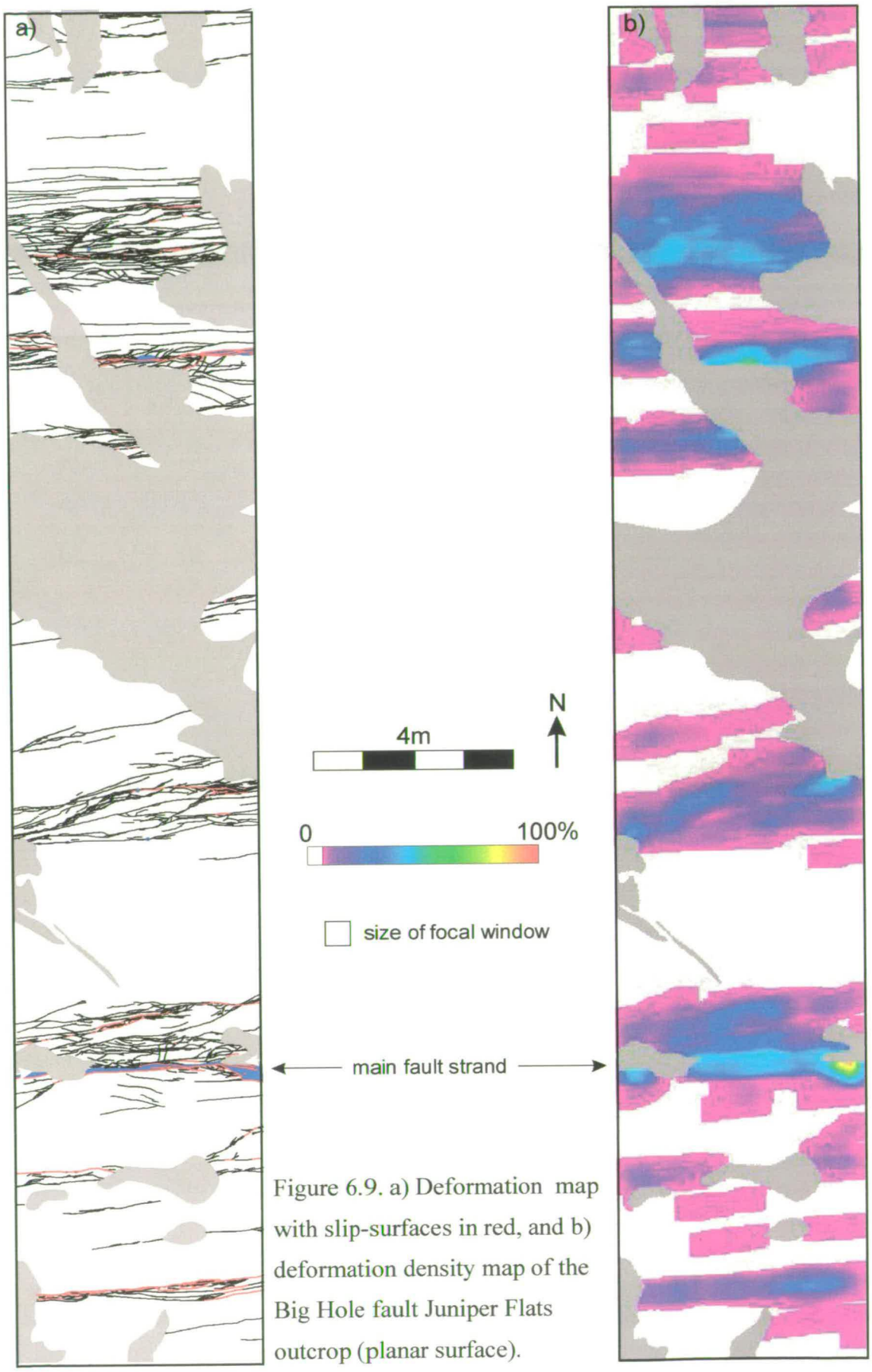

Figure 6.9. a) Deformation map with slip-surfaces in red, and b) deformation density map of the Big Hole fault Juniper Flats outcrop (planar surface).

6.3.3. Results: Blueberry and Big Hole fault cluster maps

Figures 6.10a and 6.11a show the off-fault deformation maps for the Big Hole and Blueberry faults. The cluster widths are scaled to fit the scale of the image. Structures in the non fault-parallel regional strike direction are not considered to be part of the deformation due to the evolution of these faults (Section 4.6.1) and have therefore not been included on the maps (compare to Figures 4.4 and 4.8). The size of the focal window is different for each map (Section 6.3.1), so the deformation densities cannot be directly compared between the two maps. However the maps help to quantify the variation in the distribution of deformation around the two faults.

Figure 6.10b shows the deformation density map for the Big Hole fault. The maximum deformation density is 29% per 50 m^2. The fault density is fairly uniform around the Big Hole fault. Local areas of higher density outside this region are associated with the subsidiary deformation band clusters (Section 4.6.1). Many small local highs are due to edge effects and should be ignored.

Figure 6.11b shows the deformation density map for the Blueberry fault. The density decreases towards the fault tip and the off-fault deformation becomes noticeably narrower. The lower densities towards the left-hand side of the map are due to the poorer quality outcrop at that point. The maximum deformation density is 75% per 5 m^2 and is seen 50 m west of the fault tip. This value is higher than the maximum density for the Big Hole fault cluster map because the cluster widths are scaled to the size of the image and are therefore proportionally larger.

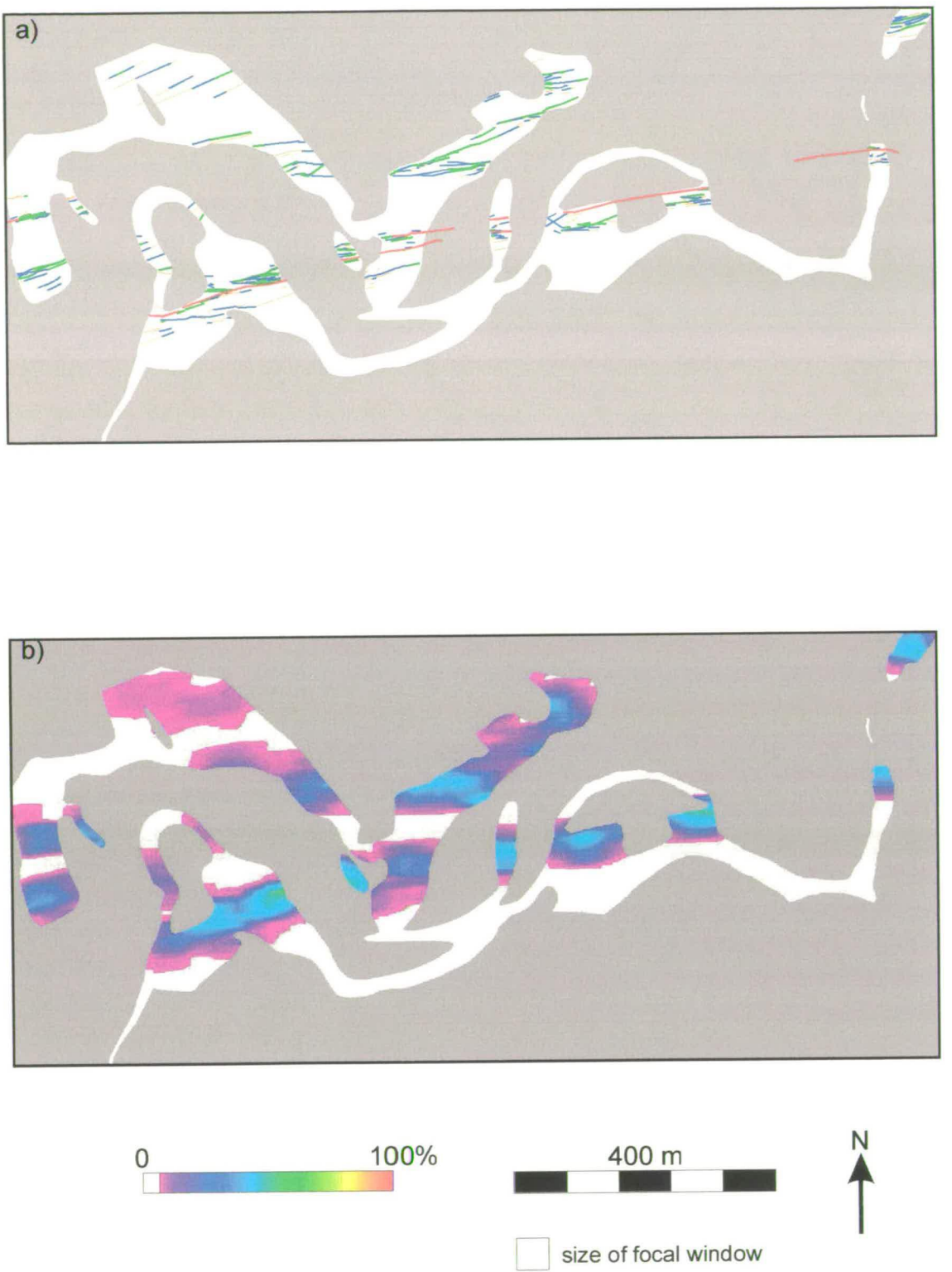

Figure 6.10. a) Deformation map and b) deformation density map of the Big Hole fault clusters. The deformation band clusters in a) are coloured according to their cluster class (Section 4.2.1), and their widths are scaled according to their deformation intensity. The main fault strand is in red.

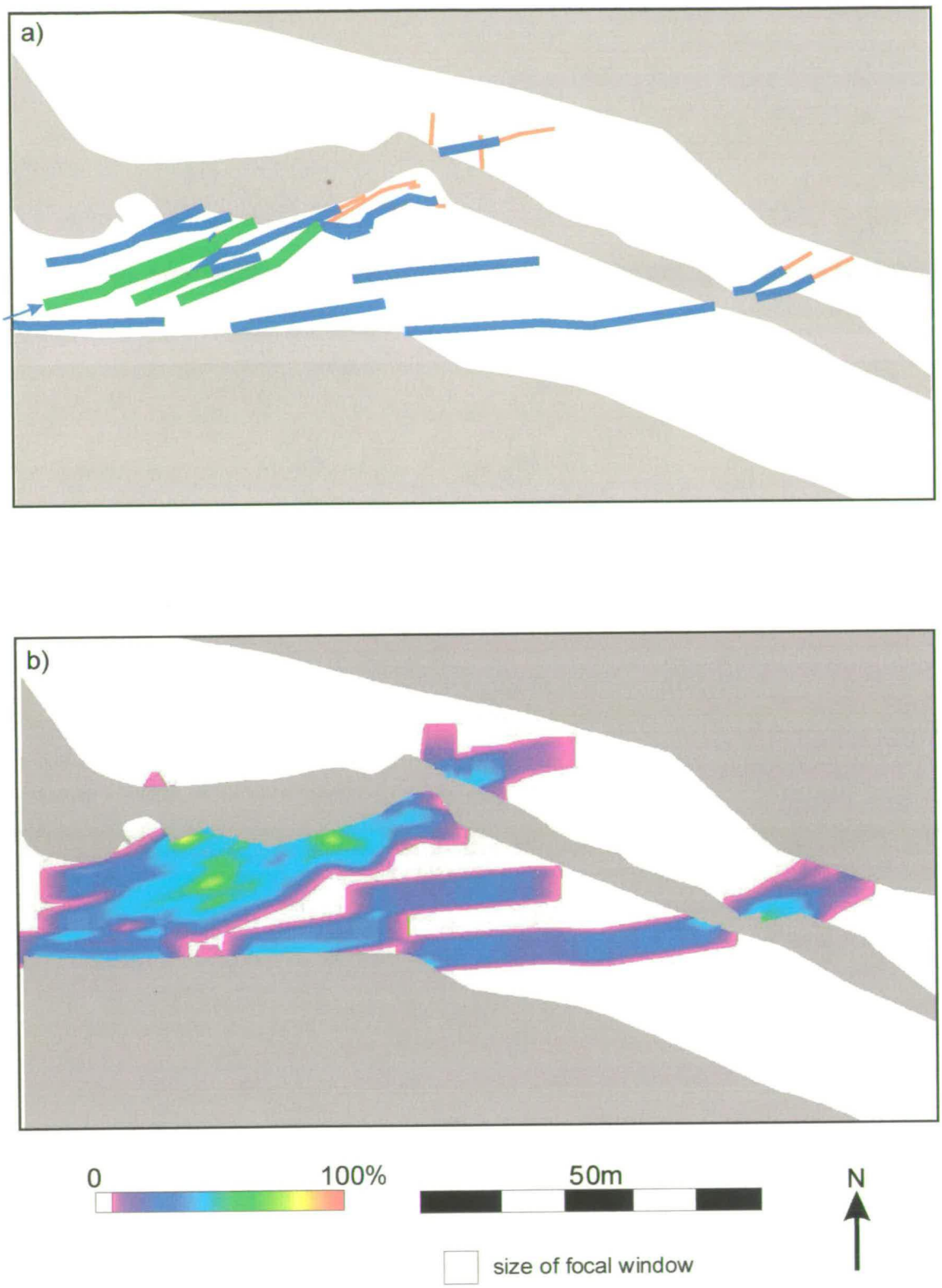

Figure 6.11. a) Deformation map and b) deformation density map of the Blueberry fault clusters. The deformation band clusters in a) are coloured according to their cluster class (Section 4.2.1), and their widths are scaled according to their deformation intensity. The main fault strand is marked with a blue arrow.

6.4. Orthorhombic symmetry and three-dimensional strain

6.4.1. Introduction

The Chimney Rock fault array consists of four mutually cross-cutting fault sets in orthorhombic symmetry (Section 2.2.3). The off-fault deformation around the Blueberry and Big Hole Faults also describes an orthorhombic system of deformation bands. Two strike sets of deformation bands and slip-surfaces, which are sub-parallel to the main faults, define narrow lozenges of undeformed rock with long axes parallel to the fault (Figure 6.12a). In cross-section, two dip sets (synthetic and antithetic) of deformation bands and slip-surfaces also define lozenges of undeformed rock with vertical long axes (Figure 6.12b). The two dip sets have a larger angle between them than the two strike sets: compare the cross-sections (Figures 6.5 and 6.6) to the map views (Figures 6.7-6.9). The off-fault deformation around the Big Hole and Blueberry faults has a much lower angle between strike sets than the main Chimney Rock fault array (compare to Figure 2.2). This implies that the off-fault deformation is growing in a local strain field associated with the growth of the main fault rather than that of the regional Chimney Rock fault array. If the strain can be deciphered, then it will be possible to gain an insight into what processes generate off-fault deformation structures in this geometry.

As described in Section 2.2.3, this geometry of four mutually cross-cutting (synchronous) fault sets is a result of three-dimensional strain (Reches 1978, 1983, Krantz 1988). This section of the chapter uses the slip model of Reches (1978, 1983) and the odd axis model of Krantz (1988), to investigate the three-dimensional strain within the off-fault deformation.

6.4.2. Methodology

The slip model for three-dimensional strain was developed by Reches (1978, 1983). In this model, the orientations of the four fault sets and their slip vectors are related to the ratio of the three principle strains, $\varepsilon_x > \varepsilon_y > \varepsilon_z$. The model assumes that all the strain is accommodated along faults, and that slip along each surface follows

Coulomb frictional behaviour. Reches (1983) used tensor analysis to minimise the differential stress and energy dissipation required to initiate slip on the surfaces that are most favourably oriented with respect to the principle strain axes. The preferred orientations of slip are presented as sets of equations for the direction cosines of poles to faults (Reches 1983).

The slip model was elaborated by Krantz (1988) into the odd axis model. This model determines the principal strain magnitudes as well as their orientations. It is based on the concept that for a three-dimensional, constant volume strain field, there will be one principle strain axis with a sign opposite to that of the other two. This is called the odd axis. If one principal extension is negative (shortening) and the other two are positive, as for normal faults, then ε_z is the odd axis and is vertical. The intermediate axis and similar axis share the same sign, and the fault sets strike in the intermediate-similar plane. The ratio of the intermediate to minimum strains is defined as k, where

$$k = \varepsilon_y/\varepsilon_z. \tag{6.3}$$

The value of k can range from -0.5 (oblate strain) to 1 (prolate strain), with plane strain occurring when $k = 0$.

The slip vector for each fault is defined by the intersection of the fault plane and a second plane containing the pole to the fault and the odd axis, called here the mutual plane. The slip vector, fault pole and odd axis are thus coplanar. Hence the odd axis can be found by determining the intersection of the planes that cut the slip vector and fault pole for each fault. With large datasets this can be done by finding the average poles and slip vectors for each fault set, and constructing the four average mutual planes. For smaller datasets the mutual planes can be calculated for each fault-slip vector pair and the average intersection of the mutual great circles can be calculated by statistical analysis. The similar and intermediate axes lie in the plane perpendicular to the odd axis, with the similar axis bisecting the acute angle between fault sets, and the intermediate axis bisecting the obtuse angle.

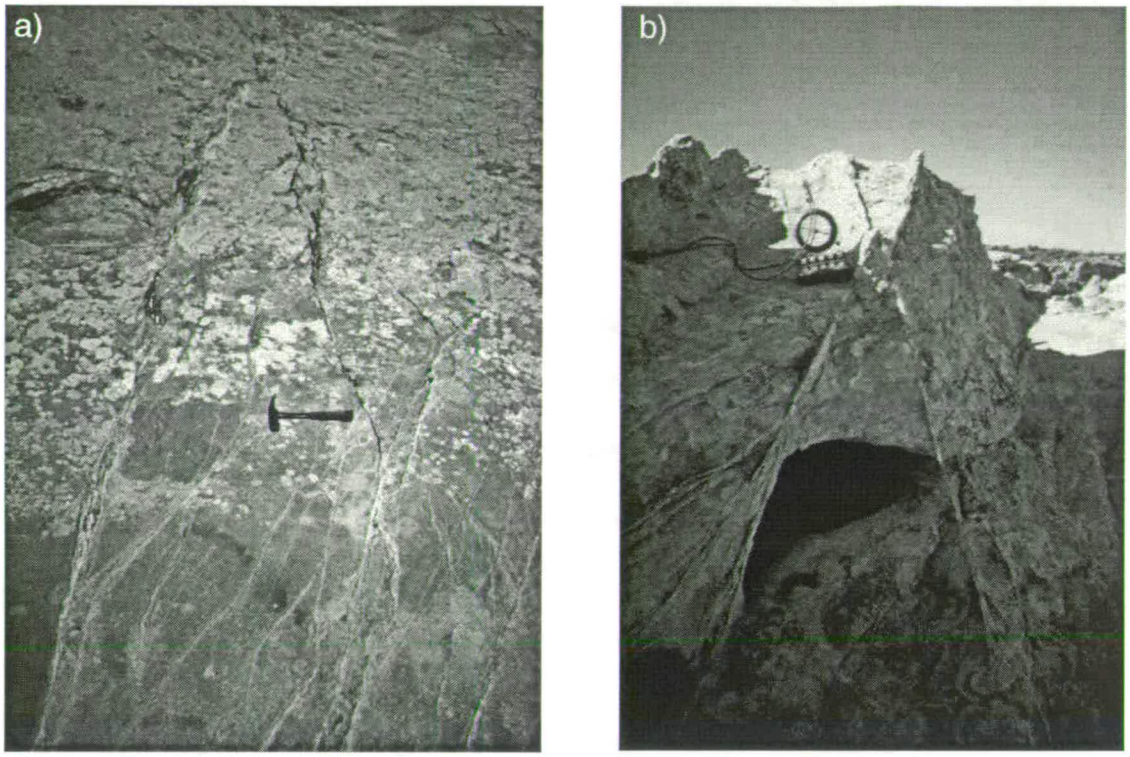

Figure 6.12. Orthorhombic symmetry (four fault sets) in the damage zone of the Big Hole fault: a) Two strike sets and b) two dip sets.

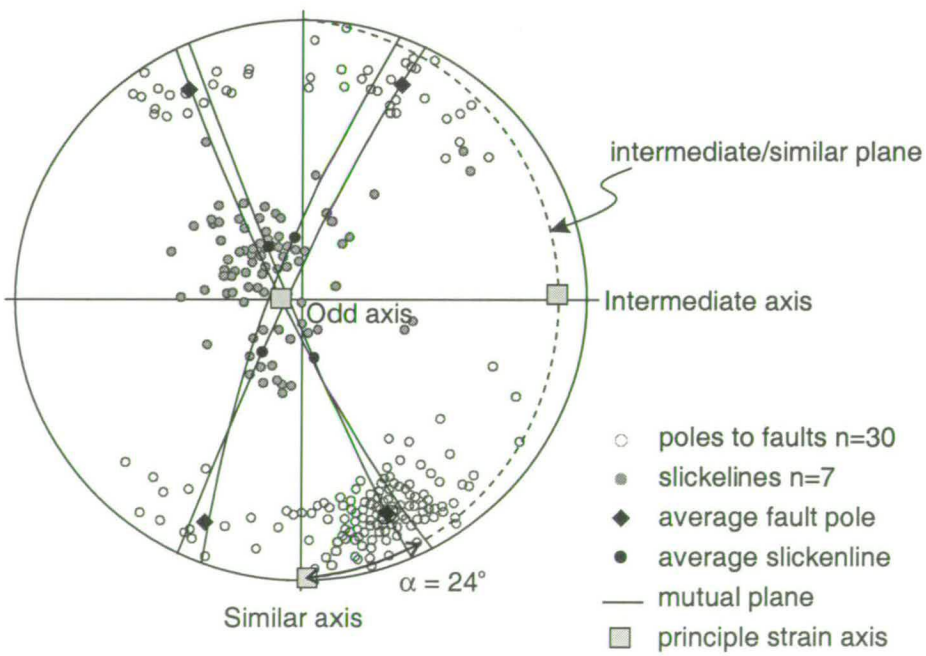

Figure 6.13. Example of the odd-axis construction for the Chimney Rock fault array, from Krantz (1988). Data points for individual faults are shown in grey, the odd-axis construction is for the average fault and slickenline, shown in black.

An example of this is shown in Figure 6.13 for the Chimney Rock fault array (from Krantz 1988). In this figure the data for each of the faults and slickenlines is shown in grey and the average fault poles and slip vectors are shown in black. The average poles and slip vectors are joined by best fit great circles (called mutual planes) and the intersection of these circles defines the odd axis. For Chimney Rock, the negative odd axis is vertical with the maximum extension oriented north-south and intermediate extension oriented east-west.

For conjugate faults the angle between fault sets is 2θ, where

$$\theta = \frac{90 - \phi}{2}, \tag{6.4}$$

and ϕ is the angle of internal friction. Within each strike set the dip of the faults, measured between the fault surface and the intermediate-similar plane, is the same as that for a conjugate pair. However the angular relationship between the strikes of each set, α, within the intermediate-similar plane is a function of the strain ratio, k. For normal faults with a sub-vertical odd axis (such as the Chimney Rock fault array), the acute angle between fault sets is given by

$$\varepsilon_y/\varepsilon_z = -\sin^2 \alpha = k. \tag{6.5}$$

This simplified relationship is shown by Krantz (1988) to be true for fault sets where the ratio of fault displacement to fault spacing is small.

To apply the slip model the field data is rotated so that the principle strains lie north-south, east-west and vertical on the stereonet. The data is then reflected into the north-east quadrant using the rules of orthorhombic symmetry (Reches 1983). The data can then be compared to a slip model net for normal faults. The value of k and ϕ can be read directly off the slip model net, and for the Chimney Rock fault array $k = -0.16$ and $\phi = 54°$ (see Figure 6.15d). Since ϕ is a property of the rock, a change in the ratio of principle strains would result in a different value for k, but not ϕ for the same lithology.

6.4.3. Results

Rose diagrams of the strike of slip-surfaces in the off-fault deformation around the Big Hole fault and Blueberry fault (Figure 6.14a and b) show that the scatter in strike is approximately symmetrically around the main fault surface. The off-fault structures have a much lower acute angle between the strike sets than the main Chimney Rock fault array: 15-30° as opposed to 48°. It is difficult to distinguish individual strike sets on a simple stereonet of deformation band poles (Figure 6.14c and d). As displacement is accumulated on slip-surfaces, these may produce off-fault deformation of their own. This would explain why well-developed slip surfaces away from the main fault plane are always associated with relatively dense clusters of deformation (e.g. Figure 6.9). This would contribute to the scatter in deformation band strikes that is seen on the plots of deformation band orientation (Figure 6.14a and b). Because the datasets for the Big Hole and Blueberry Faults are relatively small, mutual planes have been constructed for all of the fault pole and slip vector pairs for each fault.

Figure 6.15a shows the odd axis construction for the off-fault structures around the Big Hole fault. Poles to fault surfaces are shown as circles and slip vectors as diamonds. Figure 6.15b is a contour plot of the intersections of all the mutual great circles. For the off-fault deformation around the Big Hole fault the odd axis is clearly vertical, and thus the similar and intermediate axes are horizontal. An upper limit on the value of α is the acute angle between the extremes of the scatter. Because the scatter is approximately symmetrical around the main fault surface, the similar axis has been defined as bisecting the scatter and the angle α must be less than 11°. The maximum value of k indicated by $\alpha \leq 11°$ is

$$-\sin^2 \alpha = k = -0.036. \qquad (6.6)$$

In Figure 6.15c all the data for the Big Hole fault (including slip-surfaces with no slickenline measurement) are rotated about the orthorhombic axes of symmetry for this system. This shows that the slip vectors are on average dip-slip, as would be expected for normal faults. The mean reflected pole can be compared to the slip

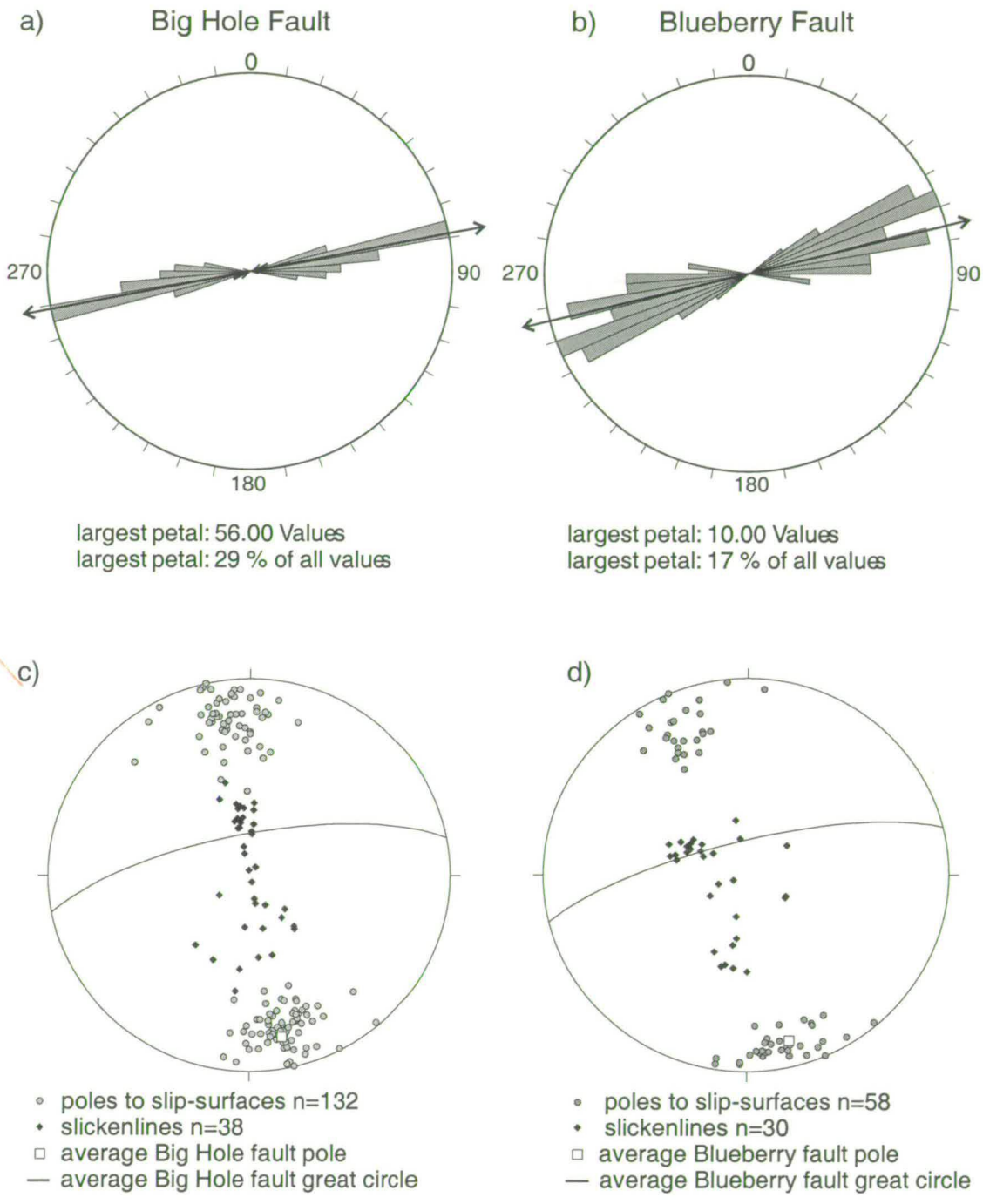

Figure 6.14. Rose diagrams of the orientations of slip-surfaces in the damage zone of a) the Big Hole fault and b) the Blueberry fault. The arrow represents the average strike of the main fault zone. The scatter in deformation band cluster orientations is symmetrical about the main faults. Poles to slip-surfaces and slickenlines for c) the Big Hole fault and d) the Blueberry fault. The square and the great circle is the average fault surface for the main fault. Note that the slickenlines are dip-slip for the Big Hole fault and oblique-slip (~20° W) for the Blueberry fault.

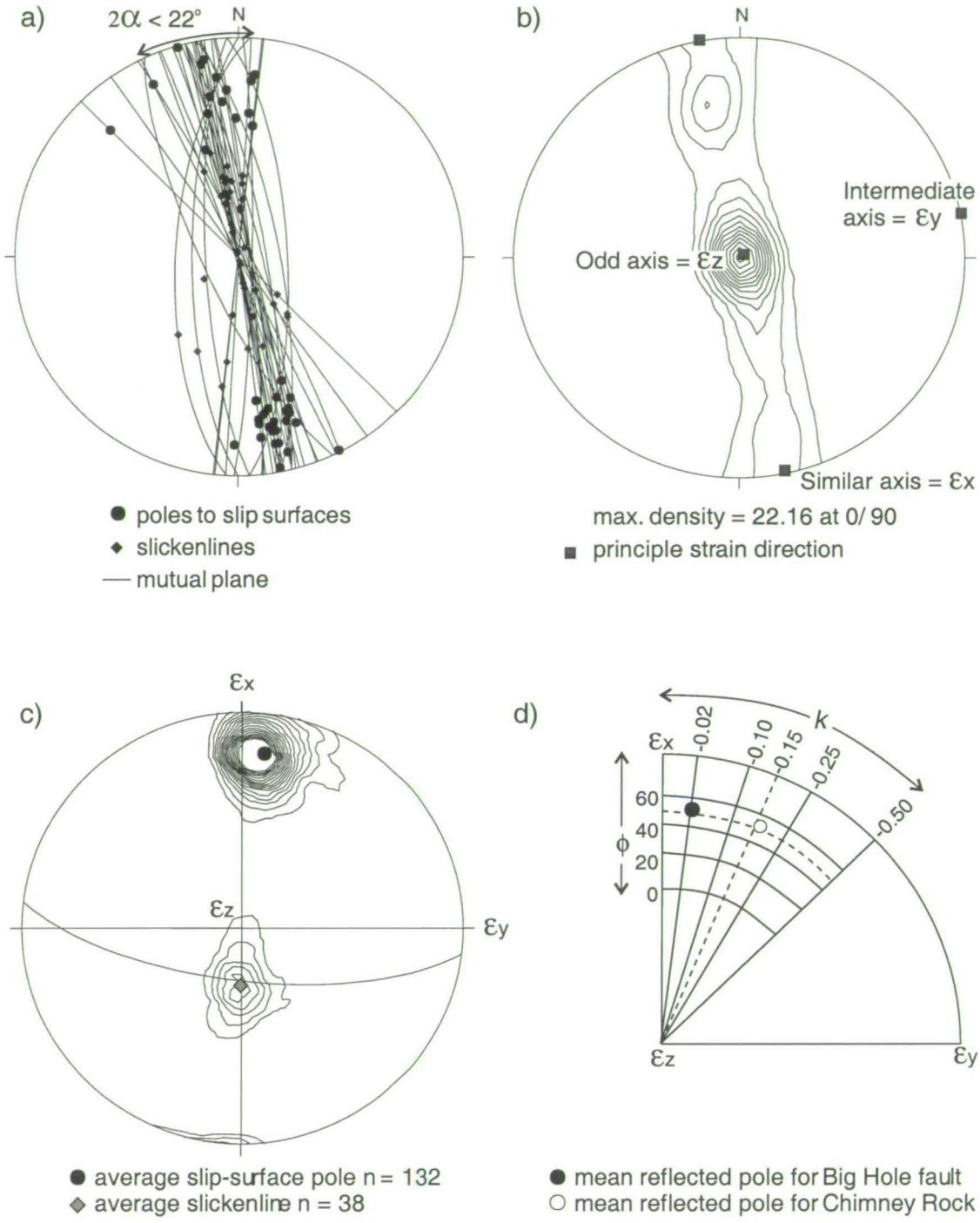

Figure 6.15. a) The odd-axis construction for the Big Hole fault. Great circles connect poles to slip-surfaces and their slickenlines. b) Contoured plot of mutual great circle intersections, the average intersection is the position of the odd axis. c) Contoured plot of fault pole and slip vector data rotated according to the rules of orthorhombic symmetry. d) The mean reflected pole plotted on the slip model net for normal faults (Reches 1983). The mean pole predicts k = -0.02 and $\phi = 53^{\circ}$. The mean reflected pole for the Chimney Rock fault array is shown for comparison

model net for normal faults (Figure 6.15d), showing that for this system of deformation bands $k = -0.02$ and $\phi = 53°$. This value of k corresponds to an angle between strike sets of 8° which is comparable to the data shown in Figure 6.14a. The value of ϕ is consistent with the data for the Chimney Rock fault array as a whole ($\phi = 54°$). The larger value of k (closer to zero) indicates that the strain is less oblate than that for the main Chimney Rock fault array. However, the data indicate that off-fault deformation around the Big Hole fault is still consistent with three-dimensional strain rather than plane strain.

The odd axis construction for the off-fault deformation around the Blueberry fault tip is shown in Figure 6.16a. The scatter in the strike of off-fault deformation bands and slip-surfaces is lower for the Blueberry fault tip than for the Big Hole fault (Figure 6.14b), which would indicate that a lower value of k might be expected. When the intersections of the mutual great circles are contoured (Figure 6.16b), two maxima are apparent indicating that there are two possible odd axes. The strongest is horizontal and oriented 348°-168°. A second maximum dips 57° towards 309°. The slip vectors on the fault surface at the tip of the Blueberry fault are not pure dip-slip (Figures 2.10c and 2.11d). This is also the case for slip-surfaces within the off-fault deformation around the fault tip. The slickenlines at the tip of the Blueberry fault consistently pitch about 70° to the west of pure dip-slip (Figure 4.7b). In this case, the deformation band clusters are symmetrical about an oblique fault slip vector, and the odd axis must be sub-vertical and compressional so the second of the two intersection maxima is more likely to be the odd-axis. The principle strain axes are thus oriented with a sub-horizontal maximum extension, ε_x, sub-perpendicular to the fault, a sub-horizontal minimum extension ε_y, sub-parallel to the fault and sub-vertical compression ε_z (Figure 6.16b).

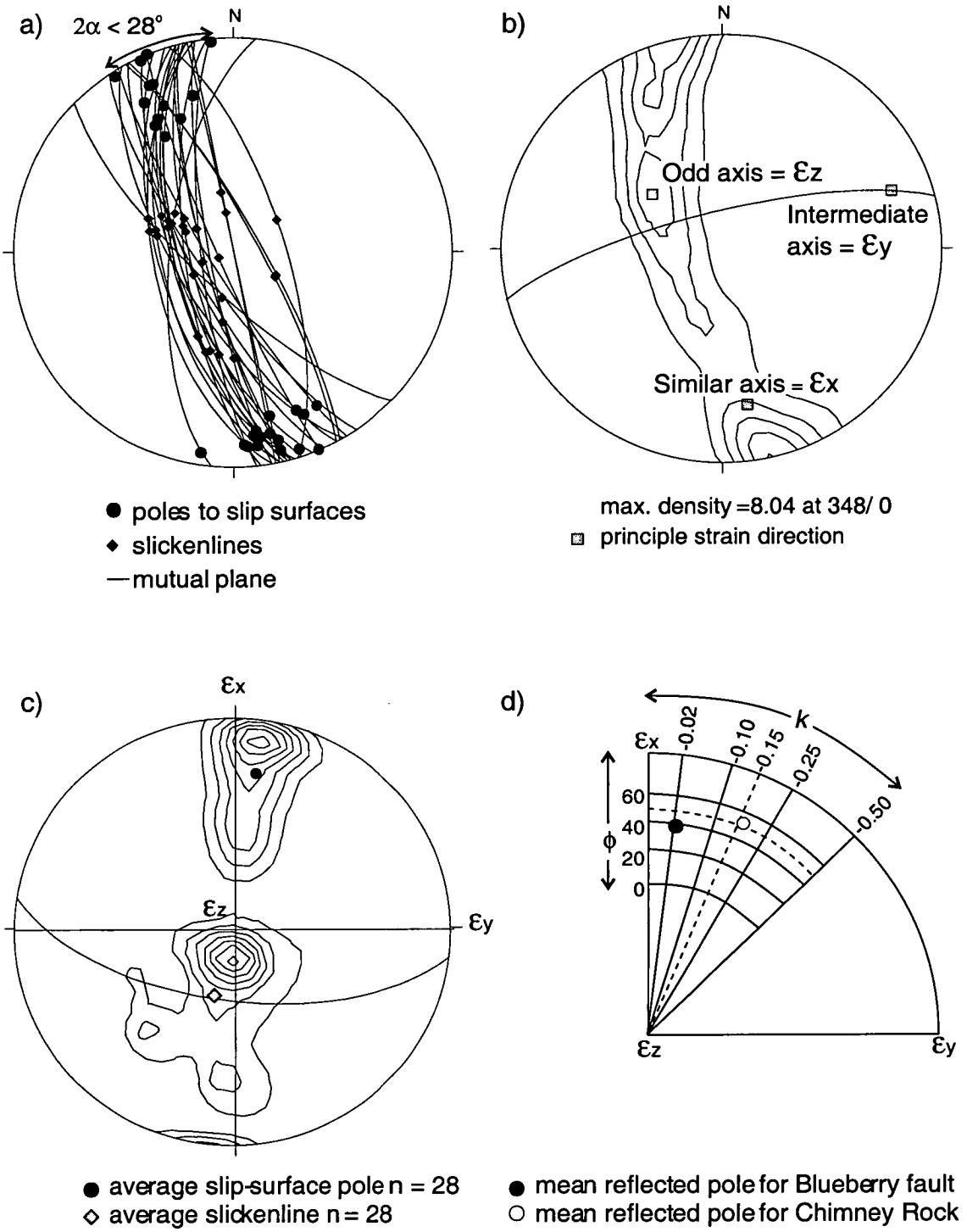

Figure 6.16. a) The odd-axis construction for the Blueberry fault. b) Contoured plot of mutual great circle intersections, the average intersection is the position of the odd axis. c) Contoured plot of data rotated according to the rules of orthorhombic symmetry. d) The mean reflected pole plotted on the slip model net for normal faults (Reches 1983). The mean pole predicts k = -0.02 and $\phi = 40°$. The mean reflected pole for the Chimney Rock fault array is shown for comparison.

The scatter in the strike directions places an upper limit on α of 14° ($k < -0.059$). When the data is rotated according to the rules of orthorhombic symmetry, the average slickenlines are down-dip of the average fault pole, meaning that the slip model net for normal faults is applicable (Figure 6.16c). On the slip model net, the average fault pole defines a k value of –0.02 and a ϕ of 40° (Figure 6.16d). The value of ϕ is rather lower than that for the overall Chimney Rock fault array data. This may be a function of the scatter in the data. The minimum value of k is larger than that for the off-fault deformation around the Big Hole fault but the value indicated by the slip model net is the same.

6.5. Discussion

6.5.1. Deformation density

From the deformation density maps it can be seen that the value of deformation density within a metre of the fault surface increases systematically with the displacement on the fault. The deformation density is 27% per 0.5 m^2 at the fault tip (D = 0) rising to 77% per 0.5 m^2 at the Juniper flat outcrop (D = 24 m). When this deformation density is plotted against the displacement on the main fault strand at that point, a good positive correlation ($R^2 = 0.88$) is seen (Figure 6.17a). The maximum deformation density at greater distances from the fault, however, seems to be fairly constant on all of the outcrop maps (around 30% per 0.5m^2). The strain represented by transects of the off-fault deformation shows no systematic along strike variation in strain with the value of displacement on the main fault.

These results imply that close to the fault (i.e. at distances less than a metre), the deformation density is related to the displacement on the fault at that point. Conversely, away from the fault the off-fault deformation width increases as displacement is accumulated but the maximum deformation density stays relatively constant. This is illustrated in cartoon form in Figure 6.17b. A mechanism that could generate this distribution of deformation density is suggested in Chapter 7.

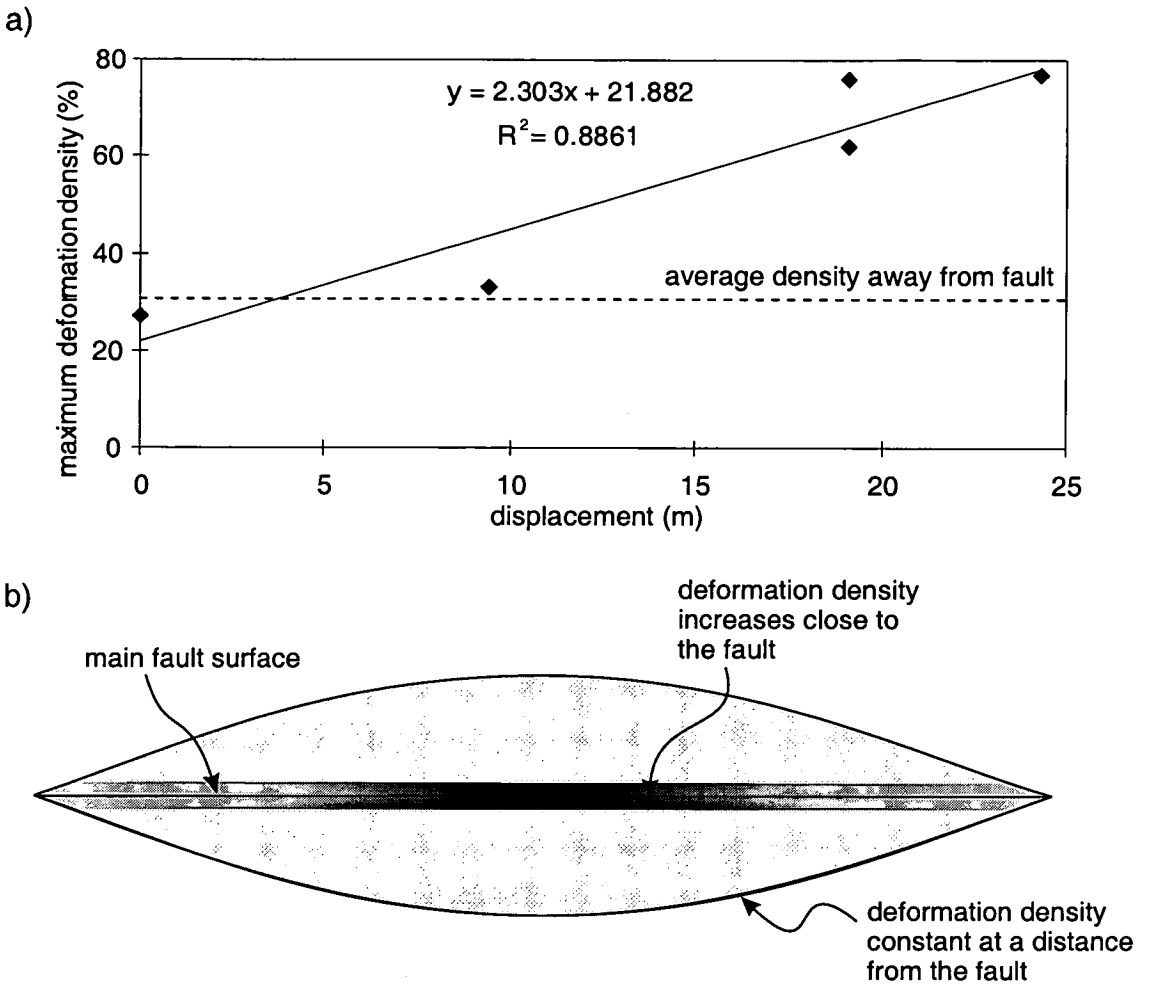

Figure 6.17. a) Maximum deformation density within the first few metres of the fault vs. displacement on the fault, from the outcrop scale deformation density maps. b) Cartoon map of the pattern of deformation density around the Big Hole and Blueberry faults. Darker shading indicates a higher deformation density. Within the first few metres of the fault the deformation density is proportional to the displacement on the fault. Further away from the fault the deformation density is constant.

6.5.2. Three-dimensional strain

The geometry of the off-fault deformation around the Big Hole fault is consistent with a three-dimensional strain field with a horizontal maximum extension, ε_x, perpendicular to the main fault surface, a horizontal minimum extension, ε_y, parallel to the fault and a vertical compression, ε_z (Figure 6.15). It has been suggested that along-strike extension is due to flexure of the hangingwall and footwall, which occurs to accommodate increasing displacement on the fault (Wu and Bruhn 1994, Roberts 1996a). This strain can be estimated for the Big Hole fault by assuming that the beds were originally horizontal so that the original along-strike length, l_o, of the beds is half the trace length of the fault (Figure 6.18). This is a reasonable approximation because the beds dip at only 5° in this area (see Figure 3.4). The final length, l_f, is the length of the beds after they have been displaced by the fault. Assuming a triangular displacement profile and symmetrical footwall uplift and hangingwall subsidence, l_f is then the hypotenuse of a triangle whose height is equal to the maximum displacement divided by two (Figure 6.18). According to this calculation the fault parallel strain is in the order of 3×10^{-5}.

The value of *k* resulting from the odd axis and slip models for both the Big Hole fault and the Blueberry fault, would indicate that the fault perpendicular strain is between 30 and 50 times the fault parallel strain. If the value of the fault parallel strain is taken from the calculations above, the fault perpendicular strain should be in the order of 0.9×10^{-3} to 1.5×10^{-3}. These values are lower than, but within the same order of magnitude as, the strain estimates from the transects of off-fault deformation (8.7×10^{-3}). Therefore the three-dimensional strain that gives rise to the orthorhombic off-fault deformation geometry is due to a component of along-strike strain, resulting from along-strike flexure of the hangingwall and footwall, in addition to fault perpendicular extension.

The off-fault deformation is not growing in the regional strain field that produced the orthorhombic symmetry of the overall fault array. Instead, the geometry of off-fault deformation is consistent with local three-dimensional strain around the Big Hole

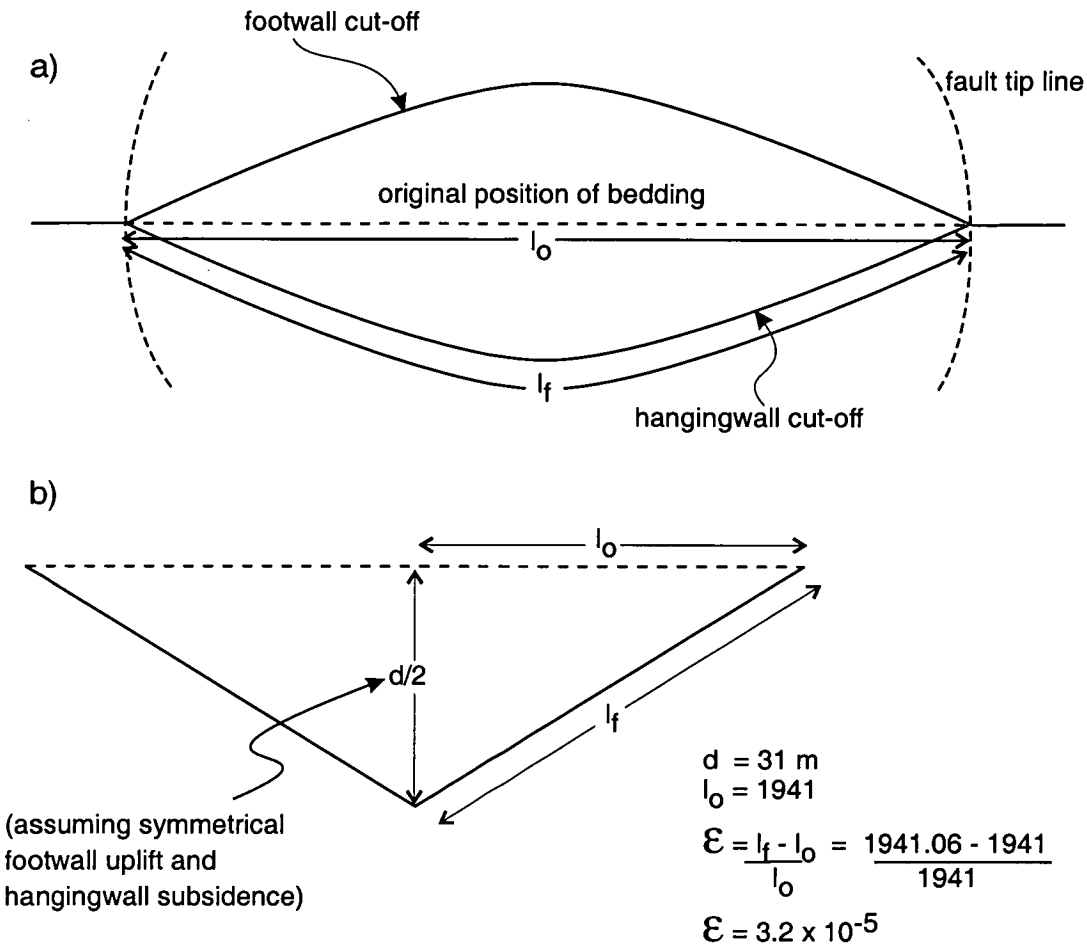

Figure 6.18. a) Cartoon of a faulted bed. The original length is that when the bed was flat and the final length is that when the bed has been stretched to accommodate hangingwall subsidence or footwall uplift. b) Diagram showing the calculation of the strain developed perpendicular to the fault due to stretching of the hangingwall and footwall. This calculation assumes that the displacement profile is linear.

and Blueberry faults i.e. fracture induced by slip on a pre-existing fault plane. It is important to note that analysis of the structures around one fault will give the contribution of that fault to the entire fault array. The sum of the strain represented by all the structures in the regional (Chimney Rock) fault array including the off-fault deformation around all the individual main faults would give the same strain as that for just the main faults in the array. Thus care must be taken when extrapolating from local to regional scales.

6.5.3. Fault slip vectors

Around the Blueberry fault the strain axes are rotated with respect to those around the Big Hole fault, reflecting the oblique slickenlines at the fault tip. Oblique slickenlines have previously been observed at the tips of individual fault segments along otherwise dip-slip faults in the Gulf of Corinth, Greece (Roberts 1996a and b). Roberts interpreted these oblique slickenlines as being due to differential fault parallel strain. The uplift in the footwall of the Gulf of Corinth faults is less than the subsidence in the hangingwall, resulting in larger fault parallel strains in the hangingwall. Wu and Bruhn (1994) also noted this effect in larger scale mountain range-bounding faults. However there is no evidence for differential uplift and subsidence at the Big Hole and Blueberry faults. Differential uplift and subsidence is not a requirement for faults that do not interact with the earth's surface (Gibson 1989, Gupta and Scholz 1998). Smaller faults are more symmetrical; they do not feel the effects of isostasy or loading of the hangingwall by sediment. Therefore the oblique slickenlines at the Blueberry fault tip, which is not considered to have been active at the earth's surface, are unlikely to de due to differential uplift and subsidence.

Martel and Boger (1998) documented the progressive change of style and orientation of fractures around the rim of re-activated joints. The fractures rotated from an angle of 45° with the fault for the Mode III tip to 70° at the Mode II tip. This is in agreement with the theoretical stress field which must rotate from Mode II at the upwards and downwards propagating tips of a normal fault to Mode III at the laterally propagating tips. It is possible that the rotation of the strain field that is

implied by the oblique slickenlines is a function of the stress field at a mixed-mode tip. This is an interesting possibility because it may allow us to estimate the position of the fault trace on the fault surface. Further studies of the geometry of structures at fault tips are required before this could become a useful tool.

6.5.4. Variation between the fault tip and fault centre

The along-strike variation of slip vectors described above suggests that the geometry of deformation at the fault tip is significantly different than that forming alongside a well-developed fault (Section 6.5.3). The value of k indicated by the scatter in deformation band strike is larger for the Blueberry fault tip (Figure 6.14a) than for the Big Hole fault (Figure 6.14b). Morewood and Roberts (1997) found that strain was more oblate (lower values of k) at the tips of individual fault segments and closer to plane strain in the centre of faults. This has not been convincingly demonstrated for the Blueberry fault due to the scatter in the data, but it suggests another way that the deformation at the fault tip could be distinguished from deformation alongside well-developed fault surfaces.

The angular relationship between the four fault sets in an orthorhombic array will have a critical effect on the connectivity and hence permeability of the resulting fault zone. The size and axial ratios of the pods of relatively undeformed host rock will control the amount of anisotropy of the system. If there is a change in the geometry of the fault system between the tip region and the main part of the fault, then this would be reflected in the permeability structure of the fault zone. This is an important result, which remains to be tested.

6.6. Summary

1. A zone of high deformation density is observed immediately adjacent to the main fault surface (within 1 m). The value of deformation density within this zone scales with the displacement on the main fault surface. This scaling implies that the density of deformation within a few metres of the fault is controlled by the accumulated amount of repeated slip on the fault surface.

2. Away from the main fault surface there is no difference between the maximum density (the number of deformation bands per unit area) at the fault tip and the well-developed fault. There is no correlation in the strain represented by transects across the off-fault deformation with the displacement on the main fault surface. Thus, away from the fault, the main effect of increased displacement is an increase in the width of the off-fault deformation, with no corresponding increase in deformation density.

3. Deformation band clusters within the off-fault deformation have an orthorhombic geometry, indicating that the strain is three-dimensional. An analysis of the geometry shows that the deformation band clusters near the centre of the fault grew in response to the local strain field around the fault, rather than in the regional (Chimney Rock fault array) strain field. This three-dimensional strain is due to fault parallel extension and along-strike flexure of the beds around the fault

4. Slip vector data is different for the fault tip and the well-developed fault surface. A component of oblique-slip is seen on slip-surfaces at the Blueberry fault tip, while slip-surfaces around the well-developed main Big Hole fault surface are dip-slip. This is reflected in the orientation of the principle axes of strain at the fault tip. The origin of oblique-slip at fault tips is unclear, but may be related to the stress field at a mixed-mode tip.

5. A method of determining the position of a fault trace on the fault ellipse is suggested by these findings. The structures at the fault tip are likely to be

influenced by the stresses ahead of the fault tip and will therefore be in different orientations at the Mode III sideways propagating lateral tips and the mode II upwards and downwards propagating tips. Further studies of structures around fault traces which cut fault ellipses at different levels are necessary to illustrate this conclusively.

7. DISCUSSION

7.1. Introduction

The purpose of this chapter is to synthesise and interpret the results of the displacement and off-fault deformation measurements presented in previous chapters. Firstly a brief review of the results is presented in Section 7.2. In the light of these results, three categories of off-fault deformation have been identified and are discussed in Section 7.3. A new model proposed by Cowie and Shipton (1998), which conceives of fault growth as occurring by repeated slip on small patches is discussed in Section 7.4. This model combines numerical modelling by P. Cowie with the field observations presented in this thesis. In the Cowie and Shipton (1998) model the summation of many small slip events on a fault results in the formation of triangular displacement profiles without creating unrealistic stress concentrations at the fault tips. The slip-patch model is used to interpret the observations of the Big Hole and Blueberry faults in Section 7.5. This model provides a good explanation for the displacement profile data, as well as providing a framework for a new conceptual model of fault zone evolution (Section 7.6).

7.2. Summary of displacement and off-fault deformation data

7.2.1. Displacement profiles

The data presented in this study are extremely high resolution measurements of vertical fault displacement (throw) across two fault zones. The data at the Blueberry fault tip is especially well constrained, and is the most detailed study of a fault tip displacement profile to date (Section 3.3). The fault tip, as defined by the displacement profiles, correlates well with the point where the fault is no longer represented by a single, well-formed slip-surface (Section 4.3.1). Contrary to existing models of fault displacement profiles which are either elliptical (for an elastic model, e.g. Pollard and Segall 1987) or bell-shaped (for an elastic-plastic model, Cowie and Scholz 1992a), the displacement at the Blueberry fault tip decreases in a linear

fashion towards zero at the fault tip (Section 3.4). One of the aims of this thesis is to re-evaluate and revise these models.

7.2.2. Off-fault deformation

The faults in this study consist of a fault core of tightly packed deformation bands, surrounded by off-fault deformation in the form of clusters of deformation bands (Section 4.4). One or more primary slip-surfaces can be identified within the fault core which are the surfaces upon which the majority of the fault displacement is accommodated (Section 4.6.3). Other slip-surfaces are found within the off-fault deformation zone, occurring within deformation band clusters, but these are discontinuous in lateral extent and have displacements typically between 30-200 cm. Beyond a certain distance, the rock is essentially undeformed (Section 4.6.1). When the width of the off-fault deformation is plotted against displacement it can be seen that the width is approximately twice the displacement (Section 4.6.2). This relationship suggests that the off-fault deformation formed as the fault was developing and accommodating further displacement. The off-fault deformation has a finite width at the fault tip (Section 4.3.1). Deformation ahead of the tip cannot be a direct result of the accumulation of displacement on the fault and is therefore interpreted as deformation associated with tip propagation.

Close to the fault (within ~2 m), the deformation density is greater where the displacement is larger. Although deformation is clustered, the maximum deformation density away from the main fault seems to be fairly constant, (Section 6.5.1). This would imply that, away from the main fault zone, increased slip on the fault results in an increase in the extent of off-fault deformation rather than increased deformation density. The structures surrounding the main fault surface have orthorhombic symmetry, implying that they formed within a locally controlled three-dimensional strain field (Section 6.4.3). This can be explained in terms of fault-perpendicular extensional strain that is much larger than the fault-parallel extension (Section 6.5.2). This is again consistent with these structures having formed due to displacement accumulation on the main fault surface.

7.2.3. Microstructures

Consistent with the results of previous workers (Aydin and Johnson 1978, Antonellini *et al.* 1994) I have shown that deformation bands in the Navajo Sandstone accumulate displacement by the addition of new bands to a cluster until, at some point, a slip-surface nucleates within the cluster (Section 5.5.1). The exact mechanism of slip-surface nucleation remains unclear, but there is evidence that slip-surfaces nucleate in small patches and then propagate together into an anastomosing network as described in Section 5.5.2. Repeated slip on slip-surfaces is suggested by a lower porosity and grain size immediately adjacent to the slip-surface as well as the presence of open (unhealed) microfractures and Riedel shears within this low porosity region.

There is no correlation of grain scale microfracture density in the Navajo Sandstone with distance from the fault (Section 5.5.3). I have shown that these fractures are likely to be inherited fractures rather than fractures generated by deformation on the main faults (Section 5.5.4). Microscopic deformation associated with the development of deformation bands in porous rocks generally takes place as grain boundary microfractures, which are very difficult to quantify in this rock type. In any case, experimental studies of the deformation of high porosity sandstones emphasise that only a small amount of microfractures occur before the production of deformation bands (Lockner et al. 1992, Mair 1997). From these experiments it is expected that this will be the case in sandstones with a porosity greater than 10% (e.g. Dunn *et al.* 1973, Lockner *et al.* 1992). The deformation within the Navajo Sandstone ahead of the Blueberry fault tip consists of macroscopic deformation in the form of deformation bands with an unquantifiable amount of grain boundary microfracturing (Section 5.5.5). These observations are entirely consistent with the experimental results. These results emphasise the importance of host rock lithology on the structural style of off-fault deformation.

7.3. Categories of off-fault deformation

Throughout this thesis the term *off-fault deformation* has been used to describe all of the deformation associated with and surrounding the faults in my field area. The results presented in this thesis have allowed the deformation around the Blueberry and Big Hole faults to be divided into two genetic types: deformation ahead of the fault tip due to tip propagation processes and deformation surrounding the well-developed fault surface due to the accumulation of displacement on the fault. In order to eliminate the confusion of names given to these type of structures, it has been suggested that *off-fault deformation* be used as a purely descriptive term with no implications for the genesis of the deformation. Off-fault structures at different localities around the main fault surface can then be given the specific names suggested below, which indicate the mechanism by which they form as shown in Figure 7.1. I have identified and characterised all three types of off-fault deformation.

7.3.1. The process zone

Deformation at fault tips is commonly referred to in the literature as the *process zone* (e.g. Reches and Lockner 1994, Vermilye and Scholz 1998). This reflects the concept that the faults are growing by propagation through relatively undeformed rock and that processes at the fault tip deform the rock in some way in order to break through and form new fault surface. An inactive wake of deformed rock would thus be expected to be preserved behind the propagating fault tip. The model of Cowie and Scholz (1992a) suggests that the width of the process zone scales with the length of the fault (Figure 7.1a). Previously the process zone has been visualised as a population of microfractures which decay in density with distance from the fault (Brock and Engelder 1977, Knipe and Lloyd 1994, Anders and Wiltschko 1994, Vermilye and Scholz 1998). The orientation of such microfractures has been suggested to be controlled by the stress field at the tip of the fault (Scholz *et al.* 1993, Vermilye and Scholz 1998).

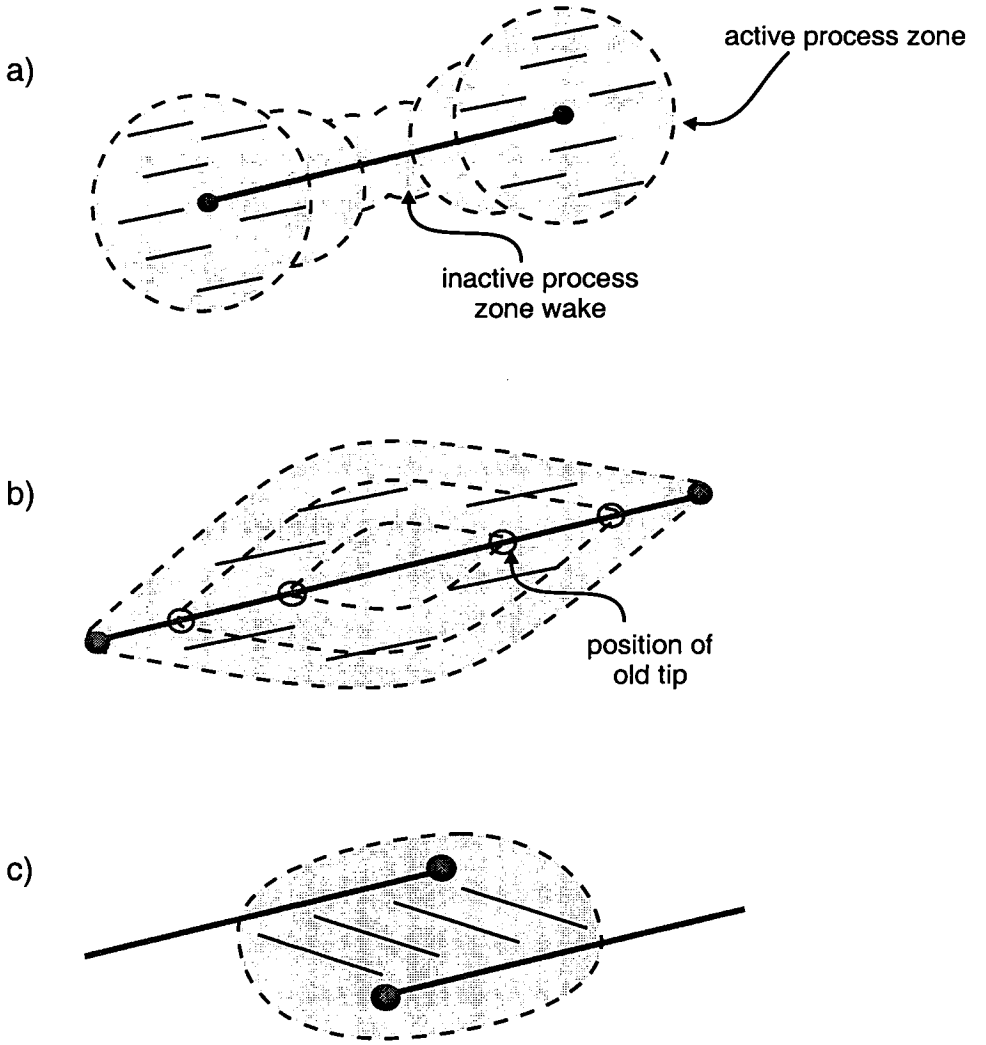

Figure 7.1. Conceptual models of damage zones. A *process zone* forms ahead of a propagating fault tip, leaving an inactive "wake" of damage as the fault propagates past its old tips. a) If the fault slips along its entire length in each growth event, the width of the wake will increase towards the tips of the fault (the stress concentration scales with fault length, Cowie and Scholz 1992a). b) A *kinematic damage zone* forms around a fault due to continuing displacement accumulation on that fault. The width and/or density of deformation will increase towards the center of the fault which has seen more slip events than the tips. c) A *linkage damage zone* forms where two faults link (segment boundaries or relay ramps).

The observations presented in this thesis show that both of these predictions do not apply to the faults in this field area. The process zone deformation at the Blueberry fault tip consists of macroscopic deformation bands rather than a population of microfractures, because the style of deformation in the process zone is a function of the rock type (Section 5.5.4). The width of the off-fault deformation at the Blueberry fault tip is much smaller than that predicted by the Cowie and Scholz (1992a) model. This model would predict that the process zone would be 10% of the length of the fault, i.e. between 360-400 m. In fact the macroscopic deformation at the fault tip extends for 12 m, i.e. only 0.3% of the length of the fault. The slip-patch model presented below (Section 7.4) provides an explanation for this observation.

7.3.2. The kinematic damage zone

Deformation will occur around a fault as it accumulates displacement. In this thesis off-fault deformation around a well-developed fault surface is called the *kinematic damage zone* (Figure 7.1b). The kinematic damage zone includes deformation due to repeated slip on the fault and the flexure of bedding surfaces around the fault (e.g. Jamison and Stearns 1982). Because the deformation is due to processes that accommodate displacement, the width and/or deformation density of the damage zone will be expected to increase where more displacement has accumulated and the fault has been active for longer (Figure 7.1b). At the Blueberry and Big Hole faults the width of deformation increases with the displacement; a mechanism that could produce scaling of this nature is presented below (Section 7.5.3).

The kinematic damage zone would overprint and may re-utilise the process zone structures. However, the stress field at the fault tip will be different than that alongside a fault that is accumulating displacement. I have shown that the geometry of deformation around the Big Hole and Blueberry faults is different at the tip than adjacent to the well-developed fault (Section 6.5.4). Structures at the fault tip have oblique-slip slickenlines whereas those around the well-developed fault have dip-slip slickenlines. Additionally there is evidence that the strain represented by off-fault deformation around the well-developed fault is closer to plane strain than at the fault

tip. Thus the process zone and kinematic damage zone have differing geometries and can therefore be distinguished.

7.3.3. The linkage damage zone

Deformation may be particularly intense where the terminations of many rupture events on the fault have been focused. These may be regions where the fault has a strong patch or a geometrical irregularity which makes it hard for ruptures to propagate through. This would agree with the observation that deformation is often concentrated at areas where two fault strands link (Peacock and Sanderson 1991, Trudgill and Cartwright 1994), or at areas where locally the fault surface has a strong patch (Vermilye 1996). The terminations of earthquake ruptures often (though not always) correspond to fault segment boundaries that are visible on the ground and in displacement profiles (King 1986). In this thesis the term *linkage damage zone* is used for this type of off-fault deformation. Linkage zones may persist as regions of low displacement on the main fault surface, even when the fault segments are geometrically hard-linked (Walsh and Watterson 1991, Section 1.5.2). We would expect to see wide and/or intense zones of deformation surround areas of low displacement on the fault surface (Figure 7.1c). Note that this is the opposite scaling relationship that is seen with a kinematic damage zone.

7.4. The slip-patch model of fault growth

7.4.1. Conceptual framework

The high resolution displacement profiles presented here show that linear fault tip displacement gradients are a real feature of fault displacement profiles. Previously published models for fault growth do not predict linear fault tip displacement profiles (Section 1.6). These models are two-dimensional and require that the fault slips along its entire length in each faulting event. These assumptions are necessary for computational simplicity, but real faults are more complex. Experimentally generated faults can be seen to propagate by the coalescence of out-of-plane fractures (Cox and Scholz 1988). In addition, deformation occurs in a zone around fault tips associated with fault propagation (McGrath and Davison 1995, Martel and Boger 1998, Vermilye and Scholz 1998, Section 4.3.1 this study). Moreover most seismically active faults slip in ruptures which are much smaller than the length of the fault, so it is not appropriate for fault models to be constrained to growth by failure of the entire fault surface.

Earthquake data show that faults rarely slip along their entire length; instead, portions of the fault surface rupture in one earthquake event. Rupture on a small patch of a fault relieves the stress on that portion of the fault but results in loading of adjacent areas (Figure 7.2a). This loading effect can be seen in the distribution of aftershocks around a fault rupture (Scholz 1990 p206, King *et al.* 1994, Hodgkinson *et al.* 1996). Fault ruptures are often terminated at segment boundaries. However, Roberts (1996a) reported surface ruptures of earthquakes on faults in the Gulf of Corinth which were shorter than the host fault segments. Thus it is not simply the geometry of the fault which controls the rupture size. Small or aseismic faults can also grow by repeated rupture of small portions of the fault surface. Vermilye and Scholz (1998) examined the microfracture population around several small faults with lengths ranging from 80 cm to 40 m. Cross cutting sets of differently oriented microfractures led them to conclude that these faults had grown by repeated propagation of ruptures which were smaller than the surface of the entire fault. Thus fault growth by multiple slip events, each of which is smaller than or equal to the size

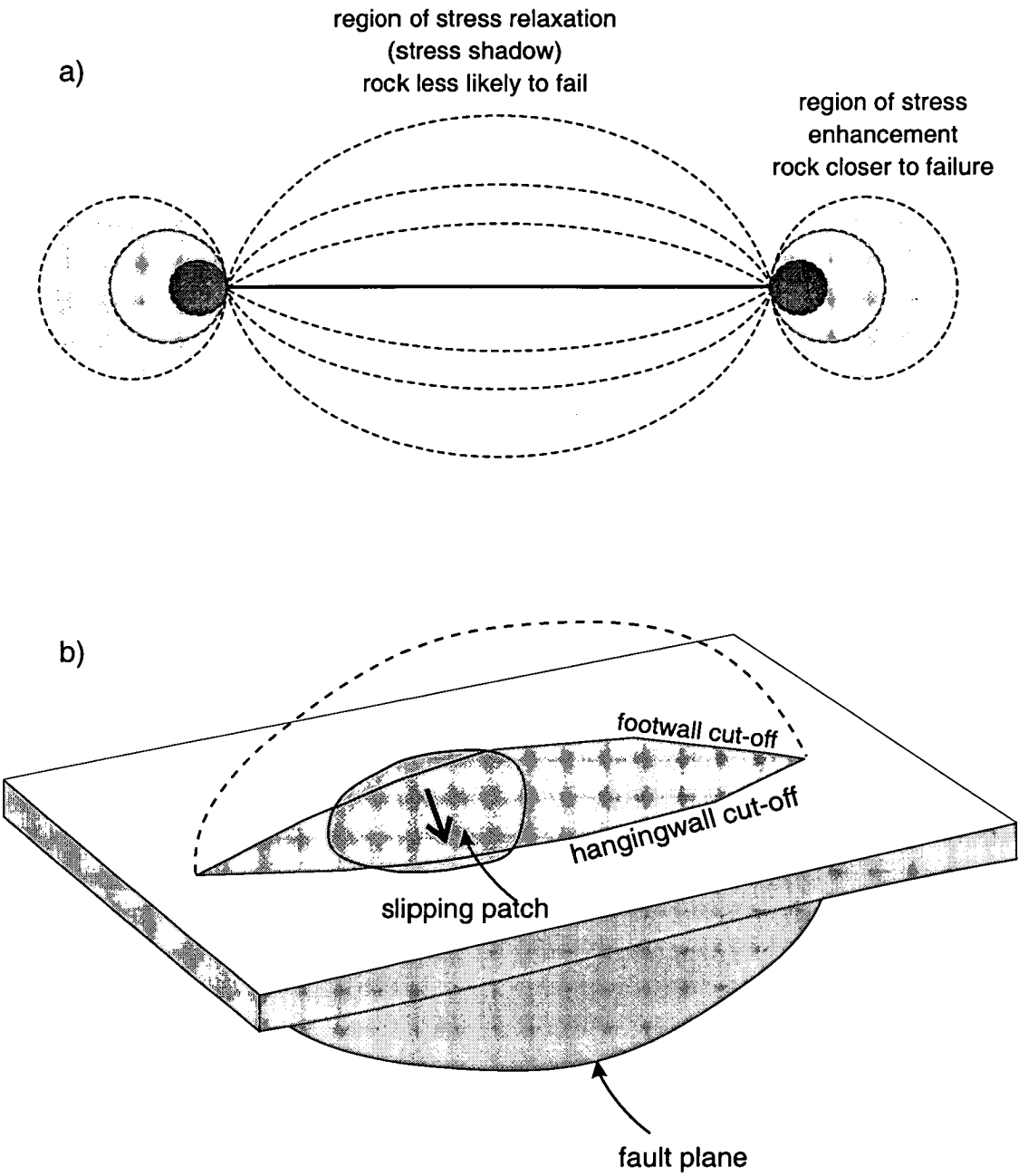

Figure 7.2. a) Idealised plan view of an elastic fault with stress enhancement along strike and regions of reduced stress adjacent to the fault. The dotted lines are countours of equal stress. The grey area is the region of enhanced stress. Deformation is likely to be triggered in the stress enhanced region and retarded in the stress shadow. b) Cartoon of a slip patch on a fault surface.

common growth mechanism in real faults. A schematic representation of such a slip-patch on a fault is shown in Figure 7.2b.

If, once a fault has ruptured, it can regain its strength through some form of healing, the slip-patch can start to accumulate stress again. Chemical healing occurs by the deposition of material on the fault surface, which is often enhanced by high fluid flow in and around fault systems. Mechanical healing occurs due to the difference between static and dynamic friction (Scholz 1998). An increased angle of friction due to tighter packing and increased interlocking within cataclastic fault gouge will also inhibit further movement. The interlocking of asperities can also cause the strength of a fault to increase with time (Heimpel 1997). One of the key assumptions of the model presented below is that the healing is fast with respect to the recurrence time of slip events. Annealing of microfractures by quartz cementation has been shown to occur very rapidly in laboratory experiments, and could occur in as short a time as a few months (Smith and Evans 1984, Brantley *et al.* 1990). Experimental data indicates that mechanical healing could occur at rates of 3-6 MPa per decade after a rupture has ceased (Marone 1998).

The effects of healing and reloading of small slip-patches have not been considered in previous models of fault growth. Two important effects become apparent if these effects are taken into account. Firstly, the rock around the tip of the fault is less stressed than if the entire fault surface had slipped. Secondly, the fault surface is reloaded by the stress changes around a slip-patch. This will bring the fault closer to failure than would be the case if only the regional tectonic stress was applied. These effects are incorporated into a new numerical model presented in Cowie and Shipton (1998), which provides an explanation for the displacement profile and off-fault deformation data observed in this study. The model is summarised below.

7.4.2. The slip-patch model

This model idealises the fault plane as consisting of a linear array of elements of different strength. These strengths are randomly picked from a pre-determined distribution which varies between the maximum strength, σ_{max}, and the minimum strength, σ_{min}. The fault therefore has uniformly random strength heterogeneity varying about a constant average strength. As the fault is loaded, the weakest element will fail. In this model, the weakest element is considered to be the most critically stressed, that is, the one that has the greatest difference between its strength and the applied stress. This failure results in a reduction of stress locally, but stress is transferred to neighbouring elements. Figure 7.3 shows the displacement profile and stress variation for two elements in the model. For simplicity the displacement on an individual slip-patch has a triangular distribution. However, the peak stress on adjacent elements is limited by the strength of the weakest of the two neighbouring elements, σ_i . The stress at either side of the slip-patch decays with distance such that

$$\sigma(r) = (\sigma_i - \sigma_{min})(R/(2r + R))^2 \qquad (7.1)$$

where R is the size of the element and r is the distance away from each end of the slip-patch (Cowie and Shipton 1998).

The broken element is healed instantaneously by assigning it a new strength drawn randomly from the initial strength distribution. The stress perturbations around the slip-patch can bring other elements in the array up to their yield strength, causing them to fail (Figure 7.3b). Only the most critically stressed element ruptures in any one failure event. The redistribution of stress for the entire array is calculated before allowing the next most critically stressed element to fail. As a consequence of the healing of slip-patches, the ruptured area can support subsequent loading. A positive feedback develops between the slipping and healed portions of the fault. As these events are summed over time, the symmetry of the reloading results in an approximately symmetrical triangular shaped profile.

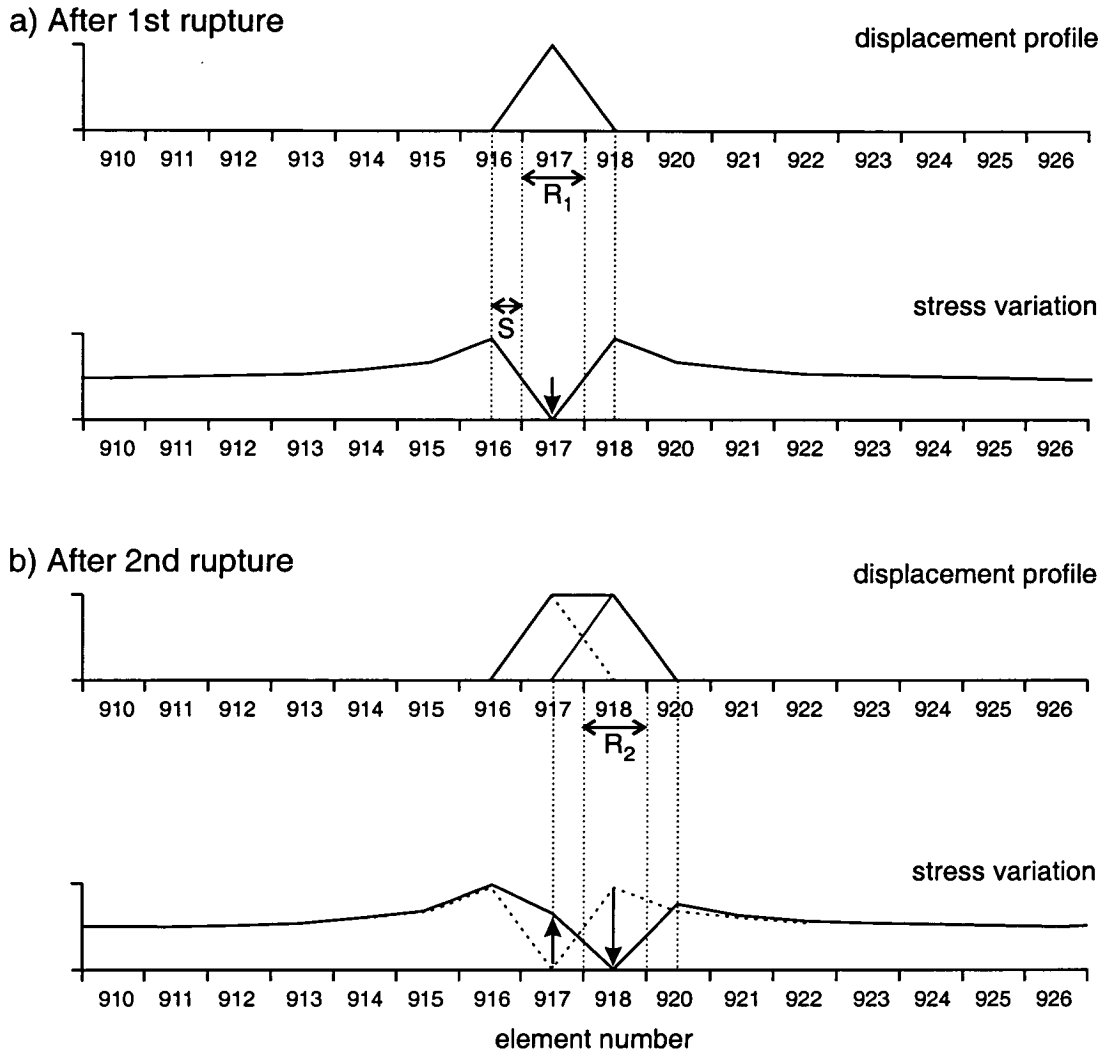

Figure 7.3. Displacement distributions and stress variations for the slip patch model after a) the first, R_1, and b) the second, R_2, rupture events. Arrows indicate where stress drop occurs and in b) reloading of a previously ruptured element. S is the length of the process zone for each element. From Cowie and Shipton (1998).

Examples of the stress distribution and displacement profile for a model run are shown in Figure 7.4. Each element is assumed to be 1 m long and each slip event accumulates a maximum of 1 cm displacement. The displacement profile in the vicinity of the tip of a 870 m long fault with 11 m maximum displacement is shown in Figure 7.4a. The displacement profile has an approximately constant gradient as far as the tip. Figure 7.4b shows the distribution of stress (solid line) compared to the strength of the material that the fault is propagating through (dotted line). The material strength varies randomly about an average value of 1.0 with $\sigma_{max} = 1.4$ and $\sigma_{min} = 0.6$. The strength of the healed slip-patches also varies randomly; no strain softening or hardening is assumed. The stress on the fault fluctuates strongly, reflecting the continual process of rupturing, healing and reloading with each rupture event. At the tip, the stress is approximately equal to the local strength. Away from the tip, the stress decays away rapidly to a background level which is approximately the same as the average level on the fault. Many elements, including some beyond the tip, have a stress which is greater than their strength. However these elements do not fail because rupture only occurs on the most critically stressed element.

In the examples presented above, the size of the slip-patch was constant throughout the lifetime of the fault. However slip-patches could potentially be any size up to the length of the fault. The model of Cowie and Scholz (1992a), where the entire fault surface fails in each slip-event, is an end member of the slip-patch model.

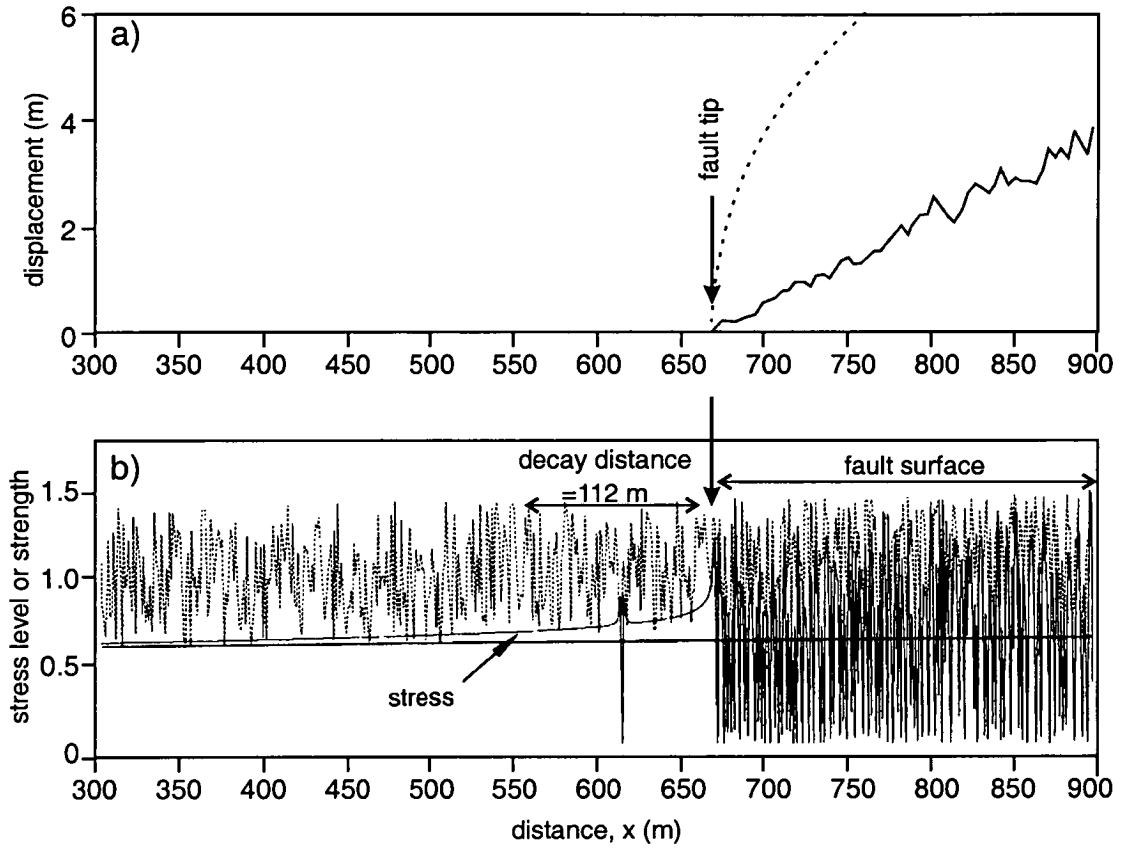

Figure 7.4. Displacement profile and stress distribution near the left-hand tip of a fault generated using the slip patch model. The fault has a total length, L, of 870 m and the size of one element is 1 m. a) Displacement profile on the fault showing an approximately linear decrease towards the tip. The dots indicate an elliptical (elastic) profile for a fault with the same D_{max} and L. b) Stress (solid line) compared to the strength of the material (dashed line). The strength properties vary randomly and no mechanical weakening of the fault is included. The stress decays rapidly beyond the fault tip to 10% above the regional stress at ~112 m from the fault tip. From Cowie and Shipton (1998).

7.4.3. Implications of the slip-patch model for displacement profiles

Normalised displacement profiles at three stages in the model evolution are shown in Figure 7.5a. The profiles are approximately triangular with the maximum displacement near the centre of the fault. The profiles show some asymmetry and change shape as they develop through time. The maximum displacement as a function of length throughout lifetime of the model is shown in Figure 7.5b. This illustrates that the model exhibits a step-like growth pattern with periods when the tip propagation is dominant and periods when displacement accumulation is dominant. Overall, however, the model produces self-similar fault growth in the manner of the dataset for real faults (Section 1.5.1). The tip displacement profiles for six model time steps are shown in Figure 7.6. The tip gradient is roughly constant throughout the evolution of the fault. The gradient is controlled at any one time by two main processes: the formation of isolated ruptures ahead of the tip which then link to the main fault surface (decreasing the displacement gradient) and the build up of displacement behind the fault (increasing the displacement gradient). This is dependent on the strength of the elements at the tip. If the fault comes up against a strong element then displacement accumulation will be favoured: if the elements at the tip are weak then fault lengthening will occur.

The variation of the host rock strength produces variation in the shape of the fault profiles with time, but overall the fault maintains an approximately linear tip profile. The variation of stress on the fault surface reflects the irregular fault displacement profile. These are common features of real faults (Section 3.5.1). Dawers *et al.* (1993) and Cartwright and Mansfield (1998) have observed a variation in tip gradients and displacement profile symmetry for isolated (i.e. non-interacting) faults in a simple tectonic setting. Lockner *et al.* (1991) observed episodic fault growth in experimental deformation of high porosity (>10%) sandstones. They postulated that, although they had selected apparently uniform rock samples, the episodic fault growth was controlled by strong patches within the sample. This model provides an explanation for the variation in tip gradients, asymmetrical fault displacement profiles and episodic fault growth, and may explain some of the order of magnitude

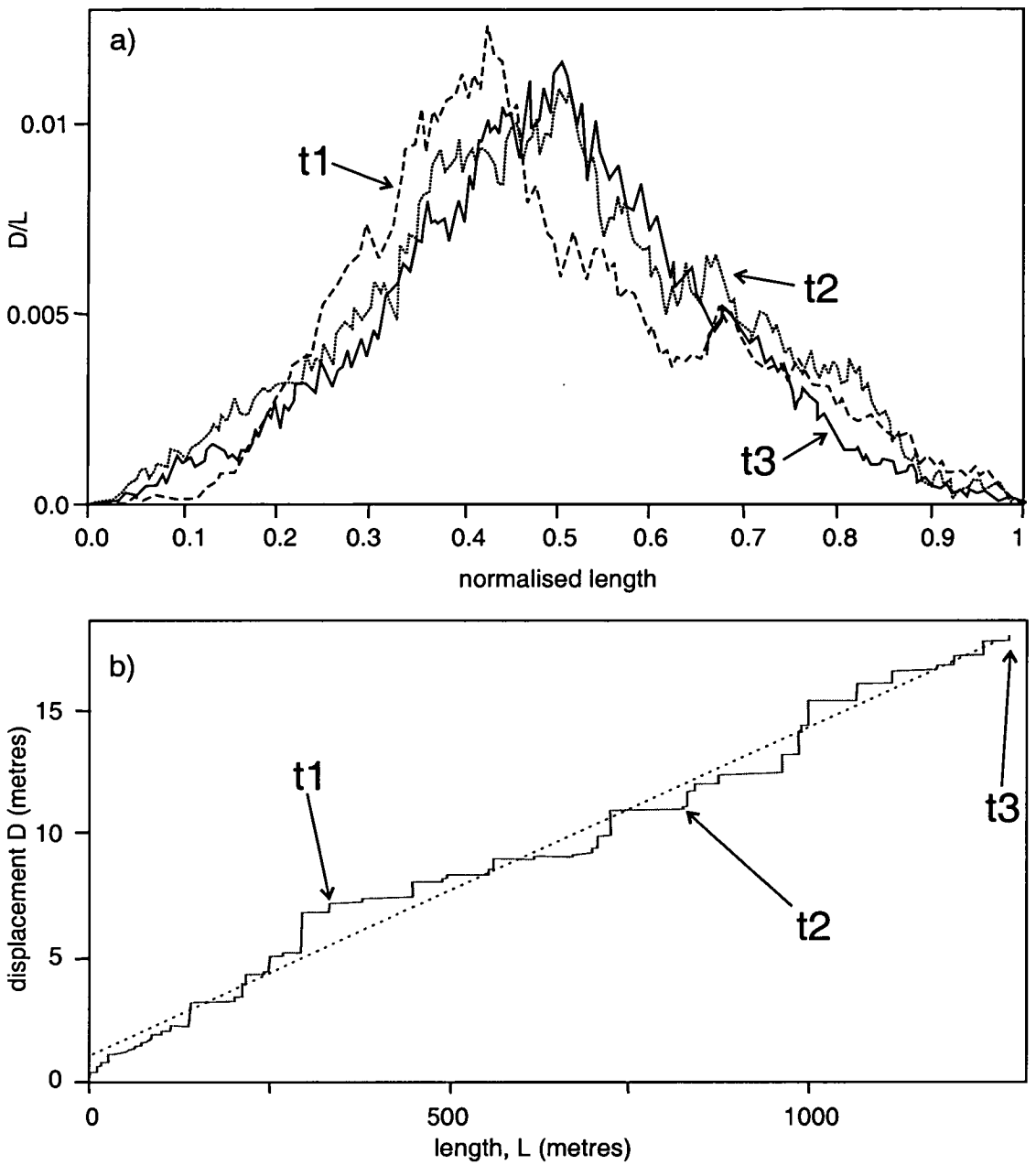

Figure 7.5. Self-similar growth in the slip patch model. a) Normalised displacement profiles calculated at three sucessive points in the fault growth history, t1, t2, t3. b) Displacement as a function of length during the progressive growth of an idividual fault. Overall the growth is self-similar with an average D/L = 0.012. The three growth stages in a) are indicated. From Cowie and Shipton (1998).

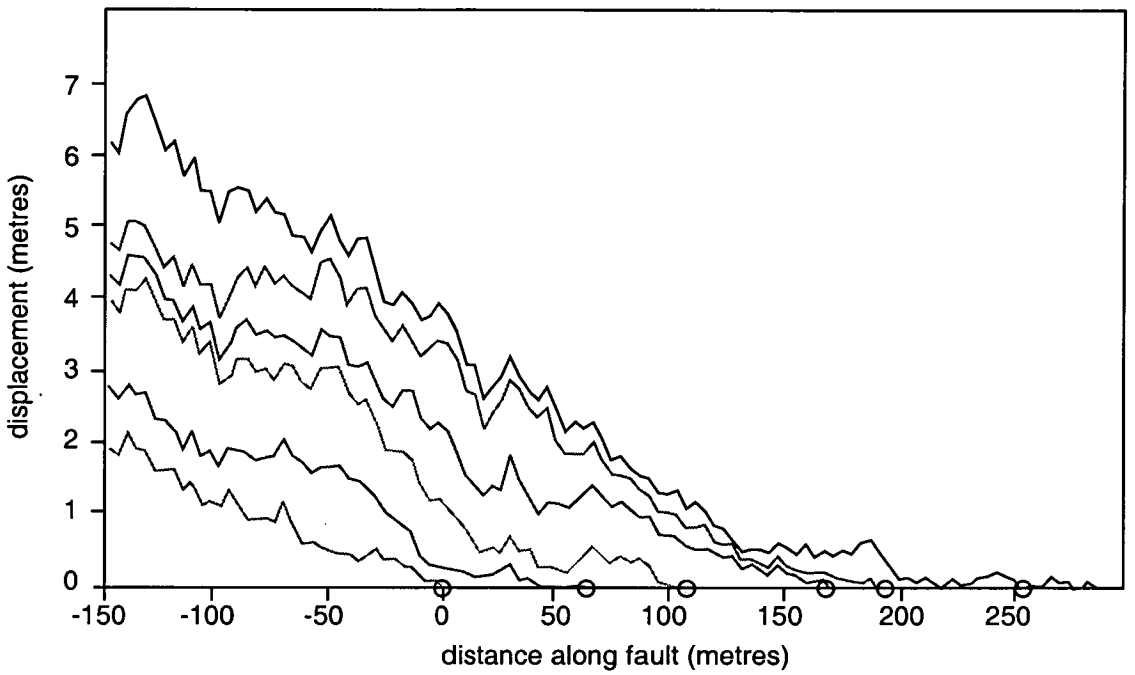

Figure 7.6. Time evolution of the displacement profile behind the right tip for the fault shown in Figure 7.4. for six successive profiles in the growth history. Grey circles indicate the tip position at each stage, defined as the point where the displacement first falls to zero away from the centre of the fault. From Cowie and Shipton (1998).

scatter in D_{max}/L plots of fault dimensions (Section 1.5.1). One important result of the slip-patch model is that the D_{max} can no longer be linked in a simple way to the properties of the host rock around the tip. However the tip gradient is sensitive to the local strength, or strength distribution of the host rock. Further studies of the variation of fault tip displacement gradients in different lithologies with varying strength anisotropy (such as joints) are necessary to investigate this control.

The individual ruptures in the model have a triangular displacement profile (Figure 7.3). This is merely for computational simplicity. Real seismic ruptures on faults can have extremely complicated shapes (e.g. McGill and Rubin 1999). Because the number of slip-patches needed to generate the displacement profiles is so large, the shape of individual slip-patches is essentially unimportant. The fundamental control which produces triangular displacement profiles is the symmetry of the reloading. If stress is always enhanced at the terminations of a slip-patch, and that patch is subsequently allowed to support stress (i.e. healed), then for a large number of ruptures the displacement profile will always tend to be triangular.

7.4.4. Implications of the slip-patch model for off-fault deformation

The numerical model described above applies to a planar fault, and deformation around the fault surface is not explicitly considered. However, this model has important implications for the form of the off-fault deformation. The fault growth model proposed by Cowie and Scholz (1992a) predicted that the width of the process zone due to fault tip propagation would scale with the length of the fault (Figure 7.1a). The new slip-patch model predicts different relationships between displacement and off-fault deformation structure which are more consistent with those observed at the Big Hole and Blueberry faults.

For a fault growing by the accumulation of many small slip-patches, each individual slip event would relieve stress adjacent to the slip-patch and concentrate stress at its terminations (Figure 7.2a). Deformation will be produced where the stress concentration exceeds the yield strength of the rock; in this case around the perimeter of each slip-patch. The size of the region of enhanced stress, and hence the width of the off-fault deformation, would be expected to scale with the size of the slip-patches. Therefore the deformation beyond the fault tip is the result of stress enhancement at the termination of the last slip-patch to rupture the fault at the tip (Figure 7.7). Structures at the fault tip are strictly speaking a process zone as defined in Section 7.3.1. (Figure 7.7). As this slip-patch is likely to be smaller than the dimension of the entire fault surface, the width of the process zone at the fault tip will not scale with the length of the fault. Instead, the process zone width is an indication of the dimensions of the last slip-patch (or slip-patches) to have ruptured the fault tip.

Every slip-patch along the fault surface will produce deformation at its terminations. This deformation is part of the kinematic damage zone, distinct from a process zone wake, because it is due to repeated slip on the fault (Section 7.3.2, Figure 7.7). The shape of the kinematic damage zone depends on the relative size of the slip-patches as the fault grows. The model of Cowie and Shipton (1998) assumes for simplicity that all the slip-patches are of the same size. This would result in a kinematic damage zone of constant width. If the slip-patches are much smaller than the fault then a

narrow zone of deformation would be expected to occur adjacent to the main fault zone (Figure 7.7a). The density of deformation in the kinematic damage zone should scale positively with the displacement on the fault according to this model, because there have been more rupture events at the centre of the fault than at the tip.

A more realistic scenario is that a fault fails by slip-patches, that can initiate at any position along the fault, of all possible sizes up to and including the size of the fault. Because stress enhancement takes place preferentially at the ends of the slip-patch, the largest slip-patches do not cause kinematic damage at the centre of the fault. Superimposing these slip-patches therefore results in a zone off-fault deformation that is wider at the fault tips (Figure 7.7.b). Additionally, because more slip events take place at the centre of the fault there would be a greater density of deformation at the centre of the kinematic damage zone and the deformation density will decay away from the fault.

A third scenario is that the structure of the fault surface itself evolves during the accumulation of displacement, for instance, due to the smoothing of asperities or jogs in the fault surface. In this case larger slip-patches may only occur along the central portion of the fault. The slip-patch size would then be proportional to the displacement on the fault and the kinematic damage zone would be wider overall towards the fault centre. However once again, because stress enhancement is located at the ends of the slip-patch, the largest slip-patches do not enhance the stress, and hence cause kinematic damage along the centre part of the fault. When the effects of stress enhancement for all of the possible slip-patches is superimposed, the result is a narrower kinematic damage zone in the very centre of the fault (Figure 7.7.c). Again, the deformation density will be higher at the centre of the fault where more slip events have taken place.

None of these scenarios produce the positive scaling of off-fault deformation *width* with displacement seen around the Big Hole and Blueberry faults that was demonstrated in Section 4.5.2 (Figure 4.29). In Figure 7.7 the regions of enhanced stress at the termination of each slip-patch have been superimposed. This means that

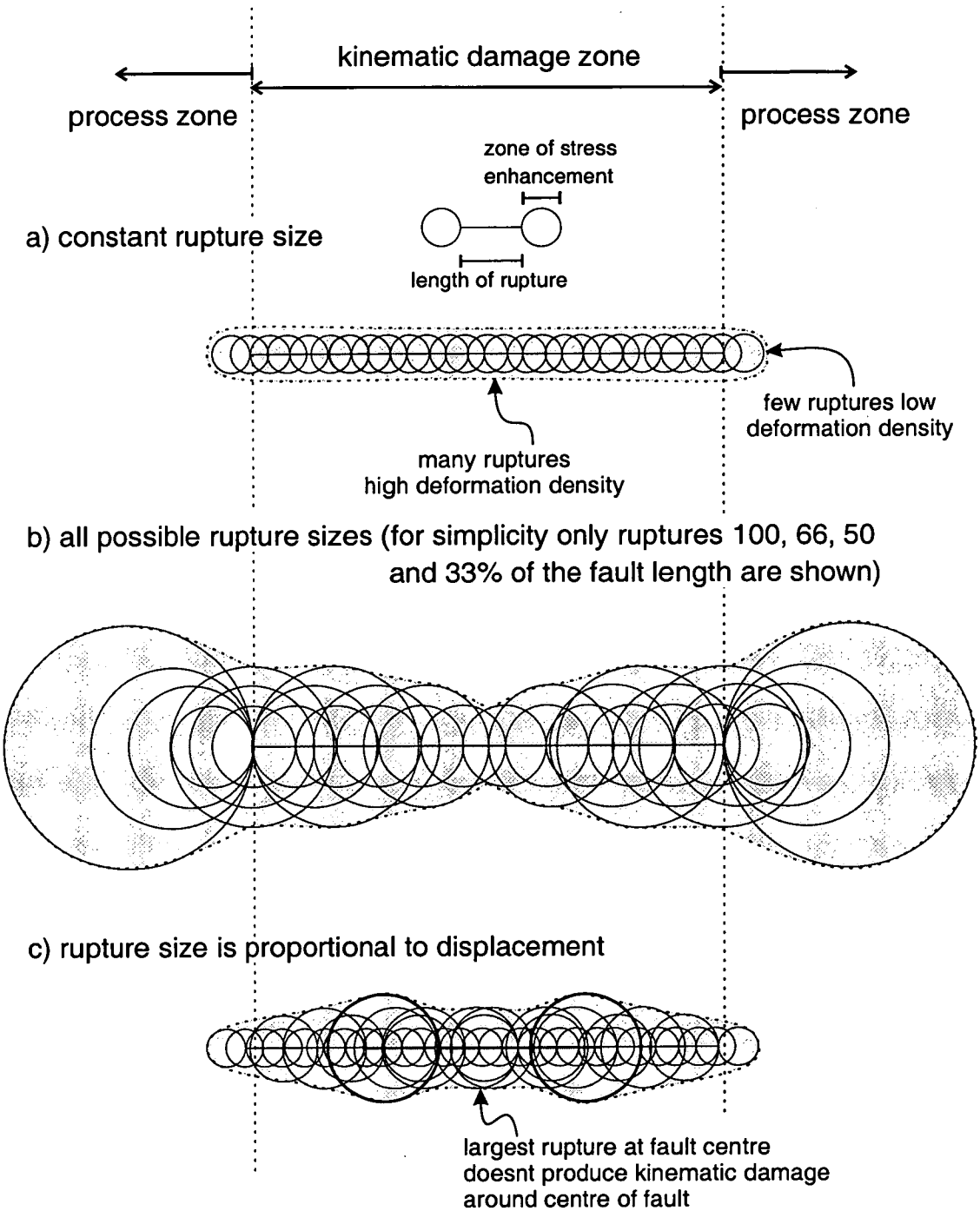

Figure 7.7. Schematic representation of the distribution of off-fault deformation produced due to enhanced stress at the termination of ruptures on the fault for a) many small slip patches of a constant size, b) slip patches of all possible sizes up to and including the size of the fault and c) slip-patches whose length is proportional to the displacemant at the point of rupture initiation. The grey area is the envelope of the off-fault deformation. None of these scenarios produces the positive scaling of damage zone width with displacement as seen at the Big Hole and Blueberry faults.

in all three scenarios, the deformation *density* should be greater at the centre of the fault because more slip events have occurred there. The maximum deformation density around the Big Hole and Blueberry faults is constant (Section 6.5.1), so an alternative explanation must be sought for the observation of scaling off-fault deformation width with displacement, but constant maximum deformation density.

7.5. The slip-patch model applied to the Big Hole and Blueberry faults

7.5.1. The Big Hole and Blueberry fault displacement profiles

The structures in and around the Big Hole and Blueberry faults are consistent with the two main assumptions of the Cowie and Shipton (1998) model, i.e. that the fault slips along small patches and that healing occurs which allows stress to be supported on the fault surface. Microstructures in the fault zone illustrate that it has had a complex history of overprinting slip events. Very low porosity (a high degree of grain crushing) is seen in the cataclasite adjacent to the main fault slip-surface. This is overprinted with open microfractures and Riedel shears in orientations which suggest that they formed due to dip-slip shear parallel to the fault. Multiple cross-cutting relationships between the deformation bands around the main fault surface also confirm that the fault has grown by multiple episodes of slip. The cross-hatched textures within the fault core (Section 4.5.5) suggests that the fault core has also developed through multiple episodes of slip. The evidence for healing on the fault surface is less clear, and is complicated by the lack of understanding of the mechanism of displacement accumulation on slip-surfaces in this rock type (Section 5.5.2). Although slip-surfaces are usually seen as open fractures at the surface, Evans *et al.* (1999) observed in borehole data from this locality, that they are often cemented at depth, indicating that some form of chemical healing has occurred. In addition, physical healing (interlocking of asperities, grain crushing etc.) will have been important in this lithology as evidenced by the strain-hardening deformation bands (Section 7.3.1).

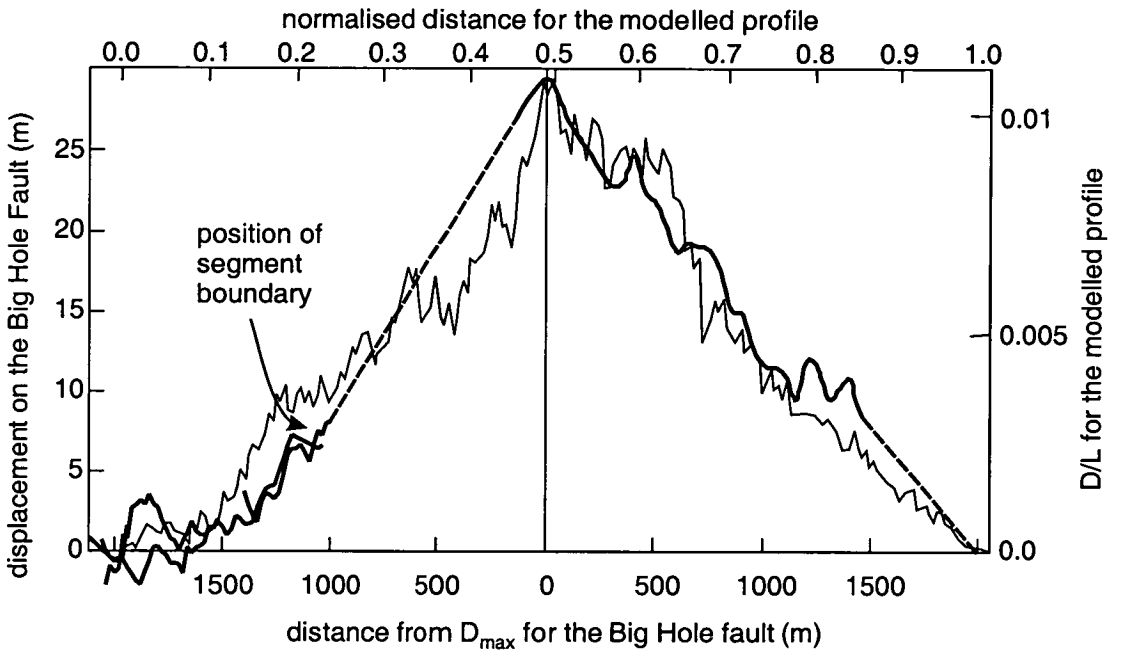

Figure 7.8. Comparison of the displacement profile for the Big Hole fault (thick line) with the modelled profile for t2 in Figure 7.4 (thin line).

The model displacement profiles compare well to the displacement profile for the Big Hole fault (Figure 7.8). This displacement profile is slightly asymmetric; the displacement gradient at the west end of the fault is shallower than at the east end. Much of this asymmetry can be ascribed to the linkage of the main Big Hole fault strand with the segment at the western end of the fault (Figure 2.11). Wu and Bruhn (1994) describe how the enhanced stress along strike of a growing fault would encourage the growth of segments beyond the tip that then link to the main fault. It seems feasible that the western segment of the Big Hole fault has grown in this fashion.

The model suggests that a range of tip gradients are possible throughout the lifetime of an isolated fault, but that the average gradient should be constant for a given rock type. As discussed in Section 3.5.1, the three tip gradients measured in this study are similar (0.007-0.017) and well within the range for isolated fault tip gradients from other studies (Figure 3.14). Because the tip gradient is dependent on the local strength of the rock, the relatively narrow range of tip gradients for the entire Chimney Rock fault array as seen in Figure 3.14 reflects the uniform nature of the Navajo Sandstone.

7.5.2. The Blueberry fault process zone

The process zone at the Blueberry fault tip is smaller than would be expected from the scaling implied by the Cowie and Scholz (1992a) model (Section 5.5.4). If the Cowie and Scholz (1992a) model was applied to this fault then the size of the process zone is predicted to be approximately 360-400 m, i.e. in the order of 10% of the length of the fault. Instead, we see a zone of deformation 12 m wide at the tip of the Blueberry fault. If we interpret this in terms of the slip-patch model, this process zone is formed within the enhanced stress region at the terminations of a small slip-patch which has just reached the end of the fault. Using the same scaling arguments (the width of the zone of enhanced stress is 10% the length of the slip-patch) the slip-patch that we infer would be in the order of 120 m long.

Using the relation between mean slip, Δu, during an earthquake and the length of the rupture, l, (Scholz 1982)

$$\Delta u = \alpha l \qquad (7.2)$$

where $\alpha = 1 \times 10^{-4}$ (Scholz *et al.* 1986), the maximum slip on a 120 m long slip-patch would be 1.2 cm. Of the order of 80 000 ruptures of this size would be required to generate a 4 km long fault with a maximum displacement of 29 m. In comparison, the modelled fault in Figure 7.4 is the product of 95 000 rupture events. This emphasises that a very large number of slip events is required to build even a small fault with only tens of metres of displacement. The precise ratio of the size of the zone of enhanced stress and the length of the slip patch depends on rock properties, which can vary. However if the number of slip events on the fault is large, the extent of the zone of increased stress around individual slip-patches is less important than the symmetry of the reloading along the fault (Section 7.3.3).

No evidence has yet been gathered to demonstrate the size of slip-patches on the Big Hole and Blueberry faults. The resolution of the displacement profiles is not high enough to pick out anomalies in the order if 1.2 cm, the expected slip in one event. It may be possible to look at cross cutting relationships within the off-fault deformation to identify the most recent rupture and its dimensions. However given that slip-patch dimensions in the order of 120 m are expected, individual outcrops around the Big Hole fault may be too small to identify patterns of this scale.

7.5.3. The kinematic damage zone of the Big Hole and Blueberry faults

A discussed in Section 7.4.4, the shape of the off-fault deformation around the Big Hole and Blueberry faults cannot be predicted by simply superimposing the effect of all the slip-patches on a developing fault surface as described in Figure 7.7 and in Cowie and Shipton (1998). This would result in off-fault deformation which is more intense at the centre of the fault where more slip events have taken place. Furthermore, an alternative mechanism is required to explain the correlation between the displacement on the fault and the width of the off-fault deformation, i.e. that the

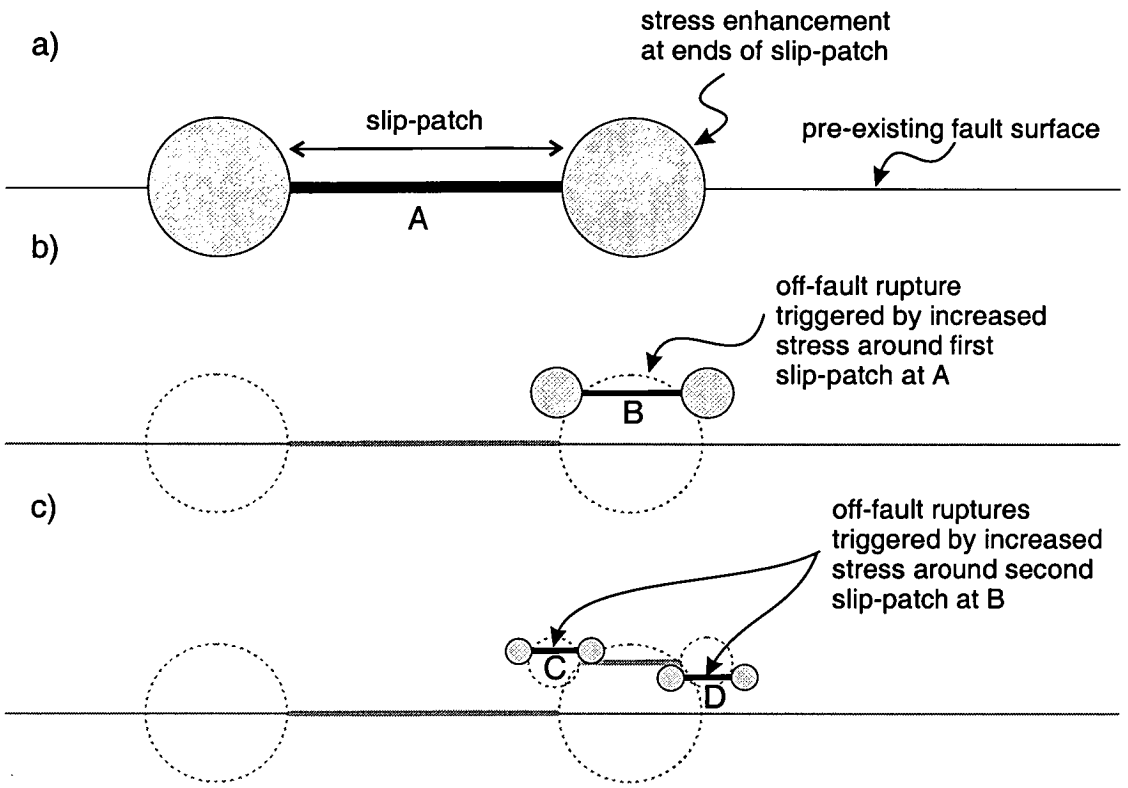

Figure 7.9. Cartoon showing the generation off-fault deformation at increasing distances from the fault. a) A slip-patch is induced on a pre-existing fault surface at point A. The grey area is the zone of enhanced stress at the fault tip. b) Stress enhancement at the tips of slip-patch A induces failure away from the fault at B. c) Stress enhancement at the tips of slip-patch B induces failure away from the fault at C and D. The rock at D is more likely to have previously been strained. Thus the rock is more likely to fail at C. If this process occurs many times the resulting kinematic damage zone will be wider at the fault centre i.e. will scale with displacement on the fault.

maximum width is at the fault centre. The observation of a constant maximum density of off-fault deformation around the Big Hole fault also implies that some form of strain hardening process is transferring deformation away from the main fault with each repeated slip event.

When a slip-patch ruptures, stress is enhanced in a volume around the slip-patch tip as well as directly along strike. This may cause failure of the rock out of the plane of the fault in addition to re-loading the fault plane along strike. Figure 7.9 illustrates this in cartoon form. The rupture at point A on the pre-existing fault surface, has induced slip out of the plane of the fault at point B, which in turn induced rupture at points C and D and so on. Strain hardening is a mechanism that is known to occur in high porosity sandstones, and if this occurs, subsequent failure would be preferentially located in undeformed host rock. It is more likely that the rock on the side of the slip-patch which is further away from the fault will be undeformed, i.e. at point C in Figure 7.9c. In this way deformation will be transferred away from the fault surface. When the effect of tens of thousands of slip events on the main fault surface is summed, the resulting kinematic damage zone will be wider at the centre of the fault. The additional ingredient of strain-hardening allows the slip-patch model to be reconciled with the field observations from the Big Hole and Blueberry faults.

Within the zone of deformation around the Big Hole fault there are places where the strain across deformation band clusters has become large enough to develop a slip-surface. Slip-surfaces allow the accumulation of much larger displacements than zones of deformation bands. If these slip-surfaces also grow by the slip-patch process then they will in turn generate their own kinematic damage zone. This will result in local increases of deformation density (i.e. Section 6.3.2). However, the maximum deformation density will be controlled by the strain hardening process. An apparent scaling of deformation density is seen within a few metres of the main fault surface (Section 6.5.1). This indicates that the deformation mechanisms at high strains close to the fault are no-longer strain hardening.

7.6. Integrated model for off-fault deformation and displacement accumulation through time

7.6.1. Evolution of a single isolated fault

The observations presented in this thesis, coupled with the slip-patch model of Cowie and Shipton (1998), suggest a new integrated model for the formation of off-fault deformation and displacement accumulation through time. The model can be illustrated by looking at the evolution of a single, isolated fault developing through time (Figure 7.10). Figure 7.10a shows the displacement profile and deformation map for a single rupture of an idealised planar fault. The rupture induces deformation in the zone of stress enhancement at its tips. Displacement accumulation on the fault is accommodated by slip on small patches, each one less than or equal to the size of the entire fault surface. For simplicity, all the ruptures are drawn the same size but could theoretically be any size up to the size of the fault. The displacement profiles drawn in Figure 7.10 are the cumulative profiles for all the ruptures on the fault. The fault propagates if a slip-patch is triggered near the fault tip and the resulting rupture propagates into the undeformed host rock around the fault. The process zone at the fault tip is small and reflects the size of the slip-patches which occur at the tip.

Depending on the local strength properties of the host rock ahead of the propagating fault tip the enhanced stress from a slip-patch at the tip could cause it to fail (Figure 7.10b). If this occurs then the tip will propagate, temporarily resulting in a shallower than average fault tip gradient. The displacement will then build up gradually behind this region. Conversely if a strong patch exists at the tip then it can support higher than average displacement gradients. In this way it is possible to get asymmetric or skewed displacement profiles simply through the local variations in host rock strength. As a result, the point of maximum displacement on the fault shifts through time and is not related to the point of nucleation of the fault which has previously been assumed (Ellis and Dunlap 1988). This asymmetry will be reflected in the shape of the kinematic damage zone. Because the width or density of off-fault deformation

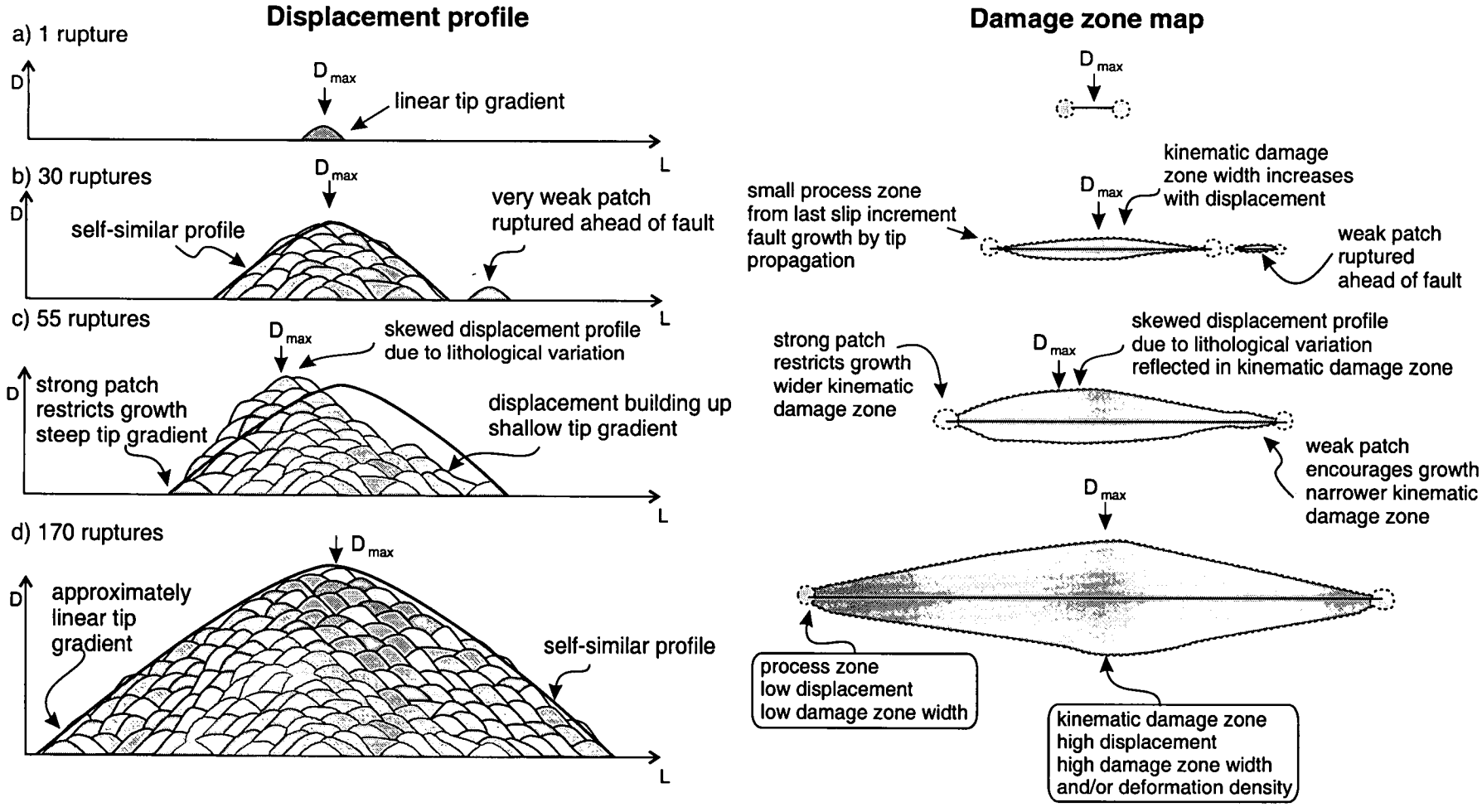

Figure 7.10. Displacement profile and plan view of an evolving fault system through time. a) A single symmetrical rupture. b) After 30 ruptures. c) After 55 ruptures. d) after 170 ruptures. The solid line represents the self-similar displacement profile, i.e. the same shape as the original fault rupture. The different scaling relations for each damage zone category are indicated in the boxes.

is simply proportional to the number of slip events, the shape or density of the kinematic damage zone broadly mirrors the displacement profile.

If the average rock properties do not change, the displacement profile will tend to be self-similar over time (Figure 7.10d). The average displacement gradient at the fault tip reflects the average strength of the rock. If the rock has a more heterogeneous strength distribution there will be more variation in tip gradients through time.

This conceptual model is based on the observations made at the Big Hole and Blueberry faults, but could theoretically be applied to the growth of any fault. The kinematic damage zone has a width and/or deformation density that depends on the number of rupture tips that have occurred on the fault at that point. The kinematic damage zone width/deformation density therefore scales with the fault displacement. Because of the observations at the Blueberry and Big Hole faults, the kinematic damage zone in Figure 7.10 is drawn so that its width scales with displacement. However, for non-strain hardening lithologies the effects of the stress enhancement at slip-patch terminations could simply be superimposed as in Figure 7.7. In this case, the kinematic damage zone width would be approximately constant and the deformation would be more intense at the centre of the kinematic damage zone. The scaling of off-fault deformation width/density with displacement will thus depend on the mechanism of deformation in the host rock. Other studies have shown scaling, but with different scaling relationships (e.g. Knott *et al.* 1996). A more extensive study of fault zones of different sizes, at different stages of evolution and in different host rock types, in particular strain hardening vs. non-strain hardening lithologies, is required to fully understand these effects.

7.6.2. Damage associated with fault linkage

The process of fault growth by linkage has not explicitly been discussed in this thesis. There is evidence for a segment boundary at the west end of the Big Hole fault but the outcrop quality is not good so a detailed investigation of the geometry of a linkage damage zone is not possible here. An integrated model of fault growth must include a consideration of this process, so this section discusses the logical

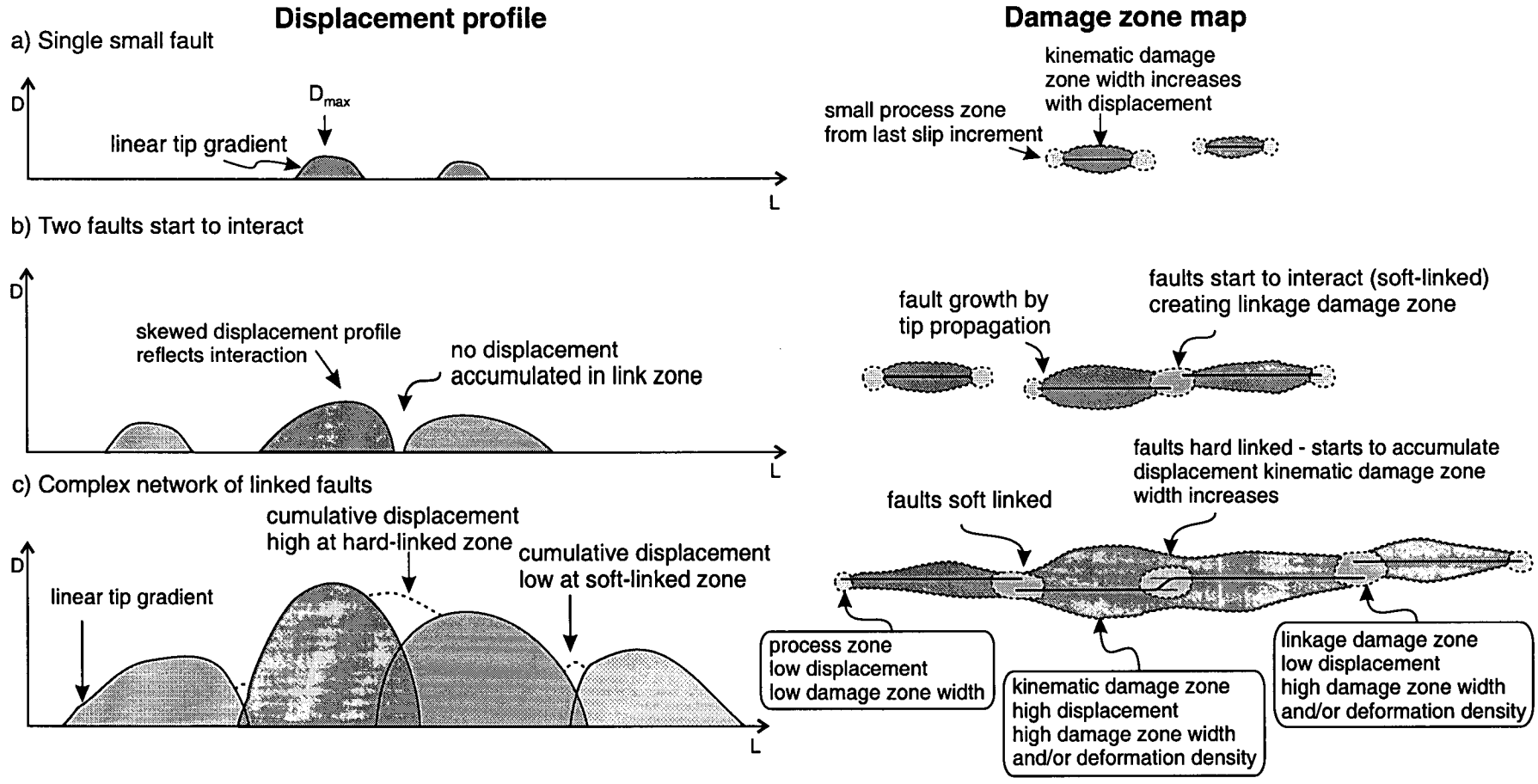

Figure 7.11. Displacement profile and plan view of an evolving fault system showing the different damage zone components. a) A single isolated fault. b) The fault starts to link up with another fault along strike. c) Four segments have linked to vaying degrees to form a long fault. The dotted line represents the cumulative displacement profile, compare to Figure 1.7c. The different scaling relations for each damage zone category are indicated in the boxes.

In Figure 7.11a two single faults are growing independently. Each fault has a small process zone, and a kinematic damage zone which scales with the displacement on the fault as in Figure 7.10. In Figure 7.11b the two faults have started to interact but are soft-linked, that is they are not behaving as a single structure (Walsh and Watterson 1991). This means that displacement is not being accumulated within the segment boundary. Deformation will be caused by the increased stress in the segment boundary producing the linkage damage zone. In Figure 7.11c the segment boundary has become hard-linked. This means that the segment boundary has been breached and the two faults are behaving essentially as one structure. In this case the fault can accumulate displacement within the segment boundary on the new through-going fault surface. The linkage damage zone will be overprinted by deformation caused by continued slip at the segment boundary and a kinematic damage zone will start to develop. However, segment boundaries are often persistent areas of low displacement on the main fault surface, implying that some deformation is permanently partitioned into the linkage damage zone.

The end result is a fault with an irregular width and intensity of damage around the main fault surface (Figure 7.11d). However the rough scaling relationships still hold: the area where the fault has maximum displacement still has the largest amount of kinematic damage, deformation occurs ahead of the propagating fault tips but in a narrow zone, and deformation is concentrated at segment boundaries. The different scaling relations expected for each of the damage zone types helps to explain why many observed fault zones do not have simple distributions of off-fault deformation. Because the generation of off-fault deformation generation is linked to several processes, the resulting shape of off-fault deformation produced by different processes acting on one fault throughout its growth will be complex. In addition, the evolution of a fault into a larger structure may involve changes in the deformation mechanisms through time (e.g. Knipe and Lloyd 1994). However the simple models (kinematic damage zone, process zone, linkage damage zone) shown here will help to distinguish different generations of off-fault structures and to decipher the fault growth history.

8. CONCLUSIONS AND FUTURE WORK

8.1. Conclusions

This thesis presents surveys of two isolated normal faults in the high porosity Navajo Sandstone. The fault displacement profiles and off-fault deformation structures have been examined as part of a linked and evolving system. This process-oriented approach has led to the construction of a more realistic model for fault growth, and to a better understanding of fault growth and the evolution of off-fault deformation through time. The main conclusions of the thesis are as follows:

Fault tip displacement profiles are linear. The displacement profiles of the simple (non-interacting) faults from this study are triangular with a maximum towards the centre of the mapped fault trace and displacement decreasing linearly towards the fault tips. This study contains the highest resolution data from a fault tip displacement profile to date, and confirms that the linear displacement profiles at isolated fault tips seen in other published studies are not an artefact of sparse data. Existing analytical models of fault growth are not compatible with linear fault tip gradients, and must therefore be revised.

A zone of deformation exists around the faults which is due to the nucleation, propagation and accommodation of displacement on the main fault surface. The off-fault deformation consists of deformation bands and slip-surfaces running sub-parallel to the fault. Beyond a certain distance few or no deformation bands are seen. Although the off-fault deformation is clustered, there appears to be a constant maximum density of deformation. Deformation in high porosity (>10%) sandstones is significantly different from that in other rock types; macroscopic structures are produced without forming a large population of microfractures. Microfractures within the host rock show no signal of the fault zone and are therefore interpreted to be inherited.

Deformation is observed ahead of the fault tip. Deformation associated with the Blueberry fault can be traced beyond the point where the displacement on the fault drops to zero. Beyond this point there are no through-going slip-surfaces. This deformation must be associated with the stress concentration at the tip of the propagating fault. Previous studies of fault tip deformation have concentrated on microscopic deformation. However, the deformation ahead of the Blueberry fault consists of a finite width of macroscopic deformation band clusters and an unquantifiable, but probably insignificant, amount of grain boundary deformation.

The off-fault deformation around the well-developed fault surface has formed to accommodate increased displacement on the main fault. The geometry of the off-fault deformation structures around the Big Hole fault surface are consistent with three-dimensional strain resulting from a large component of fault perpendicular strain and a smaller component of fault parallel strain. These are the first observations of orthorhombic geometries within off-fault deformation, and have been deciphered in terms of the strain field due to fault development. Strain parallel to the fault is a result of along-strike extension of the beds as they accommodate displacement on the main fault. The strain perpendicular to the fault is approximately constant along the length of the fault and is consistent with fault perpendicular extension. These observations are consistent with the interpretation that the off-fault deformation is locally accommodating increased slip on the fault surface rather than in the strain field of the regional fault array.

The width of off-fault deformation scales with the displacement on the fault. The width of off-fault deformation is approximately twice the displacement on the main fault. This implies that a link exists between the extent of the off-fault deformation and the number of slip events on the fault. This relationship is potentially useful in predicting sub-seismic fault architecture, however, the predicted width of off-fault deformation could vary by about as much as 10-20% of the average value at a point. The scaling of off-fault deformation width and displacement is dependent on host

rock lithology, in particular strain hardening vs. strain softening lithologies. This study demonstrates the influence of strain hardening explicitly.

The orientation of structures at the fault tip are different to those along the well-developed fault surface. Slickenlines on slip-surfaces around the Big Hole fault are dip-slip, whereas those at the Blueberry fault tip are oblique; pitching 70° to the west of dip-slip. Oblique slickenlines formed at the fault tip are overprinted by subsequent displacement accumulation, and are not seen where the displacement is greater than a few metres. There is a greater scatter in the strikes of deformation bands and deformation band clusters at the tip suggesting that the deformation in the centre of the fault is closer to plane strain compared to the tip. Based on these field observations, the oblique slickenlines may be a function of propagation of a mixed-mode tip line, i.e. between the upwards or downwards propagating, top or bottom of the fault ellipse and the sideways propagating lateral tip (Mode II and Mode III for nomral faults). These observations may help to constrain where the plane of observation intersects the fault surface in a three-dimesional volume.

A new fault growth model gives much more realistic (triangular) displacement profiles than existing analytical models. This model describes how displacement is accumulated by repeated failure and healing of small patches of the fault surface. Each slip event relieves stress adjacent to the fault and increases stress along strike. Healing of the slip-patch, either physical or chemical, allows the patch to support support subsequent loading. When many slip events are summed, the resulting displacement profile is triangular in shape. The model predicts the triangular displacement profiles and linear tip gradients similar to those seen in the field. The tip gradient at any one time is a function of the local strength of the rock and can therefore vary through the lifetime of the fault.

The slip-patch model has led to a new conceptual model for the origin and distribution of off-fault deformation structures through time. Although the slip-patch model is two-dimensional and does not strictly include off-fault deformation, it

can be used to predict the distribution of off-fault deformation. Deformation will occur where the stress is enhanced at the termination of each slip-patch. If the effect of all the slip patches on a fault is superimposed, then the deformation density would be expected to be greater at the centre of the fault. This is not the case at the Big Hole and Blueberry faults because strain hardening has caused the formation of deformation bands at increasing distances from the fault through time. This model can theoretically be applied to the growth of any fault, but the effect of host rock deformation mechanisms must be taken into account.

This study highlights the need for rigorous application of the terms used to describe off-fault deformation. In order to describe deformation around faults without implying any specific genesis it is referred to as off-fault deformation. Off-fault deformation around faults occurs in three key locations. Deformation ahead of the fault tip is referred to as the process zone. The extent of this deformation is dependent on the scale of the slip-patches that rupture the fault at the tip. Deformation associated with the accumulation of displacement on the fault is called the kinematic damage zone. Depending on the deformation mechanisms in the host rock, either the deformation density (strain softening lithologies) or the off-fault deformation width (strain hardening lithologies) will scale with the displacement on the fault. Deformation will also be concentrated at zones where fault segments have linked: the linkage damage zone. Off-fault deformation around real faults will consist of overlapping and overprinting structures from each of these three damage zone types. The process zone, kinematic damage zone and linkage damage zone can be macroscopic or microscopic features depending on the deformation mechanisms in the host rock. In the high porosity Navajo Sandstone the process zone is a macroscopic feature, this is in contrast to previous studies in low porosity sandstones and granite which found a microscopic process zone.

The existing model of deformation band evolution is too simplistic, and does not fully describe the evolution of slip-surfaces from zones of deformation bands. The model of Aydin and Johnson (1978) implies that as a slip surface nucleates

within a zone of deformation bands at either a critical strain across the band or at a critical deformation density. However, the greatest density of deformation is not always coincident with the presence of slip-surfaces. Some slip-surfaces are associated with local thickening on otherwise simple deformation band clusters or single bands. I have demonstrated that displacement accumulation on a slip surface has little effect on the grain size (porosity) of the adjacent rock. The grain size distribution cannot therefore be used to distinguish slip-surfaces formed in off-fault deformation clusters from major fault planes. Grain crushing means that slip-surfaces will have a much reduced permeability perpendicular to the structure but it is unclear to what extent the permeability is enhanced or reduced within the plane of the slip-surface.

8.2. Suggestions for future work

What does off-fault deformation look like in three-dimensions?

Most of the discussion of off-fault deformation so far has concentrated on a two-dimensional plan view. The outcrop at the Blueberry and Big Hole faults is good compared to many field areas because it allows cross-sections of the off-fault deformation to be analysed as well as plan views. However, only a fraction of the down-dip dimension of the fault can be mapped in the dry river canyons. An interesting feature is the cross-hatched pattern seen in the outcrop-scale maps and on stereonets of structures at different scales. This pattern seems to be associated with the linkage of different fault segments at all scales. An ongoing project, which involves coring through the Big Hole fault, will shed more light on the down-dip extent of the off-fault deformation (Evans *et al.* 1999). The variation of slip-vectors and orthorhombic geometry between the fault tip and the well-developed fault surface gives rise to the possibility that there could be a significant difference between process zone and kinematic damage zone geometries. In this thesis it has been suggested that the oblique slickenlines at the fault tip are a function of the

propagation of a mixed-mode tip. A study of fault traces that cut different levels of fault ellipses would be necessary to confirm this suggestion.

What effects the scaling between off-fault deformation zone width and displacement?

Other rock types exhibit very different deformation mechanisms, but do they also have different scaling relations between off-fault deformation zone width and displacement? If the scaling seen in this study is a common phenomenon, it would be an extremely useful tool in predicting the distribution of sub-seismic deformation. More detail on the controls on this scaling, such as the contribution of strain hardening and softening lithologies, and the parameters of the scaling relationships would be needed before this can be demonstrated. The models suggest that the displacement gradient at the fault tip is dependent on the strength distribution of the host rock. Further study is required on faults in host rocks with differing degrees and scales of heterogeneity in order to understand this effect fully.

How does off-fault deformation accumulate around more developed fault systems?

This thesis has examined and discussed the deformation around two single, relatively isolated normal faults only a few kilometres in length. However it is becoming increasingly recognised that deformation in the crust is more commonly taken up on systems of interlinking faults. It is more realistic to model a population of faults that interact as they grow and develop into a complex network. The increased amount of deformation seen around zones where two faults have linked (the linkage damage zone) has been discussed briefly but it would be interesting to see if any scaling exists between, for instance, the overlap/separation ratio and deformation density at segment boundaries. Future studies of off-fault deformation should be linked to displacement on the main fault surface in order to investigate the controls on scaling of off-fault deformation zone width and displacement.

How do slip-surfaces evolve?

This study has indicated that the existing model of deformation band evolution is too simplistic. Slip-surface nucleation and growth is a key to understanding deformation mechanisms in this rock type. The possibility that slip-surfaces may be preserved as open fractures at depth and can form linked arrays within low porosity deformation band clusters means that they have important implications for the permeability structure of fault zones in high porosity sandstones. More microstructural studies of slip-surfaces at all stages of development are required, especially to investigate their relationship to pods of local thickening along deformation bands. Additionally, more data on the distribution of slip-surfaces is needed to assess their contribution to strain within the off-fault deformation. Deformation bands and slip-surfaces have a significant effect on the permeability of high porosity sandstones. The effect of slip-surfaces on permeability will be enhanced if they are interconnected along-strike and down-dip, so an understanding of three-dimensional slip-surface geometry will be critical in studies of fault zone permeability.

REFERENCES

Ackerman, R.V. and Schlische, R. W. 1997. Anticlustering of small normal faults around larger faults. *Geology* 25 1127-1130.

Allmendinger, R.W., Farmer, H., Hauser, E., Sharp, J., Von Tish, D., Olive, J. and Caveman, S. 1986. Phanerozoic tectonics of the Basin and Range-Colorado Plateau transition from COCORP data and geologic data: a review. In: *Reflection seismology: the continental crust.* Barazangi, M. and Brown, L. (eds.) American Geophysical Union Geodynamic Series **14**, 257-266.

Anders, M. A., and Wiltschko, D.V. 1994. Microfracturing, palaeostress and the growth of faults. *Journal of Structural Geology* **16**, 795-816.

Antonellini, M.A. and Aydin, A. 1994. Effect of faulting on fluid flow in porous sandstones: petrophysical properties. *American Association of Petroleum Geologists Bulletin* **78**, 355-377.

Antonellini, M.A. and Aydin, A. 1995. Effect of faulting on fluid flow in porous sandstones: geometry and spatial distribution. *American Association of Petroleum Geologists Bulletin* **79**, 642-671.

Antonellini, M.A., Aydin, A. and Pollard, D. D. 1994. Microstructure of deformation bands in porous sandstones at Arches National Park, Utah. *Journal of Structural Geology* **16**, 941-959.

Aydin, A. 1978. Small faults formed as deformation bands in sandstone. *Pure & Applied Geophysics* **116**, 913-929.

Aydin, A. and Johnson, A. M. 1978. Development of faults as zones of deformation bands and as slip surfaces in sandstones. *Pure & Applied Geophysics* **116**, 931-942.

Aydin, A. and Johnson, A. M. 1983. Analysis of faulting in porous sandstones. *Journal of Structural Geology* **5** 19-31.

Aydin, A. and Reches, Z. 1982. Number and orientation of fault sets in the field and in experiments. *Geology* **10** 107-112.

Barnett, J.A.M., Mortimer, J., Rippon, J.H., Walsh, J.J. and Watterson, J. 1987. Displacement geometry in the volume containing a single normal fault. *Bulletin of the American Association of Petroleum Geologists* **71**, 925-937.

Brantley, S.L., Evans, B., Hickman, S.H. and Crerar, D.A. 1990. Healing of microcracks in quartz: implications for fluid flow. *Geology* **16**, 136-139.

Brock, W.G. and Engelder, T. 1977. Deformation associated with the Muddy Mountain overthrust in the Buffington widow, southeast Nevada. *Bulletin of the Geological Association of America* **88**, 1667-1677.

Bürgmann, R. and Pollard, D. D. and Martel, S.J. 1994. Slip distributions on faults: effects of stress gradients, inelastic deformation, heterogeneous host-rock stiffness and fault interaction. *Journal of Structural Geology* **16**, 1675-1690.

Bürgmann, R. and Pollard, D. D. 1994. Strain accommodation about strike-slip fault discontinuities in granitic rock under brittle-to-ductile conditions. *Journal of Structural Geology* **16**, 1655-1674.

Caine, J.S., Evans, J.P. and Forster, C.B. 1996. Fault zone architecture and permeability structure. *Geology* **24**, 1025-1028.

Cartwright, J.A., Trudgill, B. D. and Mansfield, C. S. 1995a. Fault growth by segment linkage: an explanation for scatter in maximum displacement and trace length data from the Canyonlands Grabens of SE Utah. *Journal of Structural Geology* **17**, 1319-1326.

Cartwright, J.A., Mansfield, C. S. and Trudgill, B. D. 1995b. Fault growth by segment linkage. In *Modern developments in structural interpretation,* P.C. Buchanan and D.A. Nieuwland (eds.) Geological Society of London Special Publication **99** 163-177.

Cartwright, J.A. and Mansfield, C. S. 1998. Lateral displacement variation and lateral tip geometry of normal faults in the Canyonlands National Park, Utah. *Journal of Structural Geology* **20**, 3-19.

Chester, F.M. and Logan, J.M. 1986a. Composite planar fabric of gouge from the Punchbowl Fault, California. *Journal of Structural Geology* **9**, 621-634

Chester, F.M. and Logan, J.M. 1986b. Implications for mechanical properties of brittle faults from observations of the Punchbowl Fault, California: internal structure of fault zones. *Pure & Applied Geophysics* 124, 77-106.

Chester, F.M, Evans, J. P. and Biegel, R.L. 1993. Internal structure and weakening mechanisms of the San Andreas fault. *Journal of Geophysical Research* **98**, 771-786.

Cladouhos, T.T. 1999. Shape preferred orientations of survivor grains in fault gouge. *Journal of Structural Geology* **21**, 419-436.

Clark, R.M. and Cox, S.J.D. 1996. A modern regression approach to determining fault displacement-length scaling relationships. *Journal of Structural Geology* **18**, 147-152.

Cowie P.A. 1998. A healing-reloading feedback control on the growth rate of seismogenic faults. *Journal of Structural Geology* **20**, 1075-1087.

Cowie P.A. and Shipton Z.K. 1998. Fault tip displacement gradients and process zone dimensions. *Journal of Structural Geology* **20**, 983-997.

Cowie P.A. and Scholz C.H. 1992a. Physical explanation for the displacement-length relationship of faults using a post-yield fracture mechanics model. *Journal of Structural Geology* **14**, 1133-1148.

Cowie P.A. and Scholz C.H. 1992b. Growth of faults by accumulation of seismic slip. *Journal of Geophysical Research* **97**, 11085-11096.

Cowie P.A. and Scholz C.H. 1992c. Displacement-length scaling relationship for faults: data synthesis and discussion. *Journal of Structural Geology* **14**, 1149-1156.

Cox, S.J.D. and Scholz, C. H. 1988. On the formation and growth of faults, an experimental study. *Journal of Structural Geology* **10**, 413-430.

Davies, G.H. 1978 Monocline pattern of the Colorado Plateau. In: Laramide folding associated with basement block faulting in the western United States, *Geological society of America Memoir* **151**, 215-232.

Dawers N.H., Anders M.A. & Scholz C. H. 1993. Growth of normal faults: displacement-length scaling. *Geology* **21**, 1107-1110.

Dawers N.H. and Anders M.A. 1995. Displacement-length scaling and fault linkage. *Journal of Structural Geology* **17**, 697-614.

Draper, G. 1976. Grain size as an indication of shear strain in brittle fault zones. *Tectonophysics* **35**, T7-T13.

Dunn, D.E., La Fountain, L.J. and Jackson, R. E. 1973. Porosity dependence and mechanisms of brittle fracture in sandstones. *Journal of Geophysical Research* **78**, 2403-2417.

Edwards, H. E., Becker, A. D. and Howell, J. A. 1993. Compartmetalisation of an aeolian sandstone by structural heterogeneities: Permo-Triassic Hopeman Sandstone, Moray Firth, Scotland. In: *Characterisation of fluvial and aeolian reservoirs.* North, C.P. and Prosser, D. J. (eds.) Geological Society of London Special Publication **73**, 339-365.

Elliott, D. 1976. The energy balance and deformation mechanisms of thrust sheets. *Philosophical Transactions of the Royal Society of London* **A283**, 289-312.

Ellis, M.A. and Dunlap,W.J. 1988. Displacement variations along thrust faults: implications for the development of large faults. *Journal of Structural Geology* **10**, 183-192.

Engelder, J. T. 1974. Cataclasis and the generation of fault gouge. *Bulletin of the Geological Society of America* **85**, 1515-1522.

Evans, J. P. 1990. Thickness-displacement relationships for fault zones. *Journal of Structural Geology* **12**, 1061-1065.

Evans, J. P. 1990. Textures, deformation mechanisms, and the role of fluids in the cataclastic deformation of granitic rocks. In: Deformation mechanisms, rheology and tectonics. Knipe, R. J. & Rutter, E.H. (eds.) *Geological Society Special Publication* **54**, 29-39.

Evans, J. P., Forster, C. B. and Goddard, J. V. 1997. Permeability of fault-related rocks, and implications for hydraulic structure of fault zones. *Journal of Structural Geology* **19**, 1393-1404.

Evans, J. P., Forster, C. B., Jarrard, R., Shipton Z.K.,and Robeson, K. 1999. Big Hole fault drilling project phase I results: Core logging, geophysical results and permeability tests. - Project report for corporate sponsors.

Fossen, H. and Gabrielsen, R.H. 1996. Experimental modelling of extensional fault systems by use of plaster. *Journal of Structural Geology* **18**, 673-687.

Fossen, H. and Hesthammer, J. 1997. Geometric analysis and scaling relations of deformation bands in porous sandstone. *Journal of Structural Geology* **19**, 1479-1493.

Fowles, J. and Burley, S. 1994. Textural and permeability characteristics of faulted, high porosity sandstones. *Marine and Petroleum Geology* **11**, 608-623.

Gauthier, B.D.M. and Lake, S.D. 1993. Probabilistic modelling of faults below the limit of seismic resolution in Pelican field, North Sea, offshore United Kingdom. *Bulletin of the American Association of Petroleum Geologists* **77**, 761-777.

Gibson, J.R., Walsh, J.J. and Watterson, J. 1989. Modelling of bed contours and cross-sections adjacent to planar normal faults. *Journal of Structural Geology* **11**, 317-328.

Gillespie, P.A., Walsh, J.J. and Watterson, J. 1992. Limitations of dimension and displacement data from single faults and the consequences for data analysis and interpretation. *Journal of Structural Geology* **14**, 1157-1172.

Gross, M.R., Gutierrez, G., Bai, T., Wacker, M.A., Collinsworth, K.B. and Behl, R.J. 1997. Influence of mechanical stratigraphy and kinematics on fault scaling relations. *Journal of Structural Geology* **19,** 171-183.

Gupta, A and Scholz, C.H. *submitted* 1999. A model of normal fault interaction based on observations and theory. *Journal of Structural Geology* **?**, ?-?.

Gupta, A and Scholz, C.H. 1998. Utility of elastic models in predicting fault displacement fields. *Journal of Geophysical Research* **103**, 823-834.

Heimpel, M. 1997. Critical behaviour and the evolution of fault strength during earthquake cycles. *Nature* **388**, 865-868.

Hodgkinson, K.M., Stein, R.S. and King, G.C.P. 1996. The 1954 Rainbow Mountain-Fairview Peak-Dixie Valley earthquakes: a triggered normal faulting sequence. *Journal of Geophysical Research* **101**, 25459-25471.

Hull, J. 1988. Thickness-displacement relationships for deformation zones. *Journal of Structural Geology* **10**, 431-435.

Jackson, J. and McKenzie, D. 1998. A hectare of fresh fault striations on the Arkitsa Fault, central Greece. *Journal of Structural Geology* **21**, 1-6.

Jackson, J. and McKenzie, D. 1983. The geometrical evolution of normal fault systems. *Journal of Structural Geology* **5**, 471-482.

Jamison, W. R. and Stearns, D. W. 1982. Tectonic deformation of Wingate sandstone, Colorado National Monument, *Bulletin of the American Association of Petroleum Geologists* **66**, 2584-2608.

Kelly, V. C. 1955 Monoclines of the Colorado Plateau. *Bulletin of the American Association of Petroleum Geologists* **66**, 789-804.

King, G.C.P. 1986. Speculation on the geometry of the initiation and termination processes of earthquake rupture and its relation to morphology and geological structure. *Pure and Applied Geophysics* **124**, 567-585.

King, G.C.P., Stein, R.S. and Lin, J. 1994. Static stress changes and the triggering of earthquakes. *Bulletin of the Seismological Society of America* **84**, 935-953.

Knipe, R. J. and Lloyd, G. E. 1994. Microstructural analysis of faulting in quartzite, Assynt, NW Scotland: Implications for fault zone evolution. *Pure and Applied Geophysics* **143**, 229-254.

Knipe, R. J., Jones, G. and Fisher, Q.J. 1998. Faulting, fault sealing and fluid flow in hydrocarbon reservoirs: an introduction. In: *Faulting, fault sealing and fluid flow in hydrocarbon reservoirs.* Knipe, R. J., Jones, G. and Fisher, Q.J. (eds.) Geological Society of London Special Publication **147**, vii-xxi.

Knott, S.D., Beach, A., Brockbank, P.J., Brown, J.L., McCallum, J.E. and Welbon, A. I. 1996. Spatial and mechanical controls on normal fault populations. *Journal of Structural Geology* **18**, 359-372.

Krantz, R.W. 1988a. Multiple fault sets and three-dimensional strain: theory and application. *Journal of Structural Geology* **10**, 225-237.

Krantz, R.W. 1988b. The odd-axis model: orthorhombic fault patterns and three-dimensional strain fields. Unpublished Ph.D. thesis. University of Arizona.

Krantz, R.W. 1989. Orthorhombic fault patterns: the odd-axis model and slip vector orientations. *Tectonics* **8**, 483-495.

Kranz, R.L. 1983. Microcracks in rocks: a review. *Tectonophysics* 100, 449-480.

Lawn, B.R. and Wilshaw, T.R. 1975. *Fracture of brittle solids.* Cambridge University Press.

Lawton, C.A. 1986. *in* Peterson, ed., Palaeotectonics and sedimentation in the Rocky Mountain Range, *American Association of Petroleum Geologists Memoir* **41**, 423.

Lin, J. and Parmentier, E. M. 1988. Quasistatic propagation of a normal fault: a fracture mechanics model. *Journal of Structural Geology* **3**, 249-262.

Little, T.A. 1996. Faulting-related displacement gradients and strain adjacent to the Awatere strike-slip fault in New Zealand. *Journal of Structural Geology* **18**, 321-342.

Lockner, D.A., Byerlee, J.D., Kuksenko, V., Ponomarev, A. and Sidorin, A. 1991. Quasi-static fault growth and shear fracture energy in granite. *Nature* **350** 39-42.

Lockner, D.A., Byerlee, J.D., Kuksenko, V., Ponomarev, A. and Sidorin, A. 1992. Observations of quasistatic fault growth from acoustic emissions. In: *Fault mechanics and transport properties of rocks.* B. Evans and T. F. Wong (eds.) 34-67.

Logan, J.M., Dengo, C.A., Higgs, N.G. and Wang, Z.Z. 1992. Fabrics of experimental fault zones: their development and relationship to mechanical behaviour. In: *Fault mechanics and transport properties of rocks.* B. Evans and T. F. Wong (eds.) 34-67.

McGill, S.F and Rubin, C.M. 1999. Surficial slip distribution on the central Emerson fault during the June 28, 1992, Landers earthquake, California. *Journal of Geophysical Research* **104**, 4811-4833.

McGrath, A.G. and Davison, I. 1995. Damage zone geometry around fault tips. *Journal of Structural Geology* **17**, 1011-1024.

McGrath, A.G. 1992. Fault propagation and growth; a study of the Triassic and Jurassic from Watchet and Kilve, north Somerset. Unpublished Masters thesis. Royal Holloway, University of London.

McMillan, R.A. 1975. The orientation and sense of displacement on strike-slip faults in continental crust. Unpublished Bachelors thesis. Carleton University, Ottowa, Ontario.

Mair, K. 1997. Experimental studies of fault zone development in a porous sandstone. Unpublished Ph.D. thesis. University of Edinburgh.

Mair, K., Main, I. and Elphick, S. 1999. Sequential growth of deformation bans in the laboratory. *Journal of Structural Geology* **22**,25-42.

Mansfield, C. S. and Cartwright, J.A. 1996. High resolution fault displacement mapping from three-dimensional seismic data: evidence for dip linkage during fault growth. *Journal of Structural Geology* **18**, 249-263.

Manzocchi, T., Ringrose, P.S. and Underhill, J.R. 1998. Flow through fault systems in high-porosity sandstones. In: *Structural geology in reservoir characterisation.* Coward, M.P., Daltaban, T.S. and Johnson, H. (eds.) Geological Society of London Special Publication **127**, 65-82.

Marone, C. 1998. The effect of loading rate on static friction and the rate of fault healing during the earthquake cycle. *Nature* **391**, 69-72.

Marret, R. and Allmendinger, R.W. 1991. Estimates of strain due to brittle faulting: sampling of fault populations. *Journal of Structural Geology* **13**, 735-738.

Martel, S.J. and Boger, W.A. 1998. Geometry and mechanics of secondary fracturing around small three-dimensional faults in granitic rock. *Journal of Geophysical Research* **103**, 21299-21314.

Morewood, N.C. and Roberts, G.P. 1997. Geometry, kinematics and rates of deformation in a normal fault segment boundary, central Greece. *Geophysical Research Letters* **24**, 3081-3084.

Muraoka, H and Kamata, H. 1983. Displacement distribution along minor fault traces. *Journal of Structural Geology* **5**, 483-495.

Myers, R. and Aydin, A. (submitted 1999). The evolution of faults formed by shearing across joint zones in sandstone. *Journal of Structural Geology* **?**, ?.

Nicol, A., Walsh, J.J. and Watterson, J. and Childs, C. 1996. The shapes, major axis orientations and displacement patterns of fault surfaces. *Journal of Structural Geology* **18**, 235-248.

Opheim, J.A. and Gudmundsson, A. 1989. Formation and geometry of fractures, and related volcanism, of the Krafla fissure swarm, northeast Iceland. *Geological Society of America Bulletin* **101**, 1608-1622.

Peacock, D.C.P. 1991. Displacement and segment linkage in strike-slip fault zones. *Journal of Structural Geology* **13**, 1025-1035.

Peacock, D.C.P. and Sanderson, D. J. 1991. Displacement, segment linkage and relay ramps in normal fault zones. *Journal of Structural Geology* **13**, 721-733.

Peacock, D.C.P. and Sanderson, D. J. 1994. Geometry and development of relay ramps in normal fault systems. *Bulletin of the American Association of Petroleum Geologists* **78**, 147-165.

Peacock, D.C.P. and Sanderson, D. J. 1996. Effects of propagation rate on displacement variations along faults. *Journal of Structural Geology* **18**, 311-320.

Peterson, F. and Pipiringos, G.N. 1979. Stratigraphic relations of the Navajo Sandstone to Middle Jurassic formations, southern Utah and northern Arizona. *United States Geological Survey Professional Paper* **1035 B**, B1-B36.

Pickering, G., Peacock, D.C.P., Sanderson, D. J. and Bull, J.M. 1997. Modelling tip zones to predict the throw and length characteristics of faults. *Bulletin of the American Association of Petroleum Geologists* **81**, 82-99.

Pittman, E.D. 1981 Effect of fault-related granulation on porosity and permeability of quartz sandstones, Simpson group (Ordovician), Oklahoma. *Bulletin of the American Association of Petroleum Geologists* **65**, 2381-2387.

Pollard, D. D. and Segall, P. 1987. Theoretical displacements and stresses near fractures in rock: with applications to faults joints, veins, dikes and solution surfaces. In: *Fracture mechanics of rock.* Atkinson, B. (ed.) Academic press, London.

Reches, Z. 1978. Analysis of faulting in a three-dimensional strain fields. *Tectonophysics* **47**, 109-129.

Reches, Z. 1983. Faulting of rocks in three-dimensional strain fields II. theoretical analysis. *Tectonophysics* **95**, 133-156.

Reches, Z. and Lockner D.A. 1994. Nucleation and growth of faults in brittle rocks. *Journal of Geophysical Research* **99**, 18159-18173.

Rippon, J.H. 1985. Contoured patterns of the throw and hade of normal faults in the Coal Measures (Westphalian) of northwest Derbyshire. *Procedings of the Yorkshire Geological Society* **45**, 147-161.

Roberts, G.P. 1996a. Noncharacteristic normal faulting surface ruptures from the gulf of Corinth, Greece. *Journal of Geophysical Research* **101**, 25255-25267.

Roberts, G.P. 1996b. Variation in fault slip directions along active and segmented normal fault systems. *Journal of Structural Geology* **18**, 835-845.

Sammis, C. G., King, G. & Biegel, R. 1987. The Kinematics of gouge deformation. *Pure and Applied Geophysics* **125**, 777-812.

Saleeby, J.B. and Busby-Spera, C. 1992. Early Mesozoic tectonic evolution of the western U.S. Cordillera. *in* Burchfiel, B.C., Lipman, P.W. and Zoback, M.L. (eds.) The Geology of North America, vol. G-3, The Cordillera Orogen: Conterminous U.S. *Geological Society of America.*

Schlische, R.W., Young, S.S., Ackerman, R.V. & Gupta, A. 1996 Geometry and scaling relations of a population of very small rift related normal faults. *Geology* **24**, 683-686.

Scholtz, C. H. 1968. Microfracturing and the inelastic deformation of rock in compression. *Journal of Geophysical Research* **73**, 1417-1432.

Scholtz, C. H. 1990. *Mechanics of earthquakes and faulting.* Cambridge University Press.

Scholtz, C.H. 1982. scaling laws for earthquakes: consequences for phsyical models. *Bulletin of the Seimological society of America* **372**, 65-70.

Scholtz, C.H. and Cowie, P.A. 1990. Determination of total strain from faulting using slip-measurements. *Nature* **346**, 837-839.

Scholtz, C.H., Dawers, N.H., Yu, J.Z. and Anders, M.H. 1993. Fault growth and fault scaling laws: preliminary results. *Journal of Geophysical Research* **98**, 21951-21961.

Segall, P. and Pollard, B. 1983. Nucleation and growth of strike-slip faults in granite. *Journal of Geophysical research* **88**, 555-568.

Sibson, R. H. 1977. Fault rocks and fault mechanisms. *Journal of the Geological Society of London* **133**, 199-213.

Smith, D.L. and Evans, B. 1984. Diffusional crack healing in quartz. *Journal of Geophysical Research* **89**, 4125-4135.

Stein, R.S., Barrientos, S.E. 1983. Planar high-angle faulting in the Basin and Range: Geodetic analysis of the 1983 Borah Peak, Idaho, earthquake. *Journal of Geophysical Research* **90**, 11355-11366.

Trudgill, B. D. and Cartwright, J.A. 1994. Relay-ramp forms and normal fault linkages, Canyonlands National Park, Utah. *Geological Society of America Bulletin* **106**, 1143-1157.

Twiss, R.J. and Moores, E.M. 1992. *Structural Geology.* W.H. Freeman and Co.

Underhill, J.R. and Woodcock, N.H. 1987. Faulting mechanisms in high porosity sandstones, New Red Sandstone, Arran, Scotland. In: *Deformation of sediments and sedimentary rocks.* Jones, M.E. & Preston R.M.F. (eds.) Geological Society of London Special Publication **29**, 29-105.

Vermilye, J.M. 1996. The growth of natural fracture systems: a fracture mechanics approach. Ph.D. thesis. Columbia University, New York.

Vermilye, J.M. and Scholz, C. H. 1995. Relation between vein length and aperture. *Journal of Structural Geology* **17**, 423-434.

Vermilye, J.M. and Scholz, C. H. 1998. The process zone: a microstructural view. *Journal of Geophysical Research* **103**, 12223-12237.

Villemin, T., Angelier, J., and Sunwoo, C. 1995. Fractal distribution of fault length and offsets: Implications of brittle deformation evaluation - Lorraine coal basin. In: *Fractals in the earth sciences.* Barton, C.C. and La Pointe, P.R. (eds.) Plenum Press, New York.

Walsh, J.J. and Watterson, J. 1987. Distribution of cumulative displacement and seismic slip on a single normal fault surface. *Journal of Structural Geology* 9, 1039-1046.

Walsh, J.J. and Watterson, J. 1988. Analysis of the relationship between displacements and dimensions of faults. *Journal of Structural Geology* **10**, 239-247.

Walsh, J.J. and Watterson, J. 1989. Displacement gradients on fault surfaces. *Journal of Structural Geology* **11**, 307-316.

Walsh, J.J. & Watterson, J. 1991. Geometric and kinematic coherence and scale effects in normal fault systems. In: *The geometry of normal faults.* Yielding, A.M. & Freeman, B. (eds.)Geological Society of London Special Publication **56**, 193-203.

Willemse, E. J. M., Pollard, D. D. and Aydin, A. 1996. Three-dimensional analysis of slip distributions on normal fault arrays with consequences for fault scaling. *Journal of Structural Geology* **18**, 295-310.

Witkind, I.J. 1988. Geologic map of the Huntingdon 30' x 60' quadrangle, Carbon, Emery and Uinta counties, Utah.

Witkind, I.J. 1991. Implications of distinctive fault sets in the San Rafael Swell and adjacent areas, east-central Utah. In: *Geology of east-central Utah.* Chidsey, T.C. Jnr. (ed.) Utah Geological Association Guidebook **19**, 141-148.

Wong, T. F 1990. Mechanical compaction and the brittle-ductile transition in porous sandstones. In: *Deformation mechanisms, rheology and tectonics.* Knipe, R. J. & Rutter, E.H. (eds.) Geological Society of London Special Publication **54**, 111-122.

Woodcock, N.H. and Underhill, J.R. 1987. Emplacement-related fault patterns around the Northern Granite, Arran, Scotland. *Geological Society of America Bulletin* **98**, 515-527.

Wu D. and Bruhn, R.L. 1994. Geometry and kinematics of active normal faults, South Orquirrh Mountains, Utah: implication for fault growth. *Journal of Structural Geology* **16**, 1061-1075.

Yielding, G, Needham, T and Jones, H. 1996. Sampling of fault populations using sub-surface data: a review. *Journal of Structural Geology* **18**, 135-146.